ISBN 978-82-326-2048-7 (printed ver.)
ISBN 978-82-326-2049-4 (electronic ver.)
ISSN 1503-8181

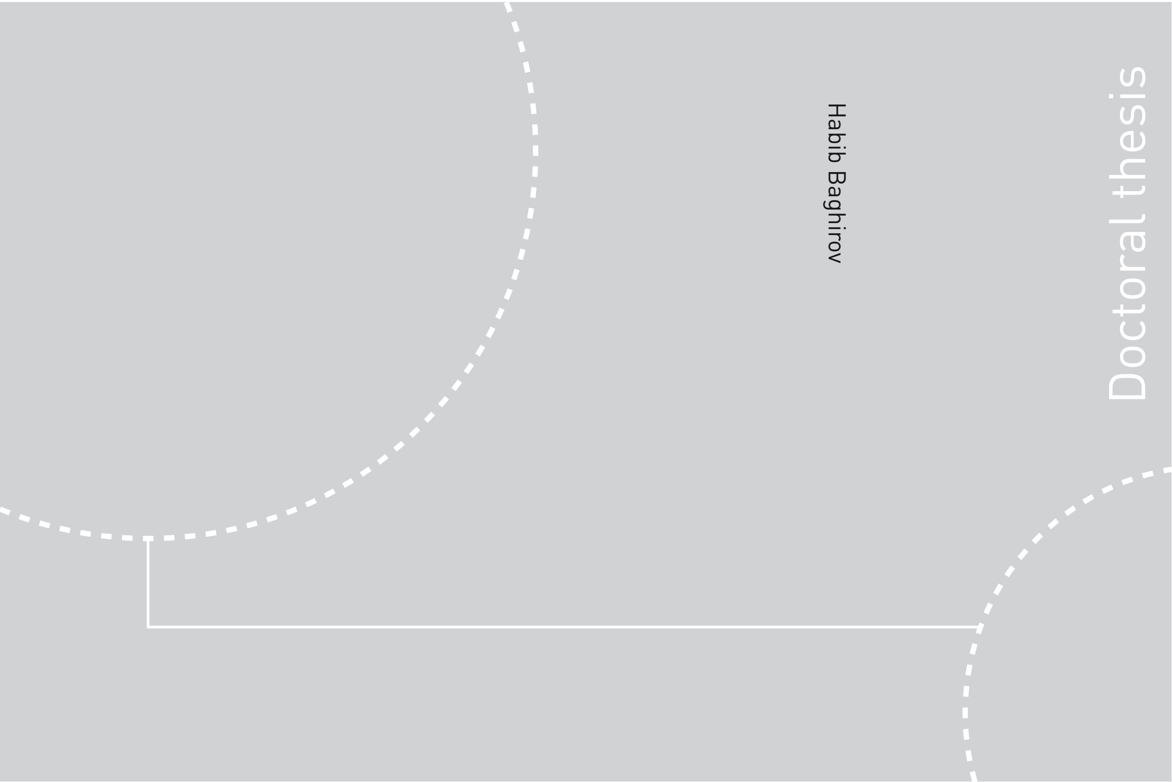

Habib Baghirov

Doctoral thesis

Doctoral theses at NTNU, 2017:3

NTNU
Norwegian University of Science and Technology
Thesis for the Degree of
Philosophiae Doctor
Faculty of Natural Sciences and Technology
Department of Physics

NTNU
Norwegian University of
Science and Technology

NTNU

Doctoral theses at NTNU, 2017:3

Habib Baghirov

Nanoparticle uptake by brain endothelial cells and focused ultrasound-mediated transport across the blood-brain barrier

NTNU
Norwegian University of
Science and Technology

Habib Baghirov

Nanoparticle uptake by brain endothelial cells and focused ultrasound-mediated transport across the blood-brain barrier

Thesis for the Degree of Philosophiae Doctor

Trondheim, December 2016

Norwegian University of Science and Technology
Faculty of Natural Sciences and Technology
Department of Physics

NTNU
Norwegian University of
Science and Technology

NTNU
Norwegian University of Science and Technology

Thesis for the Degree of Philosophiae Doctor

Faculty of Natural Sciences and Technology
Department of Physics

ISBN ISBN 978-82-326-2049-4 (printed ver.)
ISBN ISBN 978-82-326-2048-7 (electronic ver.)
ISSN 1503-8181

Doctoral theses at NTNU, 2017:3

Printed by NTNU Grafisk senter

Abstract

The treatment of brain diseases, including brain cancer, is hindered by the blood-brain barrier (BBB). Nanoparticles (NPs) can offer numerous benefits in drug delivery due to their high drug loading capacity, incorporation of poorly soluble drugs, functionalization for controlled release and targeting to specific cells. Brain delivery of NPs, however, can be improved by using versatile BBB opening techniques such as focused ultrasound (FUS) in combination with microbubbles.

In this thesis, we extensively characterized biological interactions of poly(alkyl cyanoacrylate) (PACA) NPs, promising drug delivery carriers, to study their potential for the delivery of encapsulated cargo into brain endothelial cells and across the BBB. We found that the encapsulation of model drugs in a number of NP platforms affected cargo retention and cellular uptake of NPs by brain endothelial cells and solid tumor cells, highlighting the need for a thorough assessment of NPs following any modification or incorporation of new cargo. Next we investigated whether such assessment of NP uptake potential at the BBB could be done using biomimetic cell membranes and whether different combinations of poly(ethylene glycol) (PEG), a polymer commonly used to shield NPs in the bloodstream, can facilitate cellular uptake of NPs. We found that the interaction of PACA NPs with biomimetic membranes could be a useful predictor of the uptake potential of these NPs by brain endothelial cells, and that a particular combination of PEG types strongly affected interactions of NPs both with biomimetic membranes and with cells. Our study into the cellular uptake and intracellular degradation of PACA NPs again demonstrated their high endocytic uptake by brain endothelial cells and solid tumor cells and showed that the intracellular degradation of these NPs and subsequent release of encapsulated cargo depended on the monomer chain length. Our next study into the feasibility of NPs crossing the BBB was performed with mesoporous silica NPs, another promising type of drug nanocarriers. We again showed efficient uptake of NPs at the brain endothelium both *in vitro* and *in vivo*, but did not demonstrate substantial crossing of the BBB in either scenario. Finally, we used FUS with a novel platform combining PACA NPs with microbubbles and showed successful brain delivery of NPs in a melanoma brain metastasis model.

In summary, our results indicate that NPs can be a powerful tool in drug delivery at the brain endothelium and that FUS can further improve NP delivery into the brain and its distribution in the brain tissue.

Preface

This thesis has been submitted to the Faculty of Natural Sciences of the Norwegian University of Science and Technology (NTNU) in partial fulfillment of the requirements for the degree of Philosophiae Doctor (PhD). The project has been funded by the Research Council of Norway, NANO2021. The work has mainly been carried out at the Department of Physics, NTNU, from September 2013 to August 2016 under the supervision of Professor Catharina de Lange Davies at the Department of Physics, NTNU, Dr. Wilhelm Glomm at SINTEF Materials and Chemistry, and Dr. Rune Hansen at SINTEF Technology and Society.

Acknowledgments

This work could not have been performed without the valuable contribution of numerous people to whom I am grateful.

I would like to thank my supervisor, Catharina de Lange Davies, who has always been ready to share advice and offer guidance. It has been a privilege to observe your remarkable determination to see positive outcomes in all scientific challenges.

I would like to thank the co-supervisors of my thesis, Wilhelm Glomm and Rune Hansen. Not everything went well in the side project Wilhelm and I worked on for a while, but he was never the one to throw in the towel. And while only a part of this thesis involves focused ultrasound, the science behind that part has, to a considerable extent, been Rune's contribution.

I would like to thank Jessica Rosenholm and Cecilia Sahlgren, supervisors of my MS project who first supported me when I decided to get nanoparticles into the brain to treat brain diseases. Crossing the brain endothelium safely is a daunting task, even more so with therapeutic nanoparticles, but I believe we will get there one day!

Although integrin-mediated cell adhesion is not directly linked to this thesis, I am very grateful to my former supervisor Johanna Ivaska in whose lab I learned to stop worrying and love (automated) microscopy, and gained several other skills that greatly helped me in this project.

I would like to thank everyone involved in the design and synthesis of nanoparticles used during this project. Yrr, Einar, Jessica, Didem, Sjoerd, Wilhelm and Sulalit - without your nanoparticles, the novelty of all research in my PhD project plan would be considerably

reduced. Anne Hatletveit and Maria Gellein are also thanked for technical assistance with making polymeric nanoparticles and nanoparticle-stabilized microbubbles.

I would like to thank all of the co-authors on the papers in this thesis. Without your contribution, this work would have been impossible. Come to think of it, even with your contribution it has not been easy at all.

A part of this thesis is based on experiments performed at Comenius University, and I am very grateful to Tibor Hianik and his wife Maria, as well as all members of the Hianik lab for their hospitality during my stay in Bratislava.

Another part of this thesis is based on experimental work carried out at the University of Helsinki, and I would like to thank Tapani Viitala who introduced me to surface plasmon resonance measurement.

I would like to thank everyone in who helped me with the part of this research work that involves mesoporous silica nanoparticles. In addition to those mentioned above, I would like to thank Marjo Yliperttula, Yan Ru-Lou, Diana Toivola, Adyary Fallarero, Perttu Terho, Jouko Sandholm, and Helena Saarento.

I would like to extend my gratitude to Frits Thorsen, whose experimental model is used in the project’s *in vivo* part, for arranging a training session in Bergen and teaching me how to work with the model. I would also like to thank Mari-Ann Davidsen for her assistance with some practical aspects of that training.

It has been a pleasure to work with Marion Malenge, a MS student whose enthusiasm and optimism have been truly contagious. I wish you the best in your current PhD studies and future career!

I would like to thank Annemieke van Wamel for technical assistance and advice concerning ultrasound-related experiments.

I would like to thank our trusted engineers Astrid Bjorkøy and Kristin Sæterbø for assistance with cell culturing, flow cytometry, microscopy and, possibly, other things I may have forgotten about.

I would like to thank Øystein Hagemø at the mechanical workshop for his ingenuity in designing various *in vitro* ultrasound setups that almost, but not quite made their way into this thesis.

I am grateful to Marianne Furnes, Siv Eggen and everyone else who provided feedback and helped me improve my applications for animal experiments.

The NTNU animal facility, personified by Anne Åm and Trine Skoglund for the purposes of this thesis, is thanked for caring about the animals and providing other assistance and advice related to animal work.

Marius Widerøe and Tina Bugge at the MR center – your help is much appreciated.

I would like to thank everyone at the Histology lab of the Cellular & Molecular Imaging Core Facility for their assistance with brain sectioning and immunohistochemistry.

In general, all consultants are thanked for consulting, technical assistants - for technical assistance, funders - for funding, engineers - for engineering, and lab mates - for creating and maintaining a professional and pleasant work environment.

I would like to thank the administration of the Department of Physics for its support with practical matters related to my PhD work.

Erik Ingerbritsen, Hanne Lehn, Øyvind Eiksund, Liv Falkenberg and everyone else at the Norwegian Research School in Medical Imaging (Medim) who I have been in contact with are thanked for their assistance with practical matters regarding participation at various Medim-supported conferences and courses throughout my PhD project. Dissemination of results at these conferences has been a valuable part of this work.

Most importantly, I would like to thank all of my family, immediate and extended, for their continuing support for my interest in medical research. In particular, my father Sarhad has always encouraged me to pursue what fascinates me the most, and has been a model of integrity in both science and life in general. I owe you a lot, Father!

List of Abbreviations

ARF	Acoustic radiation force
BBB	Blood-brain barrier
BBBD	Blood-brain barrier disruption
BCEC	Brain capillary endothelial cells
BCRP	Breast cancer resistance protein
BCSF	Blood-cerebrospinal fluid barrier
CAR	Coxsackie and adenovirus receptor
CED	Convection-enhanced delivery
CLSM	Confocal laser scanning microscopy
CMT	Carrier-mediated transport
CNS	Central nervous system
CSF	Cerebrospinal fluid
DLS	Dynamic light scattering
ECM	Extracellular matrix
EPR	Enhanced permeability and retention
ESAM	Endothelial cell-selective adhesion molecule
FCM	Flow cytometry
FLIM	Fluorescence lifetime imaging microscopy
FRET	Förster resonance energy transfer
FUS	Focused ultrasound
ICF	Interstitial fluid
ICV	Intracerebroventricular
JAM	Junction adhesion molecule
LDL	Low density lipoprotein
mAb	Monoclonal antibody
MB	Microbubble
MI	Mechanical index
MRP	Multidrug-resistance associated protein
MSN	Mesoporous silica nanoparticle
MW	Molecular weight
NP	Nanoparticle
PACA	Poly(alkyl cyanoacrylate)
PBCA	Poly(butyl cyanoacrylate)
PIHCA	Poly(isohexyl cyanoacrylate)
PEG	Poly(ethylene glycol)
PEI	Poly(ethylene imine)
P-gp	P-glycoprotein
RES	Reticuloendothelial system
TEER	Transendothelial resistance
TJ	Tight junction
ZO	Zonula occludens

List of Publications

Publications included in this thesis

I. Snipstad S, Hak S, **Baghirov H**, Sulheim E, Mørch Ý, Lélu S, von Haartman E, Bäck M, Nilsson KP, Klymchenko AS, de Lange Davies C, Åslund AK., *Labeling nanoparticles: Dye leakage and altered cellular uptake*. Cytometry A. 2016 Apr 14 [Epub ahead of print].

II. **Baghirov H**, Melikishvili S, Mørch Y, Sulheim E, Åslund AK, Hianik T, Davies Cde L., *The effect of poly(ethylene glycol) coating and monomer type on poly(alkyl cyanoacrylate) nanoparticle interactions with lipid monolayers and cells*, submitted.

III. Sulheim E*, **Baghirov H***, von Haartman E, Bøe A, Åslund AK, Mørch Y, Davies Cde L., *Cellular uptake and intracellular degradation of poly(alkyl cyanoacrylate) nanoparticles*. J Nanobiotechnology. 2016 Jan 8;14:1. **(* - equal contribution)**.

IV. **Baghirov H**, Karaman D, Viitala T, Duchanoy A, Lou YR, Mamaeva V, Pryazhnikov E, Khiroug L, Davies Cde L, Sahlgren C, Rosenholm J., *Feasibility study of the permeability and uptake of mesoporous silica nanoparticles across the blood-brain barrier*. PLoS One. 2016 Aug 22;11(8).

V. **Baghirov H**, Snipstad S, Sulheim E, Berg S, Hansen R, Thorsen F, Mørch Y, Davies Cde L. Åslund AK, *Ultrasound-mediated delivery and distribution of polymeric nanoparticles in the normal brain parenchyma and melanoma metastases*, manuscript in preparation.

Contribution to other papers during the PhD project period

- Mai A, Muharram G, Barrow-McGee R, **Baghirov H**, Rantala J, Kermorgant S, Ivaska J., *Distinct c-Met activation mechanisms induce cell rounding or invasion through pathways involving integrins, RhoA and HIP1*, J Cell Sci. 2014 May 1;127(Pt 9):1938-52.
- Jacquemet G, **Baghirov H**, Georgiadou M, Sihto H, Peuhu E, Cettour-Janet P, He T, Perälä M, Kronqvist P, Joensuu H, Ivaska J., *L-type calcium channels act downstream of integrin signalling at filopodia tips to regulate filopodia stability and cancer cell invasion*, awaiting formal acceptance in Nat Commun.

My contribution to the papers included in this thesis:

In **Paper I**, I performed all experiments with RBE4 rat brain endothelial cells, as well as all accompanying data analysis, prepared figures related to the results produced with RBE4 cells and contributed to the revision and discussion of the paper. Nanoparticle platforms used in this paper were made at SINTEF Materials and Chemistry (Trondheim, Norway) or synthesized by Sjoerd Hak.

In **Paper II**, I performed all experiments on the interaction of nanoparticles with lipid monolayers and cells, prepared all of the figures, performed all data analysis and wrote the manuscript. Brewster angle microscopy experiments were performed with crucial help from Sopio Melikishvili. Nanoparticles used in this paper were made at SINTEF Materials and Chemistry.

In **Paper III**, I had a leading contribution to the part of the paper related to nanoparticle uptake, performed all experiments with RBE4 rat brain endothelial cells, as well as all accompanying data analysis, prepared all figures related to the results produced with RBE4 cells and assisted in writing the manuscript. Nanoparticles used in this paper were made at SINTEF Materials and Chemistry.

In **Paper IV**, I performed most of the experiments on cells, prepared most of the figures, performed most of data analysis and wrote the manuscript. Surface plasmon resonance measurements on cells in this paper were performed jointly with Tapani Viitala who also performed all accompanying data analysis and prepared the figures. Nanoparticles used in this paper were made at the Pharmaceutical Sciences Laboratory (Turku, Finland).

In **Paper V**, I performed all work related to the development of metastatic tumors in the experimental model, assisted in the experiments related to focused ultrasound-mediated blood-brain barrier opening, performed all work related to brain section imaging and image analysis, performed most of the data analysis and wrote the paper. The nanoparticle-microbubble platform used in this paper was made at SINTEF Materials and Chemistry.

Table of Contents

List of Figures

1. INTRODUCTION

The blood-brain barrier (BBB) is an interface between blood and the brain. It maintains brain homeostasis and protects the brain from exogenous and endogenous compounds that are harmful to its functioning. This, however, comes at the cost of shielding the brain from the nearly all drugs. Consequently, a number of brain diseases such as various forms of brain cancer, Parkinson's, Alzheimer's, amyotrophic lateral sclerosis disease etc. remain intractable. Nanoparticles (NPs) are a versatile tool in drug delivery owing to their large drug load capacity, ability to carry poorly soluble drugs, biofunctionalization for targeting and imaging, reduction of systemic drug toxicity and other advantages. Crossing the BBB, however, is a challenge for NPs as well, and their brain delivery can benefit from BBB opening techniques. This introduction gives a brief overview of the structure and functions of the BBB and drug delivery to the brain, with a special emphasis of NP-mediated drug delivery and the use of focused ultrasound (FUS) in BBB disruption.

1.1 Structure and functions of the blood-brain barrier

> *"Now take ye kindly my meed to-day and ferry me over. I am in truth your friend."*
> *The ferryman replied: "This may not be. My dear lords have foes, wherefore I never ferry strangers to this land."*
>
> *Nibelungenlied, Adventure XXV*

The brain's internal milieu is protected by two barriers: the BBB and the blood-cerebrospinal fluid barrier (BCSF). The BBB is by far the more extensive of the two. BCSF, formed by epithelial cells of the choroid plexus, as well as its separate structural part – the arachnoid barrier at the arachnoid epithelium – are not discussed here; more information about them can be found in [1]. The presence of a barrier between blood and the brain was observed in 1885 by Paul Ehrlich who found that intravenous injection of aniline dyes stained all organs in the body except for the brain. He mistakenly attributed this phenomenon to the dye's 'low affinity'. In 1909, Goldman found that intraventricular injection of the dye Trypan Blue stained the brain tissue, but not other organs in the body; this again indicated the presence of a barrier, although refuted the notion of the dye's low affinity to the brain. The actual term “blood-brain barrier” (*Blut-Hirn Schranke* in German), however, was coined in 1900 by Lewandovsky who, working on the effect of cholic acids after intravenous and intraventricular administration, observed that symptoms in the central nervous system (CNS) developed only in the latter case. The location of the BBB was found much later when Reese and Karnovsky in 1967 observed that 40 kDa horseradish peroxidase did not enter the brain after intravenous administration; using electron microscopy, they established the presence of tight junctions (TJs) between brain capillary endothelial cells (BCEC).

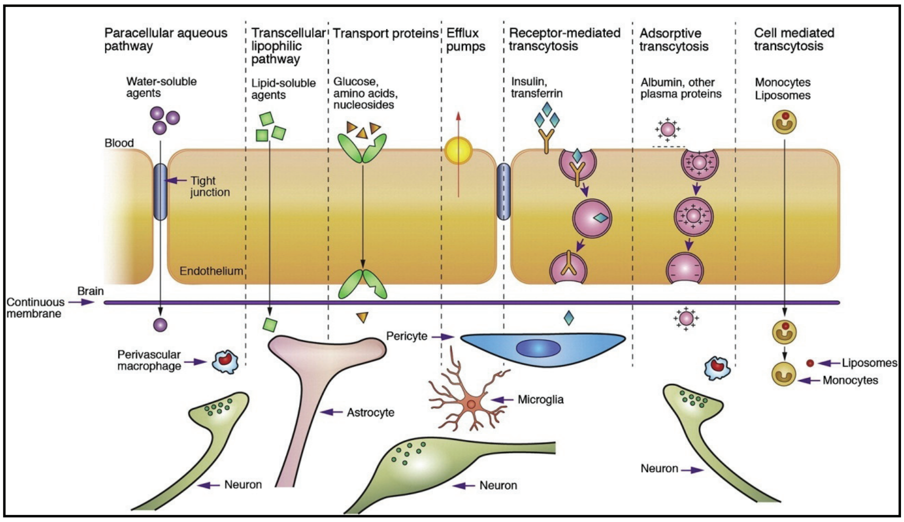

Fig. 1. Cellular structure and transport mechanisms of the BBB. Reproduced with permission from reference [2]

An overview of the BBB is shown in Fig. 1. Structurally, it is formed by BCEC. Unlike endothelial cells in the rest of the body, BCEC have a number of distinguishing properties such as TJs sealing the paracellular space, lack of fenestrations, diminished pinocytosis, high mitochondrial activity, elevated level of proteins in the plasma membrane and presence of various efflux transporters, as well as the expression of BBB-specific markers. BCEC are located on the basal lamina formed by the extracellular matrix (ECM). The barrier function of the brain endothelium is dynamic and highly regulated, responding to signals from either side of the BBB. In particular, pericytes (approx. 3 per a BCEC) regulate endothelial cell proliferation and inflammation response, and astrocytes play a critical role in the induction and maintenance of BBB properties [3]. Neurons have been shown to regulate blood flow and brain capillary permeability through monoaminergic and cholinergic innervation, and neural stem cells are implicated in BBB formation [4]. Together with the basal membrane, pericytes embedded in it, microglia and perivascular astrocytes, BCEC form the so-called neurovascular unit supplying a small number of neurons (<8) located within the unit [3].

1.1.1 Paracellular barrier

Paracellular transport across the BBB is restricted by TJs located in the apical region of the BCEC. A schematic overview of TJs at the BBB is shown in Fig. 2.

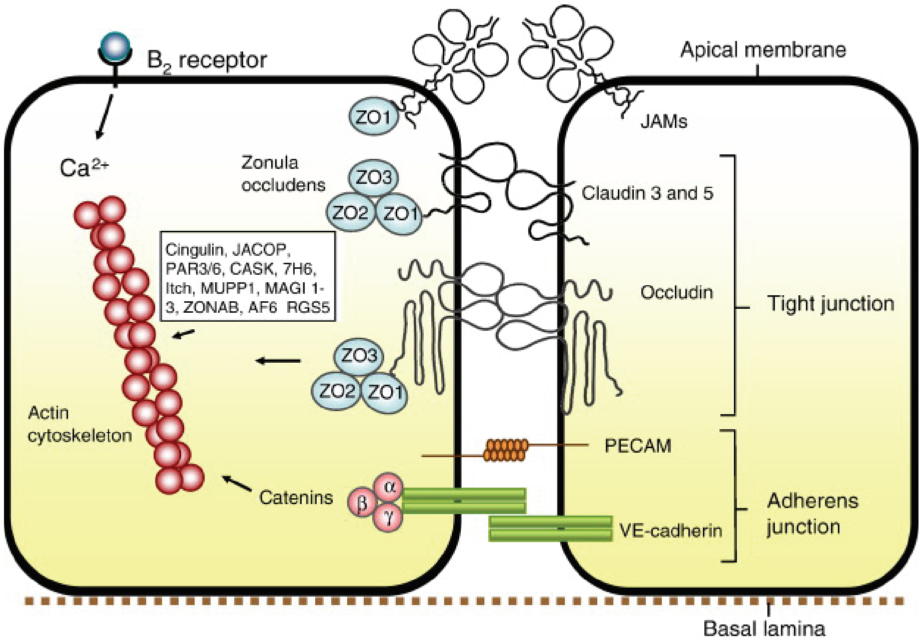

Fig. 2. A schematic overview of BBB tight junctions. Reproduced with permission from reference [3]

TJs are present in other endothelial cells as well, but in the BBB they have a characteristic structure in electron microscopy and predominant association with the protoplasmic (P), rather than the external (E) face. The sealing of paracellular clefts by TJs is responsible for the restricted passage of ions and, consequently, very high values of transendothelial resistance (TEER) in the range of 1500-2000 $\Omega\ cm^{-2}$ [5]. In this property, the brain endothelium is markedly different from other endothelia and resembles epithelial layers. TJs have pores of approx. 4 Å [6], and although larger solutes and tracer molecules can get through TJs, this is mainly attributed to cytoskeletal modulation of TJ intactness and breaks in their continuous network.

TJs consist of integral transmembrane proteins (claudins, occludins, junction adhesion molecules etc.) and intracellular adaptor proteins (zonula occludens 1-3, cingulin, afadin etc.) linking the former to the cytoskeleton. Occludin was the first identified TJ protein; it has a MW of 65 kDa and is a tetraspan transmembrane protein with two extracellular loops connecting adjacent cells. Its loss, e.g. in knockout mice, does not morphologically affect TJ strands, although it does induce histological alterations, e.g. calcification in the brain [7]. Its phosphorylation has also been linked to increased BBB permeability [8, 9]. In general, occludin plays a regulatory role in TJ formation rather than being part of the TJ assembly.

This latter function is performed by claudins, a group of 26 proteins (in humans) with an MW of 21-34 kDa that are structurally similar to occludin but share no homology with it. Unlike occludin-deficient mice, knockout mice lacking claudins are not viable. Various tissues have a typical claudin distribution pattern: e.g. the brain expresses claudins 3, 5, 12 and, possibly, 1; in particular, claudin 3, predominantly linked to the P-face association of TJ strands in endothelial cells, is rarely found in endothelia outside the brain, as those are typically leakier with TJs having mainly E-face association. More comprehensive information about claudins is provided in [10].

Junction adhesion molecules (JAMs), as well as other immunoglobulin superfamily members, e.g. coxsackie and adenovirus receptor and endothelial cell-selective adhesion molecule (CAR and ESAM, respectively) are another group of TJ proteins. JAMs have a MW of about 40 kDa. Of the several known JAMs, only JAM-A is specifically expressed at the brain endothelium, while the others can be found in other endothelia. Overall, JAMs maintain the stability of TJs and participate in their formation, although experiments with monoclonal antibodies (mAbs) against JAMs show that JAMs are inaccessible in the well-formed TJs of confluent monolayers [11]. The functions of CAR and ESAM at the BBB are less clear.

Transmembrane TJ proteins are linked to cytoplasmic accessory proteins. Those can be divided into first order adaptors directly linked to TJ proteins, and second order adaptors, mediating the link between the TJ complex and the cytoskeleton. Of the first order adaptors, the best known are zonula occludens (ZO) proteins and Ca2+-dependent serine protein kinase. ZO proteins are members of membrane-associated guanylate kinase family. Among other domains, they contain three PDZ domains that bind transmembrane TJ proteins. ZO-1 is especially critical for BBB permeability and overall viability. In addition to binding integral TJ proteins, ZO proteins may also affect their localization. Second order adaptors, e.g. cingulin, afadin, 7H6 antigen and junction-associated coiled-coil protein modulate the interaction of membrane TJ complexes with the actin/vinculin cytoskeleton. The cytoskeleton stabilizes and arranges the localization of TJ complexes, thereby regulating BBB permeability. This process is sensitive to external stimuli, modulated by a host of signaling proteins, crucially important in drug delivery and described in greater detail in [12] or [3].

Another important function of TJs is the regulation of cell polarity [13]. TJs separate the apical and basolateral fractions of membrane lipids and proteins, restricting their distribution in the plasma membrane (the fence function). While apicobasal polarity forming a distinct and often organ-specific protein composition of the apical membrane is important in the function of BCEC, its description is outside the scope of this introduction; a comprehensive review can be found in [14].

1.1.2 Transcellular barrier

In addition to TJs sealing the paracellular space, the BBB is formed by BCEC bodies that contribute to the BBB function in two ways: with the physical barrier formed by the plasma membrane, and with the combined effect of various interceptor proteins, mainly efflux transporters, that jointly form the metabolic and enzymatic components of the BBB. In combination with low paracellular permeability, this makes it necessary to have transport mechanisms to carry essential nutrients to the brain. The following types of transport exist at the BBB: passive diffusion, carrier-mediated transport (CMT) and endocytosis.

Passive diffusion at the BBB refers to the passage of compounds across the plasma membrane according to the concentration gradient. The plasma membranes of BCEC hinder the passive diffusion of large and hydrophilic molecules. In this aspect, BCEC are similar to other cells. A distinguishing feature of BCEC plasma membranes is the abundance of glycocalyx with sialic acid that confers a highly negative charge and disfavors the transport of acidic compounds [15, 16] The cut-off size for passive diffusion at the BBB is approximately 400-500 Da [17].

CMT can be divided into passive and active transport. Passive CMT can be referred to as facilitated diffusion; it involves carrier molecules to shuttle solutes across the cell membrane, but does not expend energy in the process. This form of CMT plays a key role in the delivery of polar nutrients to the brain. Active CMT, or active efflux transport, requires energy and is the primary mechanism that shields the brain from those toxins and xenobiotics that are small and lipophilic enough to cross the plasma membrane passively. Passive and active CMT are one of the reasons for the high protein content in BCEC plasma membranes (with carriers accounting for 10% of all membrane proteins [18]), while active CMT, with its substantial energy expenditure, entails high mitochondrial activity – another BBB feature.

Passive CMT at the brain endothelium enables the uptake of various sugars, including glucose, neutral and monocarboxylic amino acids, nucleosides and others (reviewed in [19, 20]. Passive transporters are members of various solute carrier groups that, in addition to influx of nutrients, also participate in brain efflux, e.g. organic anion transporters shielding the brain from various antibiotics (on a side note, it is those transporters that are responsible for the efflux of compounds relevant in research, e.g. fluorescein [21] and phenol red [22]). Due to this dual function, organic anion transporters can be found on both luminal and abluminal membranes of BCEC [23].

While passive transporters do have a certain role in efflux, it is active efflux transporters that are key to the efflux of drugs at the BBB where they play a particularly important role in drug kinetics [24]. Active efflux transporters belong to the ABC cassette superfamily. In addition to P-glycoprotein (P-gp), the first identified efflux transporter, this family includes multidrug resistance-associated proteins (MRP 1-9) and breast cancer resistance protein (BCRP) (reviewed in [25-27]). P-gp is primarily responsible for the efflux of hydrophobic and, often, aromatic and cationic substances [27]. It is arguably the best studied efflux transporter due to the broad spectrum of its targets including various anticancer drugs, antibiotics, human immunodeficiency virus protease inhibitors etc. ([20, 27]). Of the nine identified MRPs, MRP1 and MRP5 are expressed in the brain, and their efflux targets are primarily anionic and neutral compounds, as well as various metabolites e.g. glutathione, glucuronides and sulfate conjugates [28]. BCRP is found in several tissues and is responsible for the efflux of a number of anticancer drugs; there is evidence that BCRP is more highly expressed at human brain endothelium than P-gp [29]. P-gp and BCRP are mainly found on the luminal side of BCEC [30], while MRPs are also present on the abluminal side, although only the ones expressed on the luminal membrane may contribute to the efflux function [31].

Endocytosis at the BBB has a far broader size range than CMT [32] and is responsible for the uptake of large molecules, e.g. insulin [33], transferrin [34], low-density lipoproteins (LDL) [35] etc. In one classification based on interaction with the plasma membrane, it is divided into adsorptive and receptor-mediated. In this classification, adsorptive endocytosis is driven by electrostatic interactions between the negatively charged membrane and the internalized compound; it is therefore more dependent on the compound's charge and, in the case of large peptides and proteins, the C-terminal structure, than its size. Receptor-mediated endocytosis is mediated by more specific interactions between membrane surface receptors and their ligands that may entirely or partly constitute the internalized compound, e.g. insulin, transferrin, leptins etc. Endocytosis of those ligands may lead to transcytosis, e.g. in the case of LDL [36]. In addition to this classification based on material-membrane interactions, another, a more comprehensive system, is based on the proteins involved in endocytosis [37].

Endocytosis requires energy and can be inhibited by energy depletion or low temperatures; in addition, electrostatic interactions, if involved, can be blocked by using competitors (e.g. polycations that act as competitors to proteoglycans [38]), and the involvement of specific interactions with receptors can be determined by using receptor antagonists [39] or competitors [40]. Another property distinguishing endocytosis from passive diffusion mechanisms is saturable uptake.

The enzymatic barrier at the BBB is formed by several enzymes with varying degree of BBB specificity [41] e.g. alkaline phosphatase, gamma-glutamyl transpeptidase, monoamine oxidase, adenosine triphosphatase, cytochromes P450 and others. An illustration of the BBB enzymatic barrier effect is the entry of circulating adenosine from blood into BCEC. While adenosine is transported across the plasma membrane by the concentrative nucleoside transporter, once inside the cell it is rapidly metabolized, which severely restricts the amount of free adenosine able to cross the abluminal membrane [42].

1.1.3 Functions of the BBB

The key function of the BBB can be broadly divided into two somewhat overlapping components: maintaining brain homeostasis and protecting the brain from various compounds that are damaging to the central nervous system [3].

The brain, highly dependent on chemical and electrical signaling, requires a stable and carefully controlled microenvironment that is different from the volatile environment of blood, affected by concentration surges. For instance, the levels of various ions in the brain such as K^+, Ca^{2+}, Mg^{2+} are both different from their blood levels and regulated much more strictly than in the blood where they can spike after exercise or a meal. Another example is glutamate: while in the brain it is an excitatory neurotransmitter, in blood it is yet another amino acid that can be ingested with food. Its unrestricted access to the brain can induce neuronal damage (as it happens e.g. after stroke), and the brain therefore regulates glutamate passage [43, 44]. The presence of the BBB also keeps the pools of neurotransmitters in the central and peripheral nervous systems separate as the same neurotransmitters are often used in the brain and in the rest of the body. Yet another example of the BBB's protective function is the transport of various serum components. The protein composition of the interstitial fluid (ICF) and blood are different and, with very few exceptions, the brain has a much lower concentration of any given protein than blood. Many critical blood serum components such as albumin, pro-thrombin and plasminogen have a neurotoxic effect if present in the brain - the former by itself, and the latter two after conversion to thrombin and plasmin, respectively. Their presence in the ICF is therefore tightly regulated, partly by the BBB itself and partly by other metabolic mechanisms, e.g. the action of the serine protease inhibitor cystatin A, one of the few proteins whose levels in the cerebrospinal fluid (CSF) are higher than in blood [11, 45, 46]. Protection from neurotoxins, either endo- or exogenous, is another function of the BBB; when the neutotoxins in question are small lipophilic molecules, this function is performed in large part by efflux transporters. Finally, BBB tightly controls the passage of immune cells to the brain, and while this process can be regulated, e.g. mononuclear cells can enter the brain through an intact BBB via diapedesis, a transcellular migration that does not involve TJ rearrangement, the healthy brain remains an immune privileged organ. It is during inflammation and other diseases that the BBB becomes more transparent to the peripheral immune cells that can gain entry using both the transcellular and paracellular pathways, while cytokine production plays a role in activating the brain's own immune system – microglia and perivascular macrophages. Other roles of the BBB are a necessary consequence of its barrier function: e.g. the brain must still be supplied with essential nutrients and cleared of metabolic waste, both functions being largely performed by BBB transporters. In addition, the BBB regulates the brain's osmotic pressure as limited lymphatic drainage and rigid skull matter make self-regulation complicated.

1.2 Nanoparticles in drug delivery across the blood-brain barrier

> *"Would you tell me, please, which way I ought to go from here?"*
> *"That depends a good deal on where you want to get to"*
> *Lewis Carroll, Alice in Wonderland*

For all its benefits, the BBB does pose a major obstacle in pharmaceutics. As far as the BBB is concerned, there is little difference between e.g. anticancer drugs and neutotoxins – all seen as xenobiotics whose brain access prevention is the key task of the BBB. It restricts brain access of 100% of large (over 500 Da) and 98% of small molecules after systemic administration. Novel therapeutics, such as peptides, oligonucleotides and antibodies are even less likely than small drugs to reach their target sites in the brain on their own, and even once there, many require means of delivery across the target cell membranes. Brain delivery of drugs, both across the BBB and to target cells, is therefore not only a challenge but also an opportunity that can greatly improve therapeutic approaches.

1.2.1 Benefits of nanoparticles in drug delivery

A noted in [47], nanotechnology and nanomedicine use different definitions of NPs; while the strict range of 1-100 nm is used in the former, its upper limit is relaxed in the latter where more importance is attached to therapeutic benefits and safety than to dimensions. In addition, definitions of NPs often exclude e.g. liposomal carriers. In this introduction, we will not discuss the finer points of terminology, and while the more general term 'nanocarrier' could be better suited for our purposes, we will refer to all colloidal drug carriers sized 1-1000 nm as NPs to avoid confusion.

In drug delivery, NPs can offer several advantages owing to the flexibility and broad range of tools employed in materials science. They can be made in various sizes and shapes and tailored further by surface modification. Their high drug loading capacity allows loading many drug molecules into a single NP, thereby reducing the amount of NPs required for administration. Drugs can be loaded into NPs by encapsulation, thus avoiding chemical binding and preserving drug activity. Drug encapsulation in NPs can increase bioavailability of poorly soluble drugs [48] and improve the delivery of novel therapeutics e.g. oligonucleotides or peptides that can be unstable in the bloodstream [49, 50]. In addition, when delivery to cancer cells is involved, drugs administered systemically will have to overcome multidrug resistance elevated in many types of cancer, while NP uptake by cells normally occurs by endocytosis and therefore bypasses efflux transporters responsible for this resistance. In contrast to the spontaneous and immediate release in traditional formulations, which can require several administrations, release from NPs can be sustained (i.e. more stable over time or, better yet, spanning a desired period of time at a desired concentration) and controlled (i.e. affected by the microenvironment or certain stimuli) [51, 52]. Both of these properties can be further improved by functionalization: e.g., in the case of controlled release, NPs can be capped using ‘gatekeepers’ or bind drugs using cleavable pH-sensitive links so that drug release can occur only under certain conditions. Functionalization of NPs can include agents used in imaging, e.g. fluorescent dyes, iron oxide etc. A schematic overview of a multifunctional NP platform is shown in Fig. 3:

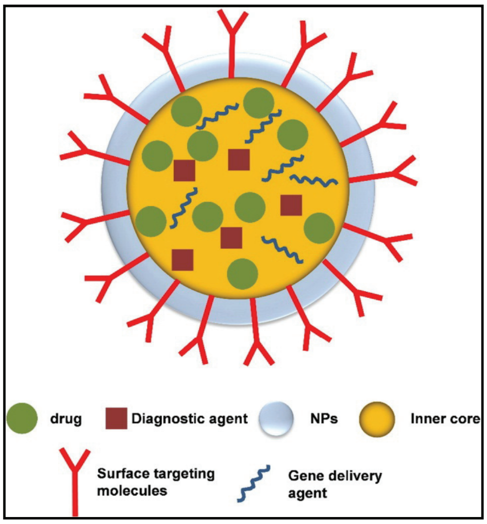

Fig. 3. A model multifunctional nanoparticle. Reproduced with permission from reference [53]

A key limitation in NP-mediated drug delivery is NP interception by the reticuloendothelial system (RES). This process depends on NP size and a number of other properties [54, 55], but, in general, non-functionalized NPs, especially those sized above 100 nm tend to have a typical biodistribution profile with disproportionally large accumulation in the liver, spleen and the lungs. While this can be seen as an advantage in the treatment of diseases affecting these organs, it does require further optimization if NPs are to be used for other purposes. Functionalization with moieties shielding circulating NPs from the RES, e.g. poly(ethylene glycol) (PEG) can offset this limitation to some extent; however, it does not, at least not currently, completely eliminate the eventual predominant accumulation of NPs in these organs and, in addition, can come at the expense of reduced interaction between NPs and target cells.

Non-specific toxicity of drugs in NP-mediated delivery can be further reduced by active and, in the case of solid tumors, passive targeting [56]. Active targeting refers to functionalization of NPs with ligands or antibodies that recognize specific receptors on target cells. Passive targeting is based on enhanced permeability and retention (EPR) - a phenomenon whereby NPs are retained in solid tumors due to the tumor's leaky neovasculature and reduced lymphatic drainage [57, 58]. Preferential accumulation in target tissues can give NP-mediated drug delivery an additional advantage if the drug dose cannot be increased due to prohibitive toxicity, as is often the case for anticancer drugs;

consequently, NPs may even ‘reclaim’ drugs deemed to be too toxic for systemic administration. It should be noted that, in the case of solid brain tumors, NPs can still benefit from the EPR effect in areas with leaky vasculature, predominantly in the tumor core, although tumor areas with an intact BBB may remain off-limits to circulating NPs unless they are functionalized for BBB transport or otherwise get access to the brain parenchyma using a BBB opening technique. Both passive and active targeting have improved NP delivery to target sites in preclinical studies, although the extent of this improvement is debatable. For instance, while active targeting undoubtedly improves cellular uptake of NPs, its contribution to the improved distribution of NPs in target tissues is less certain [56], and a recent meta-analysis of studies involving NP delivery to tumors found that only 0.7% (median) of the injected dose is retained by the tumor [59]. In the case of brain disorders, delivery of NPs across an intact BBB in therapeutic amounts is complicated even further. This is particularly true for transcellular transport across the BBB involving endocytic routes: while functionalization for efficient uptake by BCEC does not appear to be a challenge, subsequent exocytosis into brain parenchyma may very well be [60], and while shuttling of loaded cargo across the luminal membranes of BCEC is in itself an important step unavailable to nearly all small molecular drugs, it is hardly the most efficient use of the drug release flexibility that NPs can offer. In addition, the distribution of NPs in the ECM is more problematic than in the case of small molecular drugs due to NP size [61]. This is particularly applicable to NP delivery to solid tumors with often stiffened ECM [62]. Overall, while functionalization of NPs has made them powerful tools at the level of interaction with target cells, their access to and distribution in target tissues can still be complemented by other methods to ensure their optimal use.

The range of NPs that have been used in drug delivery, including delivery across the BBB, is far too broad to be covered here. Reviews of the NP platforms most commonly used in brain delivery applications, e.g. liposomes [63] , solid lipid NPs [64], iron oxide NPs [65] etc. can be found elsewhere, and we conclude this discussion of the potential benefits that NPs can bring to drug delivery with a brief overview of two types of NPs more relevant to our work: poly(alkyl cyanoacrylate) NPs and mesoporous silica NPs.

1.2.1.1 Poly (alkyl cyanoacrylate) nanoparticles

PACA NPs comprise a class of synthetic polymeric nanoparticles. Their main advantages as colloidal carriers include ease of synthesis, high drug loading capacity, biodegradability and adjustable degradation rate [66]. They are normally synthesized by emulsion polymerization of alkyl cyanoacrylate monomers commonly used in medicine as tissue glues. The monomers are hydrophobic, and PACA NPs are therefore more suitable for encapsulation of hydrophobic drugs [67]. Drug release mechanisms from PACA NPs depend on whether the drug is encapsulated into the NPs or adsorbed on the surface. Encapsulated drugs may be released either by diffusion or following NP degradation, while drugs adsorbed on the surface of the NPs can be released by desorption. Degradation of PACA NPs is mainly governed by surface erosion following ester bond hydrolysis [68] in a process that can also be catalyzed by esterases [69]; other degradation mechanisms are likely less relevant under physiological conditions. The main degradation products are poly(cyanoacrylic acid) and an alkylalcohol, and PACA NP degradation can be a cause of some cytotoxicity that depends on the degradation rate and adhesion of NPs to the cell surface (by increasing local concentration of degradation products) [70]. PACA NPs with longer chain length monomers degrade more slowly, which can be used in adjusting NP degradation and, therefore, drug release rate for encapsulated drugs either by selecting PACA NPs with a certain monomer chain length or even by including monomers of different chain length in a hybrid PACA NP platform [71, 72]. Functionalization of PACA NPs can bring the same benefits as in the case of NPs in general, e.g. PEGylation for protection against the RES, conjugation to targeting ligands etc.

PACA NPs have been extensively used in drug delivery, and one formulation is currently in Phase III clinical trial for the treatment of advanced hepatocellular carcinoma where its use is based on the preferential accumulation of NPs in the liver (see Section 1.2.1) and bypassing the multidrug resistance of cancer cells. In preclinical studies, PACA NPs have been used in the brain delivery of doxorubicin [73], paclitaxel [74], dalargin [75], tacrine [76] and a number of other drugs across the BBB [77]. In many studies, polysorbate-80 was used as a surfactant as it was found to be the most efficient in brain targeting [78]; however, PEG has been successfully used as well [79]. The mechanism of PACA NP transport across the BBB in these studies is believed to be based on surfactant-dependent recruitment of apolipoproteins E, A-I and B from serum, with their subsequent recognition by LDL receptors upregulated in BCEC, followed by uptake and transcytosis into the brain parenchyma [80, 81]. Some studies indicated involvement of non-specific TJ opening [82] and a combination of both mechanisms was proposed in [83]. Overall, PACA NPs remain a promising class of drug carriers, although numerous preclinical demonstrations of their BBB transport potential have not so far led to any translational success.

1.2.1.2 Mesoporous silica nanoparticles

The synthesis of mesoporous silica NPs (MSNs) involves silica formation around a surfactant or polymer template which is subsequently removed (reviewed in [84, 85]). MSNs have a well-defined pore structure with pores sized between 2 and 50 nm (micro- and macroporous silica NPs have smaller and larger pores, respectively) and occupying up to 95% of the NPs. This porous structure increases the total surface area of MSNs and enables independent functionalization of their pores and the external surfaces. Pore functionalization can improve the stability of loaded cargo, while the functionalization of external surfaces confers benefits common to other nanomedicine platforms and described above, e.g. sustained and controlled release, targeting etc. In multifunctional platforms, porous structure also ensures separation of cargo, e.g. fluorescent molecules and drugs [86]. In general, drugs are loaded into MSN pores where they are protected from the external environment until release, while the outer surface is used for conjugation to targeting ligands or other moieties. Among drugs that have been successfully loaded to MSNs are doxorubicin [87], cisplatin [88], paclitaxel [89] etc., many of which are hydrophobic anticancer drugs [90], although the loading of other therapeutics, including small interfering RNA, has been demonstrated as well [91-93] In contrast to many other inorganic NPs, MSNs are biodegradable, and their degradation produces monomeric silicic acid that is not linked to any toxic effects [94]. Degradation rates depend on NP functionalization and can be fine-tuned to achieve an optimal release profile [95]. MSN drug loading capacity, especially in the case of hollow MSNs, can reach unity [96]. Unmodified MSNs have a strong negative charge and exhibit low uptake [94, 97], although this may also be caused by aggregation. Functionalization of MSNs, however, can markedly increase uptake [98]. This can be achieved by conjugation to poly(ethylene imine) (PEI) [91, 97, 99] or other cationic agents [100]. The uptake of MSNs, similar to that of other NPs, appears to be primarily governed by clathrin-mediated endocytosis [101], although other mechanisms have been suggested as well [85, 100].

Brain delivery of MSNs has been attempted in several studies. Efficient accumulation at brain endothelium, but very little transport of MSNs across the BBB either *in vitro* or *in vivo* was observed in [97]. In [102], transferrin-conjugated MSNs were detected in the hippocampal neurons of Kunming mice after administration. In [103], PEGylated polyamidoamine dendrimer-conjugated magnetic MSNs, but not pure MSNs were internalized by astrocytes and neurons. In [104], transport of MSNs across an *in vitro* BBB model based on a co-culture of human brain microvascular endothelial cells and U87 MG cells was observed in a size-dependent manner. Overall, a few recent studies cited above showed transport MSNs across the BBB, showing the potential of these NPs in brain delivery; as in the case of other NPs, however, this transport appears to depend heavily on optimal MSN functionalization and/or presence of targeting ligands, although the relatively small size of MSNs does appear to be an advantage in BBB opening studies.

1.2.2 Routes of delivery across the BBB

Strategies for drug delivery across the BBB can grouped into three categories: those that bypass the BBB, those that ‘deceive’ it and those that disrupt it.

Techniques bypassing the BBB include intracerebroventricular (ICV) administration, interstitial delivery, convection-enhanced delivery (CED) and non-invasive olfactory administration. While ICV administration may directly access the brain parenchyma, after the injection the therapeutics are distributed in the ependymal surface, with further diffusion decreasing exponentially with the distance. Drugs that are injected into the CSF are also rapidly pumped back into blood through the superior sagittal sinus [105]. The fast turnover of the CSF (approx. 5 hours) further complicates this as the amount of the drug available for the already slow diffusion is rapidly reduced by this ‘sink’ effect, especially with large and hydrophilic drugs [106]. As noted in [107], these factors add up to create an ‘ICV administration paradox’ whereby drugs injected into the CSF find their way to blood faster than they reach their target sites in the brain, making this route similar to slow intravenous infusion [108].

Interstitial delivery can be achieved with an Ommaya reservoir or controlled delivery from biodegradable polymers, e.g. Gliadel wafers (reviewed in [109]). This method has been used to deliver drugs with excessive systemic toxicity and maximize availability in target tissues. However, it is similar to ICV administration in its inconvenience and risk of complications. In addition, it is even more invasive and, in the case of polymeric wafers, does not allow dose adjustment after implantation. Diffusion can be complemented by CED. In this method, therapeutics are delivered using catheters and pressure is applied continuously, increasing distribution volume [110]. Since this delivery is localized, limited diffusion in the brain tissue can in this case be seen as an advantage. However, CED can generate high pressures and, in addition, lead to inhomogeneous distribution if the local pressure of the interstitial fluid in tumors is even higher than that applied [111]. Similar to other forms of interstitial delivery, CED has not produced conclusive results in clinical trials.

Intranasal drug administration offers non-invasive delivery through the olfactory route, with direct access to the brain [112]. This route employs several mechanisms of transport involving sustentacular cells and/or olfactory neurons; however, as noted in [113], when used for brain delivery, only 1% of the applied drug reaches the CNS; for novel therapeutics such as peptides and proteins this route is even more challenging as their transport across the olfactory membrane is limited. Aside from that, a fraction of the drug in this route reaches CSF and, therefore, undergoes the same unfavorable clearance as described above [17]. In addition, much of the preclinical research on intranasal administration has been done on rodents whose olfactory area is proportionally much larger than in humans. Mucoadhesive nanoparticles, e.g. chitosan, may offer an advantage [114]; overall, however, the prospects of the intranasal route of administration in brain drug delivery appear problematic.

Compared to most strategies bypassing the BBB, systemic administration of therapeutics is non-invasive and makes use of the brain's extensive vascularization (the surface area of the BBB in humans is approx. 21.6 m^2 [42] and the distance between a capillary vessel and the nearest neuron is less than 25 µm [3]); therefore, therapeutics injected systemically quickly reach brain tissues. That alone, naturally, does not solve the issue of brain delivery. Once in the brain capillaries, therapeutics have two ways of crossing the BBB. First, they can either be taken up by BCEC with subsequent diffusion, transport or exocytosis to the abluminal side, or move across the paracellular space of the endothelial layer by inducing changes in TJs. Second, they can be transported to the brain parenchyma after either general or localized BBB disruption. Studies with strategies employing the first mechanism likely constitute the majority of all research into brain drug delivery. These strategies can be applied both to small molecular drugs and NPs, and involve various modifications conferring BBB transport properties. In the case of small drugs they involve increasing the drug's lipophilicity [115], replacing carboxylic groups (to decrease acidity – see Section 1.1.1), decreasing the number of rotatable and hydrogen bonds, increasing and decreasing affinity to influx and efflux transporters, respectively, and otherwise optimizing the drug's chemical properties for increased BBB permeability. Approaches that can be applied to small drugs, macromolecules and NPs alike include the use of endogenous targeting ligands, monoclonal antibodies, cell-targeting and cell-penetrating peptides etc. Their overview is outside the scope of this introduction, and we only note here that their common features, shared by all therapeutics, are inherent dependence on chemical properties and unpredictability of successful BBB transport. In addition, if the method mainly involves the transcellular route, there is a good chance that the therapeutic will largely remain confined to BCEC [60]. In this sense, approaches that disrupt the BBB can be preferable as they offer the circulating therapeutics immediate access to the brain parenchyma.

Various methods have been suggested for non-specific BBB disruption (BBBD). In one of the oldest approaches, chemical disruption can be achieved by mannitol to induce hyperosmolar shock, leading to BCEC shrinkage and, therefore, BBB opening [116]. This method can open the BBB for several hours, depending on the dose [117]. Chemical opening can also employ vasoactive compounds [118]. In general, however, chemical BBBD is not restricted to a particular site and can therefore be highly damaging (see section 1.1.3). In addition, it can lead to edema and increased intracranial pressure [119]. In a slightly modified approach, the BBB may be opened at tumor sites using e.g. bradykinin B2 receptor agonist. This approach appears safer than the indiscriminating osmotic BBBD. In both cases, however, BBB opening caused substantial toxicity and no significant progress was made in the past decade.

More advanced attempts at non-specific BBBD have employed FUS and photodynamic therapy. Photodynamic therapy is based on the administration of photosensitizers, e.g. 5-aminolevulinic acid, photofrin or others, with subsequent light exposure producing radicals or reactive oxygen species. As a method of treatment it has been used several clinical trials, although with most of them being Phase I/II uncontrolled trials, and is yet to become a standard of care; a detailed overview can be found in [120]. As a method of selective opening of the BBB, however, photodynamic therapy, along with photochemical internalization – a related light-based technique, has only been reported in few works [121, 122]. The combination of FUS with microbubbles (MBs) used as contrast agents in ultrasonography [123] has turned this FUS-mediated BBBD into one of the more promising approaches in brain drug delivery and is reviewed in greater detail below.

1.3 Ultrasound in drug delivery across the blood-brain barrier

> *Who is the third who walks always beside you?*
> *When I count, there are only you and I together*
> *But when I look ahead up the white road*
> *There is always another one walking beside you*
>
> *T.S. Eliot, The Waste Land*

While the BBB-opening effect of FUS was observed as early as in the 1950s [124], much of the early work on FUS was focused on thermal ablation. While thermal mechanisms did cause BBB opening, this was accompanied by tissue damage. Some evidence of BBB opening caused by FUS-generated bubble oscillation and collapse in the proximity of blood vessel walls (a process called cavitation) appeared in the 1990s, but, as in the case of thermal mechanisms, BBB disruption by cavitation was also found to be unpredictable and prone to inducing brain damage [125]. In 2001, FUS-mediated BBBD was modified by Hynynen et al. [123] to include MBs used as contrast agents in diagnostic ultrasound. FUS acting on MBs in the proximity of cerebral vessels induces their oscillation (stable cavitation) at the ultrasound frequency. That, in turn, exerts mechanical stress on the vessel wall. This mechanical stress affects BCEC [126] and causes BBB opening by several mechanisms. At the cellular level, the most important of them appears to be TJ widening and disruption, although transcellular mechanisms, e.g. elevated endocytic activity, have also been suggested [127, 128]. Various changes at the molecular level e.g. increased levels of p-AKT and p-GSK3β in [129] or down-regulation of P-gp in [130], have also been reported. Importantly, the use of MBs in this technique reduced the ultrasound energy required to open the BBB. This, in turn, reduced ultrasound-induced thermal effects and increased the safety - in particular, by allowing BBBD to be driven mainly by stable cavitation, rather than inertial cavitation that is accompanied by a violent collapse of MBs producing jet streams. While inertial cavitation can also open the BBB by exerting mechanical force, it is likely associated with hemorrhage and brain damage. Monitoring of acoustic response from MBs [131] has allowed adjusting the acoustic power based on sub-harmonic emissions, thus staying within the limits of stable cavitation [132, 133] and further improving the safety of the procedure.

In the last decade, this technique has been used to deliver a number of therapeutic agents to the brain. In many works, MRI was used to guide FUS and select the precise area of BBBD. Therapeutics delivered using this technique range from small molecular drugs (doxorubicin, both in healthy rats [134] and in a glioma model [135], but also methotrexate [136] and epirubicin [137]) to siRNA [138], to neurotropic factors (brain-derived neurotropic factor [139], glial-derived neurotropic factor [140]), to antibodies (trastuzumab [141, 142], anti-amyloid antibodies [143, 144]), NPs (see below) and even cells (natural killers [145] and stem cells [146]). The progressive increase in size toward the latter applications (neural stem cell diameter of approx. 10 μm) makes it very likely that some extent of red blood cell extravasation will follow the procedure, although an earlier study [147] found that a certain extent of red blood cell extravasation due to FUS-mediated BBBD did not cause any long-term damage. The delivery of doxorubicin using FUS-mediated BBBD is now being tested in an ongoing clinical trial (ClinicalTrials.gov Identifier: NCT02343991). The delivery of NPs using FUS is described below.

Overall, the main advantages of FUS-mediated BBBD are non-invasiveness, reversibility, focusing on a specific area in the brain and safety. Brain transport of NPs using this technique can combine the benefits of NP-based drug delivery described in 1.2.1 with generic, i.e. therapeutic platform-independent access to the brain parenchyma.

1.3.1 Focused ultrasound in the delivery of nanoparticles across the BBB

While FUS, similar to any technique that disrupts the BBB non-specifically, is likely better suited for the delivery of smaller drugs, nanomedicine, as stated above, can also benefit from FUS-mediated BBBD and bring a number of assets unavailable in the systemic administration of free drugs. However, with NPs and larger objects, size dependence of FUS-mediated transport is likely the primary factor governing successful delivery into the brain in therapeutically relevant amounts. This issue was investigated in a number of studies. In [148], brain transport of fluorescently labeled dextrans (3, 70 and 2000 kDa, with sizes either reported or estimated to be 2.33±0.38, 10.2±1.4 nm and 54.4 nm, respectively) was studied after exposure to FUS in combination with SonoVue MBs (acoustic pressure 0.57 MPa). It was reported that the size of dextrans that could be delivered using this technique was between 70 kDa and 2000 kDa, and that no delivery of 2000 kDa dextrans was observed. In [149], the size of FUS-mediated BBB opening was found to be linked to acoustic pressure, and 2000 kDa dextrans were delivered into the brain at 0.84 MPa. In [150], five contrast agents with hydrodynamic diameters between 1 and 65 nm were used to investigate passage across the BBB disrupted by FUS at 0.45 MPa with SonoVue MBs. The maximum gap between endothelial cells with the BBBD protocol used in that study was found to be close to 65 nm. The authors concluded that the transport of objects with a size over 100 nm would be difficult with purely paracellular mode of FUS-mediated BBBD. While these indications of size restrictions for FUS-mediated BBBD appear reasonable, it should be noted that this technique involves an array of adjustable parameters that can be used to affect and optimize transport of macromolecules. These include concentration and chemical properties of MBs, acoustic parameters and others [151-153], with the acoustic pressure, FUS exposure duration and the presence of NPs during sonication apparently playing a key role. For instance, in [148], dextrans were injected 10 minutes post-sonication, which, as suggested in [150], may be suboptimal for the transport of large particles that should ideally be injected right after or even during sonication. The increase of acoustic pressure in [149] (0.84 MPa vs 0.57 MPa in [148], as well as reducing the time from sonication to injection allowed delivery of larger dextrans (500 and 2000 kDa), albeit at the expense of a minor microhemorrhage in the sonicated area.

In line with these observations, FUS-mediated delivery of NPs across the BBB has been shown in several works with NP sizes varying from those covered in the studies discussed above ([148-150]) to sizes extending well beyond that range. Ultra-small iron NPs sized 5-10 nm and conjugated to MBs (and, therefore, present during sonication) have been delivered to the brain with FUS in [154] (0.32 MPa) and [155] (Power Doppler at 16 MHz with peak negative pressure of approx. 3.6 MPa, corresponding to a mechanical index of 0.9). In a more recent work, FUS (0.54 Ma) in combination with Optison MBs was used to deliver LDL NPs sized 20-22 nm to the brain [156]. In [157], brain delivery of gold NPs sized 50 nm was achieved with FUS-mediated BBBD of 2 minute duration using 0.26 MPa and Definity MBs. In [158], biodegradable polymeric NPs sized 60 and 75 nm were delivered to the brain with a 2-minute long FUS-mediated BBBD (0.4-0.6 MPa) using albumin MBs similar to Optison. NPs in that study were injected immediately before FUS exposure, and the higher pressure (0.6 MPa) considerably increased NP deposition in the brain. In [159], DNA-bearing NPs with a size of 100 nm were co-injected with the same MBs as in [158] and delivered to the brain after a FUS exposure at 0.6 MPa, with a duration of 2 minutes. In [160], Raman NPs sized 50, but also 120 nm were delivered using FUS-mediated BBBD with Definity MBs to the invading margin of gliosarcoma in an orthotopic xenograft model; estimated in situ pressure in that study was 0.23 MPa, sonication duration – 2 min, and the NPs were injected 8 minutes prior to sonication. In another study, a novel platform based on polymeric NPs sized 177 nm and stabilizing gas MBs was used to deliver the NPs to the brain after FUS-mediated BBBD with varying MPa and an exposure duration of 3 minutes. While the parameters used in all these studies into FUS-mediated NP delivery into the brain vary, complicating their direct comparison, their overview indicates that the delivery of NPs with FUS-mediated BBBD is possible even with NPs sized over 100-150 nm. Brain delivery of those larger NPs in therapeutically relevant amounts may, however, require greater optimization of FUS treatment parameters than in the case of small molecular drugs and/or accepting a greater extent of red blood cell extravasation as a necessary evil in the treatment of brain diseases, especially those where the exceedingly poor prognosis offsets the side effects of FUS treatment required for NP delivery.

2. OBJECTIVES OF THE STUDY

The aim of this thesis is to show that progressive improvement of our NP platforms and their combination with FUS can yield increasingly better results in NP-mediated drug delivery to the brain. While nanomedicine has much potential in the treatment of brain diseases, optimization of NP platforms is needed even to reach substantial accumulation of NPs at brain endothelium. Moving beyond brain capillaries through brain parenchyma can be facilitated by the use BBB-opening techniques such as FUS. This increase in delivery efficiency, however, requires understanding of how NPs interact with brain endothelium and how FUS can be used to ensure NP delivery and distribution in the brain.

Four specific objectives were accomplished to meet the overall aim of our thesis:

- To investigate the effect of NP platform modifications (incorporation of various hydrophobic model drugs) on the retention of encapsulated cargo and the association of NPs with brain endothelial cells by using a screening assay allowing rapid evaluation of NP platforms with regard to these properties. Another assay was used to evaluate whether the use of biomimetic cell membranes can be a predictor of NP uptake potential at the brain endothelium.

- To investigate whether the interactions of PACA NPs with brain endothelial cells can be affected by particular types of PEG, a polymer normally used to shield NPs from the RES *in vivo*, and whether PACA NP uptake efficiency and degradation rates were affected by monomer chain length.

- To investigate whether the surface modification and aspect ratio of NPs affected their interaction with endothelial cells and transport across the BBB both *in vitro* and *in vivo*.

- To improve NP brain delivery by using FUS in combination with a novel platform combining PACA NPs and MBs, and to quantify the distribution of NPs in the brain tissue following FUS exposure.

3. SUMMARY OF PAPERS

Paper I – *Labeling nanoparticles: Dye leakage and altered cellular uptake.*

The focus of this paper is on the assessment of how incorporation of fluorescent dyes commonly used as model drugs affects their retention in different NP platforms, as well as NP uptake by living cells. Labeling by fluorescent dyes is commonly used to visualize NPs in cells and to assess their potential in drug delivery. Dye leakage, however, may cause misinterpretation of results; in addition, labeling by different dyes may alter NP interaction with cells. In order to assess these phenomena, we used a previously described flow cytometry assay based on the differences between cell incubation with NPs at 4ºC and 37 ºC. Energy depletion at low temperature inhibits endocytosis; therefore, fluorescent signal from cells incubated with NPs at this temperature should be attributed to the leakage of the incorporated dye. Three commonly used nanoparticles platforms (PACA NPs, nanoemulsions and liposomes) were loaded with six hydrophobic dyes: NR, NR668, DiD, DiD, p-HTAM and p-HTAH. Dye leakage and interactions with cells were evaluated using co-incubation with RBE4 rat brain endothelial cells and PC3 prostate cancer cells. Co-incubation at 4ºC showed that dye retention varied strongly across the studied NP platforms. PBCA NPs generally retained the incorporated dyes better than liposomes and nanoemulsions, although dye retention by NPs was strongly dependent on the incorporated dye. Dye retention in the studied NP platforms is likely to depend on the strength of hydrophobic interactions between the dyes and NPs. Incorporation of different dyes also altered the cellular uptake of NPs, as evidenced by uptake inhibition caused by incorporation of the DiI and DiD, as well as p-HTAH. The mechanism of this inhibition was not linked to alterations in NP size or ζ-potential, as neither changed considerably after dye incorporation in the case of PBCA. Overall, our results indicate the importance of a thorough evaluation of any NP platform following platform modifications.

Paper II – *The effect of poly(ethylene glycol) coating and monomer type on poly(alkyl cyanoacrylate) nanoparticle interactions with lipid monolayers and cells*

The focus of this paper was on assessment of the effect that PACA NP properties such as monomer type and PEG coating had on NP interaction with brain endothelial cells. In addition, we also studied whether biomimetic membranes such as lipid monolayers could be used to model PACA NP interactions with living cells. We used an array of PACA NPs with most properties such as size, ζ-potential and PEG density distributed in a narrow range, in order to isolate the effects of monomer chain length and the type of PEG. We used two monomers (PBCA and poly(isohexyl cyanoacrylate) (PIHCA) and three combinations of PEG initiators and stabilizers – Brij L23 with Kolliphor HS15, Brij L23 and Jeffamine M2070 and Pluronic F68 and Kolliphor HS15. NP interactions with lipid monolayers were assessed by tensiometry and Brewster angle microscopy in a Langmuir-Blodgett system, while their association with and uptake by RBE4 cells were studied using flow cytometry (FCM) and confocal lasser scanning microscopy (CLSM). We found that interactions between NPs and lipid monolayers correlated well with the cellular association and uptake of NPs (R^2=0.85), and that a particular combination of PEG (Brij L23 and Jeffamine M2070) significantly increased the extent of NP interactions both with DMPC/DPPG lipid monolayers and with RBE4 cells as compared to NPs with other PEG combinations. Within its limited distribution range, PEG density affected NP interactions with RBE4 cells, but not with lipid monolayers. Monomer type did not have any significant effect in either model. Overall, our results indicate that PEGylation type can be used to facilitate or inhibit cellular uptake of PACA NPs, and that biomimetic membranes, while modeling only passive interactions between NPs and cell membranes, can serve as a useful tool in the characterization of interactions between PACA NPs and brain endothelial cells.

Paper III – *Cellular uptake and intracellular degradation of poly(alkyl cyanoacrylate) nanoparticles*

In this work, we used PACA NPs with different monomer chain length (PBCA and POCA) to investigate their cellular uptake mechanisms and intracellular fate. PACA NPs are promising drug carriers both across the BBB and to solid tumors; drug delivery using PACA NPs, however, depends on their efficient cellular uptake, and hydrophobic drug release from these NPs is mainly governed by NP degradation. RBE4 and PC3 cells were used as a brain endothelial cell line and solid tumor cell line, respectively. NP uptake kinetics was studied using FCM and CLSM, and inhibition of clathrin- and caveolin-mediated endocytosis was used to further elucidate NP uptake mechanisms. Incorporation of the hydrophobic dye NR668 whose spectral properties varies depending on the environment was used to study intracellular degradation of PACA NPs with emission spectrum analysis, Förster resonance energy transfer (FRET) and fluorescence lifetime imaging microscopy (FLIM). RBE4 had a considerably higher uptake of PACA NPs than PC3 cells. Uptake efficiency depended on the monomer: uptake of PBCA NPs in RBE4 cells rapidly outpaced that of POCA NPs. In PC3 cells, the uptake of POCA NPs was much higher than that of PBCA NPs, although the differences leveled out after 24 hours of incubation. Co-localization with organelles of the clathrin-mediated endocytosis pathway was observed in RBE4 cells; PC3 cells also showed co-localization of NPs with lysosomes. Endocytosis inhibition demonstrated that both endocytic pathways were involved in PACA NP uptake in both cell lines; in RBE4, inhibition affected uptake more than in PC3 cells. Degradation of PBCA NPs was much faster than that of POCA NPs both in physiological solutions and inside cells as confirmed by all three optical techniques. Overall, this study showed that the uptake of NPs was both monomer- and cell-type dependent, and that PACA NP intracellular degradation was highly dependent on the monomer, making it possible to adjust the release rate by choosing or combining appropriate PACA monomers.

Paper IV – *Feasibility study of the permeability and uptake of mesoporous silica nanoparticles across the blood-brain barrier*

In this paper, we investigated the transport, uptake and cytotoxicity of MSNs at the BBB both *in vitro* and *in vivo*. We investigated MSNs with two different aspect ratios and evaluated the effect of a PEG-PEI block copolymer where the PEG block is normally used to shield NPs from the RES *in vivo*, while PEI has been shown to increase NP uptake. In *in vitro* BBB models, RBE4 cells, being of brain endothelial origin, were chosen to study NP uptake, while MDCK II kidney epithelial cells were used to study NP transport across the BBB because of their higher barrier properties. FCM and CLSM were used to assess NP uptake, while transport studies were performed using cells grown on semi-permeable membranes. Cytotoxicity was evaluated using a cell viability assay. In addition, we used surface plasmon resonance as a novel and highly sensitive method to evaluate cellular uptake of MSNs. None of the studied MSNs showed any toxicity in either cell line. PEG-PEI copolymer increased the cellular uptake of MSNs. Cellular uptake was also cell line-dependent, with much higher uptake of MSNs by RBE4 cells, although the use of surface plasmon resonance allowed better detection of uptake differences in MDCK II cells. Transport across an *in vitro* model of the BBB based on MDCK II cells was very low. An *in vivo* experiment with two-photon imaging of MSNs was consistent with these *in vitro* results. After intravenous injection, MSNs were readily visualized in brain endothelial vessels without causing any detectable damage, but no transport across the BBB into brain parenchyma was observed. Overall, our results showed that with suitable functionalization, the studied MSNs can deliver their cargo across the luminal side of the BBB without causing any toxicity, although its subsequent transport into brain parenchyma may not be aided by the NPs.

Paper V – *Ultrasound-mediated delivery and distribution of polymeric nanoparticles in the normal brain parenchyma and melanoma metastases*

In this paper, we used a novel platform based on PACA NPs forming the shell of gas MBs to disrupt the BBB and deliver NPs into brain parenchyma in a melanoma brain metastasis model in combination with FUS. A new ultrasound platform able to generate FUS at two frequencies during the same experiment was used to open the BBB with FUS at 1.1 MHz and a mechanical index of 0.31, and enable the effect of the acoustic radiation force with FUS at 7.8 MHz. We also assessed the effect of FUS exposure on the level of P-glycoprotein, an efflux transport that is an integral part of the BBB. CSLM and image analysis were used extensively to quantify the deposition and distribution of NPs in the brain. Red blood cell extravasation after FUS-mediated BBB opening was assessed by histological examination. Substantial increase in NP extravasation and NP distribution was observed in the brain hemisphere exposed to FUS. Acoustic radiation force did not noticeably increase NP displacement from the brain blood vessels on top of the displacement caused by FUS at 1.1 MHz. We observed some extent of red blood cell extravasation dependent on the BBB opening. Overall, our results indicate that FUS in combination with our PACA NP-MB platform can efficiently transport NPs across the BBB, including delivery to metastatic tumors, and that substantial accumulation and distribution of NPs in the brain can be achieved depending on the extent of BBB opening.

4. GENERAL DISCUSSION AND CONCLUDING REMARKS

In this work, we first evaluated how changes introduced in NP platforms by incorporation of fluorescent dyes could alter the release profile of NPs and their interactions with cells (**Paper I**). Fluorescent labeling is commonly used to visualize NPs in cells or organs. Labeling, however, may cause incorrect interpretation of results due to dye leakage from NP platforms [161-163]. In addition, incorporation of fluorescent dyes may change NP properties, thus altering their interactions with cells. These changes may go beyond alterations in particle size, ζ-potential and other properties commonly correlated with NP uptake by cells and pass unnoticed by standard NP characterization methods used in most studies. Therefore, it is important to characterize NP interactions with cells after any changes are introduced in the platform, and having a versatile tool that allows screening a large number of NPs for this purpose can be an advantage.

In **Paper I**, we used a previously described FCM assay based on the incubation of cells with NPs at 4ºC vs 37ºC to evaluate dye retention and alterations of NP-cell interactions caused by incorporation of various hydrophobic dyes. We employed three commonly used NP platforms (PACA NPs, liposomes and nanoemulsions) loaded with six hydrophobic dyes (NR, NR668, DiI, DiR, p-HTAH and p-HTAM). With no cell staining at 4ºC, we could reliably assume that the dyes were still retained within the NP platforms, provided that the free dyes themselves would cross the cell membrane in a passive process. This was shown to be true for five out of the six dyes. In the case of p-HTAH, however, it was found that the free dye did not stain cells, possibly due to its excessive hydrophobicity. The results of **Paper I** indicate a large variability of dye retention across these NP platforms. Surprisingly, we also found that the incorporation of certain dyes, specifically the carbocyanines DiI and DiD, as well as the oligothiphene dye p-HTAH inhibited NP uptake. This was further confirmed by dual labeling studies with PBCA NPs where incorporation of one uptake-inhibiting dye prevented the uptake of dual-labeled NPs. This effect was not mediated by size or ζ-potential alterations, as those did not change significantly after encapsulation. We currently attribute this effect to the chemical structure of the incorporated dye, but more thorough studies will be needed to elucidate the mechanism of this inhibition.

Overall, the results of **Paper I** stress the importance of thoroughly evaluating NP platform after introduction of any changes, e.g. incorporation of new molecules. These issues, in particular the issue of dye leakage causing misinterpretation of results in studies on NPs, have been acknowledged in several works, and a number of methods has been employed to evaluate dye leakage from NP in solution, including separation methods and the use of lipid acceptor compartments [164, 165]. In a study on the uptake of various polystyrene nanoparticles in A549 lung carcinoma cells, much of the apparent uptake was attributed to the release of a labile dye [166]. In [167], contact-mediated transfer of a model hydrophobic drug from PBCA NPs was reported in PC3 cells, i.e. the release of the encapsulated dye used as model drug with subsequent diffusion through the membrane of PC3 cells was caused by dye leakage. In this regard, covalent conjugation of the fluorescent dye can be better suited for NP visualization than dye encapsulation as noted in [168]; even in the former case, however, the dye may be released following NP degradation which may not necessarily happen intracellularly and, therefore, may lead to NP-independent cell staining. While microscopy based-approaches can be useful in studying NP uptake and degradation, interpretation of their results can be complicated when the dye itself can stain hydrophobic molecules inside the cells, making the signal harder to distinguish from that of intact NPs [167, 169]. Dual labeling with subsequent analysis of dye co-localization or even FRET analysis can be useful, but it is a cumbersome procedure that further complicates NP platforms and, in the case of FRET, this also requires extensive optimization. In contrast to this, using incubation of cells with NPs at 4ºC vs 37ºC, where cell labeling at 4ºC can be reliably assumed to be caused by dye leakage from NPs in solution, is a rapid method that allows screening a large number of samples. Possible improvements of this method lie in better separation between extracellular and intracellular fluorescence in cases where efficient quenching is complicated, e.g. when the dye is not located on the surface of the NPs. This can be achieved by using more advanced FCM techniques such as imaging FCM.

Having demonstrated the importance of characterizing NP-cell interactions after incorporation of new cargo, we proceeded to evaluate whether other properties of PACA NPs unrelated to their size, ζ-potential and other physico-chemical properties they are normally characterized for can predict NP interactions with biomimetic membranes. In **Paper II**, we used a number of PACA NPs with a narrow distribution of properties such as size, ζ-potential and PEG density to isolate the effects of two specific properties - alkyl monomer chain length and the type of PEG the NPs were coated with – and investigate whether those effects were consistent between NP interactions with lipid monolayers serving as artificial cell membranes, and with RBE4 cells. Even though NP internalization normally occurs via active processes, interactions between NPs and cells are initiated at the cell membrane. Consequently, biomimetic membranes, while modeling solely the passive aspect of NP-cell interactions, may prove to be a useful model for predicting uptake potential of NPs [170]. Interactions between various surfactant-modified polystyrene NPs and model endothelial cell membranes in [171], for instance, were in line with cellular uptake experiments performed with human umbilical vein endothelial cells, while in another study biophysical interactions between polylactide NPs decorated or not with a targeting peptide were again consistent with the cellular uptake of those NPs [172]. In our experiments, performed with a much larger number of PACA NPs, we also observed a good correlation of interactions between NPs and biomimetic monolayers and brain endothelial cells, showing that these artificial membranes could be used to predict the cellular uptake of NPs.

Having shown both the importance of re-evaluation of NP platforms after their modification and an example of how this evaluation could be performed by using cell-independent tools such as biomimetic membranes, we proceeded to evaluate how various properties particularly relevant to PACA NPs affected their interactions with brain endothelial cells. Part of this evaluation was conducted already in **Paper II** where an array of PACA NPs with a narrow distribution of size, ζ-potential and PEG density allowed us to focus on how alkyl monomer chain length and, particularly, the type of PEG affected the cellular uptake of these NPs. We found that a particular combination of PEG (Jeffamine M-2070 as the initiator and Brij L23 as the stabilizer) significantly increased NP uptake in cells as compared to NPs with other PEG combinations (Koliphor HS 15/Brij L23 and Koliphor HS 15/Pluronic). Given that PEG is the predominant polymer used for shielding NPs from the RES in preclinical studies [173], this can allow fine-tuning PACA NP properties by varying their PEGylation type to strike a balance between screening by the RES and uptake by target cells (unless the target cells are themselves part of the RES). With regard to the monomer length, we did not find any considerable differences between the PBCA and PIHCA NPs in our experiments. Our investigation into the effect of alkyl chain length on PACA NP uptake continued in **Paper III**, however, where we investigated more closely how considerably larger differences in the alkyl chain length (PBCA vs POCA NPs) affected the cellular uptake of PACA NPs. In addition, given that the drug release from PACA NPs, assuming efficient drug retention, is primarily governed by NP degradation, we looked into the effect that PACA NP monomer chain length had on the intracellular degradation of these NPs. We found that the uptake of PACA NPs in RBE4 cells, as well as in PC3 cells chosen as an example of a common solid tumor cell line, was highly monomer- and cell-line dependent. It was clearly an energy-dependent process mediated by endocytosis. While some earlier studies did not observe any endocytosis of PACA NPs [174, 175], subsequent works found energy-dependent uptake of these NPs, in line with the results of **Paper III**. This discrepancy can most likely be attributed to different synthesis methods that can alter NP properties. By inhibiting endocytosis we found that both clathrin- and caveolin-mediated endocytosis were involved in PACA NP uptake in both cell lines, although the involvement of the former was likely dominant as its inhibition markedly reduced PACA NP uptake, more strongly in RBE4. Experiments with co-localization with endocytic pathway organelles showed limited but present colocalization with all of these organelles. The uptake of PBCA NPs in RBE4 cells was much higher than that of POCA NPs. While the uptake of PBCA NPs has previously been reported in several studies, **Paper III,** to the best of our knowledge, is the first study reporting the uptake of POCA NPs by brain endothelial cells; hence, our results cannot be readily compared to those in the literature. No diffuse staining was observed in NP uptake experiments either in **Paper II** or **Paper III**, which indicates efficient encapsulation of cargo preventing misinterpretation of results cautioned against in **Paper I.**

In intracellular degradation studies performed with PC3 cells, it was found that PBCA NPs degraded much faster than POCA NPs. This is well in line with earlier studies reporting faster degradation of PACA NPs with shorter monomer chain length in solution [69, 70], and similar results were obtained when PACA NP degradation was measured in buffers in our study. Intracellular degradation of PACA NPs has not, to the best of our knowledge, been studied before, and three complementary optical methods used in **Paper III** produced consistent results, indicating much slower degradation of POCA NPs with longer chain length. PACA NP degradation rate affects both NP toxicity and, assuming efficient encapsulation, drug release rate when these particles are used as drug carriers. Consequently, optimizing NP degradation rate can prevent premature degradation with release of encapsulated cargo outside the cells while, on the other hand, ensuring that the degradation does not become prohibitively slow for drug delivery. For instance, a hybrid PACA NP platform in **Paper III,** containing a mixture of BCA and OCA monomers, was found to have an intermediate degradation rate. This observation is in line with other works reporting the use of hybrid PACA NPs [72] and can be used in designing drug delivery carriers based on PACA NPs. Overall, the results of **Paper III** indicate the dependence of PACA NP uptake and intracellular degradation rates in cell models, showing how the selection of these properties can be used in drug delivery depending on the specific scenario.

Having extensively characterized the effect of PACA NP properties on their cellular uptake by brain endothelial cells, we proceeded to study NP transport across an *in vitro* model of the BBB and immediately faced an unsolvable challenge caused by the fact that PACA NPs were incompatible with the *in vitro* BBB setup we planned to use. Since our *in vitro* setup was based on a semi-permeable membrane with a cell monolayer grown on one side of the membrane, and the transported NPs detected in the basolateral chamber on the other side, the NPs would have to be able to cross the membrane on their own. This was not the case, as we found that the passage of our PACA NPs across polyethylene terephthalate membranes was restricted, possibly due to chemical interactions between the NPs and the membrane material. We therefore chose to investigate NP transport across an *in vitro* BBB model using MSNs that did not have such problem. In **Paper IV,** we studied MSNs with different aspect ratios: 1:1 (spherical) and 3:1 (rod-shaped), and each of those types had two subtypes: bare MSNs and MSNs coated with a PEG-PEI copolymer, of which the PEG part is commonly used to shield NPs from the RES, and REI confers positive charge that has been shown to facilitate cellular uptake of NPs is several works [176, 177]. In addition to the transport of these MSN in an *in vitro* BBB model, we assessed their uptake using FCM and CLSM. While RBE4 cells, being of brain endothelial origin, were still used in **Paper IV** to measure the uptake potential of the studied MSNs, their insufficient barrier properties led us to choose MDCK II kidney epithelial cells as a model of the BBB. While MDCK II cells are less suitable for studying transcellular transport across the BBB, i.e. endocytosis with subsequent transcytosis on the abluminal membrane, they are widely used in research and in the pharmaceutical industry for modeling passive transport across the BBB [178], and, in that sense, are better than RBE4 cells for modeling the paracellular barrier formed by the BBB. Having first established safe concentrations of MSNs to avoid toxicity-induced effects in MSN transport across the BBB, we then evaluated their uptake and transport potential *in vitro*. The uptake of PEG-PEI-coated MSNs was higher than that of uncoated MSNs in both cell lines, particularly in RBE4 cells where MSN uptake was much more robust. Transport across the *in vitro* BBB model, however, was very low. Based on the results of uptake studies, we chose one of the more promising MSN candidate for an *in vivo* experiment. We found efficient accumulation of the MSNs at brain endothelium, in line with the high uptake of functionalized MSNs by RBE4 cells. Transport into brain parenchyma, however, was negligible, in line with the results in our *in vitro* BBB model. Overall, our results indicated that the MSNs used in our study could, in perspective, efficiently deliver drugs into BCEC, but the drug would have to reach brain parenchyma and target cells on its own, which, as noted in Section 1.2.1, is hardly the best use of NP potential. In **Paper V**, we therefore used FUS in combination with MBs as a versatile method of opening the BBB and ensuring NP delivery into brain parenchyma. For this study, we used PACA NPs as they had recently been combined with gas MBs in a novel platform [179] that had been used to open the BBB [180], and the immediate proximity of MBs to NPs during sonication could be an advantage in NP transport delivery into the brain. We used FUS with PACA NPs stabilizing MBs in a melanoma brain metastasis model to open the BBB and achieve a substantial accumulation and distribution of NPs in the brain parenchyma, including brain metastases. In addition, we sought to investigate whether FUS exposure affected the levels of P-gp. FUS treatment was performed using a novel ultrasound platform able to generate FUS at two frequencies, with precise selection of the treatment area. 1.1 MHz FUS was used to open the BBB, and 7.8 MHz – to generate acoustic radiation force (ARF) that causes a transfer of momentum from the ultrasound wave to the propagation medium [181-183] and may push NPs further into the ECM. We found that 1.1 MHz FUS in combination with PACA NP-MBs could transport

PACA NP into the brain in a manner dependent on the BBB opening extent. This process was accompanied by red blood cell extravasation into brain parenchyma that also correlated with the extent of BBB opening. It should be noted that the NPs in **Paper V** were among the largest in studies with FUS-mediated transport of NPs across the BBB (see Section 1.3.1). In addition, 1.1 MHz FUS caused displacement of NPs away from blood vessels and their distribution in the brain parenchyma, possibly by the same cavitation-dependent mechanisms that induced the initial BBB opening. This is a considerable advantage of FUS-mediated NP transport across the BBB, considering the problems encountered by NPs in traversing ECM, especially if the NPs in question are relatively large and the ECM belongs to a tumor and is stiffened in comparison to normal brain tissue. However, we observed little effect of the ARF on top of NP displacement caused by 1.1 MHz FUS. This could possibly be caused by the limitations of our image analysis-based technique where NPs displaced from a given blood vessel by a certain distance would be unavoidably registered as originating from a different vessel. While NPs in **Paper V** could be delivered into brain metastases, their delivery into tumors was restricted compared to the surrounding normal parenchyma. This is consistent with the properties of the melanoma metastases at that particular stage (week 4 post-inoculation) of tumor development in our experimental model. As noted in [184], tumors at that stage had reduced vascularization without increased BBB permeability; the combined effect of these factors would logically diminish NP transport into tumors compared to the surrounding tissue. No apparent alterations in P-gp expression was observed immediately after sonication in our study. In a recent work by [130], localized FUS-mediated BBB opening led to P-gp down-regulation 24 hours post-sonication. This indicates that FUS-induced changes that could cause such alterations likely involve molecular mechanisms that require a certain period of time after sonication to exert their effect. Overall, the results of **Paper V** show that FUS in combination with a platform combining PACA NPs and gas MBs in a single unit can achieve a substantial transport of NPs across the BBB and their distribution further into brain parenchyma.

The past few years have seen a growing disillusionment with the progress of nanomedicine where numerous impressive preclinical results have not led to equally impressive translational successes. Much of it can be attributed to the unrealistically rosy expectations accompanying a nascent field, where products dramatically improving treatment are expected here and now. However, it does appear that most of the particularly fascinating results have been produced at the level of nanoparticle-cell interactions. There is still much to learn about the fate of nanoparticles in more complex biological systems and the human body. That knowledge, however, is essential if nanomedicine is to succeed beyond the level of incremental clinical improvements. The diversity of nanoparticle platforms, essentially unlimited if we consider further functionalization, is itself a challenge since our knowledge of general patterns governing nanoparticle interactions with biological systems is scarce at best.

Nanomedicine is here to stay, however, and its potential is immense because its underlying advantage – the remarkably sophisticated toolbox of materials science applied to biomedicine – will only become stronger with time. It may very well be that at some point nanomedicine will become self-sufficient, able to overcome any biological barrier and deliver any drugs to any targets with nearly perfect specificity, using only the tools at its disposal. Until that time, however, it can be supplemented with more generic methods aiding nanoparticles on the way to their targets. In a way, the work presented in this thesis is an illustration of the challenges nanomedicine faces today and opportunities that it can use to overcome them. Both today’s challenges and today’s opportunities may become irrelevant in the future, but that is the way of science - solving current problems and asking new questions in a never-ending quest for knowledge.

5. REFERENCES

1. Johanson, C.E., E.G. Stopa, and P.N. McMillan, *The blood-cerebrospinal fluid barrier: structure and functional significance.* Methods Mol Biol, 2011. **686**: p. 101-31.
2. Chen, Y. and L. Liu, *Modern methods for delivery of drugs across the blood–brain barrier.* Adv Drug Deliv Rev, 2012. **64**(7): p. 640-665.
3. Abbott, N.J., et al., *Structure and function of the blood-brain barrier.* Neurobiol Dis, 2010. **37**(1): p. 13-25.
4. Lu, J., *A novel hypothesis of blood-brain barrier (BBB) development and in vitro BBB model: neural stem cell is the driver of BBB formation and maintenance.* J Exp Integr Med, 2012. **2**(1): p. 39-43.
5. Crone, C. and S.P. Olesen, *Electrical resistance of brain microvascular endothelium.* Brain Res, 1982. **241**(1): p. 49-55.
6. Anderson, J.M., *Molecular structure of tight junctions and their role in epithelial transport.* News Physiol Sci, 2001. **16**: p. 126-30.
7. Saitou, M., et al., *Complex phenotype of mice lacking occludin, a component of tight junction strands.* Mol Biol Cell, 2000. **11**(12): p. 4131-42.
8. Bolton, S.J., D.C. Anthony, and V.H. Perry, *Loss of the tight junction proteins occludin and zonula occludens-1 from cerebral vascular endothelium during neutrophil-induced blood-brain barrier breakdown in vivo.* Neuroscience, 1998. **86**(4): p. 1245-57.
9. Antonetti, D.A., et al., *Vascular endothelial growth factor induces rapid phosphorylation of tight junction proteins occludin and zonula occluden 1. A potential mechanism for vascular permeability in diabetic retinopathy and tumors.* J Biol Chem, 1999. **274**(33): p. 23463-7.
10. Gunzel, D. and A.S. Yu, *Claudins and the modulation of tight junction permeability.* Physiol Rev, 2013. **93**(2): p. 525-69.
11. Liu, W.Y., et al., *Tight junction in blood-brain barrier: an overview of structure, regulation, and regulator substances.* CNS Neurosci Ther, 2012. **18**(8): p. 609-15.
12. Vandenbroucke, E., et al., *Regulation of endothelial junctional permeability.* Ann N Y Acad Sci, 2008. **1123**: p. 134-45.
13. Farrell, C.L. and W.M. Pardridge, *Blood-brain barrier glucose transporter is asymmetrically distributed on brain capillary endothelial lumenal and ablumenal membranes: an electron microscopic immunogold study.* Proc Natl Acad Sci U S A, 1991. **88**(13): p. 5779-83.
14. Worzfeld, T. and M. Schwaninger, *Apicobasal polarity of brain endothelial cells.* J Cereb Blood Flow Metab, 2016. **36**(2): p. 340-62.
15. Cucullo, L., et al., *Artificial Blood-Brain Barriers*, in *Blood-Brain Barriers*. 2007, Wiley-VCH Verlag GmbH & Co. KGaA. p. 375-401.
16. Vorbrodt, A.W., *Ultracytochemical characterization of anionic sites in the wall of brain capillaries.* Journal of Neurocytology, 1989. **18**(3): p. 359-368.
17. Pardridge, W.M., *The blood-brain barrier: bottleneck in brain drug development.* NeuroRx, 2005. **2**(1): p. 3-14.
18. Enerson, B.E. and L.R. Drewes, *The rat blood-brain barrier transcriptome.* J Cereb Blood Flow Metab, 2006. **26**(7): p. 959-73.
19. Deeken, J.F. and W. Löscher, *The Blood-Brain Barrier and Cancer: Transporters, Treatment, and Trojan Horses.* Clinical Cancer Research, 2007. **13**(6): p. 1663-1674.

20. Ohtsuki, S. and T. Terasaki, *Contribution of Carrier-Mediated Transport Systems to the Blood–Brain Barrier as a Supporting and Protecting Interface for the Brain; Importance for CNS Drug Discovery and Development.* Pharm Res, 2007. **24**(9): p. 1745-1758.
21. Angeletti, R.H., et al., *The choroid plexus epithelium is the site of the organic anion transport protein in the brain.* Proc Natl Acad Sci U S A, 1997. **94**(1): p. 283-6.
22. Dorothea, K., et al., *The Development of In Vitro Models for the Blood-Brain and Blood-CSF Barriers*, in *The Blood-Brain Barrier and Drug Delivery to the CNS.* 2000, Informa Healthcare.
23. Roberts, L.M., et al., *Subcellular localization of transporters along the rat blood-brain barrier and blood-cerebral-spinal fluid barrier by in vivo biotinylation.* Neuroscience, 2008. **155**(2): p. 423-38.
24. Birger Brodin, B.S.a.C.U.N., *Structure and function of absorption barriers*, in *Molecular biopharmaceutics*, B.B. Bente Steffansen, Carsten Uhd Nielsen ed, Editor. 2008, Pharmaceutical Press. p. 115-135.
25. Löscher, W. and H. Potschka, *Role of drug efflux transporters in the brain for drug disposition and treatment of brain diseases.* Prog Neurobiol, 2005. **76**(1): p. 22-76.
26. Loscher, W. and H. Potschka, *Blood-brain barrier active efflux transporters: ATP-binding cassette gene family.* NeuroRx, 2005. **2**(1): p. 86-98.
27. Sharom, F.J., *ABC multidrug transporters: structure, function and role in chemoresistance.* Pharmacogenomics, 2008. **9**(1): p. 105-27.
28. Jedlitschky, G., et al., *Transport of glutathione, glucuronate, and sulfate conjugates by the MRP gene-encoded conjugate export pump.* Cancer Res, 1996. **56**(5): p. 988-94.
29. Shawahna, R., et al., *Transcriptomic and quantitative proteomic analysis of transporters and drug metabolizing enzymes in freshly isolated human brain microvessels.* Mol Pharm, 2011. **8**(4): p. 1332-41.
30. Beaulieu, E., et al., *P-glycoprotein is strongly expressed in the luminal membranes of the endothelium of blood vessels in the brain.* Biochem J, 1997. **326 (Pt 2)**: p. 539-44.
31. Dallas, S., D.S. Miller, and R. Bendayan, *Multidrug resistance-associated proteins: expression and function in the central nervous system.* Pharmacol Rev, 2006. **58**(2): p. 140-61.
32. Conner, S.D. and S.L. Schmid, *Regulated portals of entry into the cell.* Nature, 2003. **422**(6927): p. 37-44.
33. Pardridge, W.M., J. Eisenberg, and J. Yang, *Human blood-brain barrier insulin receptor.* J Neurochem, 1985. **44**(6): p. 1771-8.
34. Pardridge, W.M., J. Eisenberg, and J. Yang, *Human blood-brain barrier transferrin receptor.* Metabolism, 1987. **36**(9): p. 892-5.
35. Meresse, S., et al., *Low-density lipoprotein receptor on endothelium of brain capillaries.* J Neurochem, 1989. **53**(2): p. 340-5.
36. Dehouck, B., et al., *A new function for the LDL receptor: transcytosis of LDL across the blood-brain barrier.* J Cell Biol, 1997. **138**(4): p. 877-89.
37. Sahay, G., D.Y. Alakhova, and A.V. Kabanov, *Endocytosis of nanomedicines.* J Control Release, 2010. **145**(3): p. 182-95.
38. Lu, W., et al., *Cationic albumin-conjugated pegylated nanoparticles allow gene delivery into brain tumors via intravenous administration.* Cancer Res, 2006. **66**(24): p. 11878-87.
39. Fillebeen, C., et al., *Receptor-mediated transcytosis of lactoferrin through the blood-brain barrier.* J Biol Chem, 1999. **274**(11): p. 7011-7.

40. Lopez-Atalaya, J.P., et al., *Recombinant Desmodus rotundus salivary plasminogen activator crosses the blood-brain barrier through a low-density lipoprotein receptor-related protein-dependent mechanism without exerting neurotoxic effects.* Stroke, 2007. **38**(3): p. 1036-43.
41. Saubamea, B., et al., *Heterogeneity in the rat brain vasculature revealed by quantitative confocal analysis of endothelial barrier antigen and P-glycoprotein expression.* J Cereb Blood Flow Metab, 2012. **32**(1): p. 81-92.
42. Pardridge, W.M., *Blood-brain barrier drug targeting: the future of brain drug development.* Mol Interv, 2003. **3**(2): p. 90-105, 51.
43. Hawkins, R.A., *The blood-brain barrier and glutamate.* Am J Clin Nutr, 2009. **90**(3): p. 867S-874S.
44. Cohen-Kashi-Malina, K., I. Cooper, and V.I. Teichberg, *Mechanisms of glutamate efflux at the blood-brain barrier: involvement of glial cells.* J Cereb Blood Flow Metab, 2012. **32**(1): p. 177-189.
45. Begley, D.J., *Structure and Function of the Blood–Brain Barrier*, in *Enhancement in Drug Delivery*, E. Touitou, Editor. 2006, CRC Press. p. 575-591.
46. Abbott, N.J., L. Ronnback, and E. Hansson, *Astrocyte-endothelial interactions at the blood-brain barrier.* Nat Rev Neurosci, 2006. **7**(1): p. 41-53.
47. Wong, H.L., X.Y. Wu, and R. Bendayan, *Nanotechnological advances for the delivery of CNS therapeutics.* Adv Drug Deliv Rev, 2012. **64**(7): p. 686-700.
48. Gokce, E.H., M. Ozyazici, and E.B. Souto, *Nanoparticulate strategies for effective delivery of poorly soluble therapeutics.* Ther Deliv, 2010. **1**(1): p. 149-67.
49. Han, S.K., et al., *Core–Shell Nanoparticles for Drug Delivery and Molecular Imaging*, in *Nanotechnologies for the Life Sciences*. 2007, Wiley-VCH Verlag GmbH & Co. KGaA.
50. Martins, S., et al., *Lipid-based colloidal carriers for peptide and protein delivery--liposomes versus lipid nanoparticles.* Int J Nanomedicine, 2007. **2**(4): p. 595-607.
51. Torchilin, V.P., *Nanoparticulates As Drug Carriers*. 2006: Imperial College Press.
52. Biswas, S. and V.P. Torchilin, *Nanopreparations for organelle-specific delivery in cancer.* Adv Drug Deliv Rev, 2014. **66**: p. 26-41.
53. Jia, F., et al., *Multifunctional nanoparticles for targeted delivery of immune activating and cancer therapeutic agents.* J Control Release, 2013. **172**(3): p. 1020-34.
54. Moghimi, S.M., A.C. Hunter, and J.C. Murray, *Long-circulating and target-specific nanoparticles: theory to practice.* Pharmacol Rev, 2001. **53**(2): p. 283-318.
55. Blanco, E., H. Shen, and M. Ferrari, *Principles of nanoparticle design for overcoming biological barriers to drug delivery.* Nat Biotechnol, 2015. **33**(9): p. 941-51.
56. Bertrand, N., et al., *Cancer nanotechnology: the impact of passive and active targeting in the era of modern cancer biology.* Adv Drug Deliv Rev, 2014. **66**: p. 2-25.
57. Matsumura, Y. and H. Maeda, *A new concept for macromolecular therapeutics in cancer chemotherapy: mechanism of tumoritropic accumulation of proteins and the antitumor agent smancs.* Cancer Res, 1986. **46**(12 Pt 1): p. 6387-92.
58. Maeda, H., K. Tsukigawa, and J. Fang, *A Retrospective 30 Years After Discovery of the Enhanced Permeability and Retention Effect of Solid Tumors: Next-Generation Chemotherapeutics and Photodynamic Therapy--Problems, Solutions, and Prospects.* Microcirculation, 2016. **23**(3): p. 173-82.
59. Wilhelm, S., et al., *Analysis of nanoparticle delivery to tumours.* Nature Reviews Materials, 2016. **1**: p. 16014.

60. Johnsen, K.B. and T. Moos, *Revisiting nanoparticle technology for blood-brain barrier transport: Unfolding at the endothelial gate improves the fate of transferrin receptor-targeted liposomes*. J Control Release, 2016. **222**: p. 32-46.
61. Barua, S. and S. Mitragotri, *Challenges associated with Penetration of Nanoparticles across Cell and Tissue Barriers: A Review of Current Status and Future Prospects.* Nano Today, 2014. **9**(2): p. 223-243.
62. Lu, P., V.M. Weaver, and Z. Werb, *The extracellular matrix: a dynamic niche in cancer progression.* J Cell Biol, 2012. **196**(4): p. 395-406.
63. Pattni, B.S., V.V. Chupin, and V.P. Torchilin, *New Developments in Liposomal Drug Delivery.* Chem Rev, 2015. **115**(19): p. 10938-66.
64. Patel, M., E.B. Souto, and K.K. Singh, *Advances in brain drug targeting and delivery: limitations and challenges of solid lipid nanoparticles*. Expert Opin Drug Deliv, 2013. **10**(7): p. 889-905.
65. Dilnawaz, F. and S.K. Sahoo, *Therapeutic approaches of magnetic nanoparticles for the central nervous system.* Drug Discov Today, 2015. **20**(10): p. 1256-64.
66. Kumari, A., S.K. Yadav, and S.C. Yadav, *Biodegradable polymeric nanoparticles based drug delivery systems.* Colloids Surf B Biointerfaces, 2010. **75**(1): p. 1-18.
67. Morch, Y., et al., *Nanoparticle-stabilized microbubbles for multimodal imaging and drug delivery.* Contrast Media Mol Imaging, 2015. **10**(5): p. 356-66.
68. Müller, R.H., et al., *Alkylcyanoacrylate drug carriers: I. Physicochemical characterization of nanoparticles with different alkyl chain length.* International Journal of Pharmaceutics, 1992. **84**(1): p. 1-11.
69. Müller, R.H., et al., *In vitro model for the degradation of alkylcyanoacrylate nanoparticles.* Biomaterials, 1990. **11**(8): p. 590-595.
70. Lherm, C., et al., *Alkylcyanoacrylate drug carriers: II. Cytotoxicity of cyanoacrylate nanoparticles with different alkyl chain length.* International Journal of Pharmaceutics, 1992. **84**(1): p. 13-22.
71. Sulheim, E., et al., *Cellular uptake and intracellular degradation of poly(alkyl cyanoacrylate) nanoparticles.* J Nanobiotechnology, 2016. **14**: p. 1.
72. Huang, C.Y. and Y.D. Lee, *Core-shell type of nanoparticles composed of poly[(n-butyl cyanoacrylate)-co-(2-octyl cyanoacrylate)] copolymers for drug delivery application: synthesis, characterization and in vitro degradation.* Int J Pharm, 2006. **325**(1-2): p. 132-9.
73. Gulyaev, A.E., et al., *Significant transport of doxorubicin into the brain with polysorbate 80-coated nanoparticles.* Pharm Res, 1999. **16**(10): p. 1564-9.
74. Koziara, J.M., et al., *Paclitaxel nanoparticles for the potential treatment of brain tumors.* J Control Release, 2004. **99**(2): p. 259-69.
75. Kreuter, J., et al., *Passage of peptides through the blood-brain barrier with colloidal polymer particles (nanoparticles).* Brain Res, 1995. **674**(1): p. 171-4.
76. Wilson, B., et al., *Targeted delivery of tacrine into the brain with polysorbate 80-coated poly(n-butylcyanoacrylate) nanoparticles.* Eur J Pharm Biopharm, 2008. **70**(1): p. 75-84.
77. Andrieux, K. and P. Couvreur, *Polyalkylcyanoacrylate nanoparticles for delivery of drugs across the blood-brain barrier.* Wiley Interdiscip Rev Nanomed Nanobiotechnol, 2009. **1**(5): p. 463-74.
78. Kreuter, J. and R. Alyautdin, *Using Nanoparticles to Target Drugs to the Central Nervous System*, in *The Blood-Brain Barrier and Drug Delivery to the CNS*. 2000, Informa Healthcare.
79. Calvo, P., et al., *Long-circulating PEGylated polycyanoacrylate nanoparticles as new drug carrier for brain delivery.* Pharm Res, 2001. **18**(8): p. 1157-66.

80. Wohlfart, S., S. Gelperina, and J. Kreuter, *Transport of drugs across the blood-brain barrier by nanoparticles.* J Control Release, 2011.
81. Kim, H.R., et al., *Low-density lipoprotein receptor-mediated endocytosis of PEGylated nanoparticles in rat brain endothelial cells.* Cell Mol Life Sci, 2007. **64**(3): p. 356-64.
82. Olivier, J.C., *Drug transport to brain with targeted nanoparticles.* NeuroRx, 2005. **2**(1): p. 108-19.
83. Rempe, R., et al., *Transport of Poly(n-butylcyano-acrylate) nanoparticles across the blood-brain barrier in vitro and their influence on barrier integrity.* Biochem Biophys Res Commun, 2011. **406**(1): p. 64-9.
84. Rosenholm, J.M., C. Sahlgren, and M. Linden, *Multifunctional mesoporous silica nanoparticles for combined therapeutic, diagnostic and targeted action in cancer treatment.* Curr Drug Targets, 2011. **12**(8): p. 1166-86.
85. Tang, F., L. Li, and D. Chen, *Mesoporous Silica Nanoparticles: Synthesis, Biocompatibility and Drug Delivery.* Advanced Materials, 2012. **24**(12): p. 1504-1534.
86. Wu, S.-H., Y. Hung, and C.-Y. Mou, *Mesoporous silica nanoparticles as nanocarriers.* Chemical Communications, 2011. **47**(36): p. 9972-9985.
87. Zhang, X., et al., *pH-Triggered Doxorubicin Delivery Based on Hollow Nanoporous Silica Nanoparticles with Free-Standing Superparamagnetic Fe3O4 Cores.* The Journal of Physical Chemistry C, 2010. **115**(5): p. 1436-1443.
88. Tao, Z., et al., *Mesoporous Silica Microparticles Enhance the Cytotoxicity of Anticancer Platinum Drugs.* ACS Nano, 2010. **4**(2): p. 789-794.
89. Lu, J., et al., *Mesoporous Silica Nanoparticles for Cancer Therapy: Energy-Dependent Cellular Uptake and Delivery of Paclitaxel to Cancer Cells.* Nanobiotechnology, 2007. **3**(2): p. 89-95.
90. Lu, J., et al., *Mesoporous Silica Nanoparticles as a Delivery System for Hydrophobic Anticancer Drugs.* Small, 2007. **3**(8): p. 1341-1346.
91. Mamaeva, V., et al., *Inhibiting Notch Activity in Breast Cancer Stem Cells by Glucose Functionalized Nanoparticles Carrying gamma-secretase Inhibitors.* Mol Ther, 2016. **24**(5): p. 926-36.
92. Zhang, J., et al., *Mesoporous silica nanoparticles with redox-responsive surface linkers for charge-reversible loading and release of short oligonucleotides.* Dalton Trans, 2014. **43**(10): p. 4115-26.
93. Meng, H., et al., *Engineered design of mesoporous silica nanoparticles to deliver doxorubicin and P-glycoprotein siRNA to overcome drug resistance in a cancer cell line.* ACS Nano, 2010. **4**(8): p. 4539-50.
94. He, Q., et al., *Intracellular Localization and Cytotoxicity of Spherical Mesoporous Silica Nano- and Microparticles.* Small, 2009. **5**(23): p. 2722-2729.
95. Lin, Y.-S., et al., *Well-Ordered Mesoporous Silica Nanoparticles as Cell Markers.* Chemistry of Materials, 2005. **17**(18): p. 4570-4573.
96. Zhu, Y., et al., *A facile method to synthesize novel hollow mesoporous silica spheres and advanced storage property.* Microporous and Mesoporous Materials, 2005. **84**(1–3): p. 218-222.
97. Baghirov, H., et al., *Feasibility Study of the Permeability and Uptake of Mesoporous Silica Nanoparticles across the Blood-Brain Barrier.* PLoS One, 2016. **11**(8): p. e0160705.
98. Rosenholm, J.M., et al., *Targeting of porous hybrid silica nanoparticles to cancer cells.* ACS Nano, 2009. **3**(1): p. 197-206.

99. Xia, T., et al., *Polyethyleneimine Coating Enhances the Cellular Uptake of Mesoporous Silica Nanoparticles and Allows Safe Delivery of siRNA and DNA Constructs.* ACS Nano, 2009. **3**(10): p. 3273-3286.
100. Chung, T.H., et al., *The effect of surface charge on the uptake and biological function of mesoporous silica nanoparticles in 3T3-L1 cells and human mesenchymal stem cells.* Biomaterials, 2007. **28**(19): p. 2959-66.
101. Slowing, I., B.G. Trewyn, and V.S.Y. Lin, *Effect of Surface Functionalization of MCM-41-Type Mesoporous Silica Nanoparticles on the Endocytosis by Human Cancer Cells.* J Am Chem Soc, 2006. **128**(46): p. 14792-14793.
102. Yang, J., et al., *Rapid-releasing of HI-6 via brain-targeted mesoporous silica nanoparticles for nerve agent detoxification.* Nanoscale, 2016. **8**(18): p. 9537-47.
103. Ku, S., et al., *The blood–brain barrier penetration and distribution of PEGylated fluorescein-doped magnetic silica nanoparticles in rat brain.* Biochem Biophys Res Commun, 2010. **394**(4): p. 871-876.
104. Mo, J., et al., *Tailoring Particle Size of Mesoporous Silica Nanosystem To Antagonize Glioblastoma and Overcome Blood-Brain Barrier.* ACS Appl Mater Interfaces, 2016. **8**(11): p. 6811-25.
105. Pardridge, W.M., *Drug transport in brain via the cerebrospinal fluid.* Fluids Barriers CNS, 2011. **8**(1): p. 7.
106. Davson, H. and M.B. Segal, *Physiology of the CSF and Blood-Brain Barriers* 1996: CRC Press.
107. Pardridge, W.M., *Blood-brain barrier delivery.* Drug Discov Today, 2007. **12**(1-2): p. 54-61.
108. Christy, N.P. and R.A. Fishman, *Studies of the blood-cerebrospinal fluid barrier to cortisol in the dog.* J Clin Invest, 1961. **40**: p. 1997-2006.
109. Xing, W.K., et al., *The role of Gliadel wafers in the treatment of newly diagnosed GBM: a meta-analysis.* Drug Des Devel Ther, 2015. **9**: p. 3341-8.
110. Vogelbaum, M.A. and M.K. Aghi, *Convection-enhanced delivery for the treatment of glioblastoma.* Neuro Oncol, 2015. **17 Suppl 2**: p. ii3-ii8.
111. Ali, M.J., et al., *Isolation of drug delivery from drug effect: problems of optimizing drug delivery parameters.* Neuro Oncol, 2006. **8**(2): p. 109-18.
112. Illum, L., *Transport of drugs from the nasal cavity to the central nervous system.* European Journal of Pharmaceutical Sciences, 2000. **11**(1): p. 1-18.
113. Illum, L., *Nasal drug delivery - recent developments and future prospects.* J Control Release, 2012. **161**(2): p. 254-63.
114. Vaka, S.R., et al., *Delivery of brain-derived neurotrophic factor via nose-to-brain pathway.* Pharm Res, 2012. **29**(2): p. 441-7.
115. Agrawal, H., N. Thacker, and A. Misra, *11 - Parenteral Delivery of Peptides and Proteins*, in *Challenges in Delivery of Therapeutic Genomics and Proteomics*, M. Ambikanandan, Editor. 2011, Elsevier: London. p. 531-622.
116. Rapoport, S.I., *Effect of concentrated solutions on blood-brain barrier.* Am J Physiol, 1970. **219**(1): p. 270-4.
117. Muldoon, L.L., et al., *Chemotherapy delivery issues in central nervous system malignancy: a reality check.* J Clin Oncol, 2007. **25**(16): p. 2295-305.
118. Black, K.L., *Biochemical opening of the blood-brain barrier.* Adv Drug Deliv Rev, 1995. **15**(1–3): p. 37-52.
119. Rapoport, S.I., *Osmotic Opening of the Blood–Brain Barrier: Principles, Mechanism, and Therapeutic Applications.* Cell Mol Neurobiol, 2000. **20**(2): p. 217-230.
120. Quirk, B.J., et al., *Photodynamic therapy (PDT) for malignant brain tumors--where do we stand?* Photodiagnosis Photodyn Ther, 2015. **12**(3): p. 530-44.

121. Hirschberg, H., et al., *Targeted delivery of bleomycin to the brain using photo-chemical internalization of Clostridium perfringens epsilon prototoxin.* J Neurooncol, 2009. **95**(3): p. 317-29.
122. Hirschberg, H., et al., *Disruption of the blood-brain barrier following ALA-mediated photodynamic therapy.* Lasers Surg Med, 2008. **40**(8): p. 535-42.
123. Hynynen, K., et al., *Noninvasive MR imaging-guided focal opening of the blood-brain barrier in rabbits.* Radiology, 2001. **220**(3): p. 640-6.
124. Bakay, L., et al., *Ultrasonically produced changes in the blood-brain barrier.* AMA Arch Neurol Psychiatry, 1956. **76**(5): p. 457-67.
125. Vykhodtseva, N.I., K. Hynynen, and C. Damianou, *Histologic effects of high intensity pulsed ultrasound exposure with subharmonic emission in rabbit brain in vivo.* Ultrasound Med Biol, 1995. **21**(7): p. 969-79.
126. Hosseinkhah, N. and K. Hynynen, *A three-dimensional model of an ultrasound contrast agent gas bubble and its mechanical effects on microvessels.* Phys Med Biol, 2012. **57**(3): p. 785-808.
127. Sheikov, N., et al., *Cellular mechanisms of the blood-brain barrier opening induced by ultrasound in presence of microbubbles.* Ultrasound Med Biol, 2004. **30**(7): p. 979-89.
128. Sheikov, N., et al., *Effect of focused ultrasound applied with an ultrasound contrast agent on the tight junctional integrity of the brain microvascular endothelium.* Ultrasound Med Biol, 2008. **34**(7): p. 1093-104.
129. Jalali, S., et al., *Focused ultrasound-mediated bbb disruption is associated with an increase in activation of AKT: experimental study in rats.* BMC Neurol, 2010. **10**: p. 114.
130. Cho, H., et al., *Localized Down-regulation of P-glycoprotein by Focused Ultrasound and Microbubbles induced Blood-Brain Barrier Disruption in Rat Brain.* Sci Rep, 2016. **6**: p. 31201.
131. McDannold, N., N. Vykhodtseva, and K. Hynynen, *Targeted disruption of the blood-brain barrier with focused ultrasound: association with cavitation activity.* Phys Med Biol, 2006. **51**(4): p. 793-807.
132. Arvanitis, C.D., et al., *Controlled ultrasound-induced blood-brain barrier disruption using passive acoustic emissions monitoring.* PLoS One, 2012. **7**(9): p. e45783.
133. O'Reilly, M.A. and K. Hynynen, *Blood-brain barrier: real-time feedback-controlled focused ultrasound disruption by using an acoustic emissions-based controller.* Radiology, 2012. **263**(1): p. 96-106.
134. Treat, L.H., et al., *Targeted delivery of doxorubicin to the rat brain at therapeutic levels using MRI-guided focused ultrasound.* Int J Cancer, 2007. **121**(4): p. 901-7.
135. Treat, L.H., et al., *Improved anti-tumor effect of liposomal doxorubicin after targeted blood-brain barrier disruption by MRI-guided focused ultrasound in rat glioma.* Ultrasound Med Biol, 2012. **38**(10): p. 1716-25.
136. Mei, J., et al., *Experimental study on targeted methotrexate delivery to the rabbit brain via magnetic resonance imaging-guided focused ultrasound.* J Ultrasound Med, 2009. **28**(7): p. 871-80.
137. Liu, H.L., et al., *Blood-brain barrier disruption with focused ultrasound enhances delivery of chemotherapeutic drugs for glioblastoma treatment.* Radiology, 2010. **255**(2): p. 415-25.
138. Burgess, A., et al., *Focused ultrasound for targeted delivery of siRNA and efficient knockdown of Htt expression.* J Control Release, 2012. **163**(2): p. 125-9.

139. Baseri, B., et al., *Activation of signaling pathways following localized delivery of systemically administered neurotrophic factors across the blood-brain barrier using focused ultrasound and microbubbles.* Phys Med Biol, 2012. **57**(7): p. N65-81.
140. Wang, F., et al., *Targeted delivery of GDNF through the blood-brain barrier by MRI-guided focused ultrasound.* PLoS One, 2012. **7**(12): p. e52925.
141. Kinoshita, M., et al., *Noninvasive localized delivery of Herceptin to the mouse brain by MRI-guided focused ultrasound-induced blood-brain barrier disruption.* Proc Natl Acad Sci U S A, 2006. **103**(31): p. 11719-23.
142. Park, E.J., et al., *Ultrasound-mediated blood-brain/blood-tumor barrier disruption improves outcomes with trastuzumab in a breast cancer brain metastasis model.* J Control Release, 2012. **163**(3): p. 277-84.
143. Raymond, S.B., et al., *Ultrasound enhanced delivery of molecular imaging and therapeutic agents in Alzheimer's disease mouse models.* PLoS One, 2008. **3**(5): p. e2175.
144. Jordao, J.F., et al., *Antibodies targeted to the brain with image-guided focused ultrasound reduces amyloid-beta plaque load in the TgCRND8 mouse model of Alzheimer's disease.* PLoS One, 2010. **5**(5): p. e10549.
145. Alkins, R., et al., *Focused ultrasound delivers targeted immune cells to metastatic brain tumors.* Cancer Res, 2013. **73**(6): p. 1892-9.
146. Burgess, A., et al., *Targeted delivery of neural stem cells to the brain using MRI-guided focused ultrasound to disrupt the blood-brain barrier.* PLoS One, 2011. **6**(11): p. e27877.
147. McDannold, N., et al., *MRI-guided targeted blood-brain barrier disruption with focused ultrasound: histological findings in rabbits.* Ultrasound Med Biol, 2005. **31**(11): p. 1527-37.
148. Choi, J.J., et al., *Molecules of Various Pharmacologically-Relevant Sizes Can Cross the Ultrasound-Induced Blood-Brain Barrier Opening in vivo.* Ultrasound in Medicine & Biology, 2010. **36**(1): p. 58-67.
149. Chen, H. and E.E. Konofagou, *The size of blood-brain barrier opening induced by focused ultrasound is dictated by the acoustic pressure.* J Cereb Blood Flow Metab, 2014. **34**(7): p. 1197-204.
150. Marty, B., et al., *Dynamic study of blood-brain barrier closure after its disruption using ultrasound: a quantitative analysis.* J Cereb Blood Flow Metab, 2012. **32**(10): p. 1948-58.
151. McDannold, N., N. Vykhodtseva, and K. Hynynen, *Blood-brain barrier disruption induced by focused ultrasound and circulating preformed microbubbles appears to be characterized by the mechanical index.* Ultrasound Med Biol, 2008. **34**(5): p. 834-40.
152. McDannold, N., N. Vykhodtseva, and K. Hynynen, *Effects of acoustic parameters and ultrasound contrast agent dose on focused-ultrasound induced blood-brain barrier disruption.* Ultrasound Med Biol, 2008. **34**(6): p. 930-7.
153. Choi, J.J., et al., *Noninvasive and localized blood-brain barrier disruption using focused ultrasound can be achieved at short pulse lengths and low pulse repetition frequencies.* J Cereb Blood Flow Metab, 2011. **31**(2): p. 725-37.
154. Fan, C.H., et al., *SPIO-conjugated, doxorubicin-loaded microbubbles for concurrent MRI and focused-ultrasound enhanced brain-tumor drug delivery.* Biomaterials, 2013. **34**(14): p. 3706-15.
155. Lammers, T., et al., *Theranostic USPIO-Loaded Microbubbles for Mediating and Monitoring Blood-Brain Barrier Permeation.* Adv Funct Mater, 2015. **25**(1): p. 36-43.

156. Mulik, R.S., et al., *Localized delivery of low-density lipoprotein docosahexaenoic acid nanoparticles to the rat brain using focused ultrasound.* Biomaterials, 2016. **83**: p. 257-68.
157. Etame, A.B., et al., *Enhanced delivery of gold nanoparticles with therapeutic potential into the brain using MRI-guided focused ultrasound.* Nanomedicine, 2012.
158. Nance, E., et al., *Non-invasive delivery of stealth, brain-penetrating nanoparticles across the blood-brain barrier using MRI-guided focused ultrasound.* J Control Release, 2014. **189**: p. 123-32.
159. Mead, B.P., et al., *Targeted gene transfer to the brain via the delivery of brain-penetrating DNA nanoparticles with focused ultrasound.* J Control Release, 2016. **223**: p. 109-17.
160. Diaz, R.J., et al., *Focused ultrasound delivery of Raman nanoparticles across the blood-brain barrier: potential for targeting experimental brain tumors.* Nanomedicine, 2014. **10**(5): p. 1075-87.
161. Tenuta, T., et al., *Elution of labile fluorescent dye from nanoparticles during biological use.* PLoS One, 2011. **6**(10): p. e25556.
162. Andreozzi, P., et al., *Erythrocyte Incubation as a Method for Free-Dye Presence Determination in Fluorescently Labeled Nanoparticles.* Molecular Pharmaceutics, 2013. **10**(3): p. 875-882.
163. Klymchenko, A.S., et al., *Highly lipophilic fluorescent dyes in nano-emulsions: towards bright non-leaking nano-droplets.* RSC Advances, 2012. **2**(31): p. 11876-11886.
164. Petersen, S., A. Fahr, and H. Bunjes, *Flow Cytometry as a New Approach To Investigate Drug Transfer between Lipid Particles.* Molecular Pharmaceutics, 2010. **7**(2): p. 350-363.
165. Bastiat, G., et al., *A new tool to ensure the fluorescent dye labeling stability of nanocarriers: A real challenge for fluorescence imaging.* Journal of Controlled Release, 2013. **170**(3): p. 334-342.
166. Salvati, A., et al., *Experimental and theoretical comparison of intracellular import of polymeric nanoparticles and small molecules: toward models of uptake kinetics.* Nanomedicine: Nanotechnology, Biology and Medicine, 2011. **7**(6): p. 818-826.
167. Snipstad, S., et al., *Contact-mediated intracellular delivery of hydrophobic drugs from polymeric nanoparticles.* Cancer Nanotechnology, 2014. **5**(1): p. 1-18.
168. Koch, A.M., et al., *Transport of surface-modified nanoparticles through cell monolayers.* Chembiochem, 2005. **6**(2): p. 337-45.
169. Greenspan, P., E.P. Mayer, and S.D. Fowler, *Nile Red: a selective fluorescent stain for intracellular lipid droplets.* J Cell Biol, 1985. **100**.
170. Rascol, E., J.-M. Devoisselle, and J. Chopineau, *The relevance of membrane models to understand nanoparticles-cell membrane interactions.* Nanoscale, 2016. **8**(9): p. 4780-4798.
171. Peetla, C. and V. Labhasetwar, *Biophysical characterization of nanoparticle-endothelial model cell membrane interactions.* Mol Pharm, 2008. **5**(3): p. 418-29.
172. Peetla, C., K.S. Rao, and V. Labhasetwar, *Relevance of biophysical interactions of nanoparticles with a model membrane in predicting cellular uptake: study with TAT peptide-conjugated nanoparticles.* Mol Pharm, 2009. **6**(5): p. 1311-20.
173. Knop, K., et al., *Poly(ethylene glycol) in drug delivery: pros and cons as well as potential alternatives.* Angew Chem Int Ed Engl, 2010. **49**(36): p. 6288-308.
174. de Verdiere, A.C., et al., *Reversion of multidrug resistance with polyalkylcyanoacrylate nanoparticles: towards a mechanism of action.* Br J Cancer, 1997. **76**(2): p. 198-205.

175. de Verdiere, A.C., et al., *Uptake of doxorubicin from loaded nanoparticles in multidrug-resistant leukemic murine cells.* Cancer Chemother Pharmacol, 1994. **33**.
176. Harush-Frenkel, O., et al., *Surface Charge of Nanoparticles Determines Their Endocytic and Transcytotic Pathway in Polarized MDCK Cells.* Biomacromolecules, 2008. **9**(2): p. 435-443.
177. Yue, Z.-G., et al., *Surface Charge Affects Cellular Uptake and Intracellular Trafficking of Chitosan-Based Nanoparticles.* Biomacromolecules, 2011. **12**(7): p. 2440-2446.
178. Reichel, A., *The role of blood-brain barrier studies in the pharmaceutical industry.* Curr Drug Metab, 2006. **7**(2): p. 183-203.
179. Mørch, Ý., et al., *Nanoparticle-stabilized microbubbles for ultrasound-enhanced drug delivery and imaging*, in *In review at Contrast Media Mol Imaging*. 2014.
180. Aslund, A.K., et al., *Nanoparticle delivery to the brain--By focused ultrasound and self-assembled nanoparticle-stabilized microbubbles.* J Control Release, 2015. **220**(Pt A): p. 287-94.
181. Dayton, P., et al., *Acoustic radiation force in vivo: a mechanism to assist targeting of microbubbles.* Ultrasound Med Biol, 1999. **25**(8): p. 1195-201.
182. Rychak, J.J., A.L. Klibanov, and J.A. Hossack, *Acoustic radiation force enhances targeted delivery of ultrasound contrast microbubbles: in vitro verification.* IEEE Trans Ultrason Ferroelectr Freq Control, 2005. **52**(3): p. 421-33.
183. Shortencarier, M.J., et al., *A method for radiation-force localized drug delivery using gas-filled lipospheres.* IEEE Trans Ultrason Ferroelectr Freq Control, 2004. **51**(7): p. 822-31.
184. Thorsen, F., et al., *Multimodal imaging enables early detection and characterization of changes in tumor permeability of brain metastases.* J Control Release, 2013. **172**(3): p. 812-22.

Paper I

Cytometry
PART A
Journal of the International Society for Advancement of Cytometry

Labeling Nanoparticles: Dye Leakage and Altered Cellular Uptake

Sofie Snipstad,[1] Sjoerd Hak,[1,2] Habib Baghirov,[1] Einar Sulheim,[1,3] Ýrr Mørch,[3] Sylvie Lélu,[1] Eva von Haartman,[4,5] Marcus Bäck,[6] K. Peter R. Nilsson,[6] Andrey S. Klymchenko,[7] Catharina de Lange Davies,[1] Andreas K. O. Åslund[1]*

[1]Department of Physics, Norwegian University of Science and Technology, Trondheim, Norway

[2]Department of Circulation and Medical Imaging, Norwegian University of Science and Technology, Trondheim, Norway

[3]SINTEF Materials and Chemistry, Trondheim, Norway

[4]Pharmaceutical Sciences Laboratory, Åbo Akademi University, Turku, Finland

[5]Laboratory of Physical Chemistry, Åbo Akademi University, Turku, Finland

[6]Department of Physics, Chemistry and Biology, Linköping University, Linköping, Sweden

[7]Laboratoire de Biophotonique et Pharmacologie, UMR CNRS 7213, Université de Strasbourg, Strasbourg, France

Received 20 November 2015; Revised 2 February 2016; Accepted 17 March 2016

Grant sponsor: Central Norway Regional Health Authority; Grant sponsor: Research Council of Norway, Grant numbers: NANO2021 220005 and BIOTEK2021 226159.

Additional Supporting Information may be found in the online version of this article.

*Correspondence to: Andreas K. O. Åslund, Department of Physics, Norwegian University of Science and Technology, Høyskoleringen 5, 7491 Trondheim, Norway. E-mail: andreas.aslund@ntnu.no or andreas.aaslund@gmail.com

Conflict of interest: The authors declare no conflict of interest.

International Society for Advancement of Cytometry

- **Abstract**

In vitro and in vivo behavior of nanoparticles (NPs) is often studied by tracing the NPs with fluorescent dyes. This requires stable incorporation of dyes within the NPs, as dye leakage may give a wrong interpretation of NP biodistribution, cellular uptake, and intracellular distribution. Furthermore, NP labeling with trace amounts of dye should not alter NP properties such as interactions with cells or tissues. To allow for versatile NP studies with a variety of fluorescence-based assays, labeling of NPs with different dyes is desirable. Hence, when new dyes are introduced, simple and fast screening methods to assess labeling stability and NP–cell interactions are needed. For this purpose, we have used a previously described generic flow cytometry assay; incubation of cells with NPs at 4 and 37°C. Cell–NP interaction is confirmed by cellular fluorescence after 37°C incubation, and NP-dye retention is confirmed when no cellular fluorescence is detected at 4°C. Three different NP-platforms labeled with six different dyes were screened, and a great variability in dye retention was observed. Surprisingly, incorporation of trace amounts of certain dyes was found to reduce or even inhibit NP uptake. This work highlights the importance of thoroughly evaluating every dye–NP combination before pursuing NP-based applications.

- **Key terms**

polymeric nanoparticles; nanoemulsions; liposomes; leakage; cellular uptake; flow cytometry

Nanotechnology has enabled the development of multifunctional nanoparticles (NPs) for various medical applications. Improved diagnostics and therapy of various diseases have been achieved by incorporating contrast agents for imaging and drugs for therapy (1–5). To understand the behavior of NPs in vitro and in vivo, it is necessary to trace them. This is commonly done by encapsulation of fluorescent dyes in the NPs, which allows their detection with optical techniques (6–12). Encapsulating dyes and drugs in NPs might change the properties of both the NPs and the encapsulated molecules. This could modify surface properties (13) and change the NP charge (14) and interaction between the NPs and other molecules and cells. It is well known that changing the size, shape, or surface charge of NPs can alter the NP uptake in cells (15–17). Furthermore, the NP and the fluorescent probe do not always behave as a single unit; various examples of leakage of dyes from NPs have been reported (18–21). Fluorescence from released dyes can wrongly be interpreted as NP-fluorescence, causing the apparent cellular uptake, intracellular distribution, and biodistribution to not represent that of the NPs (18,22–24). This emphasizes the importance of choosing a fluorescent dye that is compatible with the NP-platform into which it is incorporated. Various procedures have been developed to evaluate NP-labeling stability (18,20,23,25–29). However, the majority of these assays do not include cells or serum, which could strongly affect dye release as these serve as

DOI: 10.1002/cyto.a.22853

acceptor compartments for released dye in vivo (18,24,29–33).

We have previously shown that Nile Red (NR) leaks out of poly(butyl cyanoacrylate) (PBCA)-NPs on cell contact (24), which is in line with various studies showing NR release from NPs (18,19,25,26). The hydrophobic analog NR668 was found to leak much less than NR from nanoemulsions (NEs; Ref. 18), and to be suitable for tracing the PBCA-NPs, as it was not released from the NPs until they were endocytosed and degraded (12). In search of alternative dyes for stable NP labeling and potential Förster resonance energy transfer (FRET) pairs, we performed the current study and applied a flow cytometric cell-based assay to screen a variety of dye–NP combinations. Cells were incubated with NPs at 4°C or 37°C, and cellular binding and uptake of dyes or NPs were quantified by flow cytometry (FCM). Energy depletion at 4°C (20,23) was used to determine whether cellular uptake was active or passive (22,34,35). Energy-dependent uptake (28,36) is likely the main mechanism for internalization of NPs. Thus, lack of fluorescence at 4°C indicates no leakage of the dye from the NP, whereas cellular fluorescence at 4°C might be due to dye leakage and subsequent energy-independent transfer of the dye to the cell or due to cell surface-associated NPs. No fluorescence at 37°C indicates lack of NP uptake, and the enhanced fluorescence from incubation at 4°C to 37°C results mainly from NPs being endocytosed (37) or associated with the plasma membrane (38). Thus, the assay provides information about both dye retention in NPs as well as how labeling NPs affects their association with and uptake by cells. Two different cell lines, with different propensities to take up PBCA-NPs (12), were used. The rat brain endothelial cell line RBE4 was chosen because of the reported ability of PBCA-NPs to cross the blood–brain barrier (39), and the human prostate cancer cell line PC3 was chosen because it is a widely used cancer cell line.

Six different hydrophobic fluorophores (Fig. 1) encapsulated in three commonly used NP-platforms, PBCA-NPs, NEs, and liposomes, were studied systematically. Hydrophobic dyes are often used as models for hydrophobic drugs, which because of their low solubility in water benefit from encapsulation in a nanocarrier. Three of these dyes, NR, DiI, and DiD (Fig. 1), are commercially available and commonly used for NP encapsulation. The other dyes were synthesized: NR668 designed to be more hydrophobic than NR, the oligothiophene p-HTAM has been used in a previous study of cellular uptake of NPs (12), and similarly to NR668, p-HTAH was designed to be more hydrophobic than p-HTAM. We demonstrate a large variability in NP-dye retention, and surprisingly found that encapsulation of different dyes significantly alters NP uptake in cells.

MATERIALS AND METHODS

Cell Cultures

Human prostate adenocarcinoma cells (PC3; American Type Culture Collection, CRL-1435, Manassas, VA) were cultured in

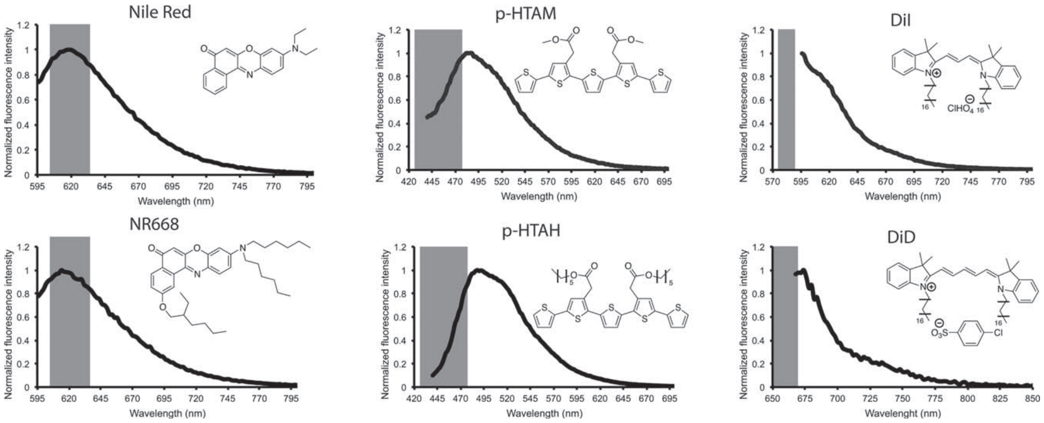

Figure 1. Chemical structures and emission spectra of the six dyes encapsulated in NPs at the excitation wavelengths used for FCM: 561 nm for NR and NR668; 405 nm for p-HTAM and p-HTAH; 561 nm for DiI and 633 nm for DiD. The detection bandpass filter used in FCM is shown in gray. The lack of overlap between the detection bandpass and spectrophotometer fluorescence spectra in some cases is due to limitations of the spectrophotometer (detection must start at least 35 nm above excitation). DiI, 1,1′-dioctadecyl-3,3,3′,3′-tetramethylindocarbocyanine perchlorate; DiD, 1,1′-dioctadecyl-3,3,3′,3′-tetramethylindodicarbocyanine 4-chlorobenzenesulfonate salt; NR668, 9-dihexylamino-2-(2-ethyl-hexyloxy)-benzo[*a*]phenoxazin-5-one; p-HTAH, (3‴-carboxymethyl-[2,2′;5′,2″;5″,2‴;5‴,2⁗]quinquethiophen-4′-yl)-acetic acid hexyl ester; p-HTAM, (3‴-carboxymethyl-[2,2′;5′,2″;5″,2‴;5‴,2⁗]quinquethiophen-4′-yl)-acetic acid methyl ester.

Dulbecco's modified Eagle's medium (DMEM; Gibco, Thermo Fischer Scientific, Waltham, MA) supplemented with 10% fetal bovine serum (Sigma-Aldrich, St. Louis, MO) at 37°C and 5% CO_2.

Rat brain endothelial cells (RBE4, a kind gift from Dr. Aschner, Vanderbilt University, Nashville, TN) were cultured at 37°C and 5% CO_2 in 1:1 mix of Ham's F-10 medium and MEM medium (both from Thermo Fischer Scientific) supplemented with 10% fetal bovine serum, 300 μg/ml G418, and 1 ng/ml basic fibroblast growth factor (Thermo Fischer Scientific).

Dyes Used to Label NPs

NR (catalog number 72485; Sigma-Aldrich), NR668 (18), p-HTAM (40), p-HTAH, DiI, and DiD (catalog numbers D-7757 and D-282, respectively; last two from Thermo Fischer Scientific) were encapsulated in NPs. The structures of the different dyes are shown in Figure 1, along with their emission spectra in NPs at the excitation wavelengths used for FCM.

Synthesis of p-HTAH

The synthesis of p-HTAH is given in Supporting Information and Supporting Scheme S1.

Synthesis of Polymeric- and Lipid-Based NPs

PBCA-NPs were synthesized by the miniemulsion process as described previously (41) and presented in the Supporting Information. Oil-in-water NEs were prepared as described previously (42) and presented in the Supporting information. Liposomes were prepared as the NEs, with the following differences: no soybean oil was added, and the sonication time was only 10 min.

Characterization of the NPs

The NPs were characterized for size and polydispersity index (PDI) using dynamic and electrophoretic light scattering (Zetasizer Nano ZS, Malvern Instruments, Westborough, MA) in 0.01 M phosphate buffer, pH 7. Surface charge (zeta-potential) was measured for the various PBCA-NPs.

To verify successful labeling of NPs, a spectrophotometer (Tecan Infinite 200Pro, Männedorf, Switzerland) was used to measure the fluorescence spectra from NPs in deionized water (20 μg/ml of PBCA for NPs, and 76 μg/ml amphiphilic lipid for liposomes and NEs) at the excitation wavelengths used in FCM.

Incubation with Cells

PC3 cells (125,000; passage 40–70) were seeded in 12-well plates (Corning, Corning, NY). After 48 h, the medium was changed, and at 72 h, the medium was replaced with medium containing 20 μg/ml PBCA-NPs or 76 μg/ml amphiphilic lipid for NEs and liposomes. The cells were incubated at 37°C or 4°C for 3 h. The cells at 4°C were preincubated at 4°C for 15 min before the addition of NPs. Before FCM, the cells were washed with PBS (4°C or 37°C) three times to remove surface-associated NPs, trypsinized, resuspended in 4°C medium, and placed on ice.

To study the association with RBE4 cells, 100,000 cells (passage 14–18) were seeded in 12-well plates (Corning). Forty-eight hours after seeding, the medium was changed to medium containing PBCA-NPs, NEs, or liposomes at concentrations given above, and the cells were prepared for FCM after 3 h incubation as described above, except that no incubation at 4°C was performed.

Table 1. Physiochemical properties of the PBCA-NPs, NEs, and liposomes

	DIAMETER (NM)	PDI
PBCA-NPs	118–203	0.10–0.27
NEs	125–169	0.09–0.13
Liposomes	121–143	0.21–0.26

For coincubation of cells with NPs and free dyes, PC3 and RBE4 cells were coincubated with either DiI dye and PBCA-NPs containing p-HTAM, or with P-HTAH dye and PBCA-NPs containing NR668 for 3 h at 37°C, and the cells were prepared for FCM as described above. Cells were also incubated with the free dyes only. Concentrations of free dyes were similar to the amount of dye incorporated in NEs/liposomes.

Quantification by FCM

Fluorescence from cells was measured using FCM (Beckman Coulter Gallios, Fullerton, CA). NR and NR668 were excited at 561 nm, and fluorescence was detected at 620 nm using a 30-nm bandpass filter. p-HTAM and p-HTAH were excited at 405 nm, and fluorescence was detected at 450 nm using a 50-nm bandpass filter. DiD was excited at 633 nm, and fluorescence was detected at 660 nm using a 20-nm bandpass filter, whereas DiI was excited at 561 nm and detected at 582 nm with a 15-nm bandpass filter.

A minimum of 10,000 cells were counted per sample, and cellular fragments and debris were excluded from the analysis by subjectively choosing a collection gate from the distribution in the side-scatter versus forward-scatter dot plot (an example is shown in Supporting Information Fig. S1). The data were analyzed using Kaluza Flow Cytometry Analysis software v1.2 (Beckman Coulter). Additional FCM details are presented in the Supporting information.

RESULTS

The range of sizes and PDIs of the PBCA-NPs, NEs, and liposomes are presented in Table 1. All the NPs were successfully fluorescently labeled (Supporting Information Table S1). Zeta-potential of the various PBCA-NPs were -2 to -4 mV.

Dye Retention in NPs

FCM analysis of PC3 cells incubated with the various NPs at 4°C showed that dye retention varied greatly between the various dyes and NPs studied (Fig. 2A). In general, dyes were more stably incorporated into PBCA-NPs than in lipid-based NPs. The results are summarized in Table 2.

NR leaked out of all three NP platforms. The cellular fluorescence was almost the same at 4 and 37°C, indicating extensive NR release from the NPs, in accordance with our previously reported study of PBCA-NPs (24) and NEs (18).

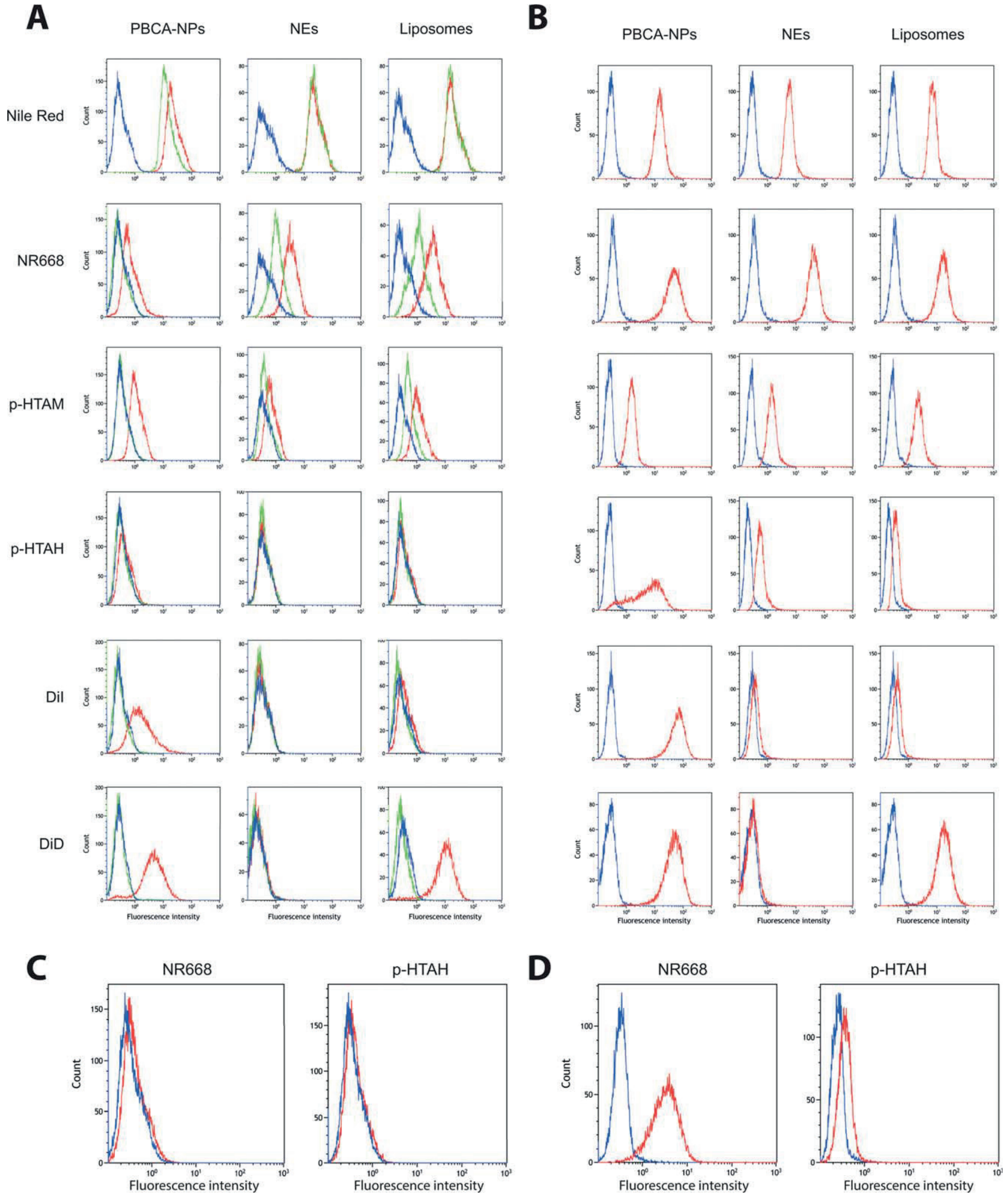

Figure 2. Flow cytometry histograms illustrating fluorescence from cells after incubation with NPs. The histograms show one representative experiment. Autofluorescence (blue), incubation at 4°C (green), and incubation at 37°C (red). Fluorescence from PC3 (**A**) or RBE4 (**B**) cells after incubation with NPs at 4 or 37°C. All experiments were repeated 2-3 times. NP association with PC3 (**C**) or RBE4 (**D**) cells, incubated with dual-labeled (p-HTAH and NR668) PBCA-NPs at 37°C. [Color figure can be viewed in the online issue, which is available at wileyonlinelibrary.com.]

Table 2. Summary of dye retention after incubation of PBCA-NPs, NEs, or liposomes with PC3 cells at 4°C

	NR	NR668	p-HTAM	p-HTAH	DiI	DiD
PBCA-NPs	+	−	−	−[a]	−	−
NEs	+	+	−	−[a]	−	−
Liposomes	+	+	+	−[a]	−	−

No fluorescence from cells denotes stable NP systems, and no dye leakage (−) and fluorescent cells indicate possible leakage (+).

[a] Retention uncertain, as free p-HTAH did not stain cells.

The hydrophobic analog of NR, NR668 (12,18), was retained within the PBCA-NPs; however, for the lipid-based NPs, some leakage was observed. The commonly used lipophilic carbocyanines, DiI and DiD, were retained within all three NP-platforms as no cellular fluorescence was detected at 4°C. p-HTAM was retained in PBCA-NPs and NEs; however, some leakage from liposomes was observed. Incubation using our newly synthesized oligothiophene, p-HTAH, which has hexane alkyl chains instead of methyl like p-HTAM, did not show any cellular fluorescence at 4°C, indicating that the dye is retained in the NPs. Surprisingly, no cellular fluorescence was detected at 37°C either, and free p-HTAH did not stain cells (data not shown).

Dye Encapsulation Can Prevent Cellular NP Uptake

The uptake of p-HTAH-NPs in PC3 cells was inhibited when compared with those with p-HTAM, even though p-HTAH-NPs showed higher or similar fluorescence intensity (Supporting Information Table S1). Similar to NPs with p-HTAH, NEs labeled with the two carbocyanines and liposomes labeled with DiI did not show cellular fluorescence at 37°C either (Fig. 2A). We have also found that PBCA-NPs encapsulating DiO were not taken up at 37°C (Supporting Information Fig. S2). NR668 and p-HTAM encapsulated in all three NPs as well as DiI and DiD in PBCA-NPs and DiD in liposomes showed higher cellular fluorescence at 37°C than 4°C, indicating endocytosis and/or surface binding of the NPs (Table 3 and Fig. 2A).

To further study the lack of cellular uptake of the various NPs at 37°C, RBE4 cells which internalizes PBCA-NP more efficiently than PC3 cells (12) were included. All PBCA-NPs, including those with encapsulated p-HTAH, showed RBE4 cell association (Table 3 and Fig. 2B). For liposomes and NEs, however, the association with RBE4 cells varied depending on the dye. NEs and liposomes labeled with NR668, p-HTAM, or p-HTAH all showed cellular fluorescence at 37°C. In accordance with the results from PC3 cells, RBE4 cells showed hardly any cellular fluorescence after incubation at 37°C with neither NEs nor liposomes labeled with DiI or NEs labeled with DiD.

To investigate whether the lack of fluorescence in PC3 cells incubated with p-HTAH encapsulated in PBCA-NPs was due to NPs not being endocytosed, PC3 and RBE4 cells were incubated at 37°C with PBCA-NPs labeled with both p-HTAH and NR668. No fluorescence from either dye was detected by FCM in PC3 cells, but both fluorophores were detected in RBE4 (Figs. 2C and 2D, respectively). This strengthened the indication that p-HTAH prevented NPs from being taken up in PC3 cells.

Furthermore, PC3 cells were coincubated at 37°C with one NP shown to be cell-associated and one NP that was not. The combinations used were NEs or liposomes with DiI (no cell association) together with PBCA-NPs containing p-HTAM (cell association), and NEs or liposomes with p-HTAH (no cell association) together with PBCA-NPs containing NR668 (cell association). Only the combination of DiI liposomes and PBCA-NPs with p-HTAM showed cellular fluorescence from PBCA-NPs. NEs with DiI and NEs/liposomes with p-HTAH thus prevented cellular association of both NR668 as well as p-HTAM-labeled PBCA-NPs (Supporting Information Fig. S3A). Interestingly, free DiI and p-HTAH did not affect cellular association of PBCA-NPs in coincubation experiments (Supporting Information Figs. 3B and 3C).

DISCUSSION

In the current study, a rapid FCM-based screening method was used to evaluate the retention of six different dyes in three different NP-platforms. Various approaches are reported in the literature to determine the leakage of fluorescent dyes from NPs (12,18,20,23–29). Several studies are based on in vitro dye/drug release in aqueous solution by separation methods (25). Others have used lipid acceptor compartments to evaluate the dye's propensity to leak out of the NP (25–27). We chose to use a simple cell-based FCM assay which can be used with a wide variety of cell lines (20,22,24). The advantage of using FCM is that it is a rapid and quantitative method allowing screening of a large number of samples. A limitation is that the method does not separate fluorescence from internalized and surface-bound dyes or NPs (43). Thus, additional methods are needed to verify whether the NPs are internalized. Microscopy is another method used for studying uptake and distribution of NPs (18,22,37,43). However, microscopy should be used with care in the assessment of dye leakage, as free hydrophobic dyes will bind to intracellular hydrophobic molecules resulting in both diffuse and spotted staining pattern (12,24,30,33), thereby making the dye hard to separate from the fluorescence of intact NPs. In a previous study, we have shown that PBCA-NPs with NR668 are taken up in PC3 cells by endocytosis, verified by the use of time-consuming

Table 3. Summary of association (+) of PBCA-NPs, NEs, and liposomes with PC3/RBE4 cells at 37°C. No association is denoted by (−)[a]

	NR668	p-HTAM	p-HTAH	DiI	DiD
PBCA-NPs	+/+	+/+	−/+	+/+	+/+
NEs	+/+	+/+	−/+	−/−[b]	−/−
Liposomes	+/+	+/+	−/+	−/−[b]	+/+

[a] NPs with NR are not included in the table. NR was not retained in the NPs, whereas the majority of the other NPs resulted in increased fluorescence at 37°C when compared with 4°C, indicating NP–cell association.

[b] Hardly any association with RBE4.

intracellular spectral microscopy and fluorescence-lifetime imaging microscopy (12). This illustrates that although highly useful, microscopy is not suitable for rapid screening of a large number of samples. In several other studies, FRET has been used to study release from NPs (18,21,28). Although this represents an elegant approach and allows for real-time in vivo follow-up of dye release, it requires successful incorporation of two dyes, one donor and one acceptor, and extensive optimization and control experiments.

Dye Retention and Leakage from NPs

In the current study, some dyes were found to be retained in the NPs (NR668 for PBCA-NPs, p-HTAM for PBCA-NPs and NEs, and DiD and DiI in all NPs). In case of the other fluorophores (NR for all NPs, NR668 for NEs and liposomes, and p-HTAM for liposomes), dye leakage could not be ruled out. These results demonstrate that dye retention is highly dependent on both dye and NP-platform and that thorough evaluation of labeling stability is critical.

When no fluorescence was observed at 4°C, we concluded that the dyes are retained in the NPs. This is correct when the assumption that free dyes would enter the cells via energy-independent processes holds. The free dyes NR, NR668, and p-HTAM have indeed been confirmed to stain cells in our previous work using microscopy (12,24). In addition, DiD and DiI are known to diffuse across the plasma membrane (28,44,45). Thus, DiI and DiD in NEs and liposomes are most likely retained, as any leakage of the dyes from NPs would presumably stain the cells. However, free p-HTAH was not found to label cells, and it is possible that not even a DMSO formulation is enough to solubilize the very hydrophobic p-HTAH in aqueous solutions, thus retention of this fluorophore by the NPs is uncertain.

The problem of fluorophore leakage has also been recognized by others, and their observations are largely in agreement with our results (18,19,21,22,25,26,28,46–48). NR has repeatedly been shown to leak out of various NPs (18,19,25,26), and we concluded in a previous study that NR was taken up by cells through contact-mediated transfer within minutes after addition of PBCA-NPs (24). The retention of a dye in a NP is largely governed by hydrophobic and electrostatic interactions between the dye and NP. Its compatibility with the hydrophobic phase in the NPs (polymer core in the case of PBCA-NPs, oil core and phospholipid monolayer in the case of NE, and phospholipid bilayer in the case of liposomes) plays an important role in dye release. For dyes which do not leak from the NPs, the dye is likely to have a strong preference for the hydrophobic phase and to be confined within the hydrophobic compartment. Thus, it is not released from the NP until the NP degrades. A dye that is not retained efficiently is presumably more present at the NP-surface when compared with nonleaky dyes (18). Accordingly, these dyes are present in the shell of the NP, and a continuous release not associated with NP degradation may occur.

Dye Encapsulation Can Prevent Cellular NP Uptake

The study of cellular uptake of NPs is commonly done by labeling the NPs with fluorescent dyes. In accordance with this practice, we studied the uptake of PBCA-NP in PC3 and RBE4 cells, and to our surprise found that when encapsulating some dyes, no cellular uptake was detected. Thus, we performed the systematic study presented here. Both the carbocyanines DiI and DiD and the oligothiophene p-HTAH inhibited cellular uptake of NPs. To further study this inhibition, we encapsulated both NR668 (that is taken up by PC3-cells) and p-HTAH (that is not taken up) in PBCA-NP. As a result, the NP was not taken up in PC3 cells; however, a clear uptake in RBE4 was still detected, in accordance with the uptake behavior of the individually encapsulated dyes. Next, PC3 cells were coincubated with an NP that was taken up and one that was not. In three of the four combinations, uptake of the NPs was inhibited by the NP-dye that inhibits uptake. The mechanisms underlying the observed effect are not clear. The reduced cellular uptake was not due to the size or zeta-potential of the NPs; the encapsulation of the dyes did not change the size of the NPs significantly, and for all the PBCA-NPs, the zeta-potential was −2 to −4 mV.

The chemical composition and structure of the encapsulated dye might affect the cellular uptake. The common denominators for NP-encapsulated dyes that inhibit cellular uptake are long alkyl chains (hexyl or longer) and quartenary amines. However, NR668 has both these functionalities but did not inhibit cellular uptake of NPs. The carbocyanines on the other hand, having quartenary amines, inhibited cellular uptake of lipid-based NPs. This inhibition also depended on the interaction with the NPs, as cellular uptake of liposomes with DiD was not inhibited. To fully elucidate how the NP interaction with the cell changes on a change of dyes would require a more thorough study of both the NP chemistry and the processes involved in endocytosis.

CONCLUSIONS

A systematic study of different hydrophobic dyes encapsulated in three different NP-platforms has been performed. Dye retention was found to vary greatly between the various dyes and NPs studied. Moreover, we have shown that the choice of dye may also impact the uptake behavior of the NP. The implications of our observations are significant for anyone that is studying the properties of NPs with fluorescence-based methods or when trace amounts of a fluorophore are replaced with high payloads of drugs for drug delivery purposes. Our findings highlight the importance of evaluating every combination of encapsulated agent and NP-platform before making conclusions about interactions with cells and tissue or payload release.

ACKNOWLEDGMENTS

The authors thank Anne Rein Hatletveit, Lars Erik Parnas, Sidsel Sundseth, and Kristin Grendstad Sæterbø for technical support. The authors also thank Henkel Loctite, Cremer, and Huntsman for kindly providing cyanoacrylate, Miglyol, and Jeffamine, respectively.

Literature Cited

1. Murthy SK. Nanoparticles in modern medicine: State of the art and future challenges. Int J Nanomed 2007;2:129–141.
2. Naahidi S, Jafari M, Edalat F, Raymond K, Khademhosseini A, Chen P. Biocompatibility of engineered nanoparticles for drug delivery. J Control Release 2013;166: 182–194.
3. Salata O. Applications of nanoparticles in biology and medicine. J Nanobiotechnol 2004;2:3.
4. Etheridge ML, Campbell SA, Erdman AG, Haynes CL, Wolf SM, McCullough J. The big picture on nanomedicine: The state of investigational and approved nanomedicine products. Nanomedicine 2013;9:1–14.
5. Skotland T, Iversen TG, Sandvig K. Development of nanoparticles for clinical use. Nanomedicine 2014;9:1295–1299.
6. Licha K, Olbrich C. Optical imaging in drug discovery and diagnostic applications. Adv Drug Deliv Rev 2005;57:1087–1088.
7. Sokolova V, Epple M. Synthetic pathways to make nanoparticles fluorescent. Nanoscale 2011;3:1957–1962.
8. Elsabahy M, Wooley KL. Design of polymeric nanoparticles for biomedical delivery applications. Chem Soc Rev 2012;41:2545–2561.
9. Liong M, Lu J, Kovochich M, Xia T, Ruehm SG, Nel AE, Tamanoi F, Zink JI. Multifunctional inorganic nanoparticles for imaging, targeting, and drug delivery. ACS Nano 2008;2:889–896.
10. Torchilin VP. Fluorescence microscopy to follow the targeting of liposomes and micelles to cells and their intracellular fate. Adv Drug Deliv Rev 2005;57:95–109.
11. Hak S, Helgesen E, Hektoen HH, Huuse EM, Jarzyna PA, Mulder WJ, Haraldseth O, Davies Cde L. The effect of nanoparticle polyethylene glycol surface density on ligand-directed tumor targeting studied in vivo by dual modality imaging. ACS Nano 2012;6:5648–5658.
12. Sulheim E, Baghirov H, von Haartman E, Bøe A, Åslund AK, Mørch Y, Davies CL. Cellular uptake and intracellular degradation of poly(alkyl cyanoacrylate) nanoparticles. J Nanobiotechnol 2016;14:1.
13. Panyam J, Labhasetwar V. Biodegradable nanoparticles for drug and gene delivery to cells and tissue. Adv Drug Deliv Rev 2003;55:329–347.
14. Sahoo SK, Panyam J, Prabha S, Labhasetwar V. Residual polyvinyl alcohol associated with poly(d,l-lactide-*co*-glycolide) nanoparticles affects their physical properties and cellular uptake. J Control Release 2002;82:105–114.
15. He C, Hu Y, Yin L, Tang C, Yin C. Effects of particle size and surface charge on cellular uptake and biodistribution of polymeric nanoparticles. Biomaterials 2010;31: 3657–3666.
16. Champion JA, Katare YK, Mitragotri S. Particle shape: A new design parameter for micro- and nanoscale drug delivery carriers. J Control Release 2007;121:3–9.
17. Ma N, Ma C, Li C, Wang T, Tang Y, Wang H, Moul X, Chen Z, Hel N. Influence of nanoparticle shape, size, and surface functionalization on cellular uptake. J Nanosci Nanotechnol 2013;13:6485–6498.
18. Klymchenko AS, Roger E, Anton N, Anton H, Shulov I, Vermot J, Mely Y, Vandamme TF. Highly lipophilic fluorescent dyes in nano-emulsions: Towards bright non-leaking nano-droplets. RSC Adv 2012;2:11876–11886.
19. Xu P, Gullotti E, Tong L, Highley CB, Errabelli DR, Hasan T, Cheng JX, Kohane DS, Yeo Y. Intracellular drug delivery by poly(lactic-*co*-glycolic acid) nanoparticles, revisited. Mol Pharm 2009;6:190–201.
20. Andreozzi P, Martinelli C, Carney RP, Carney TM, Stellacci F. Erythrocyte incubation as a method for free-dye presence determination in fluorescently labeled nanoparticles. Mol Pharm 2013;10:875–882.
21. Simonsson C, Bastiat G, Pitorre M, Klymchenko AS, Bejaud J, Mely Y, Benoit JP. Inter-nanocarrier and nanocarrier-to-cell transfer assays demonstrate the risk of an immediate unloading of dye from labeled lipid nanocapsules. Eur J Pharm Biopharm 2016;98:47–56.
22. Salvati A, Aberg C, dos Santos T, Varela J, Pinto P, Lynch I, Dawson KA. Experimental and theoretical comparison of intracellular import of polymeric nanoparticles and small molecules: Toward models of uptake kinetics. Nanomedicine 2011;7: 818–826.
23. Tenuta T, Monopoli MP, Kim J, Salvati A, Dawson KA, Sandin P, Lynch I. Elution of labile fluorescent dye from nanoparticles during biological use. PLoS One 2011;6: e25556.
24. Snipstad S, Westrøm S, Mørch Y, Afadzi M, Åslund AK, Davies CL. Contact-mediated intracellular delivery of hydrophobic drugs from polymeric nanoparticles. Cancer Nanotechnol 2014;5:8.
25. Petersen S, Fahr A, Bunjes H. Flow cytometry as a new approach to investigate drug transfer between lipid particles. Mol Pharm 2010;7:350–363.
26. Bastiat G, Pritz CO, Roider C, Fouchet F, Lignieres E, Jesacher A, Glueckert R, Ritsch-Marte M, Schrott-Fischer A, Saulnier P, et al. A new tool to ensure the fluorescent dye labeling stability of nanocarriers: A real challenge for fluorescence imaging. J Control Release 2013;170:334–342.
27. Shabbits JA, Chiu GN, Mayer LD. Development of an in vitro drug release assay that accurately predicts in vivo drug retention for liposome-based delivery systems. J Control Release 2002;84:161–170.
28. Chen HT, Kim SW, Li L, Wang SY, Park K, Cheng JX. Release of hydrophobic molecules from polymer micelles into cell membranes revealed by Forster resonance energy transfer imaging. P Natl Acad Sci USA 2008;105:6596–6601.
29. Zhao Y, van Rooy I, Hak S, Fay F, Tang J, Davies Cde L, Skobe M, Fisher EA, Radu A, Fayad ZA, et al. Near-infrared fluorescence energy transfer imaging of nanoparticle accumulation and dissociation kinetics in tumor-bearing mice. ACS Nano 2013;7: 10362–10370.
30. Greenspan P, Mayer EP, Fowler SD. Nile red: A selective fluorescent stain for intracellular lipid droplets. J Cell Biol 1985;100:965–973.
31. Greenspan P, Fowler SD. Spectrofluorometric studies of the lipid probe, Nile Red. J Lipid Res 1985;26:781–789.
32. Skajaa T, Zhao Y, van den Heuvel DJ, Gerritsen HC, Cormode DP, Koole R, van Schooneveld MM, Post JA, Fisher EA, Fayad ZA, et al. Quantum dot and Cy5.5 labeled nanoparticles to investigate lipoprotein biointeractions via Forster resonance energy transfer. Nano Lett 2010;10:5131–5138.
33. Brown WJ, Sullivan TR, Greenspan P. Nile Red staining of lysosomal phospholipid inclusions. Histochemistry 1992;97:349–354.
34. Verma A, Uzun O, Hu Y, Hu Y, Han HS, Watson N, Chen S, Irvine DJ, Stellacci F. Surface-structure-regulated cell-membrane penetration by monolayer-protected nanoparticles. Nat Mater 2008;7:588–595.
35. Mahmoudi M, Abdelmonem AM, Behzadi S, Clement JH, Dutz S, Ejtehadi MR, Hartmann R, Kantner K, Linne U, Maffre P, et al. Temperature: The “ignored” factor at the NanoBio interface. ACS Nano 2013;7:6555–6562.
36. Dausend J, Musyanovych A, Dass M, Walther P, Schrezenmeier H, Landfester K, Mailander V. Uptake mechanism of oppositely charged fluorescent nanoparticles in HeLa cells. Macromol Biosci 2008;8:1135–1143.
37. Brambilla D, Nicolas J, Le Droumaguet B, Andrieux K, Marsaud V, Couraud PO, Couvreur P. Design of fluorescently tagged poly(alkyl cyanoacrylate) nanoparticles for human brain endothelial cell imaging. Chem Commun (Camb) 2010;46: 2602–2604.
38. Lesniak A, Salvati A, Santos-Martinez MJ, Radomski MW, Dawson KA, Aberg C. Nanoparticle adhesion to the cell membrane and its effect on nanoparticle uptake efficiency. J Am Chem Soc 2013;135:1438–1444.
39. Weiss CK, Kohnle MV, Landfester K, Hauk T, Fischer D, Schmitz-Wienke J, Mailander V. The first step into the brain: Uptake of NIO-PBCA nanoparticles by endothelial cells in vitro and in vivo, and direct evidence for their blood–brain barrier permeation. ChemMedChem 2008;3:1395–1403.
40. Åslund A, Sigurdson CJ, Klingstedt T, Grathwohl S, Bolmont T, Dickstein DL, Glimsdal E, Prokop S, Lindgren M, Konradsson P, et al. Novel pentameric thiophene derivatives for in vitro and in vivo optical imaging of a plethora of protein aggregates in cerebral amyloidoses. ACS Chem Biol 2009;4:673–684.
41. Mørch Y, Hansen R, Berg S, Hansen Y, Åslund A, Schmid R, Kubowicz S, Johnsen H, Eggen S, Blom H, et al. Nanoparticle-stabilized microbubbles for multimodal imaging and drug delivery. Contrast Media Mol Imaging 2015;10:356–366.
42. Jarzyna PA, Skajaa T, Gianella A, Cormode DP, Samber DD, Dickson SD, Chen W, Griffioen AW, Fayad ZA, Mulder WJ. Iron oxide core oil-in-water emulsions as a multifunctional nanoparticle platform for tumor targeting and imaging. Biomaterials 2009;30:6947–6954.
43. Gottstein C, Wu GH, Wong BJ, Zasadzinski JA. Precise quantification of nanoparticle internalization. ACS Nano 2013;7:4933–4945.
44. Cheng C, Trzcinski O, Doering LC. Fluorescent labeling of dendritic spines in cell cultures with the carbocyanine dye “DiI”. Front Neuroanat 2014;8:30.
45. Bananis E, Nath S, Gordon K, Satir P, Stockert RJ, Murray JW, Wolkoff AW. Microtubule-dependent movement of late endocytic vesicles in vitro: Requirements for Dynein and Kinesin. Mol Biol Cell 2004;15:3688–3697.
46. Sun X, Li F, Wang Y, Liang W. Cellular uptake and elimination of lipophilic drug delivered by nanocarriers. Pharmazie 2010;65:737–742.
47. Hofmann D, Messerschmidt C, Bannwarth MB, Landfester K, Mailander V. Drug delivery without nanoparticle uptake: Delivery by a kiss-and-run mechanism on the cell membrane. Chem Commun 2014;50:1369–1371.
48. Chan M, Schopf E, Sankaranarayanan J, Almutairi A. Iron oxide nanoparticle-based magnetic resonance method to monitor release kinetics from polymeric particles with high resolution. Anal Chem 2012;84:7779–7784.

Paper II

The effect of poly (ethylene glycol) coating and monomer type on poly (alkyl cyanoacrylate) nanoparticle interactions with lipid monolayers and cells

Habib Baghirov[a*], *Sopio Melikishvili*[b], *Yrr Mørch*[c], *Einar Sulheim*[a,c], *Andreas Åslund*[a], *Tibor Hianik*[b‡], *Catharina de Lange Davies*[a‡]

[a]Department of Physics, The Norwegian University of Science and Technology (NTNU), 7491 Trondheim, Norway

[b]Faculty of Mathematics, Physics and Informatics, Comenius University, 84248 Bratislava, Slovakia

[c]SINTEF Materials and Chemistry, 7465 Trondheim, Norway

‡These authors contributed equally

*Tel.: +4773593492. Email: habib.baghirov@ntnu.no

The authors declare no competing financial interest.

This manuscript contains 5375 words excluding the abstract and references. This combined number of table and figures in the manuscript is 8.

Graphical Abstract

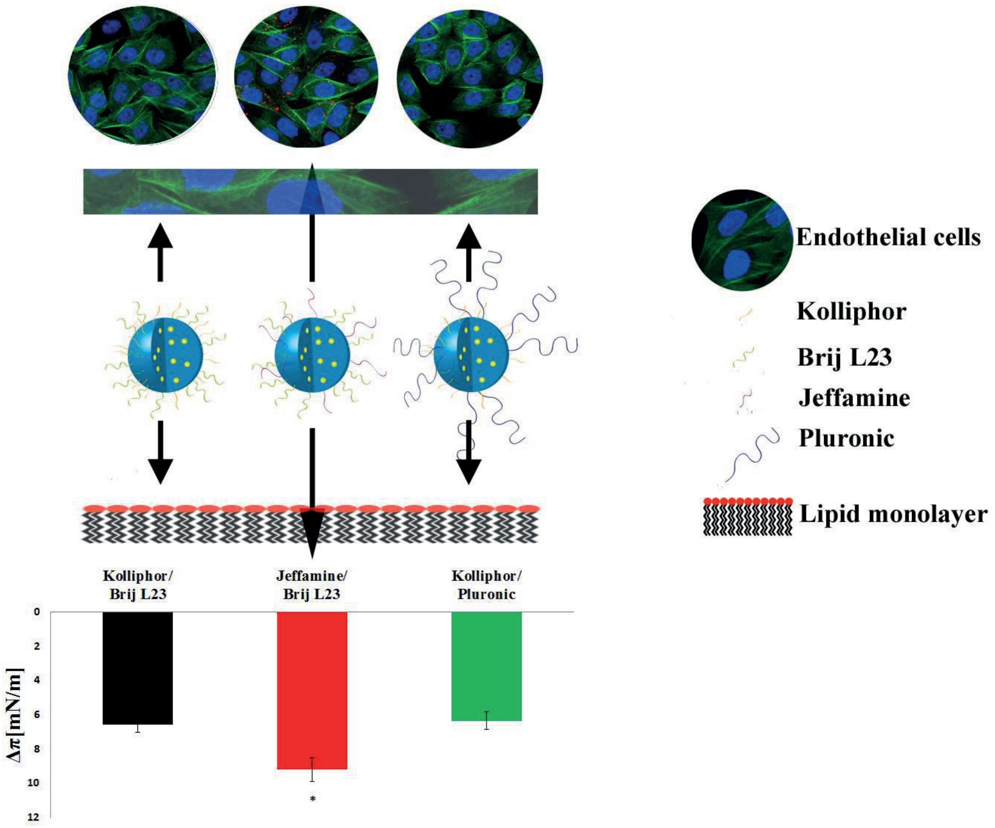

Abstract

The interaction of the promising drug carriers poly (alky cyanoacrylate) nanoparticles (PACA NPs) with lipid monolayers modeling the cell membrane and with RBE4 immortalized rat brain endothelial cells was compared to assess the relevance of lipid monolayer-based cell membrane models for PACA NP cellular uptake. NP properties such as size and charge of NPs and density poly (ethylene glycol) coating (PEG) were kept in a narrow range to assess whether the type of PEG coating and the PACA monomer affected NP-monolayer and NP-cell interactions.

The interaction with lipid monolayers was evaluated using surface pressure measurements and Brewster angle microscopy. NP association with and uptake by cells were assessed using flow cytometry and confocal laser scanning microscopy.

The interaction between NPs and both lipid monolayers and the plasma membrane depended on the type of PEGs used. PEG density affected the cellular uptake but not the interaction with lipid monolayers. NP monomer, NPs size and charge had no effect on the interactions. This might be due to the fact that the size and charge distribution was kept rather narrow to study the effect of PACA monomer and PEG type.

In conclusion, while modeling solely the passive aspect of NP-cell interactions, lipid monolayers nevertheless proved a valuable cell membrane model whose interactions with PACA NPs correlated well with NP-cell interactions. In addition, both NP-monolayer and NP-cell interactions were dependent on PEGylation type, which could be used in the design of NPs to either facilitate or hinder cellular uptake, depending on the intended purpose.

Keywords: poly(alkyl cyanoacrylate) nanoparticles, lipid monolayers, nanoparticle-cell interactions, cellular uptake, poly (ethylene glycol)

1. Introduction

Nanoparticles (NPs) have emerged as promising drug carriers owing to their ability to accumulate in tumor tissues due to the enhanced permeability and retention effect [1], potential for functionalization with moieties that increase cellular uptake of NPs, and ensuring sustained and controlled release of drugs [2, 3]. Uptake of NPs by living cells depends on various physico-chemical properties of the NPs such as NP size [4-6], aspect ratio [4, 7], charge [5, 6], hydrophobicity [8], and others.

One of the properties whose effect on NP-cell interactions is relatively poorly understood is the amount and type of poly (ethylene glycol) (PEG) coating that is commonly employed to shield NPs from the reticuloendothelial system (RES) in vivo [9]. PEGylation has been shown to extend the circulation time of NPs in blood, although it may come at the expense of reduced cellular uptake due to reduced interaction with proteins [10]. This is generally thought to be the very mechanism that protects PEGylated NPs from opsonization and interception by macrophages in vivo [11].

Poly (alkyl cyanoacrylate) NPs (PACA NPs) have shown promise in drug delivery due to the ease of their synthesis and functionalization [12], with one type of PACA NPs currently being in Phase III clinical trial for the treatment of advanced hepatocellular carcinoma [13]. The composition of PACA NPs varies depending, in particular, on the nature of the alkyl monomer and the type of surfactant (e.g. PEG) coating. Various combinations of PACA NP properties allow adjusting their degradability, circulation half-life and other parameters relevant for drug delivery and biodistribution [5, 14].

While cellular uptake of NPs is normally dominated by active processes such as endocytosis, [15], passive association of NPs with the cellular membrane is the first step in the internalization of non-targeted NPs. That association can be studied using biomimetic membrane models such as lipid monolayers comprising lipids found in the cell membrane[16]. Indeed, while lipid monolayers have commonly been used to study interactions between small molecular drugs and lipid-based cell membrane models [17], a few studies probed their interactions with NPs [18-22], showing in some instances that they can be relevant models of NP-cell interactions correlating well with NP uptake [19, 20]. NP properties that have been studied in those models include size [23], charge [18], and the presence of targeting moieties [20]. To the best of our knowledge, however, the relevance of biomimetic membrane models for NP cellular uptake has not been studied with regard to PEG coating density or type, nor have those models been applied to studies of PACA NPs. In addition, while the alkyl chain length in PACA NPs has been shown to affect NP degradability [5, 24] and cytotoxicity [25], its effect on NP uptake has received less attention and, as far as we are aware, has not been studied systematically.

We therefore investigated whether lipid monolayers could be used to model the interaction between PACA NPs and living cells, and whether those interactions were dependent on the nature of both monomer and PEG type on PACA NPs. Toward that end, we produced an array of PACA NPs with properties such as particle size, charge and PEGylation density distributed in a relatively limited range in order to identify the effects of PACA NP monomer and PEG type. The two monomer types chosen in our study were (butyl cyanoacrylate) (BCA) and (isohexyl cyanoacrylate) (IHCA), as these have been most relevant in preclinical studies and clinical trials. The artificial cell membrane was composed of a mixture of 1.2-dimyristoyl-sn-glycero-3-phosphocholine (DMPC) and 1.2-dipalmitoyl-sn-glycero-3-phosphoglycerol (DPPG) lipids commonly used in cell membrane models [22]. Rat brain endothelial cell line RBE4 was chosen for cellular association and uptake studies due to the high uptake of PACA NPs by RBE4 cells observed in our previous study [24]. Interactions between PACA NPs and the artificial membrane were compared to PACA NP association with and uptake by RBE4 cells. We found that the lipid monolayers could be a relevant model for the cellular association and uptake of PACA NPs, and that PACA NP interactions both with the artificial DMPC/DPPG membrane and RBE4 endothelial cells were affected by the type of PEG coating, while the monomer type did not significantly affect interactions in either model.

2. Experimental section

2.1. Nanoparticles

PACA NPs were synthesized using miniemulsion polymerization as previously described [26]. Briefly, the oil phase was prepared by mixing the monomer, BCA or IHCA (all from Henkel Loctite), containing a co-stabilizer (Miglyol 810N, Cremer), a radical initiator (V65, Azobisdimetyl valeronitril, Wako) and, in some NP, a fluorescent dye. The dyes used were either NR668 [27] (a kind gift from Dr. Klymchenko, University of Strasbourg), p-HTAH [28] (a kind gift from Peter Nilsson, Linköping University), or DiR (Life Technologies). The particles were PEGylated using four different non-ionic PEG-based surfactants: BrijL23 (23 ethylene glycol units, MW~1225, Sigma Aldrich), Kolliphor HS 15 (15 ethylene glycol units, MW~960, Sigma Aldrich), Pluronic F68 (triblock copolymer composed of a central hydrophobic chain of poly(propylene oxide) flanked by two PEG chains of 78 ethylene glycol units each, MW~8400, Sigma Aldrich), and Jeffamine®M-2070, 31 ethylene glycol units, MW~2000, Huntsman

Corporation). The oil-in-water emulsion was made by mixing the oil phase with a water phase (0.1 M HCl) containing one non-reactive stabilizing (BrijL23 or Pluronic F68), and one reactive initiating (Kolliphor HS 15 or Jeffamine® M-2070) PEG-based surfactant. The polymerization reaction was initiated by the amino and hydroxyl group on the lipophilic chains of Jeffamine® M-2070 and Kolliphor HS 15, respectively. Components in each batch of NPs are shown in Table 1. Polymerization was carried out for 24 hours at room temperature, followed by 8 hours at 50°C (to activate the radical initiator to ensure polymerization of any un-reacted monomer). After polymerization, the NPs were dialyzed against 1.1 μM HCl with MWCO 12-14000 Da to remove the excess of surfactants.

2.2. Nanoparticle characterization

The NPs were characterized for size distribution, polydispersity index (PDI) and surface charge (ζ-potential) using dynamic light scattering (DLS, Zetasizer Nano ZS, Malvern Instruments) in 0.01 M phosphate buffer, pH 7. PEGylation of NPs was confirmed by 1H-nuclear magnetic resonance (NMR) using a Bruker Avance DPX 400 MHz with autosampler. Prior to NMR, the dialyzed NPs were washed with distilled water and centrifuged three times before drying at 50°C overnight. The samples were dissolved in Acetone-D6 and scanned for 32 scans. The spectra were processed in Mestrenova 9.0.1 (Mestrelab Research S.L.) and the solvent residual peak at 2.05 ppm was used as reference. To calculate PEGylation, the characteristic PEG-peaks at 3.6 ppm, the peak of a triplet from Miglyol 810N at 2.33 ppm and methylene groups of poly (alkyl cyanoacrylate) at 1.75 ppm were integrated. From the integrals, number of protons corresponding to each integral, the dry weight of the material and the size, concentration and density (1.148 g/ml) of NP, it was possible to calculate the number of ethylene units/nm^2.

2.3. Phospholipids and monolayer preparation

DMPC and DPPG lipids were purchased from Avanti Polar Lipids Inc. Their mixture with a DMPC/DPPG molar ratio of 10:1 was prepared in chloroform (Slavus) and stored at 4º until further use. The mixture of DMPC/DPPG lipids had a negative charge (-25.6±1.58) typical for cell membranes [29, 30]. DMPC/DPPG monolayers were prepared by homogenous deposition of DMPC/DPPG mixture droplets onto 10 ml of subphase (phosphate-buffered saline, Sigma) (PBS) pre-added to an in-house Teflon container of circular shape (volume 10 ml). The lipid mixture was deposited using a Hamilton syringe (Hamilton Company), and surface pressure of the monolayer was monitored using a PS4 surface pressure sensor (NIMA Technology) until a required initial surface pressure value was reached. We analyzed interaction of NPs with monolayers of surface pressure 10, 20 and 30 mN/m corresponding to the liquid-condensed (10 mN/m) and solid state (20-30 mN/m) of the monolayer. Monolayers were allowed to equilibrate under stirring at ambient temperature (T=23±1 ºC).

After the formation of DMPC/DPPG monolayers on the subphase, NPs were injected to the subphase at an initial concentration of 20 µg/ml using a Hamilton syringe, still under stirring and while monitoring the surface pressure using a surface pressure sensor. The initial concentration of 20 µg/ml was chosen because it was used in our previous studies on the cellular uptake of PACA NPs without any cytotoxic effect [24]. NPs were further added to the subphase to reach total concentrations of 40, 60 and 80 µg/ml once the effect on the surface pressure following the previous NP injection had reached a plateau. Changes in the surface pressure values were calculated based on the values in such graphs. All experiments were conducted at ambient temperature (T=23±1 ºC).

2.4. Brewster angle microscopy

DMPG/DPPG monolayers were formed on the subphase and NPs were injected at gradually increasing concentrations as described in Section 2.3, except that a black glass plate was placed on the bottom of the in-house Teflon container to allow visualization of the interactions between NPs and the lipid monolayers with Brewster angle microscopy (BAM) (BAM 3, NIMA Technology). The BAM was equipped with a HeNe laser emitting p-polarized light with a wavelength of 659 nm that was reflected off at the air/buffer interface at the Brewster angle (53.1˚). The reflected light passed through a focal lens into an analyzer and finally to a CCD camera. The collection of this reflected radiation with a video camera allowed in situ, real time visualization of the lipid monolayer at the air/buffer interface in the presence and absence of NPs. The lateral resolution of the microscope was 10 µm. All experiments were performed at ambient temperature (T=23±1 ºC).

2.5. Cell culture

RBE4 cells (a generous gift from Dr. Aschner, Vanderbilt University) were cultured on rat tail collagen type I (Millipore) at 37 °C and 5 % CO2 in 1:1 mixture of Minimum Essential Medium and Ham's F-10 medium supplemented with 10 % fetal bovine serum, 300 µg/ml geneticin and 1 ng/ml basic fibroblast growth factor (all from Thermo Scientific).

2.6. Flow cytometry

RBE4 cells were seeded on collagen type I in 12-well plates (Costar) at a density of 100,000 cells per well. When reaching the log phase, the cells were incubated with the NPs at 20 µg/ml in 1 ml of medium for 3 hours. After the cells were trypsinized and washed twice with phosphate-buffered saline (Sigma), they were analyzed by flow cytometry (Gallios, Beckman Coulter). NR668-loaded NPs were excited at 561 nm and fluorescence was detected at 620 nm using a 30 nm bandpass filter. p-HTAH-loaded NPs were excited at 405 nm and fluorescence was detected at 450 nm using a 50 nm bandpass filter. 10,000 cells were use in the analysis; cell debris, dead cells and aggregates were excluded by gating the cell population on a dot plot of forward light scatter signal versus side scatter signal. The cellular association and uptake of NPs was measured as the percentage of positive cells in flow cytometry histograms, and the amount of NPs per cell was estimated using median fluorescence intensity. To compare the cellular association and uptake of NPs which had different amount of encapsulated dye and, therefore, different fluorescence intensities, a normalization factor was used. This factor was found by measuring the fluorescence intensity of NPs in PBS using a spectrophotometer (Infinite 200Pro, Tecan) and was in the range of 1.0-2.9 depending on the NP.

2.7. Confocal laser scanning microscopy

The cells were seeded on collagen type I in 8-well Ibidi plates (Ibidi) at a density of 20,000 cells per well and grown to reach the log-phase. Following that, the cells were incubated with the NPs at 20 µg/ml in 250 µl of medium for 3 hours, then fixed in 4% paraformaldehyde and counter-stained with Hoechst 33258 (Life Technologies) to visualize the nuclei and Alexa Fluor 488-labeled phalloidin (Life Technologies) to visualize the actin cytoskeleton. After staining, the cells were prepared for imaging by mounting using SlowFade Gold Antifade Mountant (Life Technologies). Confocal images were obtained using a Leica SP8 CLSM with a 63 × 1.2 water objective. For NR668 excitation, a white light laser at 514 nm was used, and the emission was detected at 580–660 nm using a photon counting hybrid detection system. For p-HTAH excitation, a 405 nm laser was used, and the emission was detected at 450-480 nm. Z-stacks of cells were obtained to distinguish between intracellular and surface-associated NPs.

2.8. Data analysis

Data on lipid monolayers were analyzed using Origin 8.1 software (OriginLab). Confocal images were analyzed using ImageJ. 1.48g. Flow cytometry data were analyzed using Kaluza Flow Cytometry Analysis software v1.2 (Beckman Coulter). Statistical analysis was performed using SPSS Statistics v20 (IBM).

3. Results

3.1. Nanoparticle composition and characterization

NPs with varying composition (type of PEG and monomer) were synthetized by miniemulsion polymerization and characterized with regard to size, charge and PEG density. NP composition, size and ζ-potential are given in Table 1.

Table 1. Composition and characterization of the NPs used in this study

Nanoparticles	Monomer	Size, nm	PDI	ζ-potential, mV	Initiator	Stabilizer	Dye	Ethylene glycol units/nm^2
B_Kol_Brij_1	BCA	117	0.11	-3	Kolliphor HS 15	BrijL23		14.8
B_Kol_Brij_1 *	BCA	145	0.24	-3	Kolliphor HS 15	Brij L23	NR668	20.0
IH_Kol_Brij_1	IHCA	143	0.13	-1	Kolliphor HS 15	BrijL23		27.9
IH_Kol_Brij_1	IHCA	172	0.25	-2	Kolliphor HS	Brij L23	NR668	24.1

*					15			
IH_Kol_Brij_2	IHCA	163	0.15	-1	Kolliphor HS 15	BrijL23	NR668	25.1
B_Jeff_Brij_1	BCA	103	0.26	-4	Jeffamine M-2070	BrijL23		17.4
B_Jeff_Brij_2	BCA	150	0.18	-2	Jeffamine M-2070	BrijL23	DiR	12.7
B_Jeff_Brij_3	BCA	158	0.32	-4	Jeffamine M-2070	BrijL23		19.8
B_Jeff_Brij_4	BCA	118	0.26	-3	Jeffamine M-2070	BrijL23	pHTAH	17.5
IH_Jeff_Brij_1	IHCA	169	0.21	-2	Jeffamine M-2070	BrijL23	NR668	21.9
IH_Jeff_Brij_2	IHCA	148	0.19	-3	Jeffamine M-2070	BrijL23		22.3
B_Kol_Plu_1	BCA	141	0.11	-5	Kolliphor HS 15	Pluronic F68		13.0
B_Kol_Plu_2	BCA	151	0.11	-5	Kolliphor HS 15	Pluronic F68	NR668	14.0
IH_Kol_Plu_1	IHCA	167	0.34	-2	Kolliphor HS 15	Pluronic F68		26.5

Throughout the text, the following conventions are used to describe the NPs for the sake of brevity: first, the monomer type (B or IH, denoting BCA and IHCA, respectively), followed by PEG type where Kol refers to Kolliphor, Jeff – to Jeffamine M-2070 and Brij – to BrijL23, and, ultimately, the number, in order to distinguish between NPs that share both the same monomer and a particular combination of PEG. It should be noted that B_Kol_Brij_1 and IH_Kol_Brij_1 were produced in two variants, with or without a fluorescent dye. This is reflected in the text below and discussed in more detail in the Discussion.

All NPs were within a relatively narrow size distribution (103-169 nm) and had a slightly negative charge (- 1 to -5 mV). Using PEG-based amphiphilic molecules as both stabilizers and initiators resulted in PEGylated particles with PEG density values in the range 14-28 ethylene glycol units per nm^2, and with PEG covalently linked to the particle surface. The proposed surface functionalization of the three different PEGylation strategies used is illustrated in Supplementary Figure 1. Briefly, four different PEG-based surfactants were used to form three different PEG coating combinations. A: Brij L23 + Kolliphor HS15; B: Brij L23 + Jeffamine M2070 and C: Pluronic F68 + Kolliphor HS15.

3.2. Nanoparticle interaction with lipid monolayers

The kinetics of the interactions between the NPs and DMPC/DPPG monolayers modeling the cell membrane is shown in Supplementary Figure 2 for the initial surface pressure of π_0 = 20 mN/m. The addition of NPs induced an increase in the surface pressure, and the effect the NPs exerted on the monolayers is expressed in the changes in monolayer surface pressure $\Delta\pi$.

Such measurements were done for a variety of NPs, and NP-monolayer interaction is grouped in Figure 1 based on the magnitude of the surface pressure change. The cumulative changes in $\Delta\pi$ for different NPs (reached at the NP concentration of 80 μg/ml) are shown as well. These changes varied in the range of $\Delta\pi$ = 5-11 mN/m.

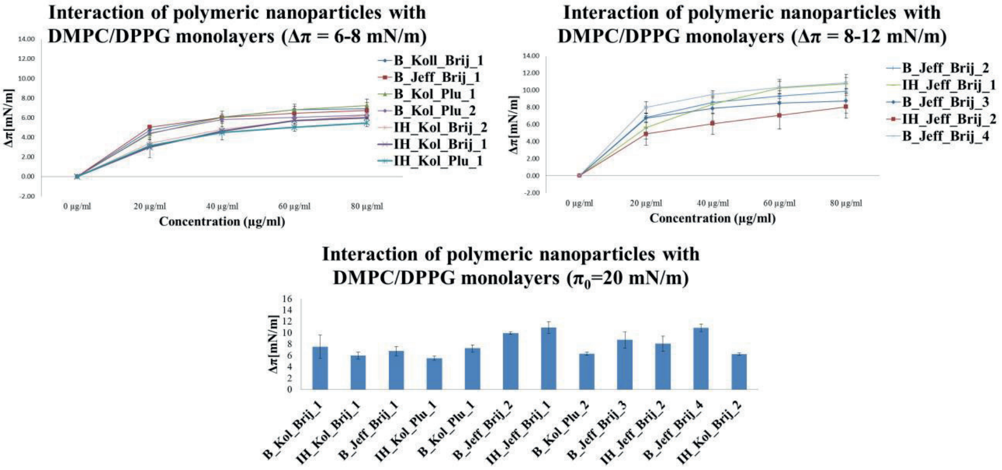

Figure 1. The plot of the changes in surface pressure vs. concentration of NPs following the interaction PACA NPs with DMPC/DPPG monolayers at the initial surface pressure π_0=20 mN/m. n=3-4. Interactions with a magnitude of Δπ reaching 5-8 and 8-11 mN/m, respectively, are grouped together. Cumulative Δπ at the NP concentration of 80 μg/ml at the end of the experiment are shown as well.

Next we looked at the patterns of NP-monolayer interactions that could identify their correlation with various NP properties. Dependence of the cumulative surface pressure changes induced by NP-monolayer interactions on the PEG type, NP monomer type, PEG density, size and surface charge is shown in Figure 2.

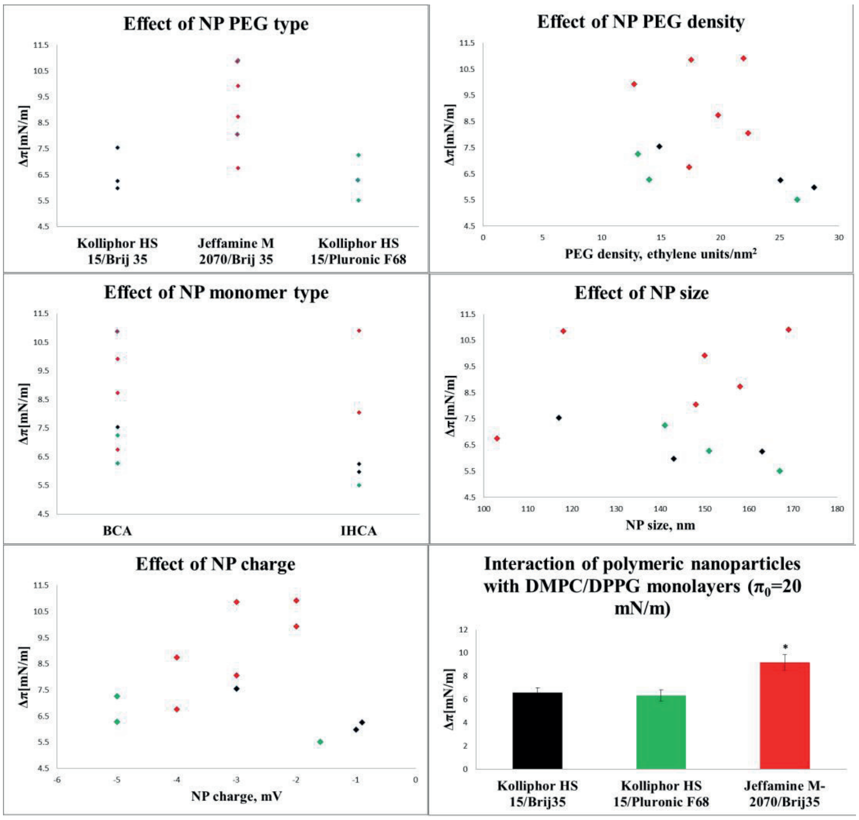

Figure 2. The effect of NP properties on the cumulative change in monolayer surface pressure change reached at the NP concentration of 80 µg/ml. Figure shows the effect of NP PEG type, PEG density, monomer type, NP size and NP surface charge. Black diamonds: Koliphor HS 15/Brij 35; red diamonds: Jeffamine M 2070/Brij 35; green diamonds: Koliphor HS 15/Pluronic F68. Changes of cumulative surface pressure for PACA NPs having the same PEG combination and interacting with DMPC/DPPG monolayers at π_0=20 mN/m. n=3-15 depending on the group are shown as well. Asterisk denotes statistically significant difference ($p<0.05$) according to Mann-Whitney U test.

NP monomer type did not have any statistically significant effect on the strength of NP-monolayer interactions in the Mann-Whitney U test. PEG density, NP size and NP surface charge did not correlate with the effect that PACA NPs exerted on lipid monolayers either (R^2=0.11, R^2<0.1 and R^2<0.1, respectively, according to linear regression analysis). With respect to the last three properties, this can be attributed to their relatively narrow distribution in the NPs used. However, various PEG type combinations induced markedly different changes in the monolayer surface pressure. Except for one outlier (B_Jeff_Brij_1), all NPs having the PEG combination Jeffamine M2070/BrijL23 induced surface pressure changes ($\Delta\pi$ = 8.74-10.91 mN/m) well above the other NPs which caused cumulative surface pressure changes in the range of $\Delta\pi$ = 5.51-7.54 mN/m. To emphasize this, data points in Figure 2 were color-coded according to the PEGylation type. Further illustration of this point is also provided in Figure 2 where cumulative surface pressure changes induced by NPs were averaged for all NPs with the same PEG type. This shows that the effect of PACA NPs with Jeffamine M 2070/BrijL23 is significantly larger than the effect produced by NPs with other PEG combinations.

In order to visualize interactions between polymeric NPs and DMPC/DPPG monolayers, we chose NPs producing the largest cumulative effect on the monolayer surface pressure and monitored its interactions with the monolayer using Brewster angle microscopy (Figure 3).

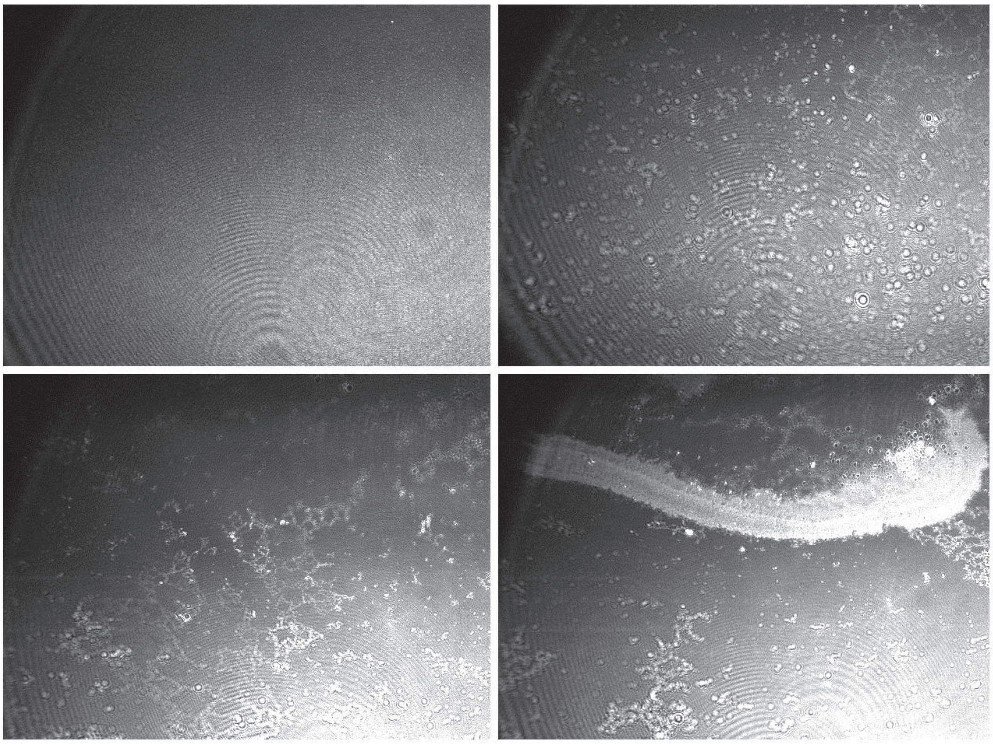

Figure 3. Visualization of interaction between B_Jeff_Brij_4 and DMPC/DPPG monolayer at π_0=20 mN/m. Figure shows the monolayer before the addition of NPs and progressive formation of NP-induced lipid clustering after the addition of B_Jeff_Brij_4 NPs at 20, 60 and 80 µg/ml, respectively.

The effect of B_Jeff_Brij_4 NPs can be seen in in the formation of increasingly denser bright clusters caused by the interaction of the NPs with the monolayer. A recording showing real-time monitoring of NP interactions with a DMPC/DPPG monolayer is shown in Supplementary Video 1.

While most of the monolayer interaction results were produced by measuring NP interactions with the DMPC/DPPG monolayer at an initial surface pressure of 20 mN/m, in separate experiments we found that the extent of the effect depended on the initial surface pressure π_0. At the initial surface pressure values of 10 and 30 mN/m, surface pressure changes induced by NPs with the largest effect the PEG combination producing the largest effect (B_Jeff_Brij_4) were found to be respectively larger and smaller than the values reached at $\pi_0 = 20$ mN/m (Supplementary Figures S3-S4). Additionally, we investigated whether the presence or absence of a fluorescent dye in B_Kol_Brij_1 could cause any changes in NP-monolayer interactions. Both types of B_Kol_Brij_1 caused similar changes in the surface pressure of the lipid monolayers (Supplementary Figure S5).

3.3. Cellular association and uptake

In order to investigate whether the cellular association and uptake of the NPs by living cells are affected by NP properties and compare that to the effect of the NPs on lipid monolayers, we incubated RBE4 cells with the NPs for 3 hours and measured fluorescence of the cell populations using flow cytometry. Since detection of cell surface-associated or internalized NPs by flow cytometry relies on their fluorescence, we could only use NPs labeled with a fluorescent dye. In the case of B_Kol_Brij_1 and IH_Kol_Brij_1 (all labeled with NR668), the NPs were originally made in two variants: with and without a fluorescent dye. Representative flow cytometry histograms illustrating low and high cellular fluorescence intensities, as well as the median fluorescence intensity for all NPs studied, corrected for the difference in fluorescence intensities, are shown in Figure 4.

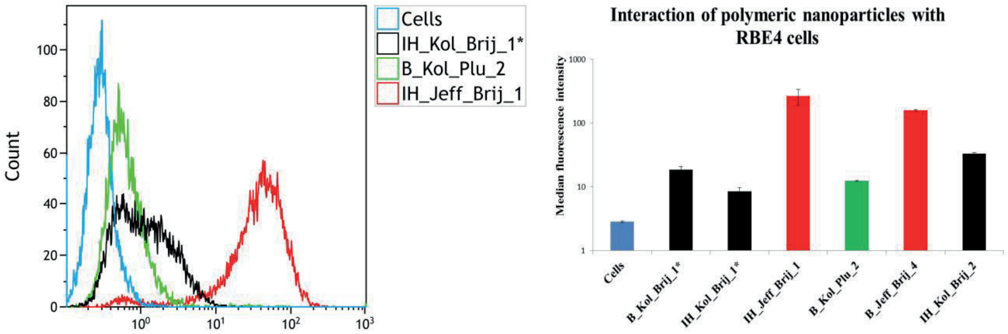

Figure 4. Cell surface association and uptake of polymeric NPs by RBE4 cells showing representative flow cytometry histograms and median fluorescence intensities of cells incubated with the NPs and corrected for variations in fluorescence intensities.

The fluorescence of RBE4 cells incubated with NPs for 3 hours was mainly limited, with the exceptions of two NPs: IH_Jeff_Brij_1 and B_Jeff_Brij_4. It should be noted that both of these NPs also had the largest effect on DMPC/DPPG monolayer surface pressure in the lipid monolayer experiments. In order to detect any dependence between NP properties and cellular association/uptake, we plotted the changes in fluorescence intensity induced by cellular association and uptake against the various NPs properties (Figure 5).

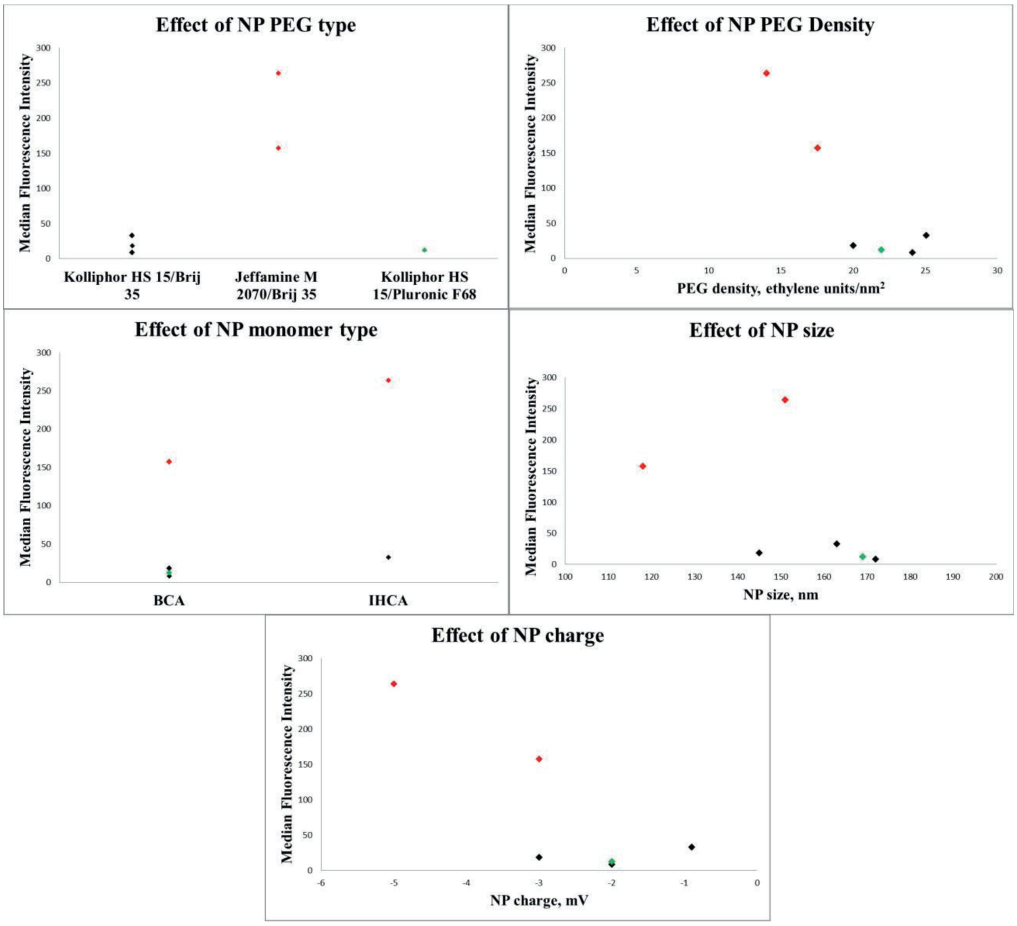

Figure 5. The effect of NP properties on the cellular association and uptake of NPs by RBE4 cells. Figure shows the effect of NP PEG type, PEG density, monomer type, NP size and NP surface charge. Black diamonds: Koliphor HS 15/Brij 35; red diamonds: Jeffamine M 2070/Brij 35; green diamonds: Koliphor HS 15/Pluronic F68.

Figure 5 shows that the type of PEG and PEG density affected NP uptake by cells or their association with the plasma membrane. Increased PEG density resulted in reduced cellular association and uptake (R^2=0.80 according to linear regression analysis), an observation in line with the literature [10]. However, this did not translate into reduced interaction with lipid monolayers regardless of whether linear regression analysis included all NPs in the lipid monolayer studies (R^2=0.11) or only those that were also used in cellular association and uptake studies (R^2=0.04). NP size and charge were not strongly correlated with NP cellular uptake either (R^2=0.27 and 0.69, respectively). One result that was clear both in the cellular studies and in PACA NP interactions with lipid monolayers was the effect of the PEG type. Both NPs that showed the highest association and uptake by RBE4 cells were PEGylated using Jeffamine M-2070 as the initiator and BrijL23 as the stabilizer. As in Figure 2, data points in Figure 5 were color-coded to emphasize this observation.

Flow cytometry cannot distinguish between surface-associated and internalized NPs, and since the dyes in our particles are encapsulated rather than bound to the surface of the NPs, quenching them with traditional quenching agents such as Trypan Blue may be problematic due to the increased distance between the dyes and the quencher. We therefore acquired confocal images of RBE4 cells incubated with the polymeric NPs, taking Z-stacks in order to verify the intracellular location of the NPs (Figure 6).

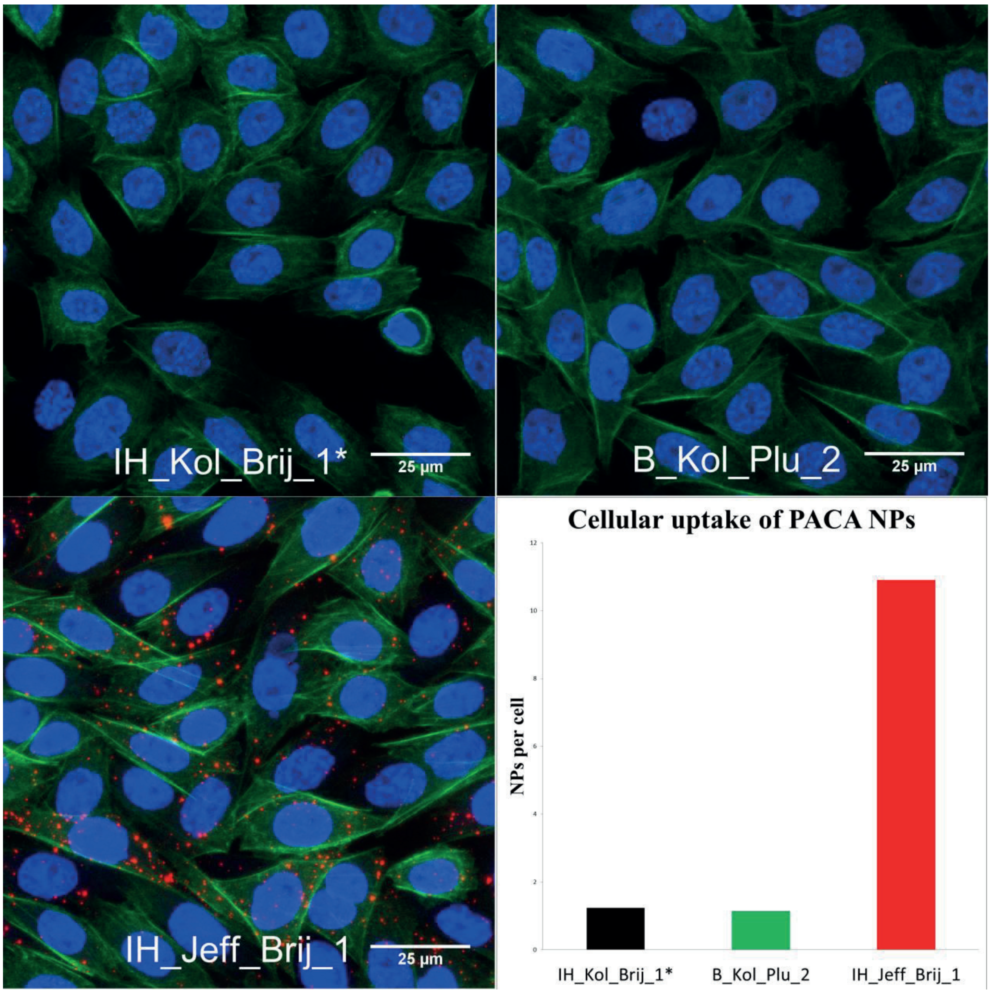

Figure 6. Uptake of NPs by RBE4 cells. Confocal images of the uptake of various NPs by RBE4 cells shown with quantification of NP uptake using image analysis to count the number of NPs per cell. Blue: cell nuclei, green: actin filaments, red: NPs; maximum intensity projections.

Confocal microscopy images are consistent with the flow cytometry data. In Figure 6, the uptake of IH_Jeff_Brij_1 NPs appears to be far greater than that of the other NPs. Visual inspection is supported by image analysis estimating the number of NPs per cell.

Finally, we analyzed the correlation between surface pressure changes induced by PACA NPs and the extent of their cellular uptake (Figure 7).

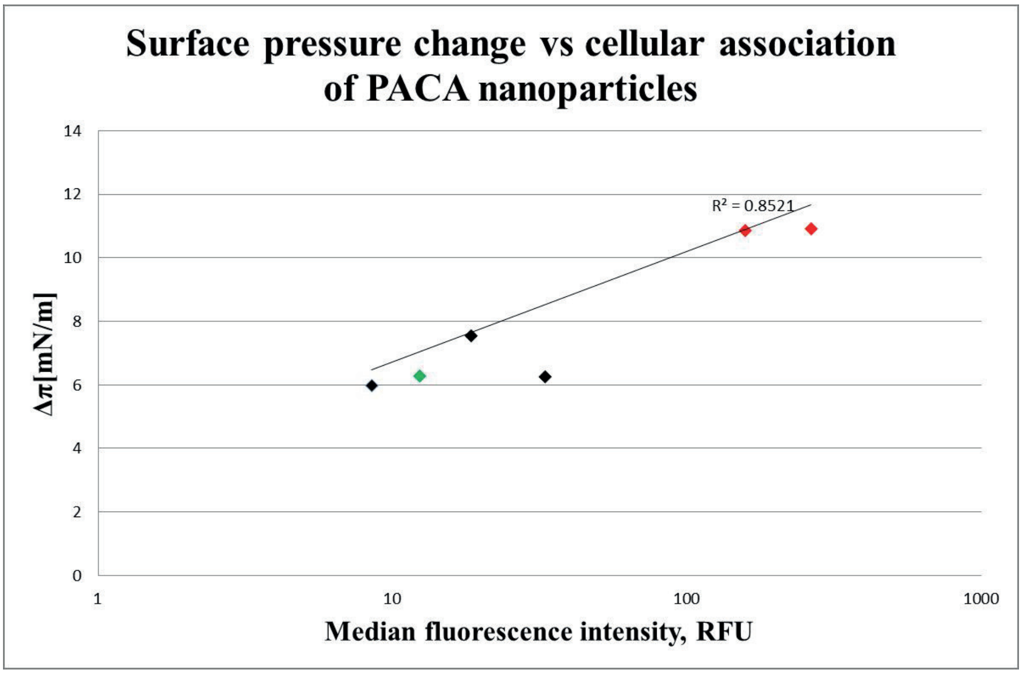

Figure 7. Correlation between PACA NP effects on lipid monolayers and their cellular association and uptake

Figure 7 clearly shows a correlation between changes in surface pressure and cellular uptake, i.e. the PACA NPs that had the largest effect in monolayer studies also exhibited the highest cellular uptake.

4. Discussion

The interactions between NPs and cells are initiated at the cell membrane. Therefore, understanding how these interactions are affected by various NP properties is crucial for designing NPs for drug delivery. The interactions may be probed in a variety of cell membrane models including lipid monolayers, liposomes and supported lipid bilayers. Our study with lipid monolayers shows that the addition of NPs into the water subphase resulted in increased surface pressure depending on the type of NP coating. This is evidence of interactions between NPs with phospholipid head groups of the monolayer. The adsorption of charged NPs results in increasing repulsive forces in the monolayers, which is the main reason of the surface pressure changes. Surface pressure changes therefore can be used to assess the extent of the effect that the NPs exert on the lipid monolayer. The surface pressure depends on the mean molecular area and reflects the spacing of lipid molecules in the monolayer. High surface pressure and low molecular area indicate that the lipid molecules are closely packed, and vice versa [23]. Changes in the surface pressure can be induced by interaction with foreign agents such as PACA NPs in this study. Different surface pressure values can be used to model normal cells (30 mN/m) and cancer cells (20 mN/m) which have varying lipid densities in the outer cell membrane.

The effect of NP size and charge on the cellular uptake has been demonstrated in numerous works [31, 32], and the general trends seem to be valid for interactions between NPs and model membranes as well. In [23], relatively small polystyrene NPs (20 nm) increased the surface pressure of a model endothelial membrane regardless of surface chemistry, while larger NPs (≥60 nm) either reduced it or had no effect, depending on the surface group. At a size of 60 nm, aminated NPs increased the surface pressure of the endothelial monolayer model, while unmodified NPs reduced it and carboxylated NPs had no effect. In our study, PACA NPs were in a rather narrow size range of 103-167 nm and surface charge range of -1 - -5 mV, and these two properties did not have any effect on the magnitude of NP-monolayer or NP-cell interactions. The discrepancy between our results and the results in the study referred to might be due to the different type or size of the NPs.

NPs used as drug carriers are commonly coated or otherwise functionalized to ensure specific drug delivery. Such coatings and functional groups are on the external surface of the NP and, therefore, are the first moieties recognized by the plasma membrane. Consequently, their interactions with the cell membrane largely define the outcome of NP-cell interaction. The effect of cationic surfactants on the interactions between PLGA NPs of approximately the same size and model plasma and endosome membranes [19] indicated that cationic PLGA NPs coated with didodecyldimethylammonium bromide (DMAB) or cetyltrimethylammonium bromide (CTAB) increased the surface pressure of the model membranes as opposed to unmodified anionic NPs, and that the increase induced by DMAB NPs was faster and larger than that caused by CTAB NPs. Cellular uptake studies were in line with monolayer experiments. The same group demonstrated that neither ritonavir-loaded poly(l-lactide) NPs (RNPs), nor RNPs conjugated to a scrambled trans-activating transcriptor peptide had an effect on a lipid monolayer mimicking an endothelial cell membrane, while RNPs conjugated to the actual peptide affected the membrane depending on the amount of the peptide on the RNPs; cellular studies using human vascular endothelial cells showed good correlation with lipid monolayer experiments. [20]

NP PEGylation is among the most common methods to avoid NP interception by the RES in vivo. Among factors that affect the balance between efficient shielding from the RES and uptake by target cells are PEG molecular weight, chain structure, conformation and coating density.

PEG chain length, in particular, has been shown to affect cell binding and uptake of several NP platforms [33, 34]. It has also been noted, however, that the evaluation of PEGylation efficiency suffers from a large variability of results across different NP platforms [35]. Our aim with regard to PEG properties was therefore to test a number of PEG combinations with short and long chains to determine if any of them facilitates NP-lipid monolayer and NP-cell interactions. Assuming that the chain length of each individual PEG component on the NP used in our study is given by the number of ethylene glycol units, our results indicate that the chain length is not an important parameter for the NP-monolayer interactions. However, such conclusions should be carefully considered as the actual PEG lengths on the NPs may change during synthesis and in solution. Therefore, each combination of PEG initiators and stabilizers used in our study is treated as a separate property without further assumptions concerning the length of individual components of the PEG coating.

While this study is the first to probe the effect of PEG type on PACA NP interactions with model membranes, the interactions of various polymers with cell membrane models have been assessed in several studies. With regard to PEG, a study comparing various Pluronic copolymers found that their effect on drug efflux activity in brain endothelial cells and cancer cells depended on molecule hydrophobicity and the lengths of the hydrophobic and hydrophilic segments [36]. A subsequent study found that not only the overall hydrophobicity, but also the structure of PEG copolymers affected their interactions with lipid bilayers [37]. It should be noted that both the membrane model itself and the readouts were markedly different from the ones used in the present study. The effects of various Pluronics on lipid monolayer surface pressure [38] showed that Pluronics with higher hydrophobicities exerted greater effects on DMPC and DPPC monolayers. In yet another study, it was found that the size of Pluronic molecules governed their insertion in DPPC and DPPG monolayers, with smaller molecules being able to insert into monolayers at higher surface pressure than larger ones [39]. It should be emphasized that in our study, the external agents interacting with the DMPC/DPPG monolayer were PACA NPs coated with PEG, as opposed to surfactant molecules alone; however, since the size distribution of the NPs remained relatively narrow, the structure and relative sizes of the copolymer blocks may have played a dominant role in the interaction.

We should note that the encapsulation of dyes into NPs can cause misinterpretation of their cellular uptake in flow cytometry due to potential dye leakage [40-42]. We therefore confirmed that no dye leakage has taken place by incubating RBE4 cells with PACA NPs at 4 ºC [43]. In addition, CLSM images confirmed that the NPs were internalized.

Various properties of NPs, particularly the size and charge that most NP platform are normally characterized for, have been shown to affect NP cellular uptake to some extent; however, as noted by [44, 45], those properties can hardly be used as reliable predictors, and NP interactions with model cell membranes having properties typical for target cells may be employed to assess NP cellular uptake potential with greater precision [23].

In conclusion, this is to the best of our knowledge the first study investigating the interactions between PACA NPs and a model cell membrane and correlating these interactions with NP cellular uptake, with particular emphasis on PACA NP monomer type and PEGylation. We observed a good correlation between PACA NPs interactions with a model membrane and their actual cellular uptake, and found that a particular combination of PEG altered NP effects in both systems. These results could be used in predicting PACA NP interactions with target cells and in designing PACA NP-based drug delivery systems with desired cellular uptake properties.

ACKNOWLEDGEMENTS:

Anne Rein Hatletveit, Zuzana Garaiova, Pavol Vitovič, Július Cirák, Juraj Chlpík and Tomas Vary are thanked for technical assistance with nanoparticle synthesis, Langmuir-Blodgett troughs and Brewster angle microscopy experiments. This study was funded by The Central Norway Regional Health Authority and The Research Council of Norway (NANO2021 project number 220005 and BIOTEK2021 project number 226159), as well as the Stipend program EEA Slovakia - institutional collaboration between high education institutions EEA/EHP-SK06-IV-V-01 (project No. SK06-IV-01-005) - and Agency for Promotion Research and Development under the contract APVV-14-0267.

REFERENCES:

[1] N. Bertrand, J. Wu, X. Xu, N. Kamaly, O.C. Farokhzad, Cancer nanotechnology: the impact of passive and active targeting in the era of modern cancer biology, Advanced drug delivery reviews, 66 (2014) 2-25.

[2] J.L. Markman, A. Rekechenetskiy, E. Holler, J.Y. Ljubimova, Nanomedicine therapeutic approaches to overcome cancer drug resistance, Advanced drug delivery reviews, 65 (2013) 1866-1879.

[3] E.H. Chang, J.B. Harford, M.A. Eaton, P.M. Boisseau, A. Dube, R. Hayeshi, H. Swai, D.S. Lee, Nanomedicine: Past, present and future - A global perspective, Biochemical and biophysical research communications, 468 (2015) 511-517.

[4] B.D. Chithrani, A.A. Ghazani, W.C. Chan, Determining the size and shape dependence of gold nanoparticle uptake into mammalian cells, Nano letters, 6 (2006) 662-668.

[5] C. He, Y. Hu, L. Yin, C. Tang, C. Yin, Effects of particle size and surface charge on cellular uptake and biodistribution of polymeric nanoparticles, Biomaterials, 31 (2010) 3657-3666.

[6] R. Ferrari, M. Lupi, C. Colombo, M. Morbidelli, M. D'Incalci, D. Moscatelli, Investigation of size, surface charge, PEGylation degree and concentration on the cellular uptake of polymer nanoparticles, Colloids Surf B Biointerfaces, 123 (2014) 639-647.

[7] Y. Li, M. Kroger, W.K. Liu, Shape effect in cellular uptake of PEGylated nanoparticles: comparison between sphere, rod, cube and disk, Nanoscale, 7 (2015) 16631-16646.

[8] D.F. Moyano, K. Saha, G. Prakash, B. Yan, H. Kong, M. Yazdani, V.M. Rotello, Fabrication of corona-free nanoparticles with tunable hydrophobicity, ACS nano, 8 (2014) 6748-6755.

[9] M.J. Ernsting, M. Murakami, A. Roy, S.D. Li, Factors controlling the pharmacokinetics, biodistribution and intratumoral penetration of nanoparticles, Journal of controlled release : official journal of the Controlled Release Society, 172 (2013) 782-794.

[10] S.J. Soenen, B.B. Manshian, A.M. Abdelmonem, J.-M. Montenegro, S. Tan, L. Balcaen, F. Vanhaecke, A.R. Brisson, W.J. Parak, S.C. De Smedt, K. Braeckmans, The Cellular Interactions of PEGylated Gold

Nanoparticles: Effect of PEGylation on Cellular Uptake and Cytotoxicity, Particle & Particle Systems Characterization, 31 (2014) 794-800.

[11] D. Pozzi, V. Colapicchioni, G. Caracciolo, S. Piovesana, A.L. Capriotti, S. Palchetti, S. De Grossi, A. Riccioli, H. Amenitsch, A. Lagana, Effect of polyethyleneglycol (PEG) chain length on the bio-nano-interactions between PEGylated lipid nanoparticles and biological fluids: from nanostructure to uptake in cancer cells, Nanoscale, 6 (2014) 2782-2792.

[12] A. Kumari, S.K. Yadav, S.C. Yadav, Biodegradable polymeric nanoparticles based drug delivery systems, Colloids Surf B Biointerfaces, 75 (2010) 1-18.

[13] E. Soma*, P. Attali, P. Merle, Chapter 11 A Clinically Relevant Case Study: the Development of Livatag[registered sign] for the Treatment of Advanced Hepatocellular Carcinoma, Nanostructured Biomaterials for Overcoming Biological Barriers, The Royal Society of Chemistry2012, pp. 591-600.

[14] C. Vauthier, D. Labarre, G. Ponchel, Design aspects of poly(alkylcyanoacrylate) nanoparticles for drug delivery, Journal of drug targeting, 15 (2007) 641-663.

[15] L. Treuel, X. Jiang, G.U. Nienhaus, New views on cellular uptake and trafficking of manufactured nanoparticles, Journal of the Royal Society, Interface / the Royal Society, 10 (2013) 20120939.

[16] E. Rascol, J.M. Devoisselle, J. Chopineau, The relevance of membrane models to understand nanoparticles-cell membrane interactions, Nanoscale, 8 (2016) 4780-4798.

[17] C. Stefaniu, G. Brezesinski, H. Möhwald, Langmuir monolayers as models to study processes at membrane surfaces, Advances in Colloid and Interface Science, 208 (2014) 197-213.

[18] A.A. Torrano, A.S. Pereira, O.N. Oliveira, Jr., A. Barros-Timmons, Probing the interaction of oppositely charged gold nanoparticles with DPPG and DPPC Langmuir monolayers as cell membrane models, Colloids Surf B Biointerfaces, 108 (2013) 120-126.

[19] C. Peetla, V. Labhasetwar, Effect of molecular structure of cationic surfactants on biophysical interactions of surfactant-modified nanoparticles with a model membrane and cellular uptake, Langmuir, 25 (2009) 2369-2377.

[20] C. Peetla, K.S. Rao, V. Labhasetwar, Relevance of biophysical interactions of nanoparticles with a model membrane in predicting cellular uptake: study with TAT peptide-conjugated nanoparticles, Molecular pharmaceutics, 6 (2009) 1311-1320.

[21] A. Ambike, V. Rosilio, B. Stella, S. Lepetre-Mouelhi, P. Couvreur, Interaction of self-assembled squalenoyl gemcitabine nanoparticles with phospholipid-cholesterol monolayers mimicking a biomembrane, Langmuir, 27 (2011) 4891-4899.

[22] M. Ionov, K. Ciepluch, Z. Garaiova, S. Melikishvili, S. Michlewska, L. Balcerzak, S. Glinska, K. Milowska, R. Gomez-Ramirez, F.J. de la Mata, D. Shcharbin, I. Waczulikova, M. Bryszewska, T. Hianik, Dendrimers complexed with HIV-1 peptides interact with liposomes and lipid monolayers, Biochimica et biophysica acta, 1848 (2015) 907-915.

[23] C. Peetla, V. Labhasetwar, Biophysical characterization of nanoparticle-endothelial model cell membrane interactions, Molecular pharmaceutics, 5 (2008) 418-429.

[24] E. Sulheim, H. Baghirov, E. von Haartman, A. Boe, A.K. Aslund, Y. Morch, L. Davies Cde, Cellular uptake and intracellular degradation of poly(alkyl cyanoacrylate) nanoparticles, Journal of nanobiotechnology, 14 (2016) 1.

[25] C. Lherm, R.H. Müller, F. Puisieux, P. Couvreur, Alkylcyanoacrylate drug carriers: II. Cytotoxicity of cyanoacrylate nanoparticles with different alkyl chain length, International Journal of Pharmaceutics, 84 (1992) 13-22.

[26] Y. Morch, R. Hansen, S. Berg, A.K. Aslund, W.R. Glomm, S. Eggen, R. Schmid, H. Johnsen, S. Kubowicz, S. Snipstad, E. Sulheim, S. Hak, G. Singh, B.H. McDonagh, H. Blom, C. de Lange Davies, P.M. Stenstad, Nanoparticle-stabilized microbubbles for multimodal imaging and drug delivery, Contrast media & molecular imaging, 10 (2015) 356-366.

[27] A.S. Klymchenko, E. Roger, N. Anton, H. Anton, I. Shulov, J. Vermot, Y. Mely, T.F. Vandamme, Highly lipophilic fluorescent dyes in nano-emulsions: towards bright non-leaking nano-droplets, RSC Advances, 2 (2012) 11876-11886.

[28] A. Aslund, C.J. Sigurdson, T. Klingstedt, S. Grathwohl, T. Bolmont, D.L. Dickstein, E. Glimsdal, S. Prokop, M. Lindgren, P. Konradsson, D.M. Holtzman, P.R. Hof, F.L. Heppner, S. Gandy, M. Jucker, A. Aguzzi, P. Hammarstrom, K.P. Nilsson, Novel pentameric thiophene derivatives for in vitro and in vivo optical imaging of a plethora of protein aggregates in cerebral amyloidoses, ACS chemical biology, 4 (2009) 673-684.

[29] Y. Zhang, M. Yang, N.G. Portney, D. Cui, G. Budak, E. Ozbay, M. Ozkan, C.S. Ozkan, Zeta potential: a surface electrical characteristic to probe the interaction of nanoparticles with normal and cancer human breast epithelial cells, Biomedical microdevices, 10 (2008) 321-328.

[30] O.V. Bondar, D.V. Saifullina, Shakhmaeva, II, Mavlyutova, II, T.I. Abdullin, Monitoring of the Zeta Potential of Human Cells upon Reduction in Their Viability and Interaction with Polymers, Acta naturae, 4 (2012) 78-81.

[31] V. Mailander, K. Landfester, Interaction of nanoparticles with cells, Biomacromolecules, 10 (2009) 2379-2400.

[32] K. Kettler, K. Veltman, D. van de Meent, A. van Wezel, A.J. Hendriks, Cellular uptake of nanoparticles as determined by particle properties, experimental conditions, and cell type, Environmental Toxicology and Chemistry, 33 (2014) 481-492.

[33] L.J. Cruz, P.J. Tacken, R. Fokkink, C.G. Figdor, The influence of PEG chain length and targeting moiety on antibody-mediated delivery of nanoparticle vaccines to human dendritic cells, Biomaterials, 32 (2011) 6791-6803.

[34] R. Gref, M. Luck, P. Quellec, M. Marchand, E. Dellacherie, S. Harnisch, T. Blunk, R.H. Muller, 'Stealth' corona-core nanoparticles surface modified by polyethylene glycol (PEG): influences of the corona (PEG chain length and surface density) and of the core composition on phagocytic uptake and plasma protein adsorption, Colloids and surfaces. B, Biointerfaces, 18 (2000) 301-313.

[35] M.D. Howard, M. Jay, T.D. Dziubla, X. Lu, PEGylation of Nanocarrier Drug Delivery Systems: State of the Art, Journal of Biomedical Nanotechnology, 4 (2008) 133-148.

[36] E.V. Batrakova, S. Li, V.Y. Alakhov, D.W. Miller, A.V. Kabanov, Optimal structure requirements for pluronic block copolymers in modifying P-glycoprotein drug efflux transporter activity in bovine brain microvessel endothelial cells, The Journal of pharmacology and experimental therapeutics, 304 (2003) 845-854.

[37] T. Demina, I. Grozdova, O. Krylova, A. Zhirnov, V. Istratov, H. Frey, H. Kautz, N. Melik-Nubarov, Relationship between the Structure of Amphiphilic Copolymers and Their Ability To Disturb Lipid Bilayers, Biochemistry, 44 (2005) 4042-4054.

[38] L.C. Chang, C.Y. Lin, M.W. Kuo, C.S. Gau, Interactions of Pluronics with phospholipid monolayers at the air-water interface, Journal of colloid and interface science, 285 (2005) 640-652.

[39] S.A. Maskarinec, K.Y.C. Lee, Comparative Study of Poloxamer Insertion into Lipid Monolayers, Langmuir, 19 (2003) 1809-1815.

[40] S. Snipstad, S. Westrom, Y. Morch, M. Afadzi, A.K. Aslund, C. de Lange Davies, Contact-mediated intracellular delivery of hydrophobic drugs from polymeric nanoparticles, Cancer nanotechnology, 5 (2014) 8.

[41] T. Tenuta, M.P. Monopoli, J. Kim, A. Salvati, K.A. Dawson, P. Sandin, I. Lynch, Elution of labile fluorescent dye from nanoparticles during biological use, PloS one, 6 (2011) e25556.

[42] A. Salvati, C. Aberg, T. dos Santos, J. Varela, P. Pinto, I. Lynch, K.A. Dawson, Experimental and theoretical comparison of intracellular import of polymeric nanoparticles and small molecules: toward models of uptake kinetics, Nanomedicine, 7 (2011) 818-826.

[43] S. Snipstad, S. Hak, H. Baghirov, E. Sulheim, Y. Morch, S. Lelu, E. von Haartman, M. Back, K.P. Nilsson, A.S. Klymchenko, C. de Lange Davies, A.K. Aslund, Labeling nanoparticles: Dye leakage and altered cellular uptake, Cytometry. Part A : the journal of the International Society for Analytical Cytology, (2016).

[44] J.L. Townson, Y.S. Lin, J.O. Agola, E.C. Carnes, H.S. Leong, J.D. Lewis, C.L. Haynes, C.J. Brinker, Re-examining the size/charge paradigm: differing in vivo characteristics of size- and charge-matched mesoporous silica nanoparticles, Journal of the American Chemical Society, 135 (2013) 16030-16033.

[45] L. Shang, K. Nienhaus, G.U. Nienhaus, Engineered nanoparticles interacting with cells: size matters, Journal of nanobiotechnology, 12 (2014) 5.

Supplementary Information

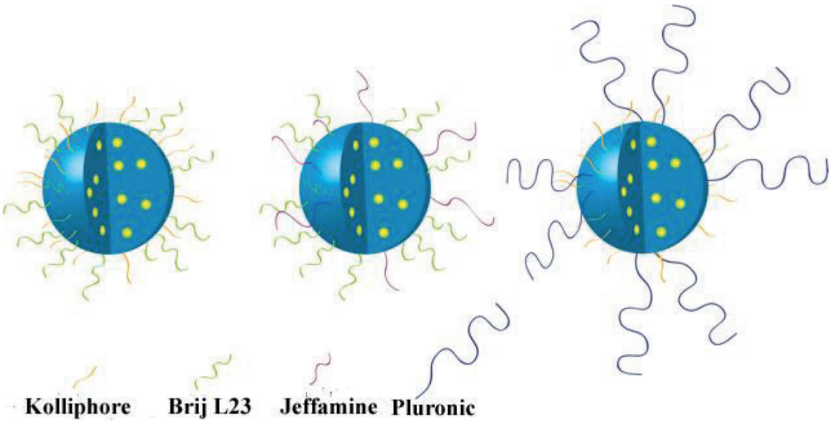

Supplementary Figure 1. Surface functionalization of the three different PEGylation strategies used in our study. The asterisks represent encapsulated fluorescent dye where applicable.

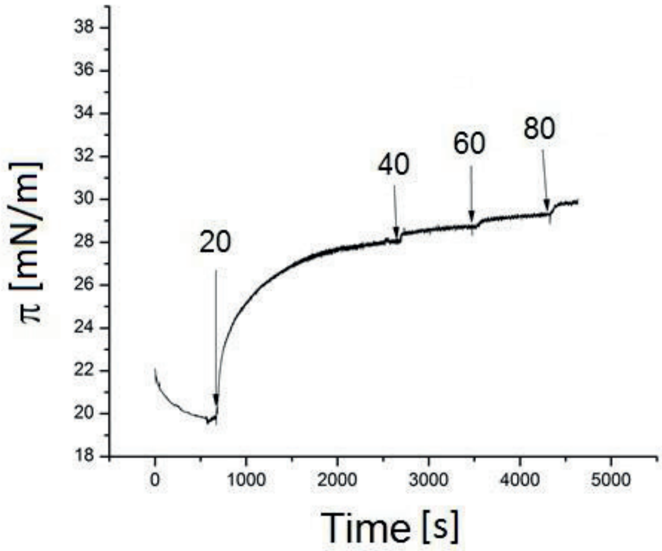

Supplementary Figure 2. Representative graph illustrating the effect of polymeric NPs at increasing concentrations (in µg/ml) on the surface pressure of DMPC/DPPG monolayers with the initial surface pressure value of π0 = 20 mN/m. The NP injections are indicated using arrows.

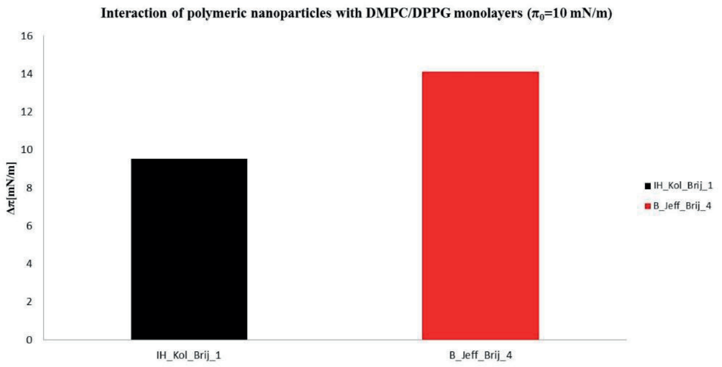

Supplementary Figure 3. The effect of PACA NPs on the surface pressure of DMPC/DPPG monolayers at the initial surface pressure π_0=10 mN/m

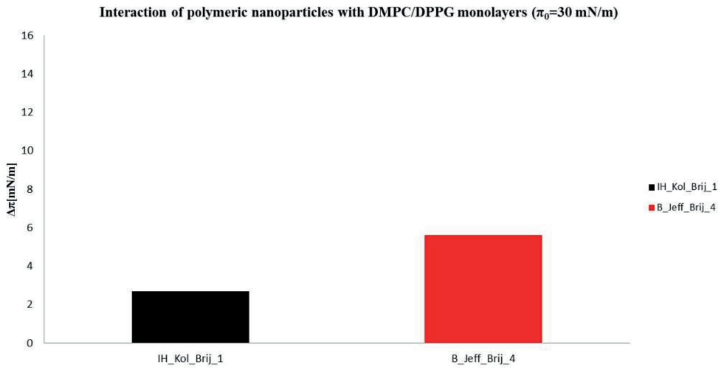

Supplementary Figure 4. The effect of PACA NPs on the surface pressure of DMPC/DPPG monolayers at the initial surface pressure π_0=30 mN/m

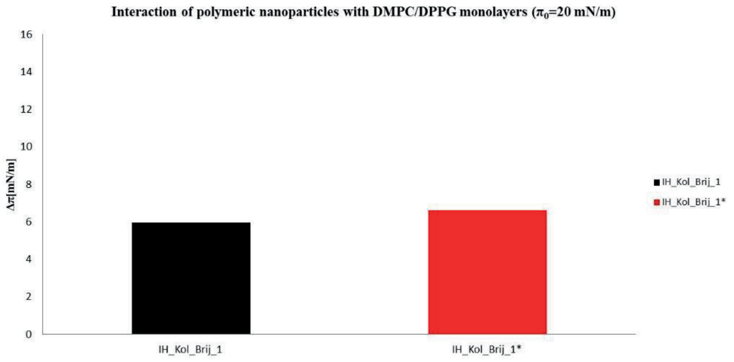

Supplementary Figure 5. The effect of two PACA NPs with or without a fluorescent dye on the surface pressure of DMPC/DPPG monolayers at the initial surface pressure π_0=20 mN/m

Paper III

Sulheim *et al. J Nanobiotechnol (2016) 14:1*
DOI 10.1186/s12951-015-0156-7

Journal of Nanobiotechnology

RESEARCH Open Access

Cellular uptake and intracellular degradation of poly(alkyl cyanoacrylate) nanoparticles

Einar Sulheim[1†], Habib Baghirov[1†], Eva von Haartman[1,3], Andreas Bøe[1], Andreas K. O. Åslund[1], Yrr Mørch[2] and Catharina de Lange Davies[1*]

Abstract

Background: Poly(alkyl cyanoacrylate) (PACA) nanoparticles have shown promise as drug carriers both to solid tumors and across the blood–brain barrier. Efficient drug delivery requires both high cellular uptake of the nanoparticles and release of the drug from the nanoparticles. Release of hydrophobic drugs from PACA nanoparticles is primarily governed by nanoparticle degradation, and this process has been poorly studied at the cellular level. Here we use the hydrophobic model drug Nile Red 668 (NR668) to investigate intracellular degradation of PACA nanoparticles by measuring changes in NR668 fluorescence emission and lifetime, as the spectral properties of NR668 depend on the hydrophobicity of the dye environment. We also assess the potential of poly(butyl cyanoacrylate) (PBCA) and poly(octyl cyanoacrylate) (POCA) nanoparticles for intracellular drug delivery in the prostate cancer cell line PC3 and rat brain endothelial cell line RBE4 and the role of endocytosis pathways in PACA nanoparticle uptake in those cell lines.

Results: Fluorescence lifetime imaging, emission spectra analysis and Förster resonance energy transfer indicated that the intracellular degradation was in line with the degradation found by direct methods such as gas chromatography and scanning electron microscopy, showing that PBCA has a faster degradation rate compared to POCA. The combined P(BCA/OCA) nanoparticles had an intermediate degradation rate. The uptake of POCA and PBCA nanoparticles was much higher in RBE4 than in PC3 cells. Endocytosis inhibition studies showed that both clathrin- and caveolin-mediated endocytosis were involved in PACA nanoparticle uptake, and that the former played a predominant role, particularly in PC3 cells.

Conclusions: In the present study, we used three different optical techniques to show that within a 24-hour period PBCA nanoparticles degraded significantly inside cells, releasing their payload into the cytosol, while POCA nanoparticles remained intact. This indicates that it is possible to tune the intracellular drug release rate by choosing appropriate monomers from the PACA family or by using hybrid PACA nanoparticles containing different monomers. In addition, we showed that the uptake of PACA nanoparticles depends not only on the monomer material, but also on the cell type, and that different cell lines can use different internalization pathways.

Keywords: Poly(alkyl cyanoacrylate), Nanoparticles, Intracellular delivery, Degradation, Fluorescence lifetime

Background

Achieving sufficient drug accumulation in the tumor and limiting toxicity towards healthy tissues are major challenges in cancer treatment [1]. One strategy is to encapsulate drugs into nanoparticles (NPs). Circulating NPs passively accumulate in some solid tumors due to fenestrations in tumor capillaries and lack of functional lymphatics, the so-called enhanced permeability and retention effect [2].

One of the advantages of NP-mediated drug delivery is the possibility of targeted, controlled and sustained

---

*Correspondence: catharina.davies@ntnu.no

†Einar Sulheim and Habib Baghirov contributed equally to this work

[1] Department of Physics, The Norwegian University of Science and Technology, NTNU, Høgskoleringen 5, 7491 Trondheim, Norway
Full list of author information is available at the end of the article

release of drugs. In most target organs, cellular uptake of NPs occurs primarily through clathrin-mediated endocytosis (CME), although caveolin-mediated endocytosis (CavME) and other mechanisms can also play a role [3]. Intracellular drug release from the NPs occurs either by NP degradation or drug diffusion out of the NP, and can also be induced by external triggers such as hyperthermia [4], ultrasound [5] or changes in the local microenvironment, for instance pH [6].

Among various nanoparticles currently investigated for their potential in cancer treatment, polymeric NPs have emerged as promising drug carriers. Their advantages include easy fabrication and functionalization, biocompatibility, sustained drug release and controllable degradation rate [6]. Certain formulations based on PACA NPs have reached Phases II and III in clinical trials [7, 8]. Recently, we described the synthesis of poly(alkyl cyanoacrylate) (PACA) NPs using a one-step miniemulsion process [9]. These particles can be made from different alkyl cyanoacrylate monomers and their mixtures, leading to varying degradability.

Release of highly hydrophobic drugs from PACA NPs appears to be primarily governed by NP degradation. Therefore, uptake profile and intracellular degradation of PACA NPs are the two key factors affecting intracellular drug availability once the NPs have reached the tumor cells. The uptake of NPs in cells, including PACA NPs, demonstrates different uptake efficacy by different cell types and organs [10, 11]. Degradation of PACA NPs mainly occurs by surface erosion [12, 13] into water-soluble poly(cyanoacrylic acid) and a primary alcohol following hydrolysis of the ester [14]. This process can also be catalyzed by esterases [15]. Other proposed degradation mechanisms are probably less important at physiological conditions [16]. To the best of our knowledge, however, degradation and drug release for PACA NPs have been mainly studied in solution using physicochemical techniques [12, 17–19]. One recent study described the intracellular payload release from poly(butyl cyanoacrylate) NPs [11], but knowledge of the intracellular degradation of different PACA NPs remains scarce.

Thus, the aim of our work was to study the cellular uptake of PACA NPs and their intracellular degradation, leading to the release of a model drug. The cellular uptake and intracellular trafficking of PACA NPs were studied in two different cell lines using flow cytometry (FCM) and confocal laser scanning microscopy (CLSM). Rat brain endothelial cells (RBE4) were chosen because of the reported ability of PACA NPs to cross the blood brain barrier [20], and human prostate cancer cells (PC3) were chosen to assess NP uptake and degradation in a common human tumor cell line. Two different monomers, butyl cyanoacrylate (BCA) and octyl cyanoacrylate (OCA), were used to produce PBCA, POCA and P(BCA/OCA) NPs. PBCA NPs are reported to degrade faster than POCA, and their copolymer could potentially have a tunable, intermediate degradation rate that could be used to achieve required drug release kinetics [13].

Degradation rates under different extracellular conditions were compared to intracellular model drug release. Nile Red 668 (NR668), a novel hydrophobic dye with the emission spectrum depending on the hydrophobicity of the local environment, was chosen due to its high hydrophobicity and unique spectral properties [21]. In addition, NR668 shows no leakage out of our PACA NPs (Additional file 1: Figure S1), which is required to avoid false interpretation of results based on fluorescence signals. Both its emission spectrum and fluorescence lifetime depend on the local environment and can be used to locate the dye intracellularly. Emission spectrum analysis has previously been used by our group to locate Nile Red [22], while the use of fluorescence lifetime imaging (FLIM) to study intracellular degradation has, to our knowledge, only been reported for doxorubicin in poly(lactide-co-glycolide) NPs [23].

The three complementary optical techniques showed that the intracellular degradation rates of the PBCA and POCA NPs are in line with the rates measured in solution. In addition, we report that the uptake of PACA NPs depends both on the monomer material and the cell line used, and that different cells can use different internalization pathways for PACA NP endocytosis.

Results

Initial NP characterization

The diameters of the three NPs were in the range of 148–177 nm with a relatively narrow size distribution [polydispersity index (PDI) ≤ 0.12]. All three NPs were slightly negatively charged with a zeta-potential of approximately −10 mV. The molecular weight of the PBCA and POCA NPs was approximately the same 3500 and 3700 Da, respectively (Table 1).

Cellular uptake of PACA nanoparticles

PBCA and POCA NP uptake kinetics in PC3 and RBE4 cells were measured using FCM (Fig. 1) and

Table 1 Physical parameters of the NPs

NP	Hydrodynamic diameter (nm)	PDI	ζ-potential (mV)	Polymer molecular weight (D)	Half-life at pH 7.4 (h)
PBCA	177	0.12	−12	3500	25
POCA	151	0.10	−10	3700	48
P(BCA/OCA)	148	0.10	−9	–	~500

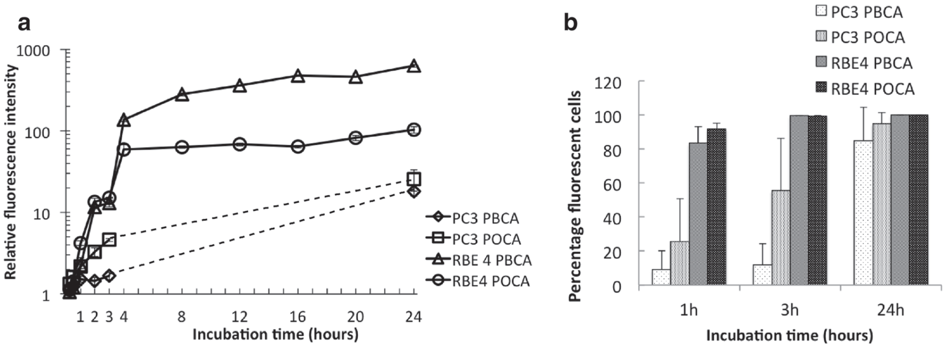

Fig. 1 **a** PBCA and POCA NP uptake kinetics in PC3 and RBE4 cells expressed as fluorescence intensity relative to untreated cells on a logarithmic scale. **b** Percentage of NP-positive cells. n = 2, *error bars* are SD, partly within the *symbols*

internalization was confirmed by CLSM (Fig. 2). Cellular uptake is presented both as fluorescence intensity (Fig. 1a) and the percentage of fluorescent cells (Fig. 1b).

RBE4 cells had a significantly higher NP uptake than PC3 cells with more than fourfold difference after 3 h. After 24 h, PBCA and POCA NP uptake in RBE4 cells was 40 and 8 times higher, respectively, compared to PC3 cells. Approximately 90 % of RBE4 cells internalized NPs after 1 h, whereas PC3 cells reached this level after approximately 24 h (Fig. 1b). The cellular uptake depended on the monomer. In RBE4 cells, PBCA and POCA NPs were initially taken up with approximately equal efficiency, while sixfold higher uptake of PBCA NPs was observed after 24 h compared to POCA NPs. On the other hand, in PC3 cells the uptake of POCA NPs was eightfold higher than PBCA NPs already after 3 h (Fig. 1a).

PBCA NP colocalized with early endosomes, late endosomes and lysosomes in RBE4 cells (Fig. 2a, b, c) and POCA NP colocalized with lysosomes in PC3 cells (Fig. 2d). Both cell lines were incubated with NPs for 3 h and, assuming continuous internalization, some NPs were expected to be found in the various endocytic compartments. Figure 2 shows some colocalization (white arrows), but many endocytic compartments contained no NPs, and several NPs did not colocalize with any endosomes or lysosomes.

Endocytosis inhibitors demonstrated that both CME and CavME were important uptake mechanisms (Fig. 3). In PC3 cells, both inhibitors reduced POCA NP uptake by approximately 40 %. Inhibiting CavME did not affect PBCA NP uptake in PC3 cells, whereas inhibiting CME reduced PBCA NP uptake by approximately 40 %. Endocytosis inhibition in RBE4 cells had a greater effect than in PC3 cells as inhibition of CME and CavME reduced POCA NP uptake by 73 and 43 %, respectively, and PBCA NP uptake by 83 and 56 %, respectively. Endocytosis is an energy-dependent process and is strongly inhibited at low temperatures [24]. Thus, the cells were incubated with NPs for minimum 2 h at 4 °C. Uptake was observed in neither PC3 nor RBE4 cells (Additional file 1: Figure S1).

PACA NP degradation

To study degradation in physiological relevant solutions, buffers at different pH as well as cell medium and human blood serum were used, and NP size and concentration were measured using Nanoparticle Tracking Analysis (NTA) (Fig. 4). PBCA NPs were found to degrade both in buffers at neutral pH, in cell medium with serum and in human serum.

The relative concentration of PBCA NPs decreased exponentially with half-lives of 144 days at pH 4, 7 days at pH 5.5 and 3 days at pH 7.4 (Fig. 4a). POCA NPs showed little sensitivity to pH. At all pH tested, the concentration decreased by only 10–20 % within the first 20 h and no further decrease was observed (Fig. 4b). A significant increase in NP diameter was observed for PBCA NPs. At physiological pH, the particle size increased by 20–30 % after 20 h, but was almost unchanged at pH 4.0 (Fig. 4c, d). POCA NPs, however, only expanded by 4 % at pH 7.4, with no changes observed at pH 4.0 (Fig. 4c, d). Both in cell medium and human serum, PBCA NP concentration decreased significantly, while POCA NP concentration was barely affected (Fig. 4e, f). For both particles, a significant increase in the initial size was observed in both cell media and serum, probably due to swelling and the formation of a protein corona (Fig. 4f, g).

More quantitative degradation experiments were performed in buffers at pH 7.4 using gas chromatography

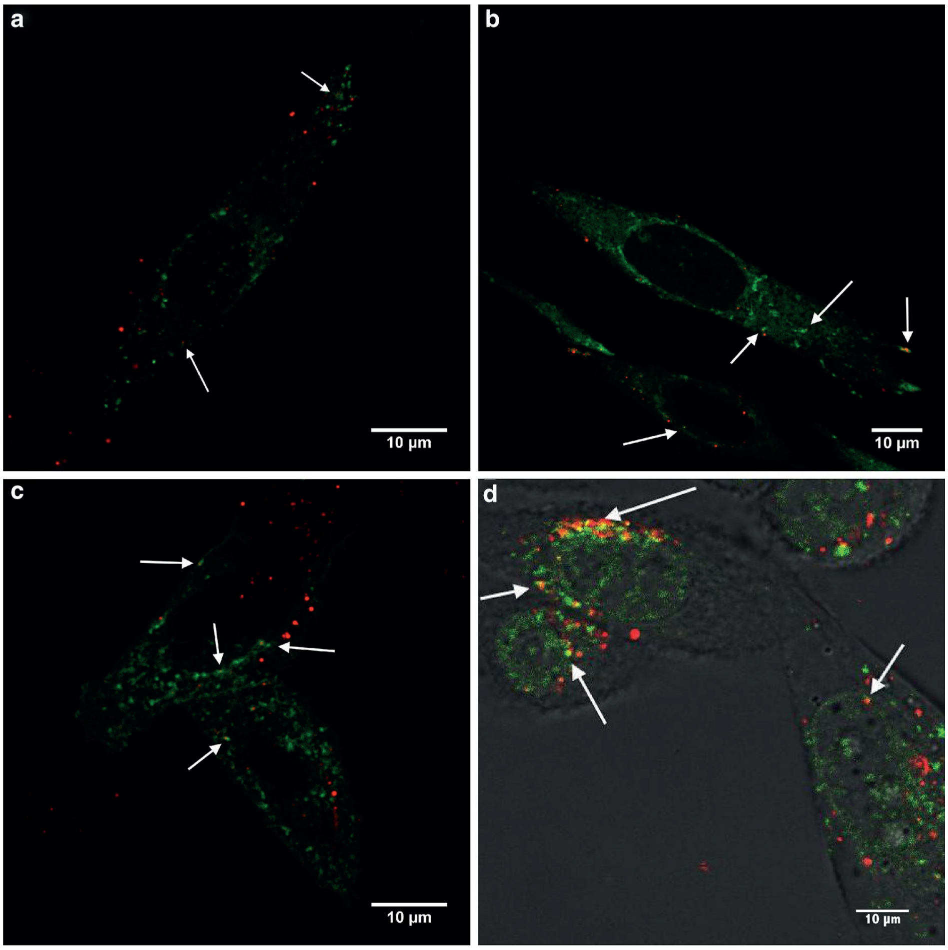

Fig. 2 **a** Colocalization (*white arrows*) of PBCA NPs (*red*) with early endosomes), **b** late endosomes and **c** lysosomes (all in *green*) in RBE4 cells. **d** Colocalization of POCA NPs and lysosomes in PC3 cells. Both colors in the same pixel are seen as *yellow*. Cells were incubated with NPs for 3 h after labeling the endocytic compartments

(GC) to measure the degradation products butanol and octanol. The degradation was measured as percentage of complete hydrolysis in glycine buffer at pH 9 (Fig. 5). After 48 h, 88 % degradation was found for PBCA NPs, as compared to only 3 % for POCA NPs, confirming much faster degradation of PBCA. Assuming a linear degradation rate, this gives a half-life of 25 h for PBCA NPs, which is 33 % of what was found using NTA (Fig. 4a; Table 1). However, while NTA measures degradation in terms of NP concentration, GC measures the amount of degradation products. For the copolymer P(BCA/OCA), an intermediate rate of degradation (45 %) was found after 48 h. For POCA, linear regression gave a poor fit, but indicated a half-life of approximately 500 h.

To visualize the degradation, NPs were imaged by scanning electron microscopy (SEM) after 0, 8 and 11 days of incubation at pH 7.4 (Fig. 6). On day 0 intact, spherical NPs were observed. After 8 and 11 days, the POCA NPs were still intact (Fig. 6d, f) whereas no PBCA NPs were seen, probably due to degradation of the NPs (Fig. 6c, e).

Intracellular degradation of the NPs was studied by measuring the release of NR688 using the spectral properties of the dye. NR668 appeared to be strongly associated with NPs as no cellular fluorescence was seen at

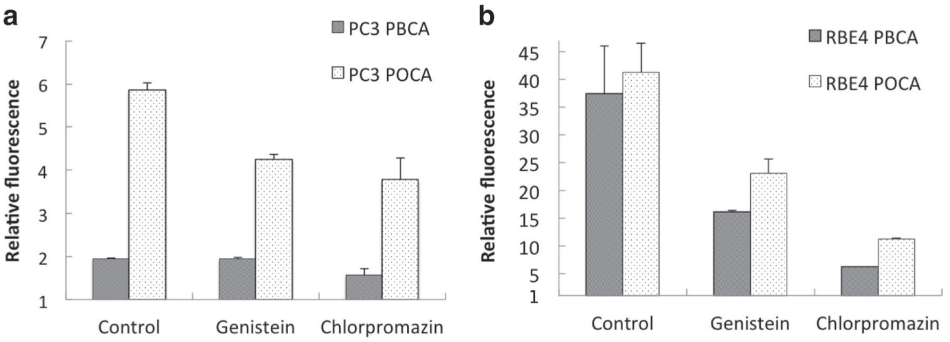

Fig. 3 The effect of inhibition of endocytosis by genistein and chlorpromazine on the uptake of PBCA and POCA NPs in **a** PC3 cells and **b** in RBE4 cells. Control is untreated cells. The median fluorescence intensity is expressed relative to autofluorescence. n = 2, *error bars* give SD

4 °C, and no diffuse cytoplasmic staining was observed in CLSM in agreement with [21]. Thus, any labeling of cytoplasmic lipid droplets or hydrophobic molecules should be caused by NR668 being released from degraded NPs. The size and distribution of lipid droplets are often visually similar to those of NPs in endosomes or lysosomes, and the dye location is therefore difficult to evaluate using CLSM [25]. FLIM and spectral analysis were used to study whether the dye was inside intact NPs or associated with other hydrophobic cellular molecules. FLIM images of PC3 cells incubated with free NR668, PBCA NPs and POCA NPs are shown in Fig. 7a, b, c. The cells were incubated with NR668-loaded NPs or the free dye for 24 h before removing the dispersion and growing the cells for additional 5 days. The images show multiple lifetimes, from approximately 2.5 ns (blue) to 4 ns (red) in cells incubated with the free dye (Fig. 7a) and PBCA NPs (Fig. 7b), whereas a narrow lifetime distribution around 3 ns (yellow–green) was seen in cells incubated with POCA NPs (Fig. 7c).

To further quantify the variations in fluorescence lifetime, its distribution was measured in cells incubated with PBCA (Fig. 7d) or POCA NPs (Fig. 7e). In cells incubated with PBCA NPs, the fluorescence lifetimes increased significantly with time while the POCA NP lifetimes remained almost unchanged, indicating that even after 6–7 days inside the cells, POCA NPs were still intact while PBCA NPs were continuously degrading. However, 77 % of the change in lifetime (0.7 nsec) occurred already after 24–48 h. The large standard deviations (SDs) for POCA NPs after 6–7 days (Fig. 7e) indicate that those particles also underwent some changes. Figure 7d, e show the average of the long and short lifetimes, and the correlation between the two lifetimes is found in Additional file 1: Figure S2.

The fluorescence emission spectra were recorded for cells incubated with both PBCA and POCA NPs for 24 h, and compared with those of free NR668 incubated with cells for 24 h as well as NPs prior to incubation (Fig. 7f, g). After 24 h, the emission spectrum of PBCA shifted to higher wavelengths and became similar to that of free NR668 inside cells. However, the emission spectrum of POCA NPs only shifted slightly towards the spectrum of free NR668, and was similar to the spectrum of POCA NPs not incubated with cells.

To confirm that the changes in fluorescence lifetime and emission spectra were due to dye release from the NPs and not changes in the environment inside the NPs, we used pentamer hydrogen thiophene acetic acid methyl ester (p-HTAM), a hydrophobic dye that forms a Förster resonance energy transfer (FRET) pair with NR668. PC3 cells were incubated with POCA and PBCA NPs for 24 h and then grown for 3 days in medium without NPs. One hour prior to CLSM-imaging, the cells were stained with p-HTAM. p-HTAM was excited at 405 nm and detected in the interval of 500–540 nm (Fig. 8a, c). A FRET signal from NR668, detected at 650–710 nm was observed in cells incubated with PBCA NPs (Fig. 8b), but not with POCA NPs (Fig. 8d), demonstrating that NR668 from PBCA was located in close proximity to the p-HTAM molecules.

Discussion

Cellular uptake

PACA NPs are promising carriers for drugs [26] and oligonucleotides [27] both across the blood–brain barrier [28] and to cells in solid tumors [22]. Endocytosis is the predominant cellular uptake mechanism, although contradictory results have been reported. Earlier studies showed no endocytosis [29] whereas others [30, 31]

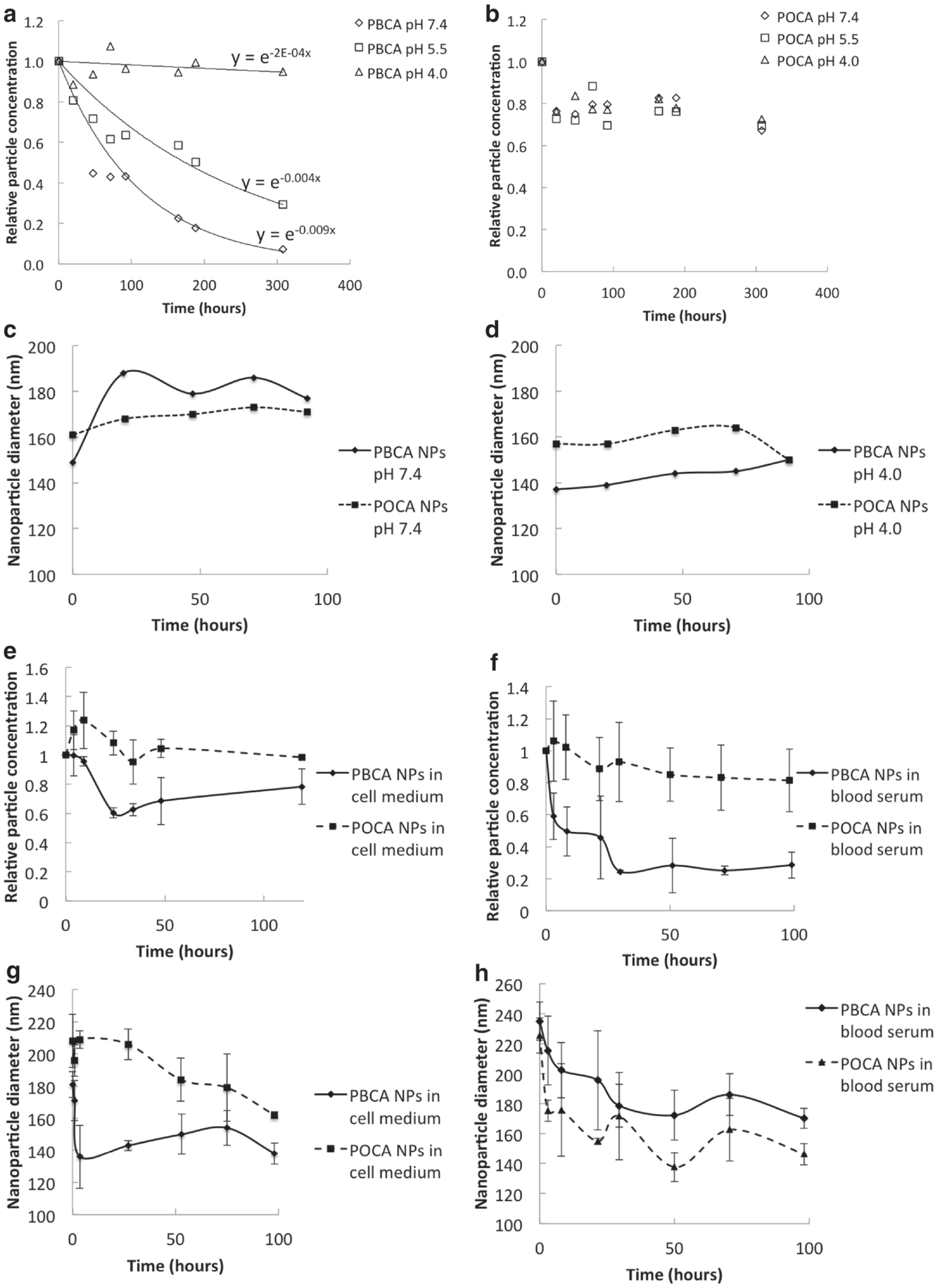

Fig. 4 **a** Concentration of PBCA NPs and **b** POCA NPs at pH 7.4, 5.5 and 4.0. An exponential decay was fitted to the results in **a**. **c** Mean NP diameter at pH 7.4 and **d** pH4.0. Relative concentration (**e**, **f**) and mean diameter of NPs (**g**, **h**) in cell medium (**e**, **g**) and human blood serum (**f**, **h**)

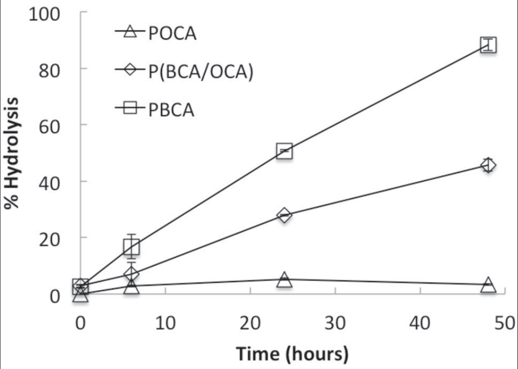

Fig. 5 Degradation of PBCA, P(BCA/OCA) and POCA at pH 7.4 measured by gas chromatography. Degradation is indicated as % hydrolysis of the NPs as a function of time. 100 % hydrolysis was obtained in glycine buffer at pH 9. n = 3, *error bars* give SD

found that PACA NP uptake was an energy-dependent process as no uptake occurred at 4 °C, similarly to the results presented here. The discrepancy could be explained by the production methods that have been shown to drastically change the interaction between cells and NPs [32]. The lack of cellular fluorescence at 4 °C also demonstrated that NR668 was not leaking out of PACA NPs or taken up by the cells through NP-cell contact-mediated transfer, as reported earlier for Nile Red [25].

Endocytosis efficiency was cell type-dependent, and RBE4 cells originating from rat brain endothelium demonstrated efficient uptake. The prostate tumor cell line PC3 showed a slow uptake and the amount of NPs per cell was 10–40 times lower than in RBE4 cells. A cell type-dependent uptake of NPs has previously been reported for gold NPs [33], chitosan NPs [34], and polystyrene NPs of various sizes [35]. In the latter work, approximately tenfold higher uptake of NPs was observed in human brain endothelial cells (HCMEC D3), as compared to cervical cancer cells (HeLa) and human lung epithelium cells (A549). Thus, the high uptake in RBE4 cells might be a property of brain endothelial cells, and in accordance with this, PACA NPs are reported to cross the blood–brain barrier when coated with certain polyethylene glycol (PEG) surfactants [20, 36].

CME and CavME inhibition showed that both endocytic pathways were active. CME seemed to be the dominant mechanism, as its inhibition more strongly affected cellular uptake in both cell lines, especially in RBE4 cells, but also PBCA uptake in PC3 cells. For RBE4 cells, the combined inhibition effect of CME and CavME inhibitors exceeded 100 %, indicating poor inhibition selectivity. For PC3 cells, the inhibition effect was lower, with possible contribution of other pathways. CavME inhibition did not affect PBCA NP uptake in PC3 cells, showing that CME represents the predominant mechanism of PBCA NP uptake. To study intracellular trafficking further, early endosomes, late endosomes and lysosomes were visualized, but only limited colocalization with those organelles was observed for both POCA and PBCA NPs. This indicates that NPs may escape the endocytic pathway or that endocytosis was not a continuous process in the studied timeframe. The mechanism of possible escape from the endocytic pathway is unclear, but other groups have also observed limited colocalization with lysosomes for polymeric NPs [27, 37].

POCA NPs were internalized more efficiently than PBCA NPs in PC3 cells, whereas the opposite was true for RBE4 cells. Two known NP properties that determine endocytosis are size and charge [34]. Lower uptake with increasing NP size has been reported for CME and CavME [38]. The size and charge of POCA and PBCA NPs were not very different when measured by dynamic light scattering (DLS) in phosphate buffer. However, incubation in cell medium for several hours could change the NPs, especially the PBCA NPs that started degrading immediately upon incubation. We have seen that PBCA degradation starts with significant enlargement, probably due to swelling [39]. Both NPs expanded instantly in serum-supplemented cell medium and human serum, likely due to both swelling and protein corona formation [40]. However, the increase in size was rather small for both NPs and does probably not fully explain the differences in internalization.

Cationic NPs are internalized more efficiently than anionic NPs [34]. Surface degradation of PACA NPs leads to the formation of carboxylic acid, making the surface more hydrophilic [41, 42]. We have found that the NP zeta-potential decreases with time in medium, where PBCA NPs became more negatively charged than POCA NPs (unpublished results). This observation might explain the higher uptake of POCA NPs in PC3 cells. However, in RBE4 cells the PBCA NPs were internalized much more efficiently. Several other studies also demonstrate a high uptake of PBCA NPs in brain endothelial cells [36] whereas, to our knowledge, POCA NP uptake by brain endothelium has not been reported. It is also noteworthy that RBE4 cells use both CME and CavME, whereas PC3 cells mainly use CME, especially for PBCA NPs, which may partly explain the observed differences between RBE4 and PC3 cells.

Degradation

NP degradation rate is crucial in terms of circulation time, stability, toxicity and drug release rate. The various degradation rates of the PACA family polymers have

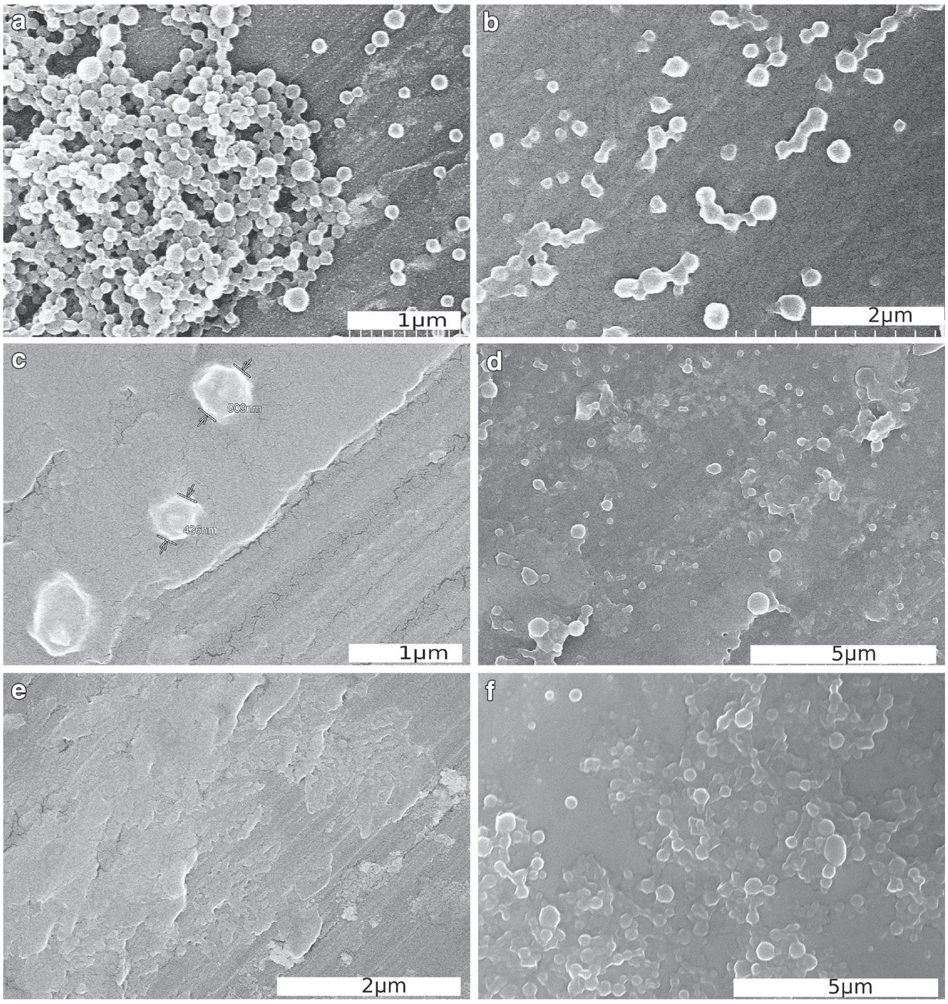

Fig. 6 SEM images of PBCA (**a**, **c**, **e**) and POCA NPs (**b**, **d**, **f**) incubated at pH 7.4 for 0 days (**a**, **b**), 8 days (**c**, **d**) and 11 days (**e**, **f**)

been shown to affect drug release rates [43]. Drug delivery through biodegradation enables continuous delivery, as opposed to burst delivery in conventional chemotherapy. Thus, depending on the alkyl monomer chain length [12] and polymerization mechanism [44], PACA NPs may be made to continuously release the drug intracellularly for weeks, potentially affecting slowly proliferating or quiescent cancer cells. Degradation in biological media is influenced by pH, but also by enzymatic degradation from esterases [16, 17]. In order to investigate the contribution of esterase-mediated degradation, esterase activity was monitored in serum-supplemented growth medium and in human serum over 96 h. No changes in esterase activity were observed that could explain the differences in PBCA and POCA NP degradation rates (Additional file 1: Figure S3). Esterase activity was reduced instantly and recovered within 24 h. Thus low degradation of NPs after approximately 48 h could not be attributed to loss of esterase activity.

In the present work, NP degradation is apparently required for NR668 release, as the dye is closely associated with the polymeric network of the NP through

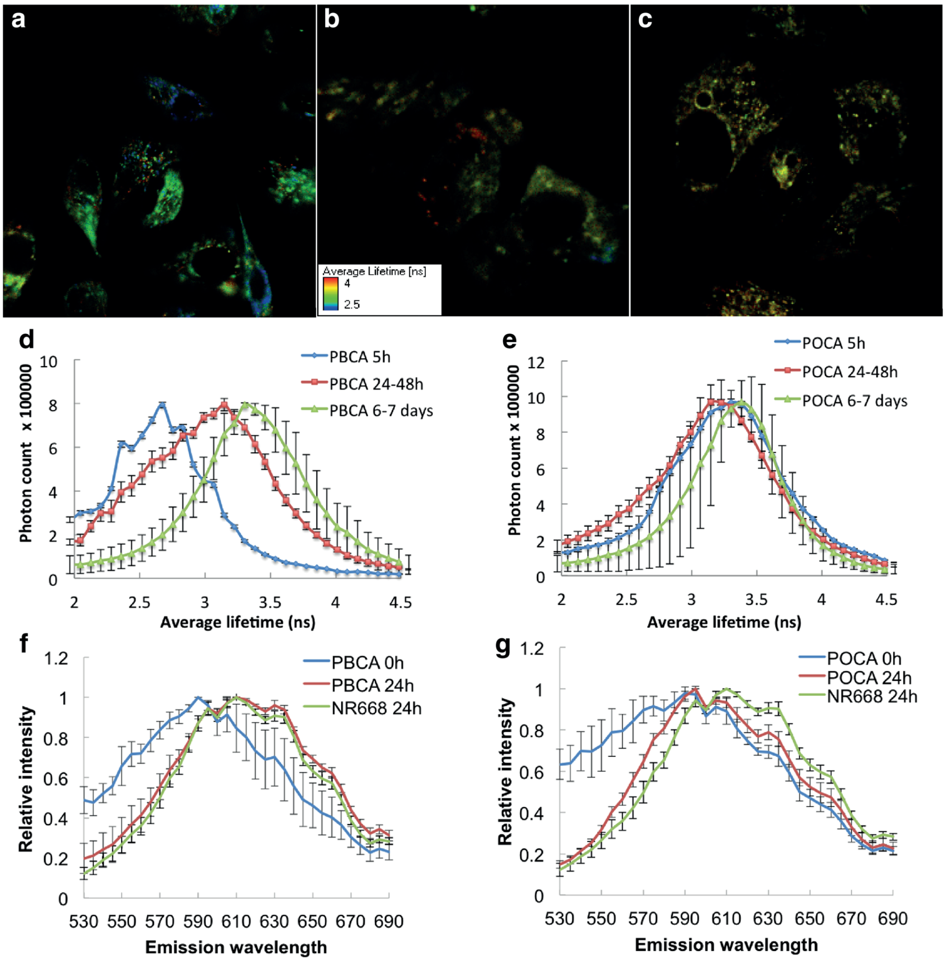

Fig. 7 a–**c** FLIM images of PC3 cells incubated for 24 h with free NR668 (**a**), PBCA (**b**) and POCA NPs (**c**) before growing for additional 5 days. Each pixel is colored based on the average lifetime. Fluorescence lifetime distribution for PBCA (D) and POCA (E) NPs inside cells at 5, 24–48 and 144–168 h (6–7 days). Emission spectra from PC3 cells incubated with free NR688 (*green*) or PBCA (**f**) or POCA NPs (**g**) after 24 h (*red*), or the NPs prior to incubation (*blue*). n = 5, *error bars* give SD

hydrophobic interactions. This was demonstrated by the correlation between the measured degradation rate of the NPs in physiological solutions and the release of NR688 from the NPs measured intracellularly. After 48 h, 88 % of the PBCA NPs had degraded as measured with GC. Similarly, 77 % of the change in fluorescence lifetime measured intracellularly had occurred at this time point. NPs were stable at low pH, but degraded rapidly at pH 7.4. The concentration of POCA NPs was still close to 80 % after over 300 h at pH values of 4.0–7.4. The degradation observed with NTA was confirmed by GC and SEM. Furthermore, GC showed that the degradation rate could be manipulated by mixing the two monomers.

Intracellular degradation of PBCA NPs was also more efficient than that of POCA NPs. Release of NR668 occurred from PBCA, but hardly from POCA NPs. This was demonstrated intracellularly by FLIM and by the spectral changes of the dye. Upon degradation, the fluorescence lifetime for PBCA NPs increased towards the lifetime for POCA NPs. This might be because released

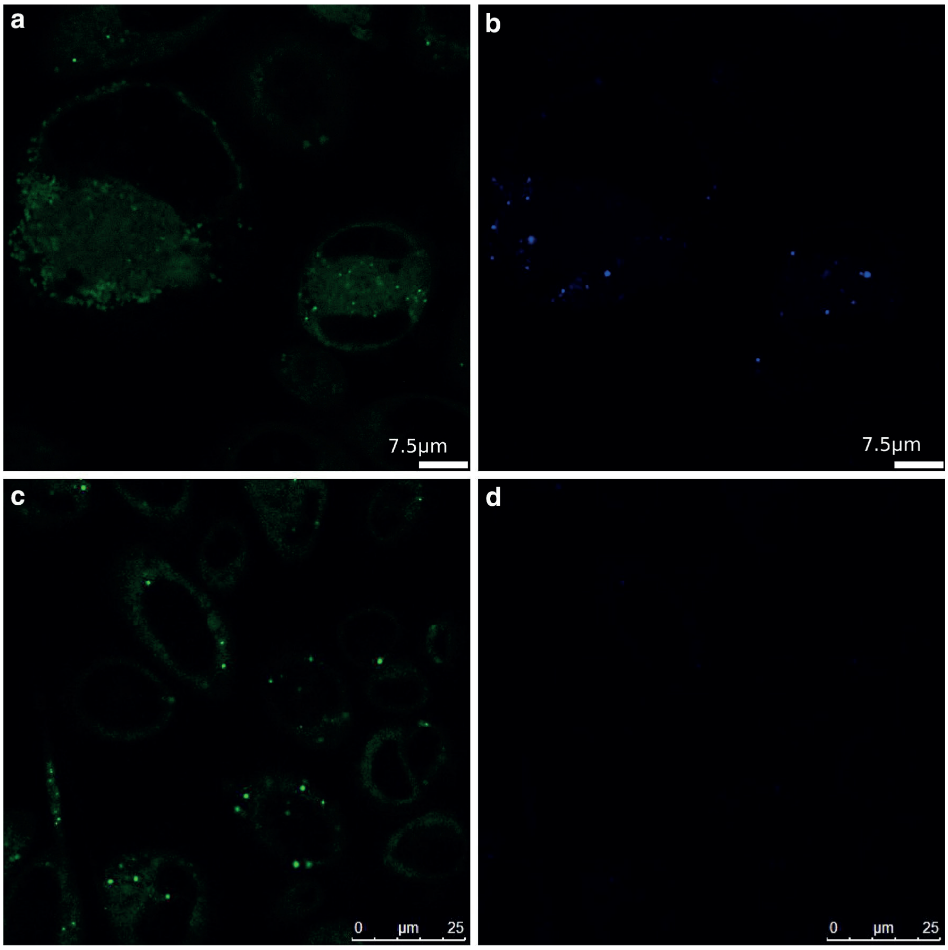

Fig. 8 PC3 cells incubated with PBCA (**a**, **b**) or POCA NPs (**c**, **d**) for 24 h and grown for additional 72 h before p-HTAM staining. Excited at 405 nm and p-HTAM fluorescence detected at 500–540 (**a**, **c**) and FRET signal at 650–710 nm (**b**, **d**)

NR668 diffuses to areas of higher hydrophobicity such as lipid droplets, thereby reaching lifetimes similar to intact POCA NPs. The emission spectra of NR668 in cells incubated with PBCA NPs showed that after 24 h the dye environment resembled that of free NR668. Furthermore, colocalization with p-HTAM also indicated a location different from endosomes/lysosomes or inside NPs, because p-HTAM enters the cell passively rather than by endocytosis. FRET requires that the fluorescent molecules be in close proximity (approximately 10 nm), making FRET impossible with the dye still encapsulated in the NPs [45]. Thus, the FRET signal observed in cells incubated with PBCA NPs, but not in cells with POCA NPs demonstrated that PBCA, but not POCA NPs were degraded. It has also been reported by others that PACA NPs with longer alkyl chains degrade more slowly [46, 47].

The bulk of our knowledge on PACA degradation originates from earlier physicochemical characterization studies [12, 17]. PACA NP-assisted drug delivery in vivo can also be indirectly linked to degradation rates. To the best of our knowledge, however, [11] remains the only work where the fate of PBCA nanocapsules was observed intracellularly using dual labeling of the nanocapsule shell and the cargo. That study, however, was performed with only one type of PACA NPs and mostly concerned the release and intracellular fate of the payload, while in the present work we studied the intracellular fate of different PACA nanocarriers.

Several groups have suggested pH-sensitive nanocarriers for drug delivery [48], increasing the degradation rate at lower pH. Our results suggest an opposite mechanism which is consistent with other results for PBCA NPs [15]. The NPs remain intact at acidic pH and the drug is released into the cytosol after NP escape from the lysosomal pathway, limiting lysosomal inactivation and exocytosis of the drug or NPs. For therapeutic effect, cytosolic release of drugs and therapeutics is reported to be far superior to lysosomal release [37].

NR668 release from PACA NPs was studied using three different optical methods. Emission spectrum analysis and FRET are well-established methods used to characterize free dye vs. intact NPs in tumor cells and tissue [22, 49]. FLIM is a novel method for studying intracellular degradation and, albeit relatively time-consuming, shows promise for probing the microenvironment of the delivered dye as it is very sensitive and less dependent on fluorophore concentration than emission spectrum analysis [50]. Since fluorescence lifetime is sensitive to hydrophobicity and pH [51], it was found to be a well-suited method for studying the release of the hydrophobic NR668 dye. Therefore, the combination of those three methods—emission spectrum analysis, FRET and FLIM, each providing complementary results,—allows reconstructing a comprehensive picture of intracellular degradation of PACA NPs and the release of a hydrophobic drug.

Conclusions

In the present study, we showed that the uptake of PACA NPs depends not only on the monomer material, but also on the cell type, and that different cell lines can use different internalization pathways. Within a 24-hour period, PBCA NPs degraded significantly inside cells, releasing their payload into the cytosol, while POCA NPs remained intact. This shows that it is possible to tune the drug release rate by choosing appropriate monomers from the PACA family.

Methods

Synthesis and characterization of nanoparticles

The NPs used were either PBCA, POCA or P(BCA/OCA). All NPs were prepared using the miniemulsion polymerization method as described previously [9]. An oil-in-water emulsion was prepared by mixing a monomer oil phase with a water phase containing the non-ionic PEG stabilizer (Brij®L23, Sigma-Aldrich, 20 mM) in 0.1 M HCl. The monomer phase contained either butyl-2-cyanoacrylate (BCA, Henkel Loctite) or octyl cyanoacrylate (OCA, Henkel Loctite) or a mixture of the two, a neutral oil as co-stabilizer (Miglyol 810N, 2 wt %, Cremer), a radical initiator (V65, Azobisdimetyl valeronitril, Wako, 0.9 wt %) and 0.2 wt % of the fluorescent dye NR668 (modified Nile Red, a kind gift from Dr. Klymchenko, University of Strasbourg). After emulsifying (Branson Digital Sonifier, 60 % amplitude, 3 min), Jeffamin®M-2070 (a polyetheramine with a 19-unit PEG chain, Huntsman Corporation, 68 mM), was added to initiate the polymerization. The polymerization was carried out at room temperature overnight and at 50 °C for 8 h to activate the radical initiator for polymerization of remaining internal monomer. Spontaneous polymerization was controlled by performing emulsification at acidic conditions (0.1 M HCl). The particles were rinsed by extensive dialysis against 0.001 M HCl using dialysis membranes with MWCO 12–14,000. The synthesized NPs were characterized for size, PDI and surface charge (zeta-potential) using electrophoretic and dynamic light scattering (DLS, Zetasizer Nano ZS, Malvern Instruments) in 0.01 M phosphate buffer, pH 7. Molecular weight (MW) analysis by size exclusion chromatography was provided by Innventia AB, Sweden. Briefly, the NPs were dissolved in tetrahydrofuran and run through the three columns containing Styragel HR4, Styragel HR2 and Styragel HR1 at 0.8 ml/min. Polystyrene standards with MW from 1000 to 350,000 was used for calibration.

Cell culture

Human PC3 prostate adenocarcinoma cells (CRL-1435, American type culture collection) were cultured at 37 °C and 5 % CO_2 in Dulbecco's Modified Eagle's Medium (DMEM, Life Technologies Corporation, USA) supplemented with 10 % fetal bovine serum (FBS).

RBE4 cells (a generous gift from Dr. Aschner, Vanderbilt University) were cultured on collagen at 37 °C and 5 % CO_2 in Ham's F-10 medium supplemented with 10 % FBS, 300 µg/ml G418 and 1 ng/ml basic fibroblast growth factor (all from Life Technologies Corporation).

Incubation with NP and inhibition of endocytosis

Cells (PC3 or RBE4) were seeded in 8-well plates (Ibidi) at 18,500 cells/well and cultured for 3 days when studying cellular uptake. NPs were added at a concentration of 20 µg/mL in growth medium and incubated for various times up to 24 h before changing the growth medium prior to imaging. For the degradation studies, 10,000 cells were seeded per well, the NPs were removed after 24 h and the cells were grown for additional 6 days changing medium every other day.

For endocytosis inhibition studies, PC3 or RBE4 cells were seeded in 12-well plates (Costar) at a density of 125,000 cells/well and grown to reach the log phase. Chlorpromazine was used as a specific inhibitor of CME [3]. Genistein is traditionally used to inhibit CavME, although some inhibition of CME subtypes has also been reported [52]. Chlorpromazine and genistein were added at 10 μg/mL and 13.5 μg/mL, respectively, as used by others [53, 54]. The inhibitors were pre-incubated with cells for 1 h before adding a dispersion containing NPs at 20 μg/ml together with the inhibitor, and incubating at 37 °C for 3 h. To achieve complete inhibition of endocytosis, the cells were pre-incubated for 5 min at 4 °C before adding NPs and incubating the cells at 4 °C for 2 or 3 h, in the case of RBE4 and PC3 cells, respectively.

CLSM and cell labeling

Confocal images where obtained using a Leica SP8 CLSM with a 63 × 1.2 water objective. For NR668 excitation, a white light laser at 514 nm was used, and emission was detected at 580–660 nm using a photon counting hybrid detection system. Z-stacks of cells were obtained to verify that the NPs were intracellular.

In PC3 cells, lysosomes were stained with the pH sensitive dye LysoTracker Blue (DND-22, Life Technologies) at 2.5 μM for 1 h and imaged using a pulsed multiphoton laser at 780 nm to excite the dye. In RBE4 cells early endosomes, late endosomes and lysosomes were labeled by cellular transduction using CellLight Early Endosomes-GFP, CellLight Late Endosomes-GFP and CellLight Lysosomes-GFP (Life Technologies), respectively, at a concentration of 40 particles per cell 24 h prior to imaging. After labeling the organelles, cells were incubated with NPs for 3 h before imaging.

Flow cytometry

The cells were analyzed using a flow cytometer (Gallios, Beckman Coulter) exciting at 561 nm and detecting at 630 nm with a 30 nm bandpass filter. Prior to FCM, the cells were washed three times in PBS. 10,000 cells were included in each sample, and a dot plot of forward light scatter signal versus side scatter signal was used to establish a collection gate that excluded cell debris, dead cells and aggregates. The cellular uptake of NPs was estimated both as the percentage of cells with NPs and as the amount of NPs per cell which was estimated from the median fluorescence intensity. To compare the uptake of PBCA and POCA NPs, which had different fluorescence intensity, a normalization factor of 1,9 (PBCA vs POCA) was used. This factor was found by measuring the fluorescence intensity using a spectrophotometer (Infinite 200Pro, Tecan). Thus the increase in median fluorescence between cells incubated with POCA NPs and the control cells was multiplied by this normalization factor and added to the autofluorescence.

Emission spectra analysis

The emission spectra were obtained using the Leica SP8 CLSM. Intracellular NR688 was excited using a white light laser at 514 nm and detected in intervals of 10 nm from 550 to 700 nm. The intervals had an overlap of 5 nm resulting in 30 intervals. The spectra were normalized to the same maximum intensity for analysis.

Flim

FLIM was recorded using a Leica SP8 microscope equipped with the PicoQuant system. NR668 was excited by a white light laser at 514 nm, with detection at 565–615 nm using a Single Photon Avalanche Detector. SymPhoTime PicoQuant was used to record lifetimes in time domain. The lifetimes τ_i were calculated using a two-exponential decay with the instrument response function E(t) that was fitted to the fluorescence decay curve:

$$F(r,t) \; = \; E(t) \; \times \; \sum_{i=1}^{2} A_i(r) e^{-\frac{t}{\tau_i(r)}}.$$

The lifetimes were recorded until reaching a maximum intensity of 1000 photons/pixel. NR668 shows a two-exponential decay, resulting in two different lifetimes which were averaged using the equation:

$$\tau_{ave} = \frac{\alpha_1 \tau_1^2 + \alpha_2 \tau_2^2}{\alpha_1 \tau_1 + \alpha_1 \tau_1}$$

The software SymPhoTime provided by PicoQuant was used.

Förster resonance energy transfer (FRET)

FRET was performed to verify that NR668 was physically removed from the NPs upon degradation. The cells were incubated with 20 μg/mL of PBCA or POCA NPs for 24 h and grown for 3 days before staining for 1 h with 1 μg/mL p-HTAM, a hydrophobic stain labeling, among others, lipid droplets [55]. NR668 released from the NPs might colocalize with p-HTAM in lipid droplets or other hydrophobic domains, enabling FRET. Images were obtained by exciting p-HTAM at 405 nm using a pulsed Hg-laser and detecting the FRET signal at 650–710 nm.

NP degradation in solutions

Nanoparticle tracking analysis (NTA, Nanosight LM10-HS, Malvern Instruments) was used to determine NP concentration and diameter in various solutions. pH dependent NP degradation was studied in buffers with pH 7.4 (0.01 M phosphate buffer), pH 5.5 and 4.0 (0.01 M acetic acid). Degradation was also measured in cell medium

(DMEM, Life Technologies) with FBS, pH 7.5 and human blood serum (a kind gift from professor Asbjørn Nilsen, Medical Faculty, NTNU). The NPs were added to the buffer at 20 µg NPs/ml and incubated for up to 336 h (14 days) at 37 °C. For cell medium and human serum, NPs were added at 5 mg/ml, and further diluted to 20 µg/ml in deionized water before NTA analysis. The buffer or medium were not changed during the incubation.

Gas chromatography

Particles were diluted to 0.1 mg NP/ml in 0.01 M phosphate buffer pH 7.4 and kept at 37 °C with slow shaking. At various time points, the particles were centrifuged using an ultracentrifuge (WX Ultra 80, Thermo Electron Corporation) at 30,000 rpm for 2 h. For complete degradation, NPs were diluted to 0.1 mg NPs/ml in glycine buffer at pH 9 (0.2 M) and kept at 37 °C while shaking for 72 h before separation by ultracentrifugation. 3 µl of the internal standard *n*-pentane and 5 ml of diethyl ether were added to 5 ml of the supernatant and vortexed. 1 ml of the organic phase was analyzed with a GC Agilent 7890A equipped with a RTX-1 capillary column and helium as carrier gas. 1 µl of the sample was injected in split mode (1:5) and run isothermally at 45 °C for 3 min before initiating a temperature gradient of 10 °C/min until 200 °C. Pure butanol, pentanol and octanol samples were used as references.

Scanning electron microscopy

For SEM, the NP-dispersion was diluted to 50 µg/ml in water and one droplet was placed on a SEM sample holder. After water evaporation, the samples were sputter-coated with a 10 nm gold layer and transferred to a Hitachi S-5500 at 15 kV acceleration voltage detecting secondary electrons.

Additional file

Additional file 1. Additional material.

Authors' contributions

ES carried out all experiments with the PC3 cell line, including cellular degradation studies and wrote the manuscript. HB carried out all experiments with RBE4 cells and assisted in writing the manuscript. EH established the protocol for uptake of nanoparticles in PC3 cells. AB carried out degradation measurements in buffers, cell medium and human serum and made SEM images. AÅ performed GC measurements. YM developed and produced the nanoparticles. CD assisted in designing the experiments and writing the manuscript. All authors read and approved the final manuscript.

Author details

[1] Department of Physics, The Norwegian University of Science and Technology, NTNU, Høgskoleringen 5, 7491 Trondheim, Norway. [2] SINTEF Materials and Chemistry, Trondheim, Norway. [3] Present Address: Pharmaceutical Sciences Laboratory, Faculty of Natural Sciences and Technology, Åbo Akademi University, Turku, Finland.

Acknowledgements

Dr. Andrey Klymchenko (University of Strasbourg) is thanked for providing NR668, Henkel Loctite for cyanoacrylate monomers, Cremer for Miglyol®, Huntsman for Jeffamine®, Professor Asbjørn Nilsen for human serum. Professor Thor Bernt Melø and Dr. Astrid Bjørkøy are acknowledged for helping on FLIM analysis. We thank Dr. Ruth Schmid for helping in developing the nanoparticles and for useful discussions.

Sources of support for research:

The Research Council of Norway: Biotek2021 project number 226159, Nano2021 project number 220005. The Norwegian Research School in Medical Imaging.

Competing interests

The authors declare that they have no competing interests.

Received: 17 September 2015 Accepted: 29 December 2015

References

1. Ferrari M. Cancer nanotechnology: opportunities and challenges. Nat Rev Cancer. 2005;5:161–71.
2. Matsumura Y, Maeda H. A new concept for macromolecular therapeutics in cancer-chemotherapy—mechanism of tumoritropic accumulation of proteins and the antitumor agent smancs. Cancer Res. 1986;46:6387–92.
3. Iversen TG, Skotland T, Sandvig K. Endocytosis and intracellular transport of nanoparticles: present knowledge and need for future studies. Nano Today. 2011;6:176–85.
4. Kong G, Anyarambhatla G, Petros WP, Braun RD, Colvin OM, Needham D, Dewhirst MW. Efficacy of liposomes and hyperthermia in a human tumor xenograft model: importance of triggered drug release. Cancer Res. 2000;60:6950–7.
5. Husseini GA, Pitt WG. Ultrasonic-activated micellar drug delivery for cancer treatment. J Pharm Sci. 2009;98:795–811.
6. Kumari A, Yadav SK, Yadav SC. Biodegradable polymeric nanoparticles based drug delivery systems. Colloids Surf B Biointerfaces. 2010;75:1–18.
7. Torchilin VP. Multifunctional, stimuli-sensitive nanoparticulate systems for drug delivery. Nat Rev Drug Discov. 2014;13:813–27.
8. Soma E, Attali P, Merle P. A Clinically Relevant Case Study: the Development of Livatag® for the Treatment of Advanced Hepatocellular Carcinoma. In: Alonso MJ, Csaba NS, editors. Nanostructured Biomaterials for Overcoming Biological Barriers. The Royal Society of Chemistry; 2012. p.591-600.
9. Mørch Y, Hansen R, Berg S, Åslund AKO, Glomm WR, Eggen S, Schmid R, Johnsen H, Kubowicz S, Snipstad S, et al. Nanoparticle-stabilized microbubbles for multimodal imaging and drug delivery. Contrast Media and Molecular imaging 2015;10:356–66.
10. Vauthier C, Dubernet C, Fattal E, Pinto-Alphandary H, Couvreur P. Poly(alkylcyanoacrylates) as biodegradable materials for biomedical applications. Adv Drug Del Rev. 2003;55:519–48.
11. Tomcin S, Baier G, Landfester K, Mailander V. Pharmacokinetics on a microscale: visualizing Cy5-labeled oligonucleotide release from poly(n-butylcyanoacrylate) nanocapsules in cells. Int J Nanomedicine. 2014;9:5471–89.
12. Muller RH, Lherm C, Herbort J, Blunk T, Couvreur P. Alkylcyanoacrylate drug carriers. 1. physicochemical characterization of nanoparticles with different alkyl chain-length. Int J Pharm. 1992;84:1–11.
13. Huang CY, Lee YD. Core-shell type of nanoparticles composed of poly[(n-butyl cyanoacrylate)-co-(2-octyl cyanoacrylate)] copolymers for drug delivery application: synthesis, characterization and in vitro degradation. Int J Pharm. 2006;325:132–9.
14. Wade CWR, Leonard F. Degradation of poly(methyl 2-cyanoacrylates). J Biomed Mater Res. 1972;6:215–20.
15. Scherer D, Robinson JR, Kreuter J. Influence of enzymes on the stability of polybutylcyanoacrylate nanoparticles. Int J Pharm. 1994;101:165–8.
16. Lenaerts V, Couvreur P, Christiaensleyh D, Joiris E, Roland M, Rollman B, Speiser P. Degradation of poly (isobutyl cyanoacrylate) nanoparticles. Biomaterials. 1984;5:65–8.

17. Muller RH, Lherm C, Herbort J, Couvreur P. In vitro model for the degradation of alkylcyanoacrylate nanoparticles. Biomaterials. 1990;11:590–5.
18. Leonard F, Kulkarni RK, Brandes G, Nelson J, Cameron JJ. Synthesis and degradation of poly(alkyl alpha-cyanoacrylates). J Appl Polym Sci. 1966;10:259–72.
19. Vansnick L, Couvreur P, Christiaens-Leyh D, Roland M. Molecular weights of free and drug-loaded nanoparticles. Pharm Res. 1985;2:36–41.
20. Andrieux K, Couvreur P. Polyalkylcyanoacrylate nanoparticles for delivery of drugs across the blood–brain barrier. Wiley Interdiscip Rev Nanomed Nanobiotechnol. 2009;1:463–74.
21. Klymchenko AS, Roger E, Anton N, Anton H, Shulov I, Vermot J, Mely Y, Vandamme TF. Highly lipophilic fluorescent dyes in nano-emulsions: towards bright non-leaking nano-droplets. RSC Adv. 2012;2:11876–86.
22. Eggen S, Fagerland SM, Morch Y, Hansen R, Sovik K, Berg S, Furu H, Bohn AD, Lilledahl MB, Angelsen A, et al. Ultrasound-enhanced drug delivery in prostate cancer xenografts by nanoparticles stabilizing microbubbles. J Controll Release. 2014;187:39–49.
23. Romero G, Qiu Y, Murray RA, Moya SE. Study of intracellular delivery of doxorubicin from poly(lactide-co-glycolide) nanoparticles by means of fluorescence lifetime imaging and confocal raman microscopy. Macromol Biosci. 2013;13:234–41.
24. Luhmann T, Rimann M, Bitterman AG, Hall H. Cellular uptake and intracellular pathways of PLL-g-PEG-DNA nanoparticles. Bioconj Chem. 2008;19:1907–16.
25. Snipstad S, Westrom S, Morch Y, Afadzi M, Aslund A, de Lange Davies C. Contact-mediated intracellular delivery of hydrophobic drugs from polymeric nanoparticles. Cancer Nanotechnol. 2014;5:8.
26. Bennis S, Chapey C, Couvreur P, Robert J. Enhanced cytotoxicity of doxorubicin encapsulated in polyisohexylcyanoacrylate nanospheres against multidrug-resistant tumor-cells in culture. Eur J Cancer. 1994;30A:89–93.
27. Fattal E, Vauthier C, Aynie I, Nakada Y, Lambert G, Malvy C, Couvreur P. Biodegradable polyalkylcyanoacrylate nanoparticles for the delivery of oligonucleotides. J Controll Release. 1998;53:137–43.
28. Kreuter J. Drug delivery to the central nervous system by polymeric nanoparticles: what do we know? Adv Drug Deliv Rev. 2014;71:2–14.
29. deVerdiere AC, Dubernet C, Nemati F, Soma E, Appel M, Ferte J, Bernard S, Puisieux F, Couvreur P. Reversion of multidrug resistance with polyalkylcyanoacrylate nanoparticles: Towards a mechanism of action. Br J Cancer. 1997;76:198–205.
30. Evangelatov A, Skrobanska R, Mladenov N, Petkova M, Yordanov G, Pankov R. Epirubicin loading in poly(butyl cyanoacrylate) nanoparticles manifests via altered intracellular localization and cellular response in cervical carcinoma (HeLa) cells. Drug Deliv. 2014:1–10.
31. Yordanov G, Evangelatov A, Skrobanska R. Epirubicin loaded to pre-polymerized poly(butyl cyanoacrylate) nanoparticles: preparation and in vitro evaluation in human lung adenocarcinoma cells. Colloids Surf B Biointerfaces. 2013;107:115–23.
32. Lira MCB, Santos-Magalhaes NS, Nicolas V, Marsaud V, Silva MPC, Ponchel G, Vauthier C. Cytotoxicity and cellular uptake of newly synthesized fucoidan-coated nanoparticles. Eur J Pharm Biopharm. 2011;79:162–70.
33. Chithrani BD, Chan WCW. Elucidating the mechanism of cellular uptake and removal of protein-coated gold nanoparticles of different sizes and shapes. Nano Lett. 2007;7:1542–50.
34. He CB, Hu YP, Yin LC, Tang C, Yin CH. Effects of particle size and surface charge on cellular uptake and biodistribution of polymeric nanoparticles. Biomaterials. 2010;31:3657–66.
35. dos Santos T, Varela J, Lynch I, Salvati A, Dawson KA. Quantitative assessment of the comparative nanoparticle-uptake efficiency of a range of cell lines. Small. 2011;7:3341–9.
36. Ramge P, Unger RE, Oltrogge JB, Zenker D, Begley D, Kreuter J, von Briesen H. Polysorbate-80 coating enhances uptake of polybutylcyanoacrylate (PBCA)-nanoparticles by human and bovine primary brain capillary endothelial cells. Eur J Neurosci. 2000;12:1931–40.
37. Panyam J, Zhou WZ, Prabha S, Sahoo SK, Labhasetwar V. Rapid endo-lysosomal escape of poly(DL-lactide-co-glycolide) nanoparticles: implications for drug and gene delivery. FASEB J. 2002;16.
38. dos Santos T, Varela J, Lynch I, Salvati A, Dawson KA. Effects of transport inhibitors on the cellular uptake of carboxylated polystyrene nanoparticles in different cell lines. PLoS One. 2011;6:e24438.
39. You JO, Auguste DT. Feedback-regulated paclitaxel delivery based on poly(N, N-dimethylaminoethyl methacrylate-co-2-hydroxyethyl methacrylate) nanoparticles. Biomaterials. 2008;29:1950–7.
40. Mahmoudi M, Lynch I, Ejtehadi MR, Monopoli MP, Bombelli FB, Laurent S. Protein-nanoparticle interactions: opportunities and challenges. Chem Rev. 2011;111:5610–37.
41. Zweers MLT, Engbers GHM, Grijpma DW, Feijen J. In vitro degradation of nanoparticles prepared from polymers based on DL-lactide, glycolide and poly(ethylene oxide). J Controll Release. 2004;100:347–56.
42. Lao LL, Peppas NA, Boey FYC, Venkatraman SS. Modeling of drug release from bulk-degrading polymers. Int J Pharm. 2011;418:28–41.
43. Grangier JL, Puygrenier M, Gautier JC, Couvreur P. Nanoparticles as carriers for growth-hormone releasing-factor. J Controll Release. 1991;15:3–13.
44. Hansali F, Poisson G, Wu M, Bendedouch D, Marie E. Miniemulsion polymerizations of n-butyl cyanoacrylate via two routes: towards a control of particle degradation. Colloids Surf B Biointerfaces. 2011;88:332–8.
45. Gravier J, Sancey L, Hirsjärvi S, Rustique E, Passarini C, Benoit JP, Coll JL, Texier I. FRET Imaging Approaches for in vitro and in vivo characterization of synthetic lipid nanoparticles. Mol Pharm. 2014.
46. Kante B, Couvreur P, Dubois-Krack G, De Meester C, Guiot P, Roland M, Mercier M, Speiser P. Toxicity of polyalkylcyanoacrylate nanoparticles I: free nanoparticles. J Pharm Sci. 1982;71:786–90.
47. Lherm C, Muller RH, Puisieux F, Couvreur P. Alkylcyanoacrylate drug carriers. 2. cytotoxicity of cyanoacrylate nanoparticles with different alkyl chain-length. Int J Pharm. 1992;84:13–22.
48. Gillies ER, Goodwin AP, Frechet JMJ. Acetals as pH-sensitive linkages for drug delivery. Bioconj Chem. 2004;15:1254–63.
49. Zhao YM, van Rooy I, Hak S, Fay F, Tang J, Davies CD, Skobe M, Fisher EA, Radu A, Fayad ZA, et al. Near-infrared fluorescence energy transfer imaging of nanoparticle accumulation and dissociation kinetics in tumor-bearing Mice. ACS Nano. 2013;7:10362–70.
50. Bastiaens PIH, Squire A. Fluorescence lifetime imaging microscopy: spatial resolution of biochemical processes in the cell. Trends Cell Biol. 1999;9:48–52.
51. Sanders R, Draaijer A, Gerritsen HC, Houpt PM, Levine YK. Quantitative Ph imaging in cells using confocal fluorescence lifetime imaging microscopy. Anal Biochem. 1995;227:302–8.
52. Skotland T, Iversen TG, Sandvig K. Development of nanoparticles for clinical use. Nanomedicine. 2014;9:1295–9.
53. Barua S, Rege K. Cancer-cell-phenotype-dependent differential intracellular trafficking of unconjugated quantum dots. Small. 2009;5:370–6.
54. Davis JN, Kucuk O, Sarkar FH. Genistein inhibits NF-kappa B activation in prostate cancer cells. Nutr Cancer Int J. 1999;35:167–74.
55. Åslund A, Sigurdson CJ, Klingstedt T, Grathwohl S, Bolmont T, Dickstein DL, Glimsdal E, Prokop S, Lindgren M, Konradsson P, et al. Novel pentameric thiophene derivatives for in vitro and in vivo optical imaging of a plethora of protein aggregates in cerebral amyloidoses. ACS Chem Biol. 2009;4:673–84.

Paper IV

PLOS | ONE

RESEARCH ARTICLE

Feasibility Study of the Permeability and Uptake of Mesoporous Silica Nanoparticles across the Blood-Brain Barrier

Habib Baghirov[1,2,3,4], **Didem Karaman**[2,5], **Tapani Viitala**[6], **Alain Duchanoy**[2], **Yan-Ru Lou**[6], **Veronika Mamaeva**[1], **Evgeny Pryazhnikov**[7], **Leonard Khiroug**[7], **Catharina de Lange Davies**[4], **Cecilia Sahlgren**[1,3,8]*, **Jessica M. Rosenholm**[2,5]*

1 Turku Centre for Biotechnology, University of Turku and Åbo Akademi University, Turku, Finland, **2** Laboratory of Physical Chemistry, Faculty of Science and Engineering, Åbo Akademi University, Turku, Finland, **3** Cell Biology, Faculty of Science and Engineering, Åbo Akademi University, Turku, Finland, **4** Department of Physics, Norwegian University of Science and Technology, Trondheim, Norway, **5** Pharmaceutical Sciences Laboratory, Faculty of Science and Engineering, Åbo Akademi University, Turku, Finland, **6** Centre for Drug Research, Division of Pharmaceutical Biosciences, University of Helsinki, Helsinki, Finland, **7** Neurotar LtD, Helsinki, Finland, **8** Eindhoven University of Technology, Eindhoven, The Netherlands

* csahlgre@btk.fi (CS); jerosenh@abo.fi (JR)

Abstract

Drug delivery into the brain is impeded by the blood-brain-barrier (BBB) that filters out the vast majority of drugs after systemic administration. In this work, we assessed the transport, uptake and cytotoxicity of promising drug nanocarriers, mesoporous silica nanoparticles (MSNs), in *in vitro* models of the BBB. RBE4 rat brain endothelial cells and Madin-Darby canine kidney epithelial cells, strain II, were used as BBB models. We studied spherical and rod-shaped MSNs with the following modifications: bare MSNs and MSNs coated with a poly (ethylene glycol)-poly(ethylene imine) (PEG-PEI) block copolymer. In transport studies, MSNs showed low permeability, whereas the results of the cellular uptake studies suggest robust uptake of PEG-PEI-coated MSNs. None of the MSNs showed significant toxic effects in the cell viability studies. While the shape effect was detectable but small, especially in the real-time surface plasmon resonance measurements, coating with PEG-PEI copolymers clearly facilitated the uptake of MSNs. Finally, we evaluated the *in vivo* detectability of one of the best candidates, i.e. the copolymer-coated rod-shaped MSNs, by two-photon *in vivo* imaging in the brain vasculature. The particles were clearly detectable after intravenous injection and caused no damage to the BBB. Thus, when properly designed, the uptake of MSNs could potentially be utilized for the delivery of drugs into the brain *via* transcellular transport.

Citation: Baghirov H, Karaman D, Viitala T, Duchanoy A, Lou Y-R, Mamaeva V, et al. (2016) Feasibility Study of the Permeability and Uptake of Mesoporous Silica Nanoparticles across the Blood-Brain Barrier. PLoS ONE 11(8): e0160705. doi:10.1371/journal.pone.0160705

Editor: Valentin Ceña, Universidad de Castilla-La Mancha, SPAIN

Received: January 28, 2016

Accepted: July 22, 2016

Published: August 22, 2016

Data Availability Statement: All relevant data are within the paper and its Supporting Information files.

Funding: Funding for this research work was provided by the Academy of Finland project #140193: "Targeting of cancer cells by design - Nanoparticles as theranostic agents" (JR). Other supporting funding sources the authors acknowledge are Norwegian Research Council projects (Biotek2021 226159 and Nano2021 220005), Academy of Finland projects (#137101, #260599, #137053 and #263861) (CD), Center for Functional Materials (DSK) and Graduate School of Materials Research (AD). Neurotar LtD

Introduction

The blood-brain barrier (BBB) is the most extensive of barriers that protect the brain's internal milieu and maintain its homeostasis [1]. Structurally, the BBB is formed by brain capillary

provided support in the form of salaries for authors EP and LK, but did not have any additional role in the study design, data collection and analysis, decision to publish, or preparation of the manuscript. The specific roles of these authors are articulated in the 'author contributions' section.

Competing Interests: The authors declare no competing interests. Evgeny Pryazhnikov and Leonard Khiroug are employed by Neurotar LtD. Neurotar LtD is a provider of in vivo two-photon imaging services. This does not alter their adherence to PLOS ONE policies on sharing data and materials.

endothelial cells (BCEC). While sharing some features with other endothelial cells, BCEC have a number of marked differences such as the structure of their tight junctions, lack of fenestrations, diminished pinocytosis, high mitochondrial activity, high percentage of proteins in the cell membrane and the expression of various BBB markers. Key components of the BBB—the paracellular barrier formed by circumferential tight junctions between adjacent BCEC and the transcellular barrier consisting of cell membranes, efflux transporters and various enzymatic filters–act together to form a dynamic interface that incorporates physical, metabolic and enzymatic mechanisms to screen the brain from harmful agents and ensure that its tightly controlled extracellular fluid microenvironment remains resistant to the much more volatile environment of blood [2, 3]. Unfortunately, this barrier function also makes the BBB filter out the vast majority of drugs, making the treatment of various brain disorders highly dependent on drug delivery limitations. The problem is widely acknowledged, and it has been estimated that 100% of large molecules (over 500 Da) and 98% of small molecules do not reach the brain after systemic administration, making the central nervous system drug market largely underpenetrated [4].

Nanoparticles, due to their high drug load capacity and possible functionalization for facilitating BBB permeability, as well as imaging and targeting, have emerged as a possible solution to this challenge [5–7]. They come in a variety of sizes and shapes and can be further tailored to desired needs by surface modification. They can carry many drug molecules without requiring chemical modification of the same, which is important for preserving drug activity. Unlike traditional drug formulations, where drug release is spontaneous and immediate, often requiring frequent administrations, drug delivery using nanoparticles can be controlled and sustained, thus increasing target availability. Both qualities may further be enhanced by functionalization, e.g. by capping porous particles with 'gatekeepers' or using cleavable agents, respectively. In addition, nanoparticles can be bound to ligands or antibodies for active targeting, which can decrease non-specific toxicity of drugs by indirectly reducing their levels in non-targeted tissues.

One class of inorganic nanoparticles that has distinct advantages in drug delivery is mesoporous silica nanoparticles (MSNs) [8–10]. MSNs have a well-defined pore arrangement with controllable pore sizes in the 2–50 nm range. The pores can occupy a large part of the total volume, and their design can be adjusted to accommodate drugs, imaging agents or both. Aside from endowing MSNs with a large surface area, porosity allows independent functionalization of inner and outer surfaces. The former can improve drug immobilization, while the latter can be used for better stability in suspension, controlled or more sustained release (e.g. by capping pore openings), charge modification, and linkage to targeting ligands, hydrophilic moieties etc. The porous structure also helps to physically separate cargo in multifunctional nanoparticles. Generally, drugs are loaded into the pores for better protection and immobilization, while various moieties, as well as imaging and targeting agents are attached to the outer surface. At neutral pH, unmodified MSNs are negatively charged, whereby their functionalization with cationic surface groups can be used for enhanced accommodation of negatively charged (e.g. acidic) drugs, but also for promoting endosomal escape [11]. MSNs are thermally and chemically stable; eventually, however, their matrix undergoes biodegradation by hydrolysis. Degradation of MSNs produces beneficial monomeric silicic acid [12], and this increases the appeal of MSNs compared to other inorganic nanoparticles, many of which are not biodegradable.

Given these potential advantages of MSNs in drug delivery, we decided to investigate whether MSNs can cross or be taken up by the BBB and whether this uptake or permeability is affected by their 1) aspect ratio or 2) the effect of a poly(ethylene glycol)-poly(ethylene imine) (PEG-PEI) block copolymer layer, of which the PEG component is commonly used to reduce the recognition of circulating particles by the reticuloendothelial system *in vivo*, thus also increasing the likelihood of BBB penetration [6], and the PEI component confers cationic properties, thus facilitating cellular uptake and, potentially, permeability [13]. One of the more promising candidates was selected for an *in vivo* detectability test. In addition, we evaluated cytotoxic effects of the studied MSNs. Three complementary methods were used to evaluate cellular uptake: flow cytometry, confocal fluorescence microscopy and surface plasmon resonance (SPR). SPR is a novel, label-free method for studying nanoparticle interactions with cells where the interactions can be followed in real time, and our observations were thus correlated with those of the more traditional methods (flow cytometry and microscopy). Further, we demonstrated the detectability of the developed particles in mice by applying two-photon *in vivo* imaging. We used RBE4 rat brain endothelial cells and Madin-Darby canine kidney epithelial cells, strain II, as BBB models; RBE4 cells are of brain endothelial origin, thus reflecting the BBB more closely, but MDCK II, while of kidney epithelium origin, may be preferable in transport studies as they form a monolayer with considerably better barrier properties.

Results and Discussion

MSN synthesis and design

In order to obtain particles in the sub-100 nm range, MSNs were synthesized according to the procedure described by Gu et al. [14] with certain modifications to further vary the aspect ratio of the resulting particles. The synthesis parameters were thus varied in order to investigate the effect of aspect ratio, where rod-shaped MSNs have previously been observed to be more efficiently internalized by cells [7, 15, 16]. In addition, rod-shaped particles have in certain cases proven to be more efficient in permeability studies [2, 3], which is why we set out to investigate whether we could detect any favorable effects related to aspect ratio in our case as well. The synthesized particles were further coated with in-house produced PEG-PEI copolymers [17] which could, if desired, be further attached to biomolecular moieties. All four particle designs are depicted in Fig 1.

After template extraction, the morphology and mesostructure of the obtained pure spherical MSN and rod-shaped MSNs were investigated with electron microscopy (EM), as shown in Fig 2 below.

The coated PEG-PEI copolymer amount on both spherical MSN and rod-shaped MSN was about 13 wt% for both particle types as determined by thermogravimetric analysis (TGA). For

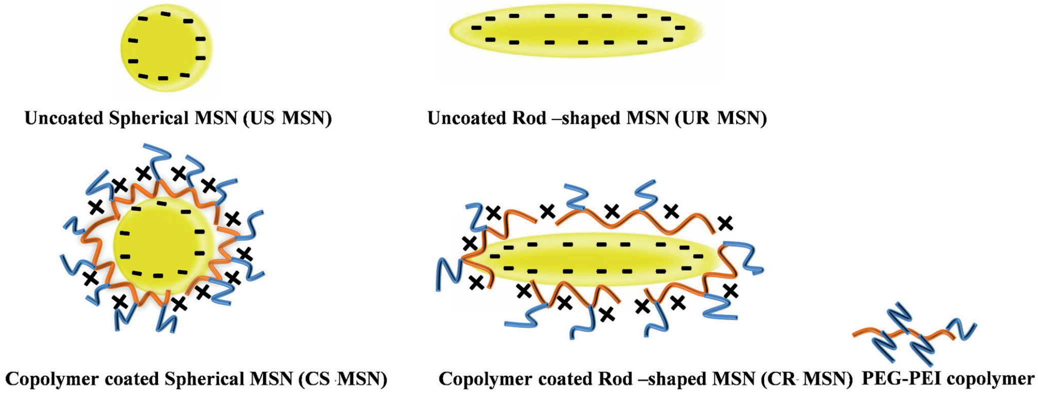

Fig 1. Particle designs implemented for this study.

doi:10.1371/journal.pone.0160705.g001

all particle types, suspensions were prepared in concentrations of 1 mg/ml in HEPES buffer (pH 7.2), and hydrodynamic size and net surface charge (ζ-potentials) were determined by using dynamic light scattering and electrokinetic analysis, respectively. Fluorescence intensity spectra were recorded and the peak value at the highest emission wavelengths upon excitation at 488 nm was noted. These maximum peak values as well as dynamic light scattering (DLS) and ζ-potential data can be found in Table 1 below.

Clearly, all particles were fully dispersible in HEPES buffer after all processing steps, including template removal and surface coating with copolymer. We note that the hydrodynamic size derived from DLS measurements is not used to establish a "real" particle size but rather dispersability, whereby EM (Fig 2) is applied for particle size determination. On the one hand, particle fluorescence may distort the DLS values obtained from such a measurement, and on the other hand, particles with non-spherical morphology cannot be size-determined using light scattering methods. Thus, according to the EM images, the uncoated spherical MSNs have spherical morphology with a diameter of 50 nm and uncoated rod-shaped MSNs have elongated morphology with the aspect ratio of 3 (length~ 300 nm width ~100 nm). The ζ-potentials at neutral pH confirmed that both particles in question were comparable to pure silica in terms of net surface charge (despite the addition of small amounts of aminosilane for the covalent attachment of the fluorescent label) and thus applicable for electrostatic coating of the produced PEG-PEI copolymer. In this specific copolymer construct, the cationic PEI part is used to anchor strongly to the negatively charged silica surface, whereas the PEG chains are expected to 'stick out' from the particle surface and thus impart the particle system with a steric stabilization component [17]. Further, PEG is probably the most commonly employed polymer coating for nanomedical systems especially with *in vivo* prospects. The electrostatic contribution of PEI could be clearly observed in the electrokinetic measurements, with a shift from the characteristic negatively charged surface of silica to positive at neutral pH (Table 1). The proximal location of PEI was also observed as a decrease in fluorescence intensity, where the local abundance of protons, owing to the 'proton trap' ability of PEI, decreases the local pH which, in turn, decreases the quantum yield and thereby the resulting fluorescence intensity of fluorescein [18].

Cytotoxicity studies

Cytotoxicity experiments were performed with both MDCK II and RBE4 cells and were based on the viability of cells following incubation with spherical and rod-shaped of MSNs for 36 hours.

As can be seen in Fig 3a and 3b, neither rod-shaped, nor spherical MSNs show any considerable toxic effect at concentrations of 50 μg/ml and below. The relatively long incubation time in the cytotoxicity experiments has allowed us to verify that MSN NPs at the studied concentrations were did not have any toxic effect in either cell line at any of the time points used in other experiments in our study.

Additionally, bright field microscopy images of MDCK II monolayers used in transport experiments were taken in order to estimate the toxic effect of the MSNs on fully polarized MDCK II cells.

In Fig 4, few to no cells stained by Trypan Blue are seen on a permeable support with PEG-PEI-coated rod-shaped MSNs (chosen here as an example), which indicates lack of a substantial toxic effect. No signs of monolayer disruption were observed in the bright field images of monolayers exposed to other MSNs (data not shown).

Having established that our MSN do not exert any toxic effect at concentrations up to 50 μg/ml, we proceeded with uptake and transport studies using the nanoparticles in the same range of concentrations.

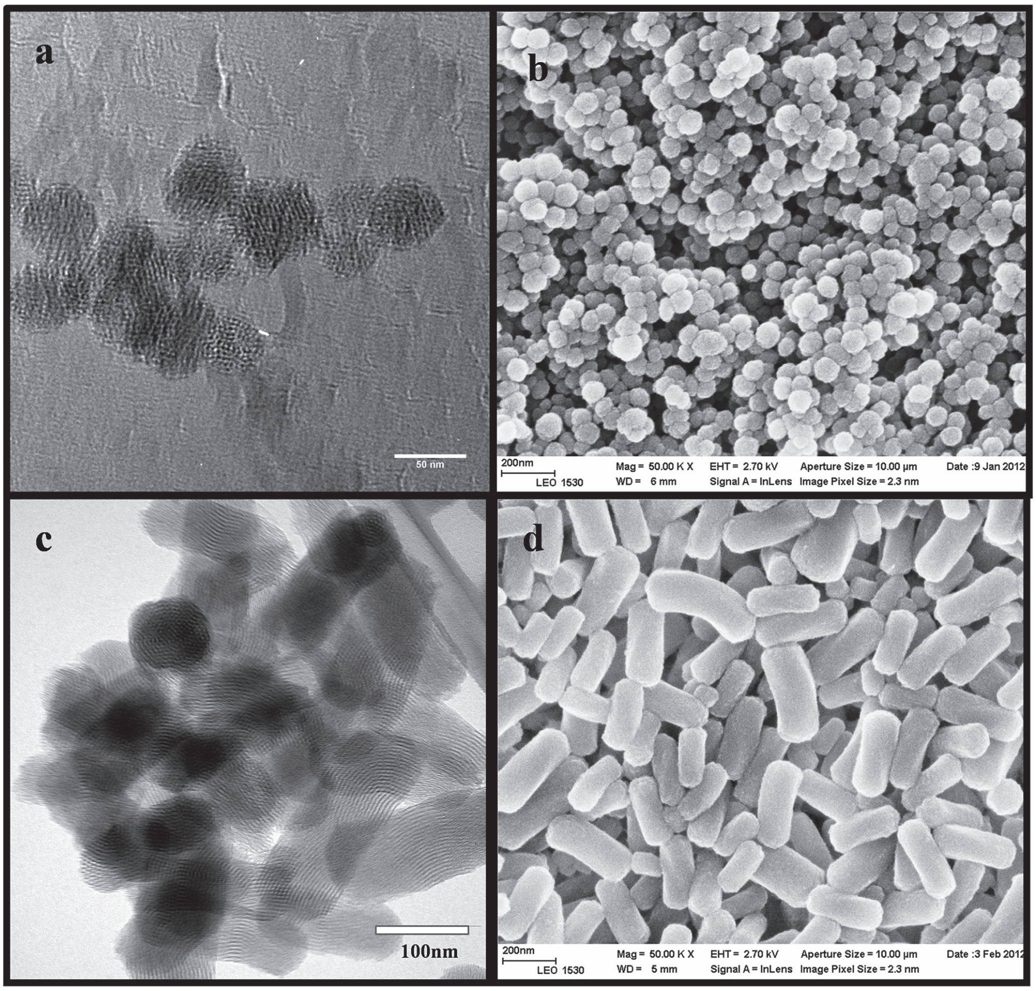

Fig 2. Electron microscopy images. a) transmission electron microscopy images of uncoated spherical MSNs b) scanning electron microscopy images of uncoated spherical MSNs c) transmission electron microscopy images of uncoated rod-shaped MSNs d) scanning electron microscopy images of uncoated rod-shaped MSNs.

doi:10.1371/journal.pone.0160705.g002

Table 1. Physicochemical characteristics of the investigated particle suspensions in HEPES buffer (pH = 7.2).

Samples	Hydrodynamic size (nm)	Net surface charge (mV)	Fluorescence intensity
Uncoated spherical MSN (US MSN)	152	-24	501
Coated spherical MSN (CS MSN)	137	8	23
Uncoated rod-shaped MSN (UR MSN)	207	-27	439
Coated rod-shaped MSN (CR MSN)	222	10	79

doi:10.1371/journal.pone.0160705.t001

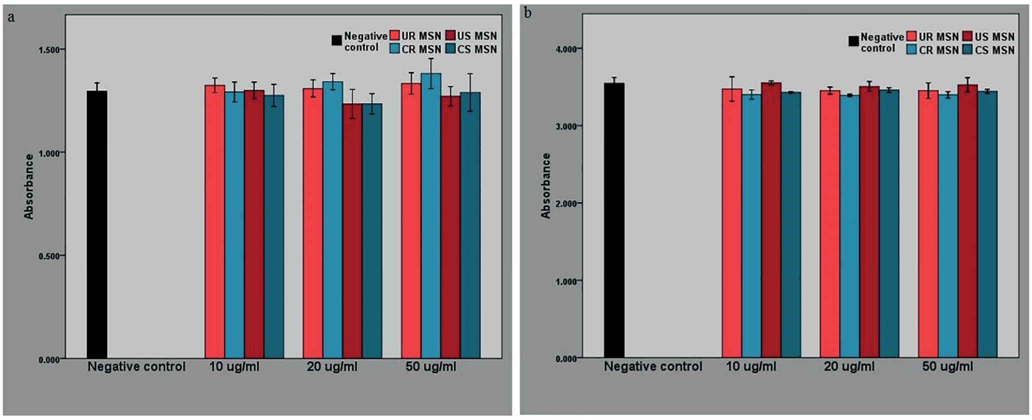

Fig 3. Cytotoxicity of various MSNs applied at concentrations of 50, 20 and 10 μg/ml in serum-free medium. Negative control–untreated cells. Data shown as M±2xSEM. **a)** MSN toxicity in MDCK II cells. **b)** MSN toxicity in RBE4 cells.

doi:10.1371/journal.pone.0160705.g003

Nanoparticle uptake in cellular models *in vitro*

As nanoparticles in general are too large to pass through the tight cell junctions of an intact BBB (paracellular route), the expected mechanism of transport over a cell layer would rather be transcytosis (transcellular route). In order for this to take place, the particles would first have to be taken up by the cells via endocytosis, be translocated across the cell, and, ultimately,

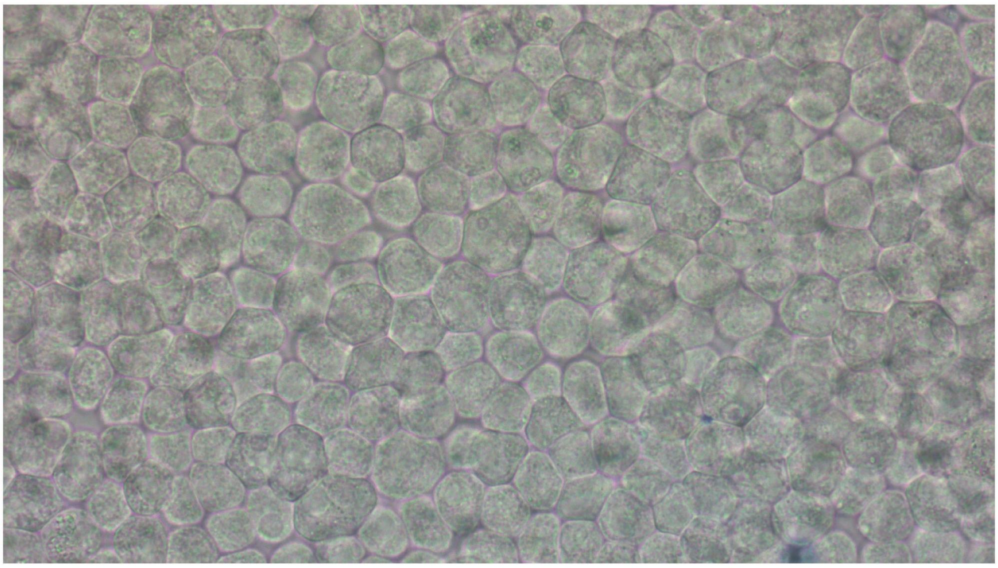

Fig 4. Bright field microscopy image of MDCK II cells grown on permeable supports and incubated with rod-shaped MSNs coated with a PEG-PEI copolymer (incubation time—36 hours).

doi:10.1371/journal.pone.0160705.g004

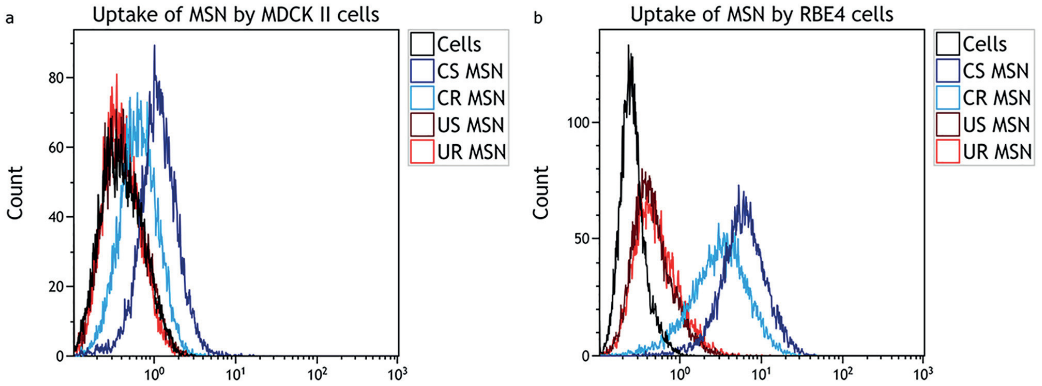

Fig 5. Flow cytometry histograms for determining the uptake of different MSNs that were incubated with the MDCK II and RBE4 cells at a concentration of 20 μg/ml for 24 hours in serum-free medium. Negative control–cells not incubated with the MSNs. a) Representative histograms showing uptake of MSNs in MDCK II cells. b) Representative histograms showing uptake in RBE4 cells.

doi:10.1371/journal.pone.0160705.g005

exocytosed. Thus, MSN uptake was evaluated by flow cytometry and confocal microscopy to detect fluorescein isothiocyanate (FITC)-labeled MSNs taken up by cells and, in a novel approach, by surface plasmon resonance measurements which allow monitoring cell uptake of nanoparticles in real time without using labels.

As shown in Fig 5a and 5b, the uptake of copolymer-coated spherical and rod-shaped MSNs in both MDCK II and RBE4 cells is robust and manifested by complete peak shifts in their respective histograms, indicating that the copolymer coating was very efficient in improving the cellular uptake of both spherical and rod-shaped MSNs. The uptake of uncoated particles is much less prominent, even though some uptake can be detected as judged by a fraction of FITC-positive cells, seen as a 'bulging' in the histogram.

Problems related to the fluorescence variability of the label used (fluorescein) lead us to refrain from drawing any conclusions regarding quantification based on flow cytometry studies. In order to further confirm MSN uptake results, however, we evaluated the internalization of MSNs using confocal microscopy.

Fig 6a–6d show the uptake of MSNs by RBE4 cells. Only few uncoated MSNs are visible inside RBE4 cells, while the uptake of PEG-PEI-coated MSNs is very robust, which is in line with the flow cytometry data. Many PEG-PEI-coated MSNs are found around the cell nuclei, which can be explained by the long incubation time used in this experiment as the nanoparticles located in endocytic pathway vesicles would have enough time to shift toward the nuclei along microtubules in a retrograde transport. Images of MDCK II cells incubated with MSN NPs show the same trends, although the uptake efficiency is lower, which is consistent with the flow cytometry results. Overall, confocal microscopy results support the importance of PEG-PEI coating for cellular uptake of MSNs.

In addition to the more established techniques such as FCM and CLSM, we also employed SPR as a novel method to study the MSN-cell interactions in greater detail in order to determine possible differences between uncoated and polymer-coated MSNs. The advantages of SPR include monitor uptake in real time, independence of fluorescent labeling and great sensitivity. In the SPR, the signal response is caused by a combination of morphological changes in the cell layer, i.e. cell spreading or contraction, and accumulation of the stimulant in the cells

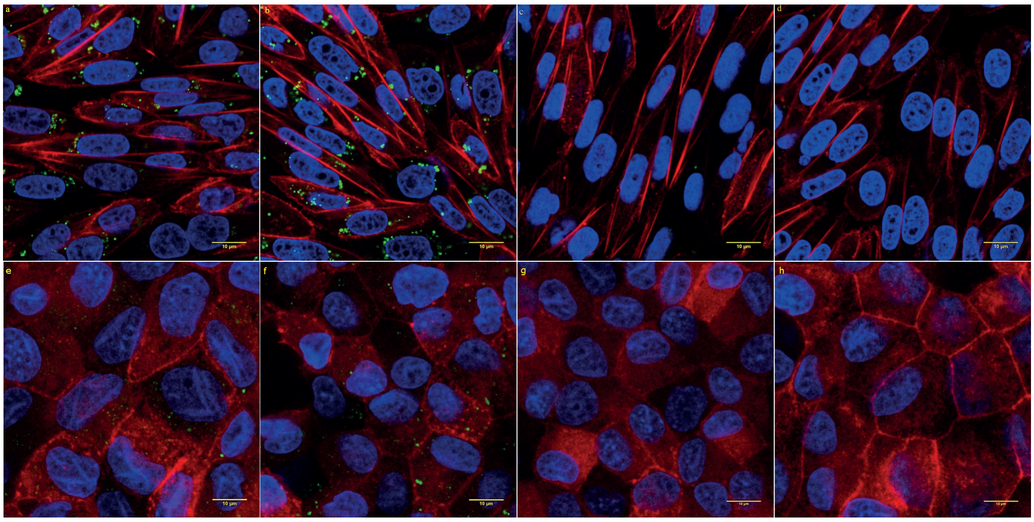

Fig 6. Confocal images of RBE4 and MDCK II cells incubated for 24 hours with MSNs applied at a concentration of 20 μg/ml in serum-free medium. Nuclei stained with Hoechst 33258 (blue). MSNs labeled with FITC (green). F-actin stained with phalloidin (red) **a)** PEG-PEI-coated spherical MSNs in RBE4. **b)** PEG-PEI-coated rod-shaped MSNs in RBE4. **c)** Uncoated spherical MSNs in RBE4. **d)** Uncoated rod-shaped MSNs in RBE4. e) PEG-PEI-coated spherical MSNs in MDCK II. f) PEG-PEI-coated rod-shaped MSNs in MDCK II. g) Uncoated spherical MSNs in MDCK II. h) Uncoated rod-shaped MSNs in MDCK II.

doi:10.1371/journal.pone.0160705.g006

[19–21] The SPR response should thus reflect the endocytotic uptake of nanoparticles and depend on the translocation of MSN-containing vesicles from the membrane.

Fig 7 represents the interactions of spherical and rod-shaped MSNs with MDCKII cells at a concentration of 20 μg/ml. The initial peak during the first minutes mainly originates from the perturbations caused by the particle stock suspension media (DMSO) and can therefore be disregarded. In Fig 7a, for the copolymer coated spherical MSNs (blue curve) the initial leveling out of the SPR response (7–18 minutes) is interpreted to be caused by the fast adherence of the positively charged MSNs to the cell surface, causing a slight cell spreading and cytoskeletal mass re-distribution within the cell closer to the basolateral side of the cells [19, 20]. The subsequent decrease in the SPR signal (18–125 minutes) is then caused by cell contraction accompanied with cytoskeletal mass re-distribution towards the apical side of the cells during endocytosis of the copolymer coated spherical MSNs [19, 21]. This is then followed by a steep increase and leveling out of the SPR response (125–300 minutes) indicating continued cell uptake and subsequent intracellular translocation of the MSNs closer to the sensor surface, i.e. closer to the basolateral side of the cells. For the uncoated MSNs (red curve) the initial morphological change accompanied with cytoskeletal mass re-distribution towards the apical side of the cells during endocytosis seen as a decrease in the SPR signal takes place between 7–35 minutes. This is then followed by a much slower increase and leveling out of the SPR signal (35–300 minutes) and a much slower uptake and intracellular translocation kinetics compared to the copolymer coated spherical MSNs.

Different behavior can be observed for the rod-shaped MSNs in Fig 7b. The uncoated rod-shaped MSNs (red curve) induce an immediate steep increase in the SPR response (10–45 minutes) followed by a leveling out (45–55 minutes) and subsequent decrease and a second leveling out of the SPR response (55–175 minutes). This is interpreted as an immediate and very rapid

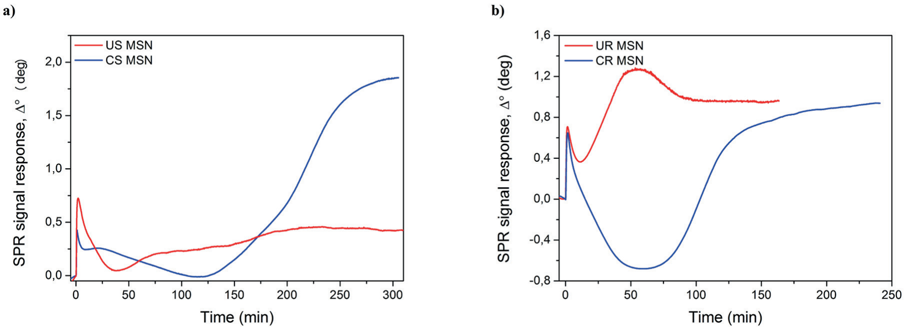

Fig 7. SPR responses reflecting uptake of MSNs by MDCK II cells. Cells were stimulated with 20 μg/ml of a) spherical and b) rod-shaped MSNs in serum-free medium at t = 20°C. Monitoring was performed for 175–240 minutes for spherical MSNs and 200–300 minutes for rod-shaped MSNs after injection of MSNs into a steady state SPR cuvette.

doi:10.1371/journal.pone.0160705.g007

uptake of the uncoated rod-shaped MSNs by the MDCK II cells accompanied with cytoskeletal mass re-distribution towards the apical side of the cells during endocytosis. With time, the uptake and intracellular translocation processes of the uncoated rod-shaped MSNs then reach a saturation point. However, the copolymer-coated rod-shaped MSNs initially display a deep decline onto the negative side in the SPR response (blue curve) followed by a steep increase and finally a leveling out in the SPR response. We again assign the initial substantial decrease in the SPR response as morphological changes in the cells accompanied with cytoskeletal mass re-distribution towards the apical side of the cells during endocytosis. These morphological and mass re-distribution changes are clearly more pronounced for the copolymer-coated rod-shaped MSNs compared to the spherical MSNs which is logical due to the different shape and size of the rod-shaped MSNs compared to the spherical MSNs. The steep increase in the SPR response towards later time points further indicates a continued and efficient uptake and intracellular translocation of the coated rod-shaped MSNs closer to the basolateral side of the cells, similarly as seen for the coated spherical MSNs.

Nanoparticle transport across cellular monolayers *in vitro*

Having established robust uptake of PEG-PEI-conjugated nanoparticles, we evaluated the transport rates of rod-shaped and spherical MSNs across MDCK II monolayers. MDCK II monolayers were incubated with 50 μg/ml MSNs in serum-free medium, with their subsequent detection in the samples of the basolateral compartment taken at different time points. MDCK II cells were chosen as a BBB model in the transport study because of their barrier properties that are considerably higher than those of RBE4 cells. Detection was based on fluorescence emitted by the fluorescent tag (FITC) used to label the MSNs.

As shown in Fig 8, the transport of different MSNs across an MDCK II monolayer is generally low at the studied concentration, with the slight exception of the transport of spherical MSNs at 36 hours. Changes in the transport of rod-shaped nanoparticles over time are not statistically significant; the increase in the transport of spherical nanoparticles, especially in the case of uncoated MSNs, is significant, but very small. We note that particle concentrations used in similar transport studies have generally been significantly higher, with concentrations of 176 μg/ml [22] and 224 μg/ml [23] reported for polymeric particle, and in the latter the same concentration for metal oxide nanoparticles, whereas concentrations of 1.0–1.5 mg per

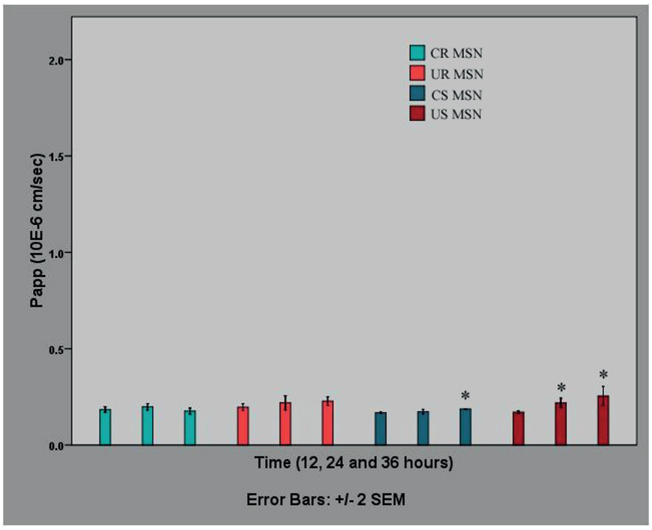

Fig 8. Transport of different MSNs across MDCK II monolayers in serum-free medium. MSNs were applied at a concentration of 50 μg/ml. Data represent the mean apparent permeability (Papp) of MSN (n = 3) at the time points 12, 24 and 36 hours, corrected for the loss of MSNs in the upper compartment, and are shown as M±2xSEM.Asterisks denote significant differences between Papp at 24 or 36 hours and Papp at 12 hours ($p<0.05$).

doi:10.1371/journal.pone.0160705.g008

monolayer have been used specifically for silicon-based particles [24], which could partly explain these results. However, in order to avoid toxic effects, which may certainly also lead to increased permeability observations in this setup, we opted to stay within reasonable particle concentrations (up to 50 μg/ml in the present case). Cell viability evaluation was also carried out to ensure the safety of the used concentrations (see above).

Nanoparticle detectability and BBB integrity *in vivo*

Having established that the MSNs were safe, *in vivo* two-photon microscopy was applied to investigate the *in vivo* detectability of rod-shaped PEG-PEI-conjugated MSNs, which we considered one of the most promising candidates on the basis of the previous uptake experiments. MSNs were injected i.v. into the tail vein of a mouse ($n = 1$).

The particles were clearly detectable in circulation within minutes of i.v. injection. Very quickly, the number of particles in the vessel lumen decreased, and for the rest of the first imaging session they remained only on the vessel walls. No penetration through BBB was evident in this experiment, which is consistent with our *in vitro* results. At 48 hours, very few if any particles were observed, despite increasing the laser intensity by a factor of three. At the end of this second imaging session, a fluorescent dextran was injected to visualize the vessels and test BBB integrity: both appeared intact (see Fig 9).

Despite showing no BBB penetration for this particular nanoparticle species, the results clearly show that the particles can be visualized in vessels and be quantified if desired (by counting the actual number of particles in each compartment at each time point). This will be a valuable tool for developing particles with optimized desired properties.

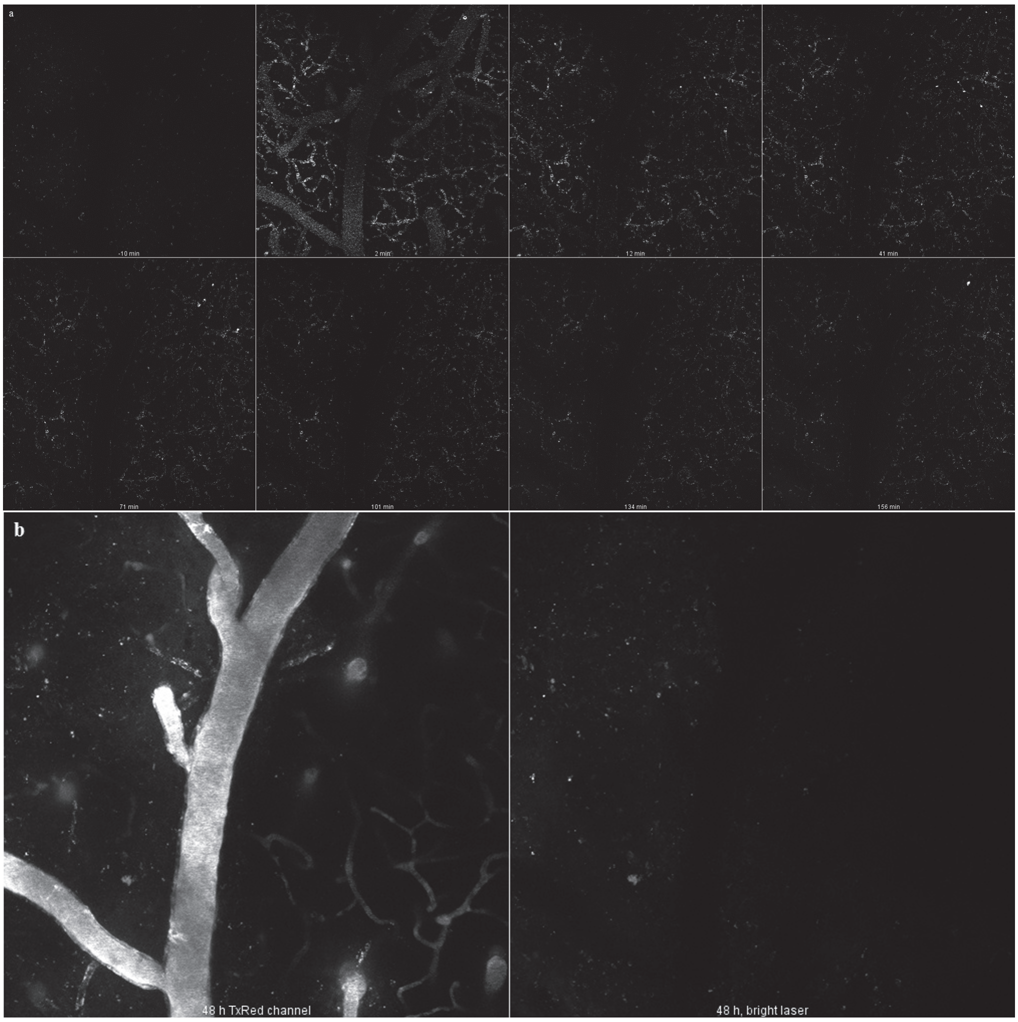

Fig 9. Brain distribution of rod-shaped MSNs after injection into the tail vein of a mouse. a) Rod-shaped MSNs imaged at different time points up to 156 minutes. **b)** Images taken at the end of the experiment (48 hours), showing brain vessels visualized with FITC-dextran, as well as the remaining red-shaped MSNs.

doi:10.1371/journal.pone.0160705.g009

The dimensions of the MSNs used in our study (ranging from 50 to 240 nm) would make their paracellular transport across a cell monolayer with fully formed tight junctions unlikely, therefore restricting their passage to the transcellular route or, more specifically, to endocytosis and subsequent exocytosis. So far, research into transcytosis of nanoparticles has produced varying results. On the one hand, it has been observed in numerous studies [25–28]. In [29], the authors found that the exocytosis of transferrin-coated gold nanoparticles in HeLa cells was even faster than endocytosis, especially for small nanoparticles. In many other studies, however, transcytosis of internalized nanoparticles was shown to be low to inexistent [24, 30]. One important factor could be incubation duration: e.g. in [31], the authors determined two stages of translocation: slow lag state phase (up to 8 hours) and steady state phase (9–27 hours). It should also be noted that many studies rely on fluorescent tags for the detection of exocytosed nanoparticles; this may interfere with the interpretation of results due to particle dissolution (with subsequent release of the dye) and pH-dependent fluorescence of certain dyes (e.g. FITC in our study). This limitation is seldom acknowledged [32], and studies involving natively fluorescent (quantum dots, nanodiamonds), luminescent (gold), paramagnetic (ferrous oxide) and otherwise detectable nanoparticles offer, in this sense, a distinct advantage.

We are aware of several studies where silica (not necessarily mesoporous) nanoparticles were reported to cross the BBB. In one study, FITC-labeled and TAT-conjugated silica particles were detected in the brain after intra-arterial administration [33]. In another, FITC-labeled silica nanoparticles were reported to cross static hCMEC/D3-based BBB model; however, while the uptake of nanoparticles was confirmed, transport rates were very low, and the authors acknowledged potential issues with dye leakage [32]. In a subsequent study, the same group found extensive evidence of silica nanoparticle endocytosis, but very few instances of their transcytosis in an hCMEC/D3-based BBB model. A similar study [34] found that 30 nm, but not larger silica nanoparticles crossed a commercial *in vitro* BBB model based of triple co-culture of primary rat endothelial cells, pericytes and astrocytes. The detection was based on a fluorescent marker; the authors did not acknowledge potential nanoparticle degradation issues. In [35], silica nanoparticles were not found in the brain of rats within 90 days after oral and dermal administration; a similar study conducted on mice, did not find silica nanoparticles the brain within 10 hours after oral exposure [36]. In [37], magnetic nanoparticles overcoated with silica were detected in the brain after intraperitoneal administration. That study spanned four weeks and the first time point was week 1; uptake by neurons was confirmed immunofluorometrically. In [38], organically modified "ORMOSIL" silica nanoparticles were found to be internalized by neurons in Drosophila; however, in an earlier biodistribution study on mice, the same nanoparticles did not accumulate in the brain [39]. In [40], PEGylated silica nanoparticles were found to cross the BBB both *in vitro* (in a model based on bEnd3 cells) and *in vivo* in athymic BALB/c mice; nanoparticle detection both *in vitro* and *in vivo* was based on a fluorescent signal from a doped Rubpy dye. In [41], PEGylated polyamidoamine dendrimer-conjugated magnetic MSNs were internalized by rat BCEC, but also by astrocytic endfeet and neurons (indicating transcytosis through BCEC); the authors observed no permeability of pure MSNs. To the best of our knowledge, it is the only study in which MSN-based nanoparticles were shown to cross the BBB in mammals. We also note that the design of this particle was very similar to ours, with sub-100 nm particles with a mesoporous silica coating to which PEG chains were anchored via a mediating polyamine layer, further emphasizing that the copolymer layer may be feasible for BBB crossing.

Assuming that the uptake study results do indicate more efficient uptake of coated MSNs compared to pure MSNs, this would be consistent with conclusions made by other authors in studies on cationic MSNs or many other types of nanoparticles. The size of the MSNs we used is also favorable to their internalization, and while coating may slightly increase the size of an individual particle, it reduces particle aggregation. We can assume that the PEG-PEI copolymer used for coating MSNs improved nanoparticle internalization mostly due the PEI component conferring positive charge, as PEG has not been shown to significantly improve nanoparticle uptake in vitro, unlike *in vivo* scenarios where it is used for screening nanoparticles from the reticuloendothelial systems, thus increasing their availability.

It should be noted that surface plasmon resonance measurements have not, to our best knowledge, yet been used for real-time monitoring nanoparticle uptake in cells. Thus, it is a novel method of monitoring endocytosis of nanoparticles and, therefore, as no comparative literature exists, the interpretation of the SPR results is best supported by alternative techniques such as flow cytometry or permeability studies. The large difference between the SPR responses for the spherical MSNs at 300 min suggests a higher uptake of the copolymer-coated particles compared to the uncoated particles, which is consistent with the flow cytometry results. The difference in the cell uptake kinetics of the uncoated and copolymer-coated spherical MSNs seen in the SPR responses could indicate that the different nanoparticles are taken up by the cells through different endocytotic mechanisms or have different intracellular trafficking routes. For example, the lower and slower increase in the SPR signal in the case of uncoated MSNs could indicate that more of these nanoparticles end up in transcytotic vesicles and recycling endosomes compared to copolymer coated spherical MSNs, whereas the copolymer-coated spherical MSNs with their 'proton trap' ability originating from PEI mainly end up in the lysosomes or multivesicular bodies and remain in the cells. This scenario is supported by the permeability studies which shows that the uncoated spherical MSNs has a higher P_{app} value compared to the polymer coated spherical MSNs. Similar interpretation can be suggested for the rod -shaped MSNs. Even though the P_{app} values are in the same order of magnitude and the absolute SPR response levels out at similar values for both rod-shaped MSNs, the cell uptake kinetics, reflected in the shape of the SPR curve, is clearly different between the uncoated and copolymer coated rod-shaped MSNs. According to the flow cytometry studies there is a clearly larger cell uptake of copolymer coated rod-shaped MSNs compared to uncoated rod-shaped MSNs. Thus, the SPR responses for the rod-shaped MSNs should be interpreted so that the cell uptake of the nanoparticles is reflected in the difference between the minimum and maximum responses during cell stimulation with the rod-shaped MSNs. Using this kind of interpretation of the SPR kinetics curve clearly shows that the copolymer coated rod-shaped MSNs are more readily taken up by the cells compared to the uncoated rod-shaped MSNs. Hence, this in combination with similar P_{app} values would mean that the copolymer coated rod-shaped MSNs with their 'proton trap' ability originating from PEI remain in the cell in lysosomes and multivesicular bodies to a larger extent compared to the uncoated rod-shaped MSNs. All in all, according to our interpretation, the SPR data indicates more robust uptake of the rod-shaped MSNs, especially if we compare the uncoated forms. Furthermore, the copolymer-coating clearly enhanced the uptake readily in both (spherical and rod-shaped) cases.

Overall, the results of our study show that MSNs coated with the PEG-PEI copolymers are taken up by RBE4 and MDCK II more efficiently than pure uncoated MSNs. The transport of MSN NPs across cell monolayers with high barrier properties, however, is low. In vivo, the particles were readily detected within minutes after i.v. injection in the brain vasculature, but did not cross into the brain parenchyma. This shows that our MSNs can potentially deliver their cargo across the luminal side of the blood-brain barrier, thus overcoming the first crucial challenge of brain delivery, although its subsequent distribution beyond the abluminal side will not be aided by the nanoparticles. In our in vivo study, MSN NPs did not cause any detectable damage to the BBB. This observation correlated well with the cytotoxicity studies, where no cytotoxicity was observed for any of the chosen particle designs, further stressing the applicability of the particles as a solid platform for the further design of suitable drug delivery carriers. Finally, we conclude that no MSNs we studied exhibited any substantial toxic effect, and that the robust cellular uptake of PEG-PEI copolymer-coated MSNs show that these particles may have potential in drug delivery across selectively permeable cell monolayers such as those comprising the BBB.

Conclusions

In this study, MSNs of different morphology and surface characteristics were investigated for their potential use as drug carriers to the brain. Spherical and rod-shaped particles with the smallest dimension in the sub-100 nm range were synthesized and coated or not with PEG-PEI copolymers to facilitate permeability and uptake by cells used as a BBB model. Uptake studies indicated more efficient and robust uptake of copolymer-coated particles compared to uncoated particles. All four particle designs were safe towards the cells at the investigated concentrations, and permeability studies using an *in vitro* BBB model indicated generally low transport rates of nanoparticles across the cell layer. Microscopy evaluation confirmed the intracellular presence of copolymer-coated particles of both shapes in the cellular monolayer. Two-photon *in vivo* microscopy was applied to visualize the particles in the brain vasculature, confirming excellent *in vivo* detectability of the MSNs using multi-photon techniques. No damage to the BBB was caused by the circulating particles, further stressing the safety aspect. Thus, our study should serve as a basis for developing particles with optimized desired properties.

Materials and Methods

Mesoporous silica nanoparticles

Both spherical and rod shaped MSNs were synthesized according to the protocol described in reference [14], with slight modifications in order to provide higher aspect ratio for particle morphology, as well as to incorporate the fluorescent label (FITC) into the silica framework.

The chemicals used in the preparation of spherical and rod-shaped MSNs were purchased from Sigma-Aldrich. For spherical MSN synthesis, tetraethyl orthosilicate (TEOS) was employed as silica source and cetyltrimethylammonium bromide (CTAB) was utilized as pore structure directing agent (SDA) in the presence of ethylene glycol(EG),and the synthesis was performed under basic conditions. The aspect ratio of MSNs was altered by absence of ethylene glycol, slightly decreased (~5 w%) CTAB amount and elevated reaction temperature as compared to the original referred protocol. Briefly, the synthesis solution for spherical MSNs consisted of the following molar ratios: 1 CTAB/28.7 NH_3 /3091 H_2O/166EG/2.22TEOS, whereas for rod-shaped MSNs the molar ratio was: 1 CTAB/30.7 NH_3 /3278H_2O/2.37 TEOS. For the spherical MSN synthesis, the solution was kept under vigorous stirring for 2 hours at 323 K in 250 ml Erlenmeyer flask and subsequently, transferred to static conditions at 323 K overnight. For the rod-shaped MSN synthesis, the stirring and static condition temperature was elevated to333Kfor the same protocol. In order to remove the SDA, the resulting synthesis solution was centrifuged, the product was collected, extracted three times in ethanolic NH_4NO_3 solution and washed with ethanol. In both syntheses, in order to incorporate the fluorescent tag, fluorescein isothiocyanate (FITC)-modified aminopropyltriethoxysilanesilane APTES was mixed with the silica source before adding to the reaction solution, to provide co-condensed functionalization of FITC within the silica framework. The modification of APTES was carried out by pre-reacting FITC with APTES in 2.5 mL ethanol with a molar ratio of 2:3 and stirring for 2 h under inert atmosphere. The molar ratio between APTES and tetraethyl orthosilicate (TEOS) was kept as 1:100. The thus preserved negative surface charge was subsequently utilized for further electrostatic adsorption of PEG-PEI copolymer to the extracted MSNs.

After particle synthesis was completed, the coating was carried out for particle surface modification. The coating was proceeded by electrostatic adsorption of PEG-PEI copolymers on the particles surface in buffer solution at pH7.2 (25mM HEPES) and room temperature overnight. After the coating was completed, MSNs were centrifuged and washed carefully in order to get rid of any excess non-adsorbed copolymers in the bulk solution.

All in all the following types of spherical (S) and rod-shaped (R) MSNs were obtained, as also illustrated in Fig 1: unmodified (pure) MSNs (US-MSN and UR-MSN) and MSNs coated with a PEG-PEI copolymer (CS-MSN and CR-MSN).

The coated PEG-PEI copolymer amount on both CS-MSN and CR-MSN was calculated with the help of TGA. All the prepared MSNs were dispersed in HEPES buffer solution at pH7.2 for further investigations.

Nanoparticle characterization

The hydrodynamic size of pristine and modified MSNs were determined by dispersing the particles in HEPES buffer solution (25 mM, pH7.2) with the concentration of 1 mg/mL and subsequent DLS measurements (Malvern ZetaSizer NanoZS, Malvern Instruments Ltd, Worcestershire, UK). The change in the ζ-potential potential values of MSNs after modification was also investigated by measurements with the same instrument in the HEPES buffer solution. A further confirmation of surface modification with PEG-PEI copolymer coating on MSNs was carried out by TGA (Netzsch STA 449F1 Jupiter, NETZSCH-Gerätebau GmbH, Germany). The TG resolution of the instrument is 0.025μg and the measurements were done under air atmosphere and in alumina crucibles, at the scanning rate of 10K/min. During the measurements, thermograms were recorded within the range of 30-850oC and the results were analyzed with the help of software Proteus 5.

The aspect ratio and the size of pristine MSNs were further investigated by scanning electron microscopy (SEM) performed with a Leo 1550 Gemini scanning electron microscope (LEO Electron Microscopy Inc., USA) operated at 3kV.The mesostructure of MSNs were investigated by transmission electron microscope (FEI Technai 12 Bio-Twin, 120 kV, FEI Company, Eindhoven, NL). TEM samples were prepared by dispersing the MSNs in ethanol, depositing them on a holey carbon coated grids and leaving them overnight drying.

Cell culture

MDCK II (a kind gift from Prof. Yliperttula, University of Helsinki) were grown in Dulbecco's modified Eagle's medium (DMEM) (Sigma) supplemented as necessary to contain 10% fetal bovine serum (Thermo Scientific), 1% penicillin, 1% streptomycin (both from Sigma), 25 mM HEPES and 4 mM L-glutamine (both from Thermo Scientific). The growth conditions were as follows: 37°C, 95% relative humidity, 5% $CO_{2.}$ For transport studies, the cells (passage 21–22) were seeded at a density of $4.2x10^5/cm^2$ onto Millicell® permeable supports with 1.1 cm diameter and 1.0 μm pore size, with the pore size chosen so as to allow nanoparticle permeation; the upper and lower compartments of the permeable supports contained 0.4 ml and 1.2 ml of medium, respectively. The cells were grown for 6 days with daily medium change. For uptake and cytotoxicity studies, the cells were seeded at the same density onto 12-well and 96-well cell culture plates, respectively, and grown as described above. For SPR experiments, MDCK II cells were seeded on gold-coated coverslips and grown to confluence in the medium and under the conditions described above.

RBE4 cells (a kind gift from Prof. Ashner, Vanderbilt University) were grown on rat tail type I collagen (Millipore) in a mixture of F10 and Minimum Essential Medium (1:1) (Sigma) supplemented with 1 ng/ml bFGF, 300 μg/ml G415 and 25 um HEPES (all from Thermo Scientific). The growth conditions the same as in the case of MDCK II cells. For uptake studies, RBE4 cells were seeded in 12-well plates and 8-well Ibidi dishes for flow cytometry and confocal microscopy, respectively, and grown for 7 days with medium changed every other day. For cytotoxicity studies, RBE4 we seeded on 96-well plates and grown for 7 days as described above.

Transport studies

On day 7 following seeding, MDCK II cells were washed twice in prewarmed phosphate-buffered saline (PBS) (Sigma) and incubated at room temperature for 25 minutes in medium without phenol red supplemented in the manner described above, with the exclusion of serum. The medium without serum and phenol red is referred below to as the transport medium. Monolayer resistance was measured with EVOM-2 (World Precision Instruments) using STX-2 electrodes sterilized by quick immersion into alcohol and equilibrated for 25 minutes at room temperature in the transport medium. Measurements were taken in triplicate, and the average of three readings was calculated. Transepithelial resistance (TER) was calculated as follows:

$$TER = (TERm - TERb)xA$$

where TER is the monolayer resistance, TERm–the average of three readings for permeable supports with cells, TERb—the average of three readings for blank permeable supports, and A–the membrane surface area (1.13 cm^2).

Following that, permeable inserts with monolayers were transferred to new receiver plates and incubated with various MSNs at a concentration of 50 μg/ml or 20μg/ml in 0.4 ml of the transport medium. Lucifer Yellow (LY) (Sigma) was added to permeable supports in 0.4 ml of the transport medium at a concentration of 250 μM with and without 3 mM ethylene glycol tetraacetic acid (EGTA) (Sigma), in order to verify monolayer integrity and the presence of functional tight junctions, respectively (EGTA is a Ca^{2+} chelator that disrupts tight junctions). LY with or without EGTA was not co-incubated with MSNs but rather added to separate permeable supports. The number of permeable supports containing each type of MSNs, as well as LY with or without EGTA was 3 (n = 3). At time points 12, 24 and 36 hours, permeable supports were transferred to new receiver plates containing 1.2 ml of the transport medium (for samples with EGTA it additionally contained 3mM EGTA, i.e. cells were incubated in the continued presence of 3mM EGTA) and transferred back to the incubator, while the old receiver plates were stored at 4°C. At the end of the transport study, permeable supports were once again transferred to new receiver plates containing 1.2 ml of the transport medium, and TER was measured as described above. Samples were then mixed with 10M NaOH in the proportion of 1:10, i.e. to the final NaOH concentration of 1M, and left overnight on a rocker to dissolve the silica core and improve the detection limit by releasing FITC into a basic environment. Fluorescence measurements were taken using a Varioskan Flash multimode reader (Thermo Scientific) and the following excitation and emission wavelengths: 490/520 nm and 425/538 nm for MSNs and LY, respectively. Calibration solutions were prepared using the solutions initially added to permeable supports, and their fluorescence was measured simultaneously with that of the samples. Apparent permeability coefficients were calculated for each time point according to the equation suggested in [42], modified as follows:

$$Papp = \frac{V}{C_0 \cdot A} \cdot \frac{C}{\Delta t}$$

Where V is the basolateral compartment volume, C_0 –donor concentration, A–membrane surface area, C–concentration of the compound in the basolateral compartment, and Δt–time period. For the second and third time points C_0 values were corrected to account for concentration changes in the apical compartment during the transport study.

Flow cytometry

MDCKand RBE4 cells were washed twice in serum-free medium and incubated with the MSNs at concentrations of 20 μg/ml in 1 ml of serum-free mediumfor 24 hours under the conditions described above; cells not incubated with MSNs were used as controls. The number of wells containing cells incubated with each type of MSNs, as well as control cells was 3 (n = 3). After

24 hours, the cells were washed in PBS and harvested by adding 0.25% Trypsin in 1 mM ethylenediaminetetraacetic acid (EDTA) (both from Thermo Scientific). Trypsin was neutralized by serum-supplemented medium, after which the cells were centrifuged 3 times with PBS washing in-between. Extracellular nanoparticle fluorescence was quenched by incubation with Trypan Blue at a concentration of 200 μg/ml in PBS for 7 minutes. Finally, cells in PBS were taken to the flow cytometer (Beckman Coulter) for data acquisition.

Light microscopy

For assessing MSN uptake, RBE4 cells grown on Ibidi dishes were incubated with MSNs in serum-free medium at 20 μg/ml for 24 hours, washed in PBS, fixed, incubated with Trypan blue (Sigma) at a concentration of 200 μg/ml in PBS for 7 minutes for quenching extracellular fluorescence, and mounted with SlowFade mounting medium (Thermo Scientific). Cells were visualized using a Leica SP8 confocal microscope (Leica Microsystems).

For visual evaluation of nanoparticle toxicity in transport experiments, MDCK II cells on the permeable supports from transport studies (after the final TER measurement) were washed twice in prewarmed PBS, incubated with Trypan Blue at a concentration of 200 μg/ml in PBS for 7 minutes and then washed twice in PBS. The membranes were then removed and the cells observed using a Leica DM2500 B light microscope (Leica Microsystems).

Surface plasmon resonance measurement

Surface plasmon resonance measurements were performed with an MP-SPR 200 instrument (Bionavis, Ylöjärvi, Finland). Gold-coated SPR sensor surfaces were obtained from the MP-SPR 200 instrument manufacturer (Bionavis, Ylöjärvi, Finland). Prior to the SPR measurement, MDCK II cells were seeded on gold-coated SPR sensor surfaces and allowed to form a confluent monolayer. For the measurement, the SPR sensors with cell monolayers were inserted into the MP-SPR 200 instrument and exposed to a serum-free medium containing MSNs at 20 μg/ml. The SPR response was monitored for 175–300 minutes at room temperature.

In vivo imaging experiments

All experiments on animals were performed with accordance to local guidance for animal care (The Finnish Act on Animal Experimentation (62/2006)). Animal license (ESAVI/2857/04.10.03/2012) from local authority (ELÄINKOELAUTAKUNTA-ELLA) was obtained and included all procedures used in in vivo imaging part of this study.

One female two-month old mouse was used for in vivo experiment. The mouse was ordered from Harlan—commercial supplier of laboratory animals. It was kept in individual cage in the certified animal facility and provided with food and water ad libitum. 12h light/12h dark cycle was applied.

For imaging of nanoparticles in the brain vasculature, a 5 mm cranial window was implanted in a C57BL/6 mouse. During preparation to surgery a subcutaneous injection of 0.1% lidocaine was used to reduce local pain at the incision site. Mouse was anaesthetized (i.p.) with mixture of ketamine (80 mg/kg) and xylazine (10 mg/kg). Ketamine/xylazine mixture was re-administered every hour if necessary at half-the-original dose. Body temperature was maintained using a heating pad. For cranial window formation, a ~3×3 mm round craniotomy was performed over the somatosensory cortex. Cranial bone was carefully removed, while dura mater remained intact. The brain was then covered with sterile cortical buffer (125 mM NaCl, 5 mM KCl, 10 mM glucose, 10 mM HEPES, 2 mM CaCl2 and 2 mM MgSO4 in distilled H2O), and a 5 mm diameter No. 1.5 glass coverslip (Electron Microscopy Sciences, USA) was placed over the window and sealed using dental cement.

Animal was imaged immediately after window preparation with the FV1000MPE two-photon microscope (Olympus, Japan) using the 25X water immersion high NA objective specially designed for in vivo two-photon imaging. Stacks of images were collected with vertical step of 3 μm (total depth of stack 120 μm). Imaging fields covered 500 × 500 μm2 of cortical space in XY coordinates. MSNs were injected i.v. into the tail vein of a mouse. Imaging was repeated 48 hours after the first imaging session. After the imaging, the mouse was sacrificed by CO2 inhalation.

Cytotoxicity studies

Cells were washed twice in serum-free medium and incubated with various MSNs at concentrations of 100, 50, 20 and 10 μg/ml in serum-free medium for 36 hours under the conditions described above. Untreated cells were used as the negative control. Cells treated with 0.1% Triton X were used as the positive control. The number of wells containing cells incubated with each type of MSNs was 3 (n = 3). After 36 hours, a cell viability reagent (Alamar Blue from Thermo Scientific) was added to the wells. After an incubation period recommended by the manufacturer for each reagent, measurements were read using a plate reader (Tecan Infinite M200 from Tecan Group Ltd).

Data processing and analysis

Statistical analysis was performed with Student's test using SPSS v17. SPSS v17 was also used to plot data from transport, flow cytometry and cytotoxicity studies, as well as various model validation experiments. Data from flow cytometry studies were plotted on histograms using Kaluza software (Beckman Coulter). Confocal microscopy images were read and prepared for publication using ImageJ image processing software. Data were expressed as M±2xSEM, where M is the mean and SEM is the standard error of the mean. Statistical analysis was only applied to novel results, i.e. those concerning MSN permeability, uptake and cytotoxicity.

Supporting Information

S1 Fig. Lower end of the calibration curves of PEG-PEI-coated spherical MSNs in serum-free medium. Instrument readings denote fluorescence intensity of NP-PEG-PEI solutions made by serial dilution from stock solutions after their ultrasonication for 30 minutes with shaking in-between. A. Untreated PEG-PEI-coated spherical MSNs in serum-free medium. B. PEG-PEI-coated spherical MSNs in 1M NaOH, after overnight rocking on a bench rocker.
(TIF)

S2 Fig. TER measurement in permeable support wells containing MDCK II cells incubated for 36 hours with various types of MSNs at a concentration of 50 μg/ml, as well as 250 μM LY with or without 3 mM EGTA in serum-free medium. Measurements were taken before and after transport studies. The sample size n = 3, and TER measurements were taken in triplicate with subsequent averaging. Data shown as M±2xSEM.
(TIF)

S3 Fig. Transport of LY across MDCK II monolayers on permeable supports. LY applied at a concentration of 250 μM in serum-free medium. MDCK II monolayers were incubated with LY in or without the constant presence of 3 mM EGTA. The sample size n = 3. Data represent LY Papp at 12, corrected for the loss of LY in the upper compartment of permeable supports, and is shown as M±2xSEM.
(TIF)

S4 Fig. SPR signal response showing the addition of DMSO.
(TIF)

S1 File. Supporting information file. This file contains additional information on the experimental procedures, mostly related to model validation and improvement.
(DOCX)

S1 Video. Uptake of coated spherical MSNs by MDCK II cells. Live-cell imaging. The cells were pre-incubated with Cellmask Deep Red Plasma Membrane Stain for 5 minutes in cell culture medium, and then incubated with coated spherical MSNs at 20 μg/ml in live cell imaging medium for 1 hour while being imaged.
(AVI)

Acknowledgments

Dr. Diana Toivola and the research team of the Laboratory of Epithelial Biology at Åbo Akademi University kindly provided some reagents and supplies used in our studies and shared suggestions regarding bright field microscopy.

The research team of the Heat Shock Stress group at Turku Centre for Biotechnology kindly provided some reagents used in our studies.

Ms. Helena Saarento at Åbo Akademi University and Turku Centre for Biotechnology kindly provided technical assistance with cell culturing.

Mr. Perttu Terho at Turku Centre for Biotechnology kindly provided advice regarding fluorescence-activated cell sorting.

Mr. Jouko Sandholm at Turku Centre for Biotechnology and Mr. Jari Korhonen at Åbo Akademi University kindly provided advice regarding confocal microscopy.

Dr. Adyary Fallarero at Åbo Akademi University kindly provided advice regarding fluorescence measurement.

Mr. Thomas Bymark at Åbo Akademi University kindly provided technical assistance with the use of some experimental equipment.

Author Contributions

Conceived and designed the experiments: HB DSK TV LK CS JR VM YRL.

Performed the experiments: HB DSK AD TV EP.

Analyzed the data: HB DSK TV EP.

Contributed reagents/materials/analysis tools: TV LK CD CS JR.

Wrote the paper: HB DSK TV JL CD CS JR.

References

1. Abbott NJ, Patabendige AA, Dolman DE, Yusof SR, Begley DJ. Structure and function of the blood-brain barrier. Neurobiology of disease. 2010; 37(1):13–25. Epub 2009/08/12. doi: 10.1016/j.nbd.2009.07.030 PMID: 19664713.
2. Gratton SE, Ropp PA, Pohlhaus PD, Luft JC, Madden VJ, Napier ME, et al. The effect of particle design on cellular internalization pathways. Proceedings of the National Academy of Sciences of the United States of America. 2008; 105(33):11613–8. doi: 10.1073/pnas.0801763105 PMID: 18697944; PubMed Central PMCID: PMC2575324.
3. Huang X, Teng X, Chen D, Tang F, He J. The effect of the shape of mesoporous silica nanoparticles on cellular uptake and cell function. Biomaterials. 2010; 31(3):438–48. doi: 10.1016/j.biomaterials.2009.09.060 PMID: 19800115.

4. Pardridge WM. Why is the global CNS pharmaceutical market so under-penetrated? Drug Discov Today. 2002; 7(1):5–7. Epub 2002/01/16. PMID: 11790589.
5. Wong HL, Wu XY, Bendayan R. Nanotechnological advances for the delivery of CNS therapeutics. Advanced drug delivery reviews. 2012; 64(7):686–700. doi: 10.1016/j.addr.2011.10.007 PMID: 22100125
6. Veiseh O, Sun C, Gunn J, Kohler N, Gabikian P, Lee D, et al. Optical and MRI multifunctional nanoprobe for targeting gliomas. Nano letters. 2005; 5(6):1003–8. doi: 10.1021/nl0502569 PMID: 15943433.
7. Jain KK. Nanobiotechnology-based strategies for crossing the blood-brain barrier. Nanomedicine (Lond). 2012; 7(8):1225–33. doi: 10.2217/nnm.12.86 PMID: 22931448.
8. Rosenholm JM, Sahlgren C, Linden M. Multifunctional mesoporous silica nanoparticles for combined therapeutic, diagnostic and targeted action in cancer treatment. Current drug targets. 2011; 12 (8):1166–86. Epub 2011/03/30. PMID: 21443474.
9. Wang Y, Zhao Q, Han N, Bai L, Li J, Liu J, et al. Mesoporous silica nanoparticles in drug delivery and biomedical applications. Nanomedicine: nanotechnology, biology, and medicine. 2015; 11(2):313–27. doi: 10.1016/j.nano.2014.09.014 PMID: 25461284.
10. Chen Y, Chen H, Shi J. Drug delivery/imaging multifunctionality of mesoporous silica-based composite nanostructures. Expert opinion on drug delivery. 2014; 11(6):917–30. doi: 10.1517/17425247.2014.908181 PMID: 24746014.
11. Wu S-H, Hung Y, Mou C-Y. Mesoporous silica nanoparticles as nanocarriers. Chemical Communications. 2011; 47(36):9972–85. doi: 10.1039/c1cc11760b PMID: 21716992
12. He Q, Zhang Z, Gao Y, Shi J, Li Y. Intracellular Localization and Cytotoxicity of Spherical Mesoporous Silica Nano- and Microparticles. Small. 2009; 5(23):2722–9. doi: 10.1002/smll.200900923 PMID: 19780070
13. Xia T, Kovochich M, Liong M, Meng H, Kabehie S, George S, et al. Polyethyleneimine Coating Enhances the Cellular Uptake of Mesoporous Silica Nanoparticles and Allows Safe Delivery of siRNA and DNA Constructs. ACS nano. 2009; 3(10):3273–86. doi: 10.1021/nn900918w PMID: 19739605
14. Gu J, Fan W, Shimojima A, Okubo T. Organic-inorganic mesoporous nanocarriers integrated with biogenic ligands. Small. 2007; 3(10):1740–4. Epub 2007/09/06. doi: 10.1002/smll.200700311 PMID: 17786917.
15. Meng H, Yang S, Li Z, Xia T, Chen J, Ji Z, et al. Aspect Ratio Determines the Quantity of Mesoporous Silica Nanoparticle Uptake by a Small GTPase-Dependent Macropinocytosis Mechanism. ACS nano. 2011; 5(6):4434–47. doi: 10.1021/nn103344k PMID: 21563770
16. Karaman DS, Desai D, Senthilkumar R, Johansson EM, Ratts N, Oden M, et al. Shape engineering vs organic modification of inorganic nanoparticles as a tool for enhancing cellular internalization. Nanoscale research letters. 2012; 7(1):358. doi: 10.1186/1556-276X-7-358 PMID: 22747910; PubMed Central PMCID: PMC3519764.
17. Sen Karaman D, Gulin-Sarfraz T, Hedstrom G, Duchanoy A, Eklund P, Rosenholm JM. Rational evaluation of the utilization of PEG-PEI copolymers for the facilitation of silica nanoparticulate systems in biomedical applications. Journal of colloid and interface science. 2014; 418:300–10. doi: 10.1016/j.jcis.2013.11.080 PMID: 24461849.
18. Desai D, Karaman DS, Prabhakar N, Tadayon S, Duchanoy A, Toivola DM, et al. Design considerations for mesoporous silica nanoparticulate systems in facilitating biomedical applications. Mesoporous Biomaterials. 2014; 1(1):28.
19. Viitala T, Granqvist N, Hallila S, Ravina M, Yliperttula M. Elucidating the signal responses of multi-parametric surface plasmon resonance living cell sensing: a comparison between optical modeling and drug-MDCKII cell interaction measurements. PloS one. 2013; 8(8):e72192. doi: 10.1371/journal.pone.0072192 PMID: 24015218; PubMed Central PMCID: PMC3754984.
20. Yashunsky V, Lirtsman V, Golosovsky M, Davidov D, Aroeti B. Real-time monitoring of epithelial cell-cell and cell-substrate interactions by infrared surface plasmon spectroscopy. Biophysical journal. 2010; 99(12):4028–36. doi: 10.1016/j.bpj.2010.10.017 PMID: 21156146; PubMed Central PMCID: PMC3000480.
21. Chabot V, Cuerrier CM, Escher E, Aimez V, Grandbois M, Charette PG. Biosensing based on surface plasmon resonance and living cells. Biosensors & bioelectronics. 2009; 24(6):1667–73. doi: 10.1016/j.bios.2008.08.025 PMID: 18845432.
22. Fazlollahi F, Angelow S, Yacobi NR, Marchelletta R, Yu AS, Hamm-Alvarez SF, et al. Polystyrene nanoparticle trafficking across MDCK-II. Nanomedicine: nanotechnology, biology, and medicine. 2011; 7(5):588–94. Epub 2011/02/12. doi: 10.1016/j.nano.2011.01.008 PMID: 21310266; PubMed Central PMCID: PMC3130091.

23. Schulze C, Schaefer UF, Voetz M, Wohlleben W, Venzago C, Lehr C-M. Transport of metal oxide nanoparticles across Calu-3 cell monolayers modelling the air-blood barrier. EURO-NanoTox Letters. 2011; (001:):1–11.

24. Limnell T. Mesoporous silica- and silicon-based materials as carriers for poorly water soluble drugs: University of Helsinki; 2011.

25. Harush-Frenkel O, Rozentur E, Benita S, Altschuler Y. Surface Charge of Nanoparticles Determines Their Endocytic and Transcytotic Pathway in Polarized MDCK Cells. Biomacromolecules. 2008; 9 (2):435–43. doi: 10.1021/bm700535p PMID: 18189360

26. Panyam J, Labhasetwar V. Dynamics of Endocytosis and Exocytosis of Poly(D,L-lactide-co-glycolide)) Nanoparticles in Vascular Smooth Muscle Cells. Pharmaceutical research. 2003; 20(2):212–20. doi: 10.1023/a:1022219003551 PMID: 12636159

27. Jin H, Heller DA, Strano MS. Single-Particle Tracking of Endocytosis and Exocytosis of Single-Walled Carbon Nanotubes in NIH-3T3 Cells. Nano letters. 2008; 8(6):1577–85. doi: 10.1021/nl072969s PMID: 18491944

28. Jiang X, cker C, Hafner M, Brandholt S, Doörlich RM, Nienhaus GU. Endo- and Exocytosis of Zwitterionic Quantum Dot Nanoparticles by Live HeLa Cells. ACS nano. 2010; 4(11):6787–97. doi: 10.1021/nn101277w PMID: 21028844

29. Chithrani BD, Chan WC. Elucidating the mechanism of cellular uptake and removal of protein-coated gold nanoparticles of different sizes and shapes. Nano letters. 2007; 7(6):1542–50. Epub 2007/05/01. doi: 10.1021/nl070363y PMID: 17465586.

30. Salvati A, Åberg C, dos Santos T, Varela J, Pinto P, Lynch I, et al. Experimental and theoretical comparison of intracellular import of polymeric nanoparticles and small molecules: toward models of uptake kinetics. Nanomedicine: Nanotechnology, Biology and Medicine. 2011; 7(6):818–26. doi: 10.1016/j.nano.2011.03.005

31. Koch AM, Reynolds F, Merkle HP, Weissleder R, Josephson L. Transport of surface-modified nanoparticles through cell monolayers. Chembiochem: a European journal of chemical biology. 2005; 6(2):337–45. Epub 2005/01/15. doi: 10.1002/cbic.200400174 PMID: 15651046.

32. Ragnaill MN, Brown M, Ye D, Bramini M, Callanan S, Lynch I, et al. Internal benchmarking of a human blood-brain barrier cell model for screening of nanoparticle uptake and transcytosis. European journal of pharmaceutics and biopharmaceutics: official journal of Arbeitsgemeinschaft fur Pharmazeutische Verfahrenstechnik eV. 2011; 77(3):360–7. Epub 2011/01/18. doi: 10.1016/j.ejpb.2010.12.024 PMID: 21236340.

33. Santra S, Yang H, Dutta D, Stanley JT, Holloway PH, Tan W, et al. TAT conjugated, FITC doped silica nanoparticles for bioimaging applications. Chem Commun (Camb). 2004;(24:):2810–1. Epub 2004/12/16. doi: 10.1039/b411916a PMID: 15599418.

34. Hanada S, Fujioka K, Inoue Y, Kanaya F, Manome Y, Yamamoto K. Cell-based in vitro blood-brain barrier model can rapidly evaluate nanoparticles' brain permeability in association with particle size and surface modification. International journal of molecular sciences. 2014; 15(2):1812–25. doi: 10.3390/ijms15021812 PMID: 24469316; PubMed Central PMCID: PMC3958822.

35. Shim KH, Jeong KH, Bae SO, Kang MO, Maeng EH, Choi CS, et al. Assessment of ZnO and SiO2 nanoparticle permeability through and toxicity to the blood-brain barrier using Evans blue and TEM. International journal of nanomedicine. 2014; 9 Suppl 2:225–33. doi: 10.2147/IJN.S58205 PMID: 25565840; PubMed Central PMCID: PMC4279764.

36. Lee CM, Lee TK, Kim DI, Kim YR, Kim MK, Jeong HJ, et al. Optical imaging of absorption and distribution of RITC-SiO2 nanoparticles after oral administration. International journal of nanomedicine. 2014; 9 Suppl 2:243–50. doi: 10.2147/IJN.S57938 PMID: 25565842; PubMed Central PMCID: PMC4279756.

37. Kim JS, Yoon TJ, Yu KN, Kim BG, Park SJ, Kim HW, et al. Toxicity and tissue distribution of magnetic nanoparticles in mice. Toxicological sciences: an official journal of the Society of Toxicology. 2006; 89 (1):338–47. Epub 2005/10/21. doi: 10.1093/toxsci/kfj027 PMID: 16237191.

38. Barandeh F, Nguyen PL, Kumar R, Iacobucci GJ, Kuznicki ML, Kosterman A, et al. Organically modified silica nanoparticles are biocompatible and can be targeted to neurons in vivo. PloS one. 2012; 7(1): e29424. Epub 2012/01/13. doi: 10.1371/journal.pone.0029424 PMID: 22238611; PubMed Central PMCID: PMC3250438.

39. Kumar R, Roy I, Ohulchanskky TY, Vathy LA, Bergey EJ, Sajjad M, et al. In vivo biodistribution and clearance studies using multimodal organically modified silica nanoparticles. ACS nano. 2010; 4 (2):699–708. Epub 2010/01/22. doi: 10.1021/nn901146y PMID: 20088598; PubMed Central PMCID: PMC2827663.

40. Liu D, Lin B, Shao W, Zhu Z, Ji T, Yang C. In vitro and in vivo studies on the transport of PEGylated silica nanoparticles across the blood-brain barrier. ACS applied materials & interfaces. 2014; 6(3):2131–6. doi: 10.1021/am405219u PMID: 24417514.

41. Ku S, Yan F, Wang Y, Sun Y, Yang N, Ye L. The blood-brain barrier penetration and distribution of PEGylated fluorescein-doped magnetic silica nanoparticles in rat brain. Biochemical and biophysical research communications. 2010; 394(4):871–6. Epub 2010/03/09. doi: 10.1016/j.bbrc.2010.03.006 PMID: 20206605.

42. Artursson P, Karlsson J. Correlation between oral drug absorption in humans and apparent drug permeability coefficients in human intestinal epithelial (Caco-2) cells. Biochemical and biophysical research communications. 1991; 175(3):880–5. doi: 10.1016/0006-291x(91)91647-u PMID: 1673839

Paper V

Ultrasound-mediated delivery and distribution of polymeric nanoparticles in the normal brain parenchyma and melanoma metastases

Habib Baghirov[a*], *Sofie Snipstad*[a], *Einar Sulheim*[a,b], *Sigrid Berg*[c,d], *Rune Hansen*[c,d], *Frits Thorsen*[e], *Yrr Mørch*[b], *Catharina de Lange Davies*[a], *Andreas K.O. Åslund* [a]

[a] Department of Physics, The Norwegian University of Science and Technology (NTNU), 7491 Trondheim, Norway
[b] SINTEF Materials and Chemistry, 7465 Trondheim, Norway
[c] SINTEF Medical Technology, 7465 Trondheim, Norway
[d] Department of Circulation and Medical Imaging, 7491 Trondheim, Norway
[e] Molecular Imaging Center and Kristian Gerhard Jebsen Brain Tumour Research Centre, Department of Biomedicine, University of Bergen, 5020 Bergen, Norway

*Tel.: +4773593492. Email: habib.baghirov@ntnu.no

The authors declare no competing financial interest.

Abstract

Treatment of brain cancer is hindered by an intact blood-brain barrier (BBB), preventing most chemotherapeutics from entering the brain. Focused ultrasound (FUS) in combination with microbubbles can open the BBB safely and reversibly, thereby enabling delivery of drugs. Systemic injection of drugs might induce severe toxicity, but encapsulation into nanoparticles (NPs) reduces the accumulation in normal tissue. Here a novel platform based on poly (isohexyl cyanoacrylate) (PIHCA) NPs stabilizing microbubbles was used to permeabilize the BBB in a melanoma brain metastasis model. With an ultrasound platform able to generate FUS at 1.1 MHz and 7.8 MHz, we opened the BBB using a combination of NP-microbubbles and low-frequency FUS and applied high-frequency FUS to generate acoustic radiation force (ARF) in order to push NPs through the extracellular matrix. Using confocal microscopy and image analysis, we quantified NP extravasation and distribution in the brain parenchyma following FUS exposure, and assessed the effect of the ARF. Histological examination was used to assess hemorrhage, as well as the levels of P-glycoprotein (P-gp), an integral component of the BBB, immediately after FUS exposure. We observed BBB transport of NPs into the brain and their distribution in the brain parenchyma and metastases in a manner dependent on the extent of BBB opening. ARF had no significant effect under our experimental conditions. P-gp level was not altered immediately after sonication. Our results indicate that the combination of FUS with the novel PIHCA NP-microbubble platform can be used to achieve a substantial accumulation and displacement of NPs in the brain parenchyma.

Keywords: blood-brain barrier, focused ultrasound, poly(alkyl cyanoacrylate) nanoparticles, cavitation, acoustic radiation force, P-glycoprotein

1. Introduction

Chemotherapeutic treatment of primary brain malignancies as well as metastatic brain tumors has so far shown only minimal effects on tumor growth and patient survival. One of the obstacles hindering successful treatment is the blood-brain barrier (BBB) - a dynamic interface that protects the brain's internal milieu and filters out 98% of small molecular drugs (about 400-500 Da) and all large molecular drugs [1-3]. The passage of drugs across the BBB is blocked both paracellularly, due to tight junctions connecting endothelial cells, and transcellularly, in large part due to the action of multidrug resistance transporters such as P-glycoprotein (P-gp) located in the plasma membrane. One of the challenges in drug delivery across the BBB is accumulation of drugs in therapeutically relevant doses in the brain. This has precluded the advancement of several promising drug candidates to the clinic because, after systemic administration, the doses required to achieve a therapeutic effect were also prohibitively toxic.

Drug-loaded nanoparticles (NPs) have emerged as a powerful tool reducing drug toxicity after systemic administration [4] and providing controlled and sustained release, targeting and functionalization, including the use of microenvironment properties. [5]. In the case of solid tumors, NP-based drug delivery also benefits from the enhanced permeability and retention (EPR) effect whereby NPs are retained in the tumor mass due to its leaky neovasculature and reduced lymphatic drainage [6, 7]. Poly (alkyl cyanoacrylate) NPs (PACA NPs) have been shown to be promising drug carriers due to the ease of their synthesis and functionalization, as well as biodegradability [8, 9]. These properties have recently allowed them to reach a Phase III clinical trial in advanced hepatocellular carcinoma [10]. In the case of brain malignancies, however, NP transport across the BBB is complicated even more than it is with small molecular drugs. Paracellular transport across an intact BBB is virtually impossible [11], and NP size is far above the transcellular transport threshold. Biofunctionalization of NPs with moieties conferring BBB transport properties, as well as the use of EPR in solid tumors does offer benefits, but the efficiency of the former approach is highly dependent on the carrier and the transport moiety, and the use of EPR has so far produced only a modest increase in drug accumulation [12].

Focused ultrasound (FUS) in combination with microbubbles (MBs) that are normally used in diagnostic ultrasonography has been shown to open the BBB safely and reversibly [13-15]. It has been employed to transport NPs across the BBB in several studies [16-19]. The use of MBs in combination with FUS to open the BBB was first demonstrated by Hynynen et al. in 2001 [20] and is based on the expansion and contraction of MBs in the proximity of blood vessels in the ultrasound (US) focus, causing a mechanical stress on the vessel wall. The use of MB considerably reduced the acoustic power required for cavitation-dependent opening of the BBB by FUS alone, thereby enabling safe application of transcranial US. Our group has recently demonstrated FUS-mediated BBB opening using a platform consisting of PACA NPs stabilizing gas-filled MBs [21]. Evaluation of NP efficiency as a platform for brain drug delivery, however, will require a precise assessment of NP transport across the BBB.

Another matter that merits attention is the fate of extravasated NPs. Penetrating the extracellular matrix (ECM) to reach target cells is no trivial task for NPs due to their size [22]. Without efficient penetration of the ECM, however, drug delivery will have to rely on NP degradation or release of drugs in the ECM with subsequent drug diffusion. This renders a number of potential NP benefits inapplicable, such as targeting to or controlled release within target cells. While FUS-induced cavitation of MBs in the proximity of brain endothelium can disrupt the BBB and facilitate NP transport into the brain, it can also push NPs further through the ECM. Acoustic radiation force (ARF) causing transfer of momentum between the US wave and the propagation medium and produced by high frequency FUS can potentially also increase the displacement of NPs in the ECM. The use of ARF has primarily been focused on improved targeting of MBs [23, 24] or improved drug delivery using drug-loaded or drug-decorated MBs [25, 26]. Compared to NPs, MBs are large and highly compressible, and they therefore experience a much larger effect caused by ARF. In a limited number of studies ARF was used for drug delivery with liquid NPs [27, 28].

In this study, we used a novel US system that can generate FUS at two frequencies, with precise selection of the exposure area. 1.1 MHz was used in combination with a poly (isohexyl) cyanoacrylate (PIHCA)-based NP-MB platform to open the BBB and deliver the NPs into the brain parenchyma and to melanoma brain metastases. In addition, 7.8 MHz was employed to induce the effect of the ARF to investigate whether it could push NPs through the ECM away from blood vessels. We also evaluated how FUS at 1.1 MHz affected the expression of P-gp in the brain tissue immediately post-sonication. We verified BBB opening and quantified NP extravasation and distribution in the brain parenchyma in relation to the extent of BBB opening. Our results show the potential of our novel PACA NP-MB platform for FUS-mediated drug delivery across the BBB and through the brain tissue.

2. Materials and methods

2.1. Nanoparticles and microbubbles

PIHCA NPs were synthesized by the miniemulsion polymerization method as described and used previously to make poly-(butyl cyanoacrylate) (PBCA) NPs [29]. In the oil phase, the monomer (IHCA, Henkel Biomed) was mixed with a co-stabilizer (Miglyol 810N, Cremer), the fluorescent dye NR668 (modified Nile red [30], a kind gift from Dr. Klymchenko) and methanesulphonic acid (MSA, Sigma-Aldrich). The water phase contained the PEG-stabilizers Kolliphor HS15 (Sigma-Aldrich) and Brij L23 (Sigma-Aldrich) and 0.1M HCl. The phases were mixed and sonified on ice for 4 minutes using an ultrasonic homogenizer (Branson), and left to polymerize for 1 hour at ambient temperature before adjusting the pH to 5. The polymerization was continued for another 2 hours. Finally, the NPs were dialyzed against 1 mM HCl for 2 days (MWCO 100,000) and centrifuged at 3000 rpm for 15 minutes. Size and ζ-potential were measured in phosphate buffer (pH 7) with dynamic light scattering (DLS, Zetasizer Nano ZS, Malvern).

MBs were made following the procedure described previously ([29], [21]). In brief, NPs were diluted to a concentration of 10 mg/ml in 5 mg/ml casein (Sigma-Aldrich) and 1x phosphate-buffered saline (PBS). The solution was then saturated with perfluoropropane gas (Fluorochem) using an Ultra Turrax (ICA Werke) for 2 minutes to create NP-stabilized MBs with a gas core. Size and concentration of MBs was analyzed using a cell counting chip (for Countess, Thermo Fisher). 8 positions in the chip were imaged using bright field microscopy at 20x magnification, and the size and concentration was calculated using Excel 2010.

2.2. Cells and animals

The H1_DL2 cell line used in this study is based on the H1 cell line isolated from a patient biopsy of human melanoma brain metastasis as described previously [31]. The H1_DL2 cell line was developed by transducing H1 cells with two lentiviral vectors encoding Luciferase and a GFP variant of Dendra [32]. The cells were cultured in Dulbecco’s modified Eagle’s medium supplemented with 10% of fetal bovine serum (Gibco), 4x the prescribed concentration of nonessential amino acids and 2% L-glutamine (Thermo Scientific). The growth medium was exchanged twice a week.

Eleven female NOD/SCID mice (eight weeks of age, 18-22 g of weight) were purchased from Harlan. The mice were housed in individually ventilated cages (Techniplast). In accordance with the recommendations set forth by the Federation of European Laboratory Animal Science Associations, animal housing conditions were free of specific pathogens. The mice were provided with sterile water and food ad libitum. All animal procedures were approved by the Norwegian National Animal Research Authorities.

2.3. Intracardiac injection of tumor cells

Before and during tumor cell inoculation, the animals were anesthetized with 3% isoflurane in oxygen (flow 2 l/min). 5×10^5 of H1_DL2 cells in 0.1 ml PBS were injected into the left cardiac ventricle of the mice using a 30G insulin syringe (Omnican50, B. Braun Melsungen AG). The injection was guided by ultrasonography using a Vevo® 2100 System with an MS200 transducer (FujiFilm Ultrasonics). The procedure of intracardiac injection of tumor cells is shown in Supplementary Video 1. After the intracardiac injection, the mice received a subcutaneous injection of temgesic (Reckitt Benckiser) (0.05 mg/kg) for prolonged analgesia. The metastases were allowed to develop for 28±2 days.

2.4. Magnetic resonance imaging

Magnetic resonance imaging (MRI) was performed using a 7.05 T horizontal bore magnet (Biospec 70/20 Avance III, Bruker Biospin). The mouse was anesthetized as described in Section 2.6 and cannulated in the tail vein with a 24G catheter (BD Neoflon, Becton Dickinson Infusion

Therapy). Temperature and respiration rate were monitored using rectal temperature and pressure-sensitive probes (SA Instruments), respectively. The animal bed was maintained at a temperature of 37 °C. Once the mice were placed in the MR scanner, the coils were tuned and matched, followed by acquisition of a localizer scan. The following MR sequences were used for pre- and post-treatment images: T1-RARE for detecting melanoma brain metastases as described previously [32], and T1 Fast Low Angle Shot (FLASH) for detecting BBB disruption based on the extravasation of a gadolinium-based contrast agent Omniscan (GE Healthcare AS, 0.5 mmol/kg, 1 ml/kg) and for detection of hemorrhages. All MR sequences had the same geometry with FOV of 40 × 27 mm, matrix size (MTX) of 200 × 135, and 12 slices at 1 mm. MRI parameters were set using Bruker Paravision v6.

2.5 Characterization of skull attenuation

The acoustic attenuation through the skull bone was measured at 1.1 MHz and 7.8 MHz on harvested mouse skulls from animals of similar size as the ones used for BBBD experiments. The measurements were conducted as described in [21].

At 1.1 MHz the acoustic pressure was attenuated between 10 and 17 %, and at 7.8 MHz the attenuation was between 70 and 75 %, depending on the angular position of the skull with respect to the incoming wave. By applying 0.38 MPa at 1.1 MHz as focal pressure from the transducer, the in-situ pressure in the brain tissue is expected to be between 0.34 and 0.31 MPa, corresponding to a mean mechanical index (MI) of 0.31. At 7.8 MHz the applied pressure was 5 MPa, which due to non-linear distortions through the water path and attenuation and reflection in the skull resulted in an in-situ positive pressure of 1.25 to 1.5 MPa and negative pressure of 0.75

to 0.9 MPa. The energy delivered in the focal region when 5ms bursts at a pulse repetition frequency (PRF) of 1Hz is used, is estimated to 10 W/cm^2.

2.6 FUS treatments

The mice were divided into three groups. Group 1 (n=6) was used for the assessment of FUS-mediated NP transport across the BBB and their distribution in the brain parenchyma after the application of FUS at 1.1 MHz, as well as for investigating the effect of the ARF after FUS exposure at 7.8 MHz (see Supplementary Figure 1). Group 2 (n=2) was used for histochemistry to detect hemorrhage after sonication. Group 3 (n=3) was used to investigate the immediate effect of FUS-mediated BBB disruption on the levels of P-gp in the brain. Animals in Groups 1 and 2 were sacrificed 2 hours post-sonication while animals in Group 3 were sacrificed immediately post-sonication.

Before FUS treatment, the animals were anesthetized using a subcutaneous injection of a 2:1:2:5 mixture of fentanyl (Actavis Group hf), medetomidine (Orion Pharma), midazolam (Accord Healthcare Limited) and water at a dose of 100 µl per 10 g of body weight. After the heads were shaved, a depilatory cream was applied to remove the remaining hair. The mice were placed in the MR bed, and the bed was placed in the scanner. Three different MRI scans were acquired (T1-RARE without Omniscan, T1-RARE with Omniscan, T1-FLASH with Omniscan). The T1-FLASH sequence was used for treatment planning according to Supplementary Fig. 1a. A grid of 6x2 treatment locations (beam width: 1.6 mm per location) was used to open the BBB in the left hemisphere in all animals, except for one animal in Group 2 where no metastases were visible in the left hemisphere. The contralateral hemisphere was used as control. The animal was placed above the transducer and Omniscan (1 mL/kg), and NP-MBs (5 mL/kg) were injected sequentially. The FUS treatment (1.1 MHz, 5 min, PRF 0.33 Hz, 0.38 MPa, 10 ms burst length) was initiated upon injection of the NP-MBs using a RK-100 system for MRI-guided FUS-mediated BBB disruption (FUS Instruments). After the treatment, the animal was scanned with MRI (T1-FLASH) for verification of BBB opening as well as indications of hemorrhage. The post-treatment T1-FLASH was used for ARF treatment planning and a grid of 2x2 treatment locations (beam width: 0.5 mm per location) was defined in the area where BBB opening had been successful (Supplementary Fig. 1b). ARF treatment was initiated 30 min after BBB opening treatment start (7.8 MHz, 60 min, PRF 1 Hz, 5 MPa, 5 ms burst length). 2 h post anesthetization a new anesthetic dose was injected s.c. at half the initial dose to maintain deep anesthesia. 2 h after BBB opening, animals in Group 1 were injected with DyLight 649-labeled Lycopersicon esculentum (tomato) lectin (Vector Laboratories Inc) (5 mg/kg) to image vasculature. Five minutes later the mice were euthanized by cervical dislocation. The brains were removed, divided according to Supplementary Fig. 1c, embedded in Tissue-Tek™ CRYO-OCT Compound (Sakura), and frozen in a mixture of 2-methylbutane on dry ice. Animals in Group 3 were euthanized by cervical dislocation immediately after the BBBD treatment. The brains were removed without prior injection of Lycopersicon esculentum (tomato) lectin and frozen as described above. Brains in Group 1 were sectioned as described in Supplementary Fig. 1c, and brains in Group 3 were sectioned axially; in both groups, the brains were cut into 4 and 20 µm cryosections. Animals in Group 2 were euthanized by i.v. injection of pentobarbital (100 mg/kg) followed by intracardiac perfusion with PBS and 4% paraformaldehyde. The brains were removed and submerged in 10 % formalin for at least 24 h before paraffin embedding and sectioning into 4 µm sections for hematoxylin and eosin (H&E) staining. Frozen sections in Group 2 were stained using an anti-P glycoprotein antibody (EPR10364-57, Abcam).

2.7. Confocal laser scanning microscopy

For quantification of NR668-containing PIHCA NPs in the brain tissue and assessment of the ARF effect, cryosections were thawed for approx. 10 min and tile scans of entire brain sections were obtained using a Leica TCS SP8 confocal laser-scanning microscope (Leica Microsystems) without mounting. Tile scans were acquired using 10x/0.45 and 20x/0.75 air objectives. For images taken with the 10x/0.45 objective, the following parameters were used: image size: 1024x1024 pixels, zoom factor: 1.5, pixel size: 758 nm. For images taken with the 20x/0.75 objective, the following parameters were used: image size: 1280x1280 pixels, zoom factor – 1.5, pixel size: 454 nm. A white light laser was used to excite NR668 (excitation wavelength – 535 nm, emission wavelength range - 560-630 nm) and DyLight 649 (excitation - 649 nm, emission wavelength range: 660-710 nm). In order to visualize melanoma brain metastases with tightly packed nuclei, some sections were mounted with Vectashield mounting medium (Vectorlabs) containing 4',6-diamidino-2-phenylindole (DAPI) as a nuclei counterstain. DAPI was excited using a 405 nm laser with a detection of 416–468 nm. H&E-stained sections were imaged using an LSM 800 (Zeiss) confocal laser scanning microscope.

2.8 Image analysis

MR images were processed using Sante DICOM Viewer v. 5.04 and ImageJ 1.49k. Processing and analysis of confocal laser scanning microscope (CLSM) images were performed, depending on the required task, by ImageJ 1.49k [33], Icy v.1.8.6.0 [34] or CellProfiler 2.1.1. [35]. ImageJ and CellProfiler were collectively used for image conversion, image stitching, calculation of intensity ratios in MR images, background removal, filtering, thresholding, quantification of NP count and quantification of NP displacement, Icy - for k-means thresholding and distance transform used in algorithm validation and comparison of different thresholding strategies. A more detailed description of image analysis is provided in Supplementary Document 1.

For the quantification of the ARF effect, NP displacement from blood vessels was analyzed in those parts of brain sections that corresponded to the hemisphere exposed to FUS at 1.1 MHz and 7.8 MHz. The area of ARF exposure was estimated using T1 Flash MR images as shown in Supplementary Fig. 1d, and the corresponding brain sections were selected appropriately to cover and slightly extend beyond this area. Control sections corresponded to areas located at a considerable distance from the estimated ARF exposure area (approx. 3 mm) and only exposed to FUS at 1.1 MHz.

The extent of BBB opening in T1 FLASH MR images was assessed by determining the ratio of intensities in the treated and untreated brain hemispheres.

2.9. Data analysis

Data were analyzed using MS Excel 2010 and SPSS v17. In addition to the filters built in the image analysis algorithm, filters were applied in data analysis software to eliminate situations with unacceptable image or staining quality. Those are described in Supplementary Document 1.

3. Results

3.1. Characterization of the PIHCA NP-MB platform

The synthesized PIHCA NPs were analyzed with DLS and had mean size by number of 118nm, Z-average of 274 nm and polydispersity index of 0.25 while the ζ-potential was 0. The

MBs had a mean size of 1.6±0.85 µm and a concentration of 6.5E8 MBs/ml, but could vary slightly from day to day as new batches were produced.

3.2 Development of melanoma brain metastases

Melanoma brain metastases were detected using T1-weighted MRI at 28±2 days after intracardiac injection of tumor cells. Tumors were visible in MRI images (Fig. 1a). Metastatic tumors were also visible in CLSM images of cryosections and in the histological examination of formalin-fixed paraffin-embedded sections, in line with the results reported in [32] (Figs. 1 b-d). In the CLSM images and H&E-stained sections, the metastases appeared at higher cell density and with larger nuclei than normal brain cells. We did not evaluate leakiness of the metastases; however, an earlier study has shown that the percentage of leaky tumors at week 4 was around 1% [32].

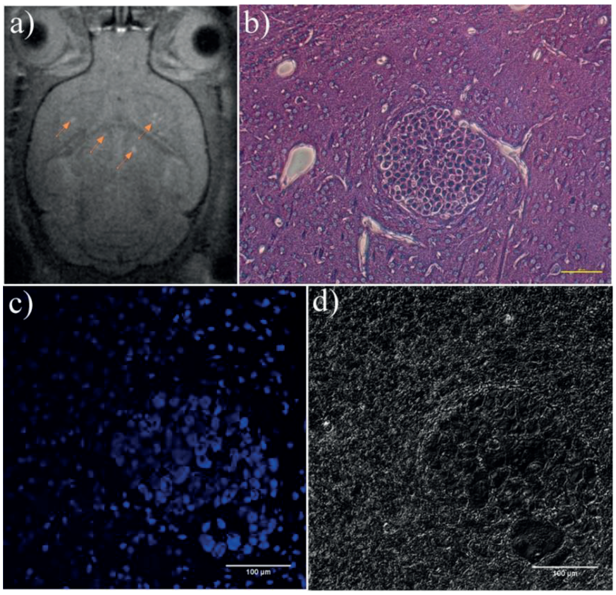

Fig. 1. Development of melanoma brain metastases 4 weeks after tumor cell inoculation. Metastatic tumors are visible in a) T1 RARE MR images without contrast enhancement, b) H&E-stained sections, as a spherical group of cells, c) CSLM with nuclei counterstaining, as a clump of tightly packed nuclei, d) in differential interference contrast, as a dark cluster of cells.

3.3 FUS-mediated BBB opening

FUS-mediated BBB disruption was observed in all animals in Group 1, but its extent, as assessed using signal intensity in T1 FLASH mages, varied depending on the animal (Fig 2 a-c).

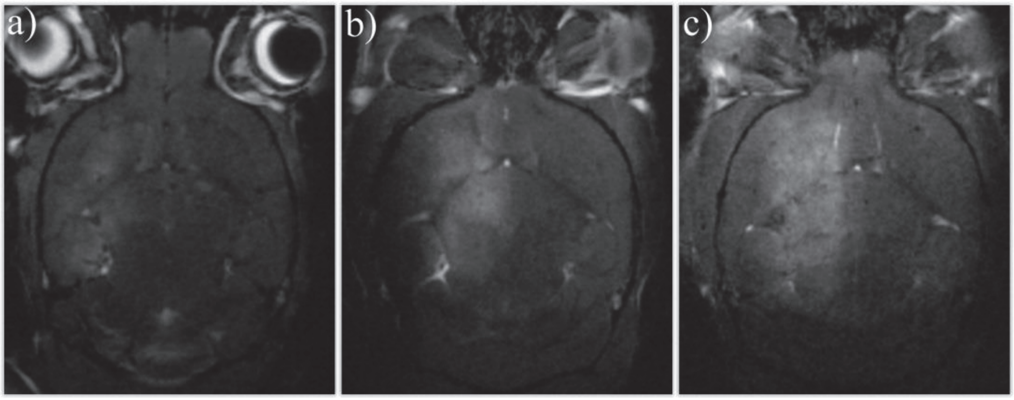

Fig. 2 FUS-mediated opening of the BBB using PIHCA NP-MB platform.

Different extents of BBB opening are shown in panels 2 a-c. The three brains show increasing amount of gadolinium-based contrast in the treated region, from hardly any contrast (Fig. 2a), to large areas of high intensity contrast (Fig. 2c) compared to the contralateral hemisphere.

T1 Flash images in MRI demonstrated some extent of red blood cell (RBC) extravasation. This was also evident from tile scans of histological brain sections (Fig 3).

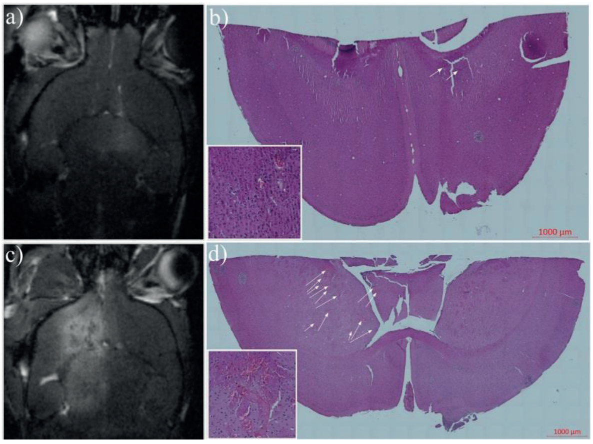

Fig. 3. RBC extravasation in H&E-stained brain sections. a-b) MR image of a brain with a corresponding H&E-stained section with limited RBC extravasation. c-d) MR image of another brain with corresponding H&E-stained section with considerable RBC extravasation. In b) and d), arrows show RBC extravasation, and insets show zoomed areas with RBC extravasation.

As shown in Fig. 3, the extent of RBC extravasation in brain sections varied from relatively small and localized, to covering large areas of the treated hemisphere.

3.4 NP transport across the BBB and distribution in the brain parenchyma and metastases

BBB opening-dependent transport of NPs following FUS exposure was demonstrated (Fig 4 a-d). The amount of NPs entering into the brain parenchyma and the extent of NP displacement from the nearest blood vessel wall correlated with increasing MR contrast agent intensity (Fig 4 e-f). As shown in Fig. 4 g-h, NPs were also visible in melanoma brain metastases, both inside and outside blood vessels.

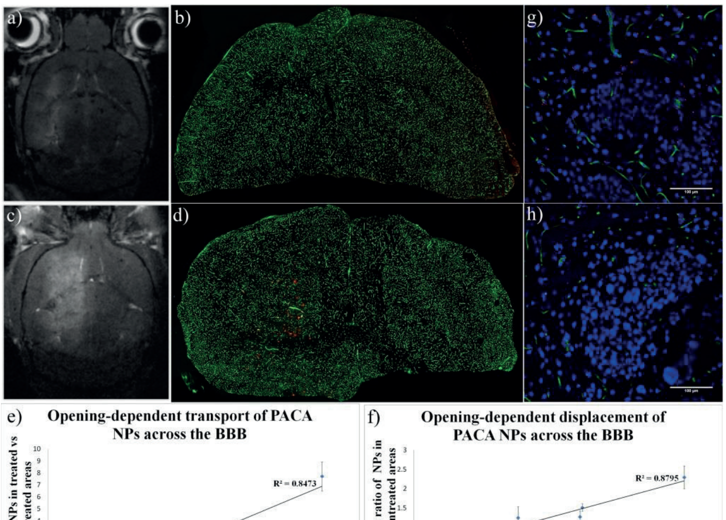

Fig. 4. FUS-mediated NP transport across the BBB and distribution in the brain parenchyma. a) MR image of a brain with a corresponding CLSM tile scan (b) showing little difference between NP content in the treated and untreated hemispheres. c) MR image of another brain with a corresponding CLSM tile scan (d) showing substantially greater differences between NP content in the treated and untreated hemispheres. e) opening-dependent transport of NPs across the BBB. n= 3-5 sections per mouse. f) opening-dependent displacement of NPs away from blood vessels. n= 3-5 sections per mouse. Error bars give standard error of the mean. g-h) CLSM images with tumor metastasis visible as a cluster of tightly packed nuclei. Red – NPs, blue – nuclei, green – blood vessels.

3.5 ARF effect on the displacement of NPs

To study whether ARF could increase the displacement of NP from blood vessels even further, smaller regions of brains were also treated with high frequency, high intensity FUS to generate ARF. A tile scan image of the entire brain is shown in Fig. 5a. Charts with individual circles representing median displacement values across one image of the tile scan of a brain section are shown for four animals in Fig 5b-5e.

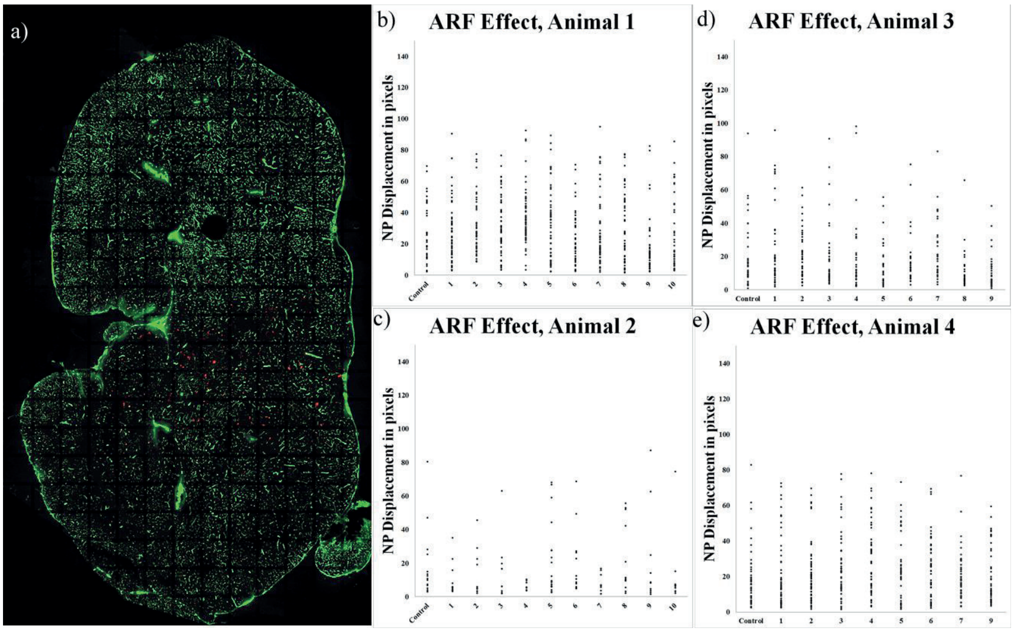

Fig. 5. The effect of the ARF on NP displacement in the brain parenchyma. a) a tile scan of an entire brain section taken with a 20x objective. NPs are shown in red and blood vessels in green. b-e) Image analysis results in four animals. Each column refers to one section. Control denotes a section from the brain area that only received 1.1 MHz FUS treatment, while numbered columns refer to sections located within and slightly extending beyond the estimate area of the ARF effect.

Little effect of the ARF can be observed in Fig. 5. Importantly, the tile scan in Fig. 5a is shown for illustration purposes only and the actual image analysis was performed on individual images (size: 1280x1280). It should also be noted that reasonable values of NP displacement from a given blood vessel in pixels were in a limited range since NPs displaced from a given vessel by a distance beyond that range would be detected as originating from another blood vessel.

3.6 P-gp effect

P-gp staining in the brains removed immediately after sonication is shown in Fig. 6 a-b.

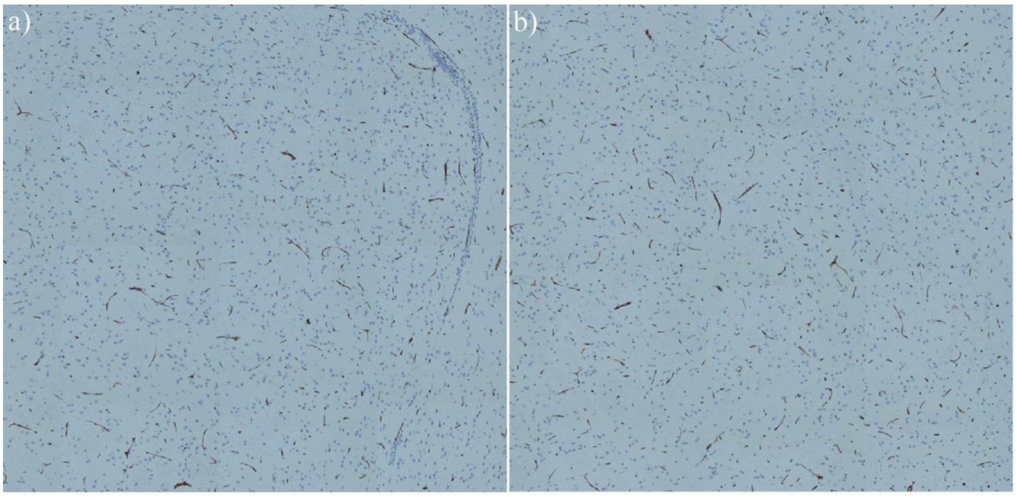

Fig. 6. The effect of FUS-mediated BBB opening on P-gp levels immediately after sonication. Fragment of a brain section tile scan showing P-gp staining in a) treated hemisphere, b) untreated hemisphere.

As can be seen in Fig. 6, FUS-mediated BBB opening does not seem to induce any apparent alteration in P-gp levels in the brain immediately after sonication.

4. Discussion

While it is difficult to deny the enormous potential advantages that materials science can confer to nanomedicine in preference to traditional drug formulations, the initial enthusiasm surrounding nanomedicine's application in the treatment of solid tumors has been called into question in light of the limited number of translational successes. A survey of the literature from the past 10 years has showed that solid tumors retain only 0.7% (median) of the administered NP dose [12]. The delivery of therapeutic NPs to the brain can be aided by BBB opening techniques such as FUS-mediated BBB disruption. However, even with FUS, the question is whether NP delivery to the brain parenchyma is sufficient to achieve a therapeutic effect.

In this work, BBB was opened using FUS in combination with a novel PIHCA NP-MB platform [29]. The platform consists of PIHCA NPs sized approx. 140-150 nm stabilizing MBs sized 1.6 µm. Our group has recently used this platform for FUS-mediated BBB opening in rats, demonstrating reversible BBB opening and the delivery of PBCA NPs into brain parenchyma [21]. In that study, several MIs were used; BBB opening could be occasionally achieved with the MI of 0.15 and consistently with an MI of 0.25 and higher. The application of MI 0.25 did not produce any pathology or RBC extravasation in histological sections. In the present work, we opened the BBB by applying FUS at a constant acoustic pressure of 0.38 MPa (MI = 0.31) throughout the study in order to obtain sufficient NP extravasation for quantitative measurement of NP distribution. The NP transport across the BBB correlated with the extent of BBB opening. In addition, the extent of BBB opening also correlated with RBC extravasation as observed in histological sections. However, a certain amount of RBC in the tissue might be clinically acceptable when treating a deadly disease such as brain tumors. We should note some important differences between this study and our previous work [21]. Here, a new MRI-guided FUS setup was used, making it possible to achieve more precise spatial control of the treated area. Another difference was the type of PACA monomer used. In [21], the PACA NP-MB platform was based on PBCA NPs, while in the current work PIHCA NPs were used as this monomer degrades more slowly which can be of therapeutic benefit. Degradation of PACA NPs is dependent on the length of the alkyl chain [9, 36] and PIHCA NPs have a slightly longer alkyl chain than PBCA NPs.

While NPs in our study were shown to be delivered to melanoma brain metastases, judging by visual inspection of CLSM images, NP delivery into metastases was restricted as compared to their delivery into the surrounding brain tissue. This is consistent with the properties of melanoma metastases at week 4 post-inoculation in our experimental model. As observed in [32], at this time point the mean vascular area fraction in the tumors is lower than in the normal brain. This is also evident in our CLSM images. In addition, as noted in [32], the BBB in melanoma metastases at week 4 post-inoculation is essentially intact, with only 1% of leaky tumors. It is therefore likely that reduced vascularization would diminish NP delivery into the tumor tissue in our study.

Assuming mainly paracellular transport across the BBB, NP size can be a critical factor. Size dependence of FUS-mediated NP transport has been investigated in several works. For instance, Choi et al. [37] used fluorescently labeled dextrans of 3, 70 and 2000 kDa and reported that the molecular weight of dextrans that could be delivered to the brain parenchyma using FUS in combination with SonoVue MBs (0.57 MPa corresponding to MI of 0.46) was between 70 kDa and 2000 kDa, and that 2000 kDa dextrans (54.4 nm) could not be delivered. However, in a subsequent study from the same group [38] 2000 kDa dextrans were delivered into brain parenchyma at 0.84 MPa. In contrast with [37], dextrans in that study were co-administered with

MBs (Definity) 6 seconds after the start of sonication. In a study using FUS exposure parameters that were similar to [37] and NPs injected after sonication at 0.45 MPa, the maximum gap between endothelial cells caused by FUS exposure was found to be close to 65 nm [39]. The authors suggested the transport of large objects >100 nm to be difficult, assuming purely paracellular mode of transport, and that in order to achieve substantial transport of large molecules with their FUS exposure protocol, they should be injected right after or present during sonication. In line with this observation, NPs of significantly larger size have been delivered into brain parenchyma using FUS-mediated BBB opening. For instance, [16] reported that biodegradable polymeric NPs sized 60 nm and 75-nm could be delivered across the BBB after FUS exposure when albumin MBs similar to Optison were co-injected with the NPs immediately prior to FUS exposure with a duration of 2 minutes. The extent of NP transport was shown to depend on the acoustic pressure. In [19], DNA-bearing NPs sized 100 nm and co-injected with the same MB as in [16] were delivered into brain parenchyma after FUS exposure with 0.6 MPa and a duration of 2 minutes. In [17], brain delivery transport of 50 nm, but also 120 nm gold NPs was reported after FUS-mediated BBB opening with approximately 0.23 MPa when NPs were injected 8 minutes prior to sonication. An overview of these studies indicates that the extent of brain delivery is dependent on numerous variables (properties of NPs, concentration and circulation time of MBs, FUS exposure parameters etc.), of which the most important ones appear to be the acoustic pressure and the presence of NPs in blood during sonication. In our study, the NPs, being part of the NP-MB platform, were present in the bloodstream during FUS and MB-mediated BBB disruption. NPs lining the shell of the MBs, moreover, were in the immediate proximity to the MBs during FUS-induced cavitation of the latter, which further facilitates their transport across the BBB.

This cavitation could further push NPs through the ECM. In addition to increased transport of NPs across the BBB, we found that FUS exposure increases NP distribution in the brain parenchyma, i.e. displacement from blood vessels, depending on the extent of BBB opening. From *in vitro* measurements, we known that the majority of the PIHCA NP-MBs will collapse at the specific acoustic settings and *in situ* acoustic pressure used in the current experiment. During sonication, the MBs will be pushed towards the endothelial cell lining, and it is well known that under asymmetric boundary conditions the bubble collapse will also be asymmetrical [40], resulting in a liquid jet impinging on, and potentially penetrating, the solid boundary (*i.e.* the endothelial lining). In addition to BBB opening, this process may also facilitate NP distribution in the brain tissue, which is a considerable advantage given that passive diffusion of NPs in the ECM can be very restricted, especially in the case of large NPs [16]. The effect of the ARF can further increase NP displacement from blood vessels, improving their distribution in the brain. It should also be noted that the intensities required to displace liquid and solid NPs using ARF are higher than in the case of gas-filled particles, and at these high intensities ARF acting on the bulk fluid can induce acoustic streaming whose effect can complement the force acting on NPs themselves and increase NP displacement in the brain parenchyma [28]. In our study, however, ARF did not produce any additional displacement on top of that caused by 1.1 MHz FUS. This may be due to the inherent limitation of the method used to assess the effect of the ARF in our work. Based on the image analysis, any NP displaced from a given blood vessel beyond the distance half way to the neighbor vessel would be registered as originating from that vessel. This makes it challenging to isolate the effect of the ARF if it is combined with the effect of another exposure (at 1.1 MHz) that already causes displacement of NPs.

Down-regulation of P-gp by US has been observed in glioma cells [41] and, in a very recent study, FUS caused localized P-gp down-regulation at the BBB 24-hour post-sonication [42]. In our study, no obvious effects of FUS on P-gp levels were observed immediately after sonication, indicating that FUS-mediated changes in P-gp activity, such as those observed in [42], are likely caused by signaling alterations that require a certain period of time post-sonication to exert their effect.

Overall, our results show that while FUS-mediated BBB opening, like any generic BBB opening technique, does appear to impose size restrictions on NP extravasation, combining NP and MP into a single unit such as the one used in our study can achieve a substantial increase in the transport and distribution of NPs larger than 100-150 nm in the brain parenchyma.

5. Conclusions

We have shown that our PACA NP-stabilized MB platform designed for application of FUS in drug delivery can transport NPs in substantial quantities across the BBB and achieve their distribution in the brain tissue, and that the NP transport and brain distribution depend on the extent of FUS-mediated BBB opening. Our results indicate that this novel platform has a potential in FUS-mediated drug delivery across the BBB and throughout the brain parechyma.

Conflict of interest:

The authors declare no conflict of interest.

Acknowledgements:

Anne Rein Hatletveit and Maria Gellein are thanked for technical assistance with NP and MB synthesis. Annemieke van Wamel and Tina Bugge are thanked for technical assistance with tail-vein cannulation. Astrid Bjørkøy is thanked for technical assistance with CLSM. Marius Widerøe is thanked for technical assistance with MRI. Brain sectioning and staining of brain sections was performed at the Cellular and Molecular Imaging Core Facility, NTNU. MRI imaging was performed at the MR Core Facility, NTNU. Animals used in this study were housed at the Comparative Medicine Core Facility, NTNU.

This study was funded by The Central Norway Regional Health Authority and The Research Council of Norway (NANO2021 project number 220005 and BIOTEK2021 project number 226159).

1. Pardridge, W.M., *The blood-brain barrier: bottleneck in brain drug development.* NeuroRx, 2005. **2**(1): p. 3-14.
2. Pardridge, W.M., *Drug transport across the blood-brain barrier.* J Cereb Blood Flow Metab, 2012. **32**(11): p. 1959-72.
3. Hawkins, B.T. and T.P. Davis, *The blood-brain barrier/neurovascular unit in health and disease.* Pharmacol Rev, 2005. **57**(2): p. 173-85.
4. Yildirimer, L., et al., *Toxicology and clinical potential of nanoparticles.* Nano Today, 2011. **6**(6): p. 585-607.
5. Sun, T., et al., *Engineered nanoparticles for drug delivery in cancer therapy.* Angew Chem Int Ed Engl, 2014. **53**(46): p. 12320-64.
6. Maeda, H., K. Tsukigawa, and J. Fang, *A Retrospective 30 Years After Discovery of the Enhanced Permeability and Retention Effect of Solid Tumors: Next-Generation Chemotherapeutics and Photodynamic Therapy-Problems, Solutions, and Prospects.* Microcirculation, 2016. **23**(3): p. 173-82.
7. Matsumura, Y. and H. Maeda, *A new concept for macromolecular therapeutics in cancer chemotherapy: mechanism of tumoritropic accumulation of proteins and the antitumor agent smancs.* Cancer Res, 1986. **46**(12 Pt 1): p. 6387-92.
8. Kumari, A., S.K. Yadav, and S.C. Yadav, *Biodegradable polymeric nanoparticles based drug delivery systems.* Colloids Surf B Biointerfaces, 2010. **75**(1): p. 1-18.
9. Sulheim, E., et al., *Cellular uptake and intracellular degradation of poly(alkyl cyanoacrylate) nanoparticles.* J Nanobiotechnology, 2016. **14**: p. 1.
10. Soma*, E., P. Attali, and P. Merle, *Chapter 11 A Clinically Relevant Case Study: the Development of Livatag[registered sign] for the Treatment of Advanced Hepatocellular Carcinoma*, in *Nanostructured Biomaterials for Overcoming Biological Barriers*. 2012, The Royal Society of Chemistry. p. 591-600.
11. Cecchelli, R., et al., *Modelling of the blood-brain barrier in drug discovery and development.* Nat Rev Drug Discov, 2007. **6**(8): p. 650-61.

12. Wilhelm, S., et al., *Analysis of nanoparticle delivery to tumours.* Nature Reviews Materials, 2016. **1**: p. 16014.
13. Hynynen, K., *Focused ultrasound for blood-brain disruption and delivery of therapeutic molecules into the brain.* Expert Opin Drug Deliv, 2007. **4**(1): p. 27-35.
14. Hynynen, K., *Ultrasound for drug and gene delivery to the brain.* Adv Drug Deliv Rev, 2008. **60**(10): p. 1209-17.
15. Etame, A.B., et al., *Focused ultrasound disruption of the blood-brain barrier: a new frontier for therapeutic delivery in molecular neurooncology.* Neurosurg Focus, 2012. **32**(1): p. E3.
16. Nance, E., et al., *Non-invasive delivery of stealth, brain-penetrating nanoparticles across the blood-brain barrier using MRI-guided focused ultrasound.* J Control Release, 2014. **189**: p. 123-32.
17. Diaz, R.J., et al., *Focused ultrasound delivery of Raman nanoparticles across the blood-brain barrier: potential for targeting experimental brain tumors.* Nanomedicine, 2014. **10**(5): p. 1075-87.
18. Lammers, T., et al., *Theranostic USPIO-Loaded Microbubbles for Mediating and Monitoring Blood-Brain Barrier Permeation.* Adv Funct Mater, 2015. **25**(1): p. 36-43.
19. Mead, B.P., et al., *Targeted gene transfer to the brain via the delivery of brain-penetrating DNA nanoparticles with focused ultrasound.* J Control Release, 2016. **223**: p. 109-17.
20. Hynynen, K., et al., *Noninvasive MR imaging-guided focal opening of the blood-brain barrier in rabbits.* Radiology, 2001. **220**(3): p. 640-6.
21. Aslund, A.K., et al., *Nanoparticle delivery to the brain--By focused ultrasound and self-assembled nanoparticle-stabilized microbubbles.* J Control Release, 2015. **220**(Pt A): p. 287-94.
22. Nance, E.A., et al., *A dense poly(ethylene glycol) coating improves penetration of large polymeric nanoparticles within brain tissue.* Sci Transl Med, 2012. **4**(149): p. 149ra119.
23. Dayton, P., et al., *Acoustic radiation force in vivo: a mechanism to assist targeting of microbubbles.* Ultrasound Med Biol, 1999. **25**(8): p. 1195-201.
24. Rychak, J.J., A.L. Klibanov, and J.A. Hossack, *Acoustic radiation force enhances targeted delivery of ultrasound contrast microbubbles: in vitro verification.* IEEE Trans Ultrason Ferroelectr Freq Control, 2005. **52**(3): p. 421-33.
25. Shortencarier, M.J., et al., *A method for radiation-force localized drug delivery using gas-filled lipospheres.* IEEE Trans Ultrason Ferroelectr Freq Control, 2004. **51**(7): p. 822-31.
26. Lum, A.F., et al., *Ultrasound radiation force enables targeted deposition of model drug carriers loaded on microbubbles.* J Control Release, 2006. **111**(1-2): p. 128-34.
27. Crowder, K.C., et al., *Sonic activation of molecularly-targeted nanoparticles accelerates transmembrane lipid delivery to cancer cells through contact-mediated mechanisms: implications for enhanced local drug delivery.* Ultrasound Med Biol, 2005. **31**(12): p. 1693-700.
28. Dayton, P.A., et al., *Application of ultrasound to selectively localize nanodroplets for targeted imaging and therapy.* Mol Imaging, 2006. **5**(3): p. 160-74.
29. Morch, Y., et al., *Nanoparticle-stabilized microbubbles for multimodal imaging and drug delivery.* Contrast Media Mol Imaging, 2015. **10**(5): p. 356-66.

30. Klymchenko, A.S., et al., *Highly lipophilic fluorescent dyes in nano-emulsions: towards bright non-leaking nano-droplets.* RSC Advances, 2012. **2**(31): p. 11876-11886.
31. Wang, J., et al., *A novel brain metastases model developed in immunodeficient rats closely mimics the growth of metastatic brain tumours in patients.* Neuropathol Appl Neurobiol, 2011. **37**(2): p. 189-205.
32. Thorsen, F., et al., *Multimodal imaging enables early detection and characterization of changes in tumor permeability of brain metastases.* J Control Release, 2013. **172**(3): p. 812-22.
33. Schneider, C.A., W.S. Rasband, and K.W. Eliceiri, *NIH Image to ImageJ: 25 years of image analysis.* Nat Methods, 2012. **9**(7): p. 671-5.
34. de Chaumont, F., et al., *Icy: an open bioimage informatics platform for extended reproducible research.* Nat Methods, 2012. **9**(7): p. 690-6.
35. Kamentsky, L., et al., *Improved structure, function and compatibility for CellProfiler: modular high-throughput image analysis software.* Bioinformatics, 2011. **27**(8): p. 1179-80.
36. Kante, B., et al., *Toxicity of polyalkylcyanoacrylate nanoparticles I: Free nanoparticles.* J Pharm Sci, 1982. **71**(7): p. 786-90.
37. Choi, J.J., et al., *Molecules of Various Pharmacologically-Relevant Sizes Can Cross the Ultrasound-Induced Blood-Brain Barrier Opening in vivo.* Ultrasound in Medicine & Biology, 2010. **36**(1): p. 58-67.
38. Chen, H. and E.E. Konofagou, *The size of blood-brain barrier opening induced by focused ultrasound is dictated by the acoustic pressure.* J Cereb Blood Flow Metab, 2014. **34**(7): p. 1197-204.
39. Marty, B., et al., *Dynamic study of blood-brain barrier closure after its disruption using ultrasound: a quantitative analysis.* J Cereb Blood Flow Metab, 2012. **32**(10): p. 1948-58.
40. Leighton, T., *The acoustic bubble. 1994.* ISBN: 0-12-44190-8, 1994: p. 531-536.
41. Zhang, Z., et al., *Low intensity ultrasound promotes the sensitivity of rat brain glioma to Doxorubicin by down-regulating the expressions of p-glucoprotein and multidrug resistance protein 1 in vitro and in vivo.* PLoS One, 2013. **8**(8): p. e70685.
42. Cho, H., et al., *Localized Down-regulation of P-glycoprotein by Focused Ultrasound and Microbubbles induced Blood-Brain Barrier Disruption in Rat Brain.* Sci Rep, 2016. **6**: p. 31201.

Supplementary Information

Supplementary Figure 1 shows FUS treatment planning, both for FUS exposure at 1.1 MHz and for FUS exposure at 7.8 MHz, as well as a schematic of brain sectioning after brain removal and estimation of the ARF exposure area using an MR image. A grid of 6x2 regions each with a diameter of 1.6 mm were treated with FUS at 1.1 MHz **(panel a)** for BBB opening. An area of 2x2 regions each with a diameter of 0.5 mm was treated with FUS at 7.8 MHz for ARF **(panel b)**. The position of ARF treated region was determined as shown in **panel d**.

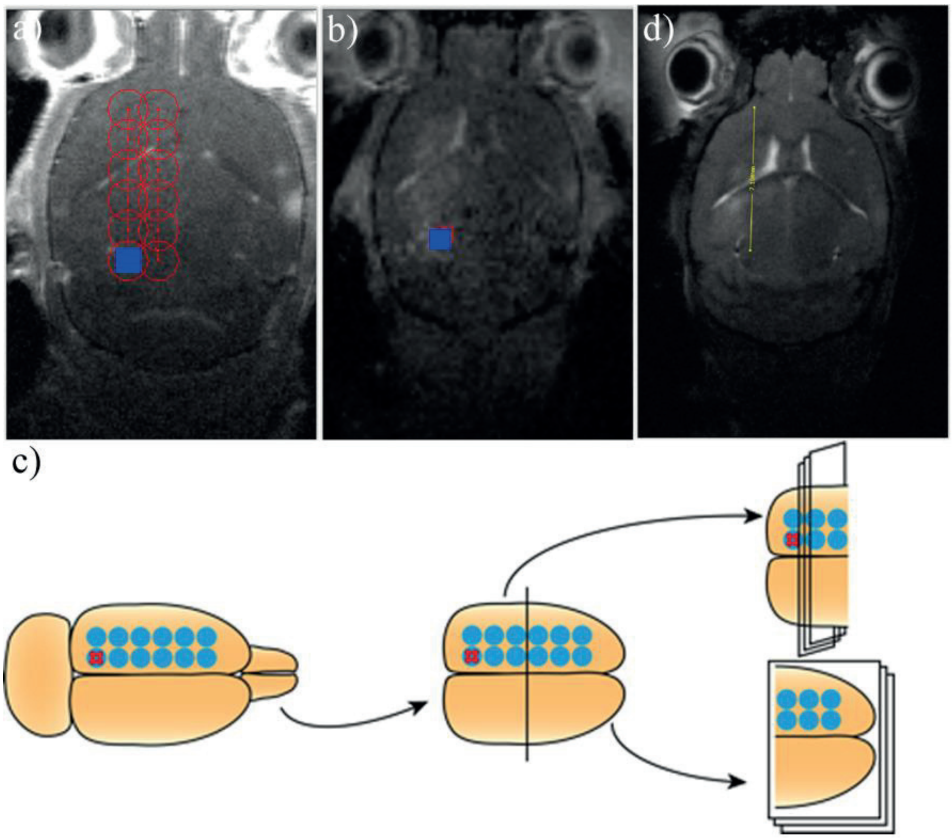

Supplementary Figure 1. Illustration of FUS treatment planning and post-treatment brain sectioning in the study. a) Treatment plan for FUS exposure at 1.1 MHz, b) treatment plan for FUS exposure at 7.8 MHz, c) brain sectioning schematics, d) estimation of the ARF exposure area.

Supplementary video 1 shows an intracardiac injection of human melanoma cells in a NOD/SCID mouse and will be available online.

Supplementary document 1 shows a description of image analysis used for the determination of NP displacement away from blood vessels.

Image analysis

For NP quantification and assessment of their displacement away from blood vessels, images with blood vessels were thresholded and segmented using a three-level Otsu thresholding algorithm. Blood vessel segmentation uses a median filter and has built-in filters to remove obvious debris. NP segmentation was performed without any median filtering and relied on the quality of the raw images, although it also has built-in filters to remove artefacts (extremely large clumps). The reason is that additional filtering even with a small filtering radius could eliminate a significant number of NP. For determining NP displacement from blood vessels, NPs with a certain axis length, deemed to be inside blood vessels even where the corresponding blood vessel staining either failed or produced a signal that was too weak, were eliminated. Afterwards, NPs located outside of blood vessels were isolated by applying a sequence of image masks. Finally, the distance between NPs and the nearest blood vessels was found by object expansion until the neighboring pixels touched. Image analysis of model images and confocal image scenarios is shown below.

Analysis of model images

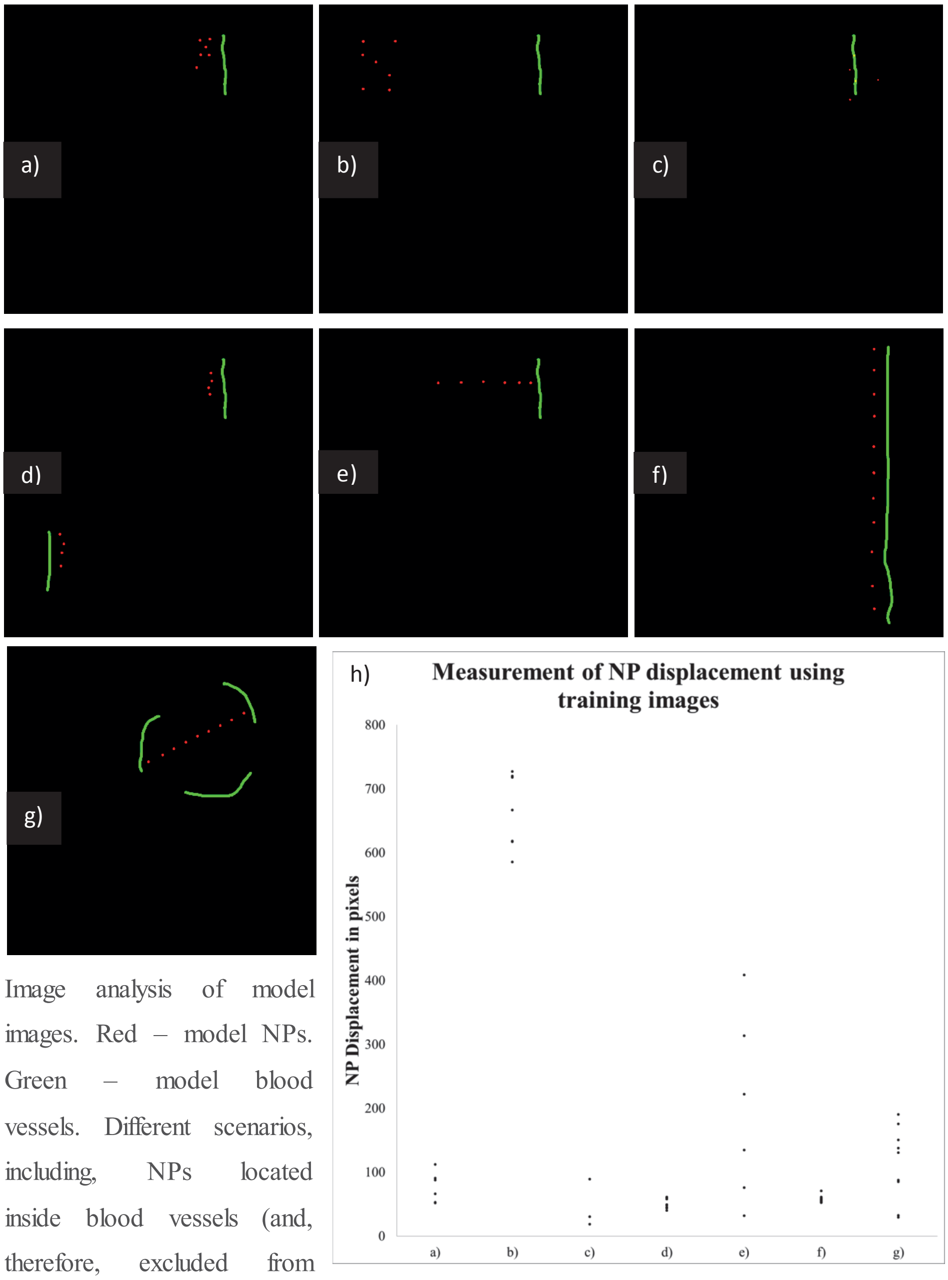

Image analysis of model images. Red – model NPs. Green – model blood vessels. Different scenarios, including, NPs located inside blood vessels (and, therefore, excluded from displacement quantification – panel c) are shown in Panels a-g. Quantification results are shown in Panel h.

Shown below are several of the actual CLSM image scenarios used in algorithm training and optimization. For illustration purposes, scenarios are divided into four images. The first two images in a row are raw unprocessed images showing blood vessels and NPs, respectively. The 3rd image shows segmented NPs overlaid on segmented blood vessels. In this image, NPs that are inside blood vessels are shown in blue (based the application of masks), and NPs outside of blood vessels are shown in red. No other filtering steps are applied in this image. The 4th image is similar to the 3rd except that NPs seemingly located outside of blood vessels have been additionally filtered to exclude those that are deemed to be inside blood vessels, even though staining of the corresponding blood vessel either failed or was too dim to be accurately segmented in a uniform segmentation applied to all images in the dataset. Additional filters applied on the image level are: **1)** blood vessel count over 50, **2)** blood vessel area between 2 and 12% of the image, **3)** number of NPs outside blood vessels over 3, and **4)** the ratio of the number of NPs located within 100 to 1000 pixels from the nearest blood vessel to the number of NPs located within 100 pixels from the nearest blood vessel less than 0.5 (this threshold substantially exceeds the average ratio of ≤ 0.1 and is set to adjust for all reasonable scenarios). These are referred to as **exclusion criteria**.

Training scenario 1: Regular Scenario

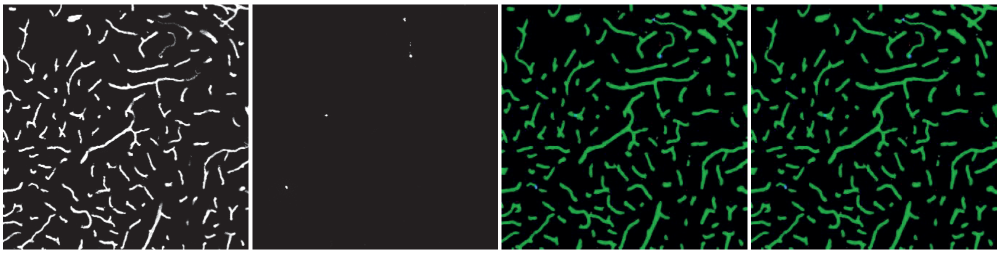

This is a good scenario showing NPs both inside and outside of blood vessels. No particular image analysis challenges are observed here.

Training scenario 2: All NPs inside blood vessels

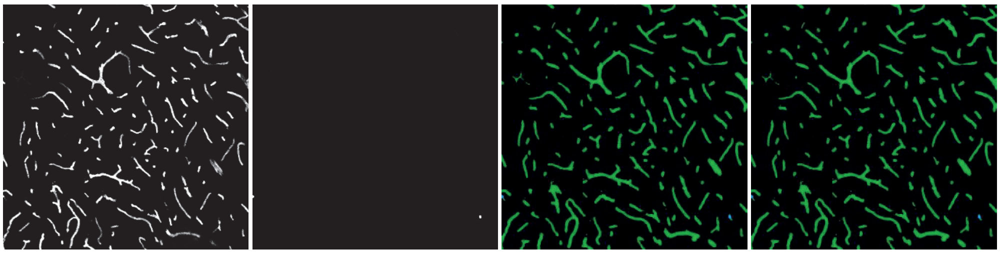

Again, relatively easy scenarios similar to Scenarios 1-2. Isolated spots are can still be detected outside of blood vessels, but the image fails the NP count exclusion criterion **(Exclusion Criterion 3).**

Training scenario 3: Unrealistic Blood Vessels

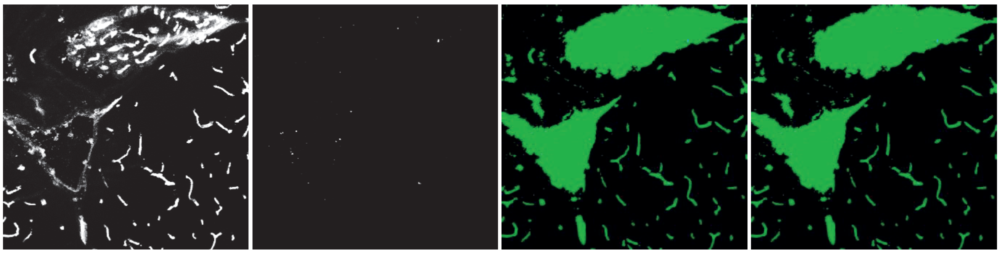

This scenario clearly shows an abnormal segmentation result. Filters could easily be applied to remove the two large 'blood vessel' clumps, but we preferred to filter out the entire image instead, based on the unreasonably large blood vessel area (25.5% of the image), i.e. this image failed **Exclusion Criterion 2**.

Training scenario 4: Dispersed NPs without blood vessels

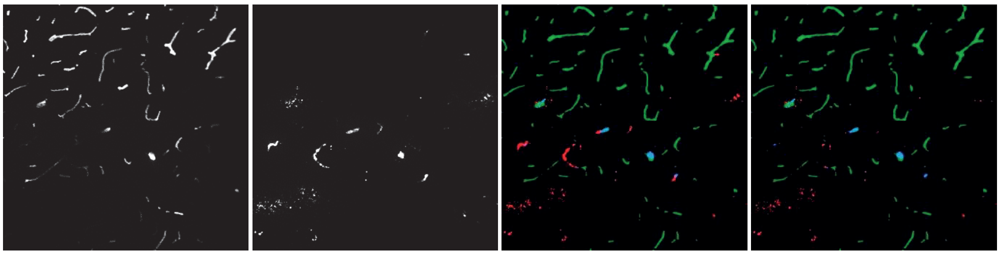

This is a relatively difficult scenario. Clumps of NPs that are clearly inside blood vessels, even though the corresponding blood vessel staining failed, can be filtered out easily (see below). However, we decided not to remove a cluster of NPs in the lower left corner even though they may or may not originate from a blood vessel that is not visible due to failed staining. This is both because of the lack of obvious exclusion criteria (no clear line connecting the NPs, unless one believes they have originated from a very thick blood vessel where the staining happens to have failed and the possibility that these NPs may have actually been displaced from the nearest visible blood vessel. In addition, the use of very sophisticated parameters (number of neighbors detected within a certain distance etc.) would considerably increase processing time and could affect segmentation in other images in a manner that can be difficult to predict, assuming uniform application of the algorithm throughout the entire dataset. However, this particular image is filtered out altogether, based on **Exclusion Criterion 4**. In this image, the ratio is 0.98, well above the average value. In addition, while this image does not fail **Exclusion Criterion 2**, it is very close to the criterion's lower limit.

Training scenario 5: Clumped NPs

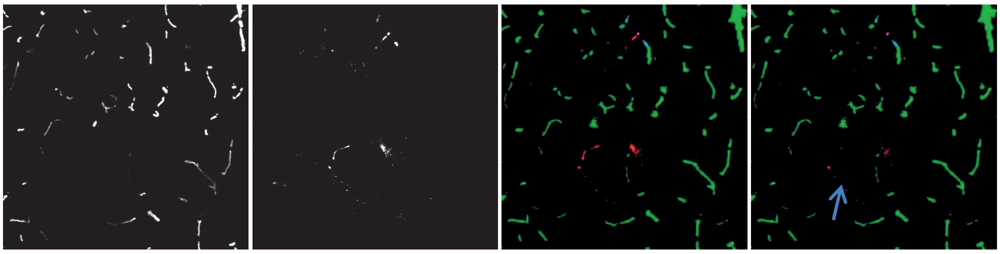

This is a fairly common case observed when there is a substantial number of NPs in an image. Some of the NPs in clumps are clearly in the blood vessels and are filtered by using axis length as a criterion. Setting the limit to exclude these and other similar clumps is a subjective call based on visual inspection of images, but the same criterion is applied to all images in the dataset. One can argue that the isolated group of the NPs located along a line (indicated by an arrow) should also be filtered. This is, however, not a trivial task to be performed consistently in automated image analysis.

Training scenario 6: Few NPs, mostly inside blood vessels

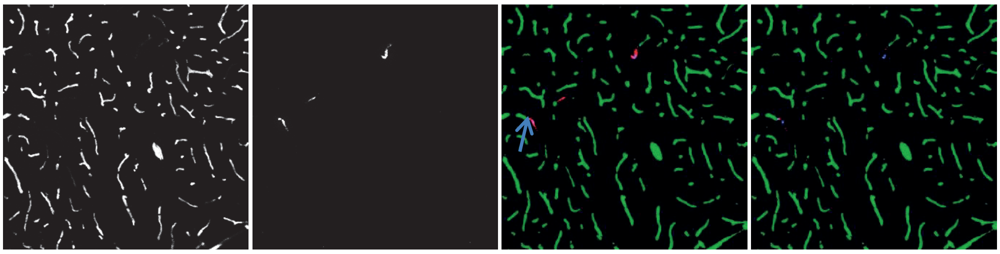

A relatively easy scenario, mostly shown to illustrate filtering or NPs that are deemed to be inside their adjacent blood vessels (indicated by an arrow).

Training Scenario 7: Clustered and elongated NPs

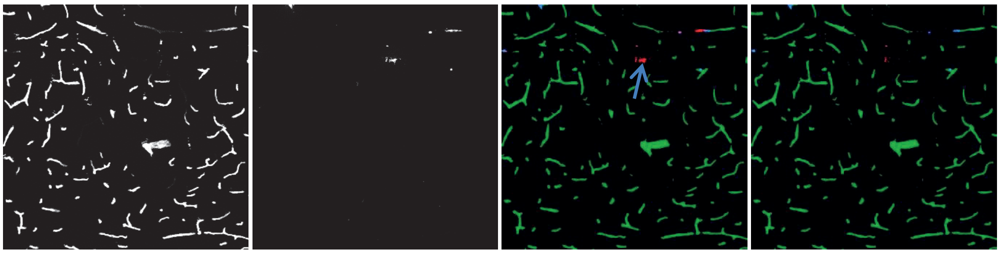

This scenario shows both clustered and elongated NPs. The group of NPs indicated by an arrow most likely originates from a blood vessel, and the central part is filtered out, although the dispersed cloud is retained. This is similar to Scenario 5.

Training Scenario 8: Very few blood vessels with poor staining, large spread of NPs

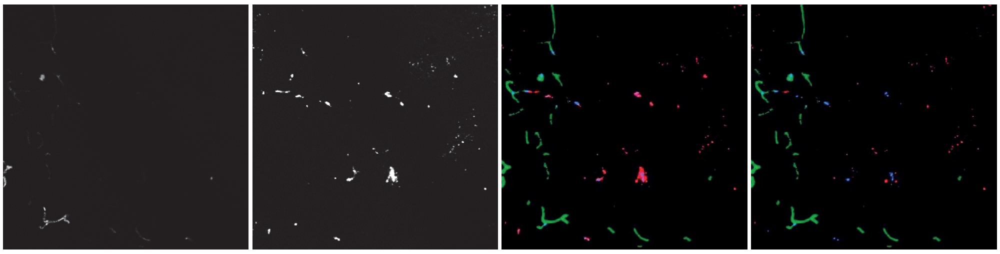

This is a relatively easy scenario. While the algorithm segments blood vessels rather well, given poor staining quality, this image fails several exclusion criteria at once (total area of blood vessels in the image being too low, number of segmented blood vessels being too low, and the ratio of NPs located within 100 to 1000 pixels from the nearest blood vessel to NPs located within 100 pixels from the nearest blood vessel being too high.